ZnO nanowire microelectrode arrays for integration with neuronal networks

by

Mohsen Maddah

A thesis
submitted to the Victoria University of Wellington
in fulfilments of the requirements for the degree of
Doctor of Philosophy
in Physics

Victoria University of Wellington
2020

Abstract

Microelectrode arrays (MEAs) have been shown as a successful approach for neuroscientists to monitor the signal communication within the neuronal networks for understanding the functionality of the nervous system. However, using conventional planar MEAs is shown to be incapable of precise signal recording from neuronal networks at single-cell resolution due to low signal-to-ratio (SNR). This thesis looks at developing an electronic platform that comprises of zinc oxide nanowires (ZnO-NWs) on MEAs as a future device to record action potential (AP) signals with high SNR from human neuronal networks at single-cell resolution. Specifically, I studied the controlled growth of ZnO nanowires with various morphologies at exact locations across the substrate. I then investigated the biocompatibility of ZnO nanowires with different morphology and geometry for interaction with human NTera2.D1 (hNT) neurons. Finally, I examined the electrical characteristics of MEAs that were integrated with ZnO nanowires and metal encapsulated ZnO nanowires in comparison to the planar MEAs.

The hydrothermal growth of ZnO nanowires is thoroughly investigated as a technique to allow synthesis of the nanowires at a low temperature (95°C) with a low cost and high scalability that can also be applied on flexible substrates. The morphology of the ZnO nanowires was varied (diameters of 20–300 nm, lengths of 0.15–6.2 µm, aspect ratios of 6–95 and densities of 10–285 NWs/µm^2) by controlling the critical growth parameters such as the precursor concentration (2.5–150 mM), growth time (1–20 h) and additive polyethylenimine (PEI) concentration (0–8 mM). The diameter and length of the ZnO nanowires were increased by increasing the precursor concentration and growth time. Using the standard precursor concentration of 25 mM, growth times of up to 4 h were found effective for the active growth of the nanowires due to the consumption of the precursor ions and precipitation of ZnO. The addition of 6 mM PEI to the growth solution was shown to mediate the growth solution, allowing the extension of the nanowire growth to 20 h or longer. The PEI molecules were also attached to the lateral faces of the nanowires that confined their lateral growth and promoted their axial growth (enhanced aspect ratio from 12 ± 3 to 67 ± 21).

Standard photolithography techniques were also introduced to selectively grow ZnO nanowires on exact locations across the substrates. The role of the ZnO seed layer geometry,

seed layer area and gap, on the growth of ZnO nanowires was also investigated. Despite using the constant growth parameters (25 mM of precursor concentration with 4 h of growth time) changing the seed line widths (4 µm–1 mm) and the gap between the seed lines (2 µm–800 µm) resulted in the morphology of the nanowires to vary across the same substrate (diameters of 50–240 nm, lengths of 1.2–4.6 µm, aspect ratios of 9–34 and densities of 28–120 NWs/µm^2). The seed area ratio of 50% was determined as a threshold to influence the nanowire morphology, where decreasing the seed area ratio below 50% (by increasing the adjacent gap or decreasing the seed layer area) increased the growth rate of the nanowires.

The biocompatibility of ZnO nanowires with human hNT neurons was investigated in this work for the first time. The adhesion and growth of hNT neurons on the arrays of ZnO nanowire florets were determined to be influenced by both geometry and morphology of the nanowires. The growth of the hNT neurons was promoted by 30% compared to the control Si/SiO$_2$ substrate surface when ZnO nanowires with lengths shorter than 500 nm and densities higher than 350 NWs/µm^2 were grown. The hNT neurons on all nanowires were also demonstrated to be functionally viable as they responded to the glutamate stimulation.

ZnO nanowires were shown to improve the electrical properties of the MEAs by reducing the electrochemical impedance due to the increased 3D surface area. The ZnO nanowires that were grown with 50 mM of precursor concentration for 4 h of growth time lowered the impedance from 835 ± 40 kΩ of planar Cr/Au MEAs to 540 ± 20 kΩ at a frequency of 1 kHz. In contrast, the ZnO nanowires that were grown with PEI for 35 h showed that despite the increased surface area by a factor of 45× the impedance was found to be quite high, 2.25 ± 0.2 MΩ at 1 kHz of frequency. The adsorption of PEI molecules to the lateral surfaces of the nanowires was thought to behave as a passivation layer that could have restricted the charge transfer characteristics of the ZnO-NW MEAs.

Encapsulation of the pristine ZnO nanowires that were grown with standard precursor concentration of 25 mM for 4 h of growth time with different metallic layers (Cr/Au, Ti and Pt) further improved the electrical characteristics of the MEAs. The ZnO nanowires that were encapsulated with a 10 nm thin layer of Ti and Pt achieved the lowest electrochemical impedance of 400 ± 25 kΩ at 1 kHz in this work. The robustness of the Ti encapsulated ZnO nanowires were also improved in comparison to the PEI ZnO nanowires. The improved electrochemical characteristics and mechanical stability of the MEAs integrated with metal encapsulated ZnO nanowires have shown a great promise for improving the SNR of recording signals from neuronal cells for long term measurements.

This work concludes that both pristine ZnO nanowire MEAs and metal encapsulated ZnO nanowire MEAs will be capable of recording AP signals from human neuronal networks at single-cell resolution. However, further optimisation and extensions of the work are required to record AP signals from human neuronal cells.

Acknowledgements

I am very grateful that I did a PhD in the area that I was very interested in. Doing it would not be possible without the support of Victoria University of Wellington, Marsden Fund, MacDiarmid Institute, my supervisors, colleagues, friends and family.

Firstly, I would like to express my sincere gratitude to my supervisor, Natalie Plank, for giving me the opportunity to do a PhD in physics. Thank you for all your advice, feedback, encouragement and guidance throughout the PhD course. You have made my PhD such a pleasant journey that I have learnt so many lessons both in academic and in real life.

To Charles Unsworth, my secondary supervisor, for your feedback and guidance that helped in my PhD and the papers. I should also acknowledge Brad Raos and Yi Wang that worked under the supervision of Charles Unsworth at The University of Auckland and collaborated with me on the papers and advised me on the biological part of this research.

To the Victoria University academics: Gideon Gouws, Franck Natali, Ben Ruck, Joe Trodahl and Ciaran Moore for all your support and guidance during my PhD. Special thanks to Gideon Gouws, my honours supervisor, that allowed me to access his laboratory and equipment, and advised me on the electrical part of my PhD and my paper.

To all of the graduate students who worked alongside me in the cleanroom laboratory: Rifat Ullah, Leo Browning, Conor Burke-Govey, Thanihaichelvan Murugathas, Hannah Zheng, Campbell Matthews, Hamish Colenso, Matthew Cryer, Hong Phan Nguyen Thi, Felicia Ullstad, Jackson Miller, Will Hewett, Ali Shaib, Erica Happe, Erica Cassie and Nireekshan Sodavaram. I am very grateful to work alongside you every day, and the knowledge and experience that you shared with me helped to solve the problems that I was facing. Special thanks to Rifat Ullah for your advice and for proofreading my papers and thesis chapters.

To all of the technicians: Alan Rennie, Nick Grinter, Alex Puglisi, David Flynn, Sarah Spencer, Peter Cord, Chris Lepper, Jason Edwards, Tim Exley, for helping me in building the mechanical parts and fixing problems in the laboratory.

To my family, who always supported me and encouraged me to do the PhD. Special thanks to my brother, Hamid Maddah, for always being there to support me on everything in my entire life. Finishing my studying would never be possible without your help. I owe you all my life, and now that you are suffering from MS for the rest of your life I will be there with you forever. To my beloved brother, Hamid Maddah:

دنیا همه هیچ و کار دنیا همه هیچ
ای هیچ برای هیچ بر هیچ مپیچ
دانی که از آدمی چه ماند پس مرگ
عشق است و محبت است و باقی همه هیچ

The world is all nothing and the work of the world is all nothing
O ' nothing, don't turn around for nothing

Do you know what is left of a human being after death
It is love and kindness and the rest is nothing

—Maulaana Jalaluddin Balkhi "Rumi" (13th century)

Contents

List of Figures

Chapter 1

Introduction

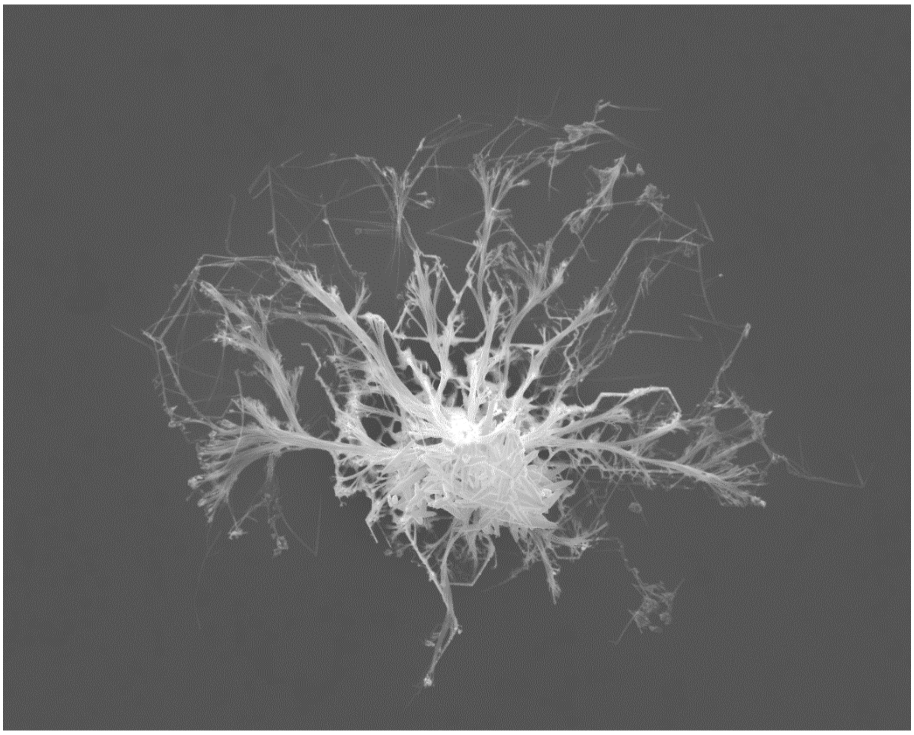

A microscale ZnO brain that is thinking about treating neurological disorders.

1.1 Motivation

Neurological disorders are one of the most common diseases among people worldwide. According to the World Health Organization (WHO) of the United Nations [1,2], around one billion people globally suffer from neurological disorders, ranging from Alzheimer's and Parkinson's disease to epilepsy and stroke. Subsequently, neuroscience has been a significant subject of research over recent years to study the nervous system thoroughly for treating neurological disorders. Advancing knowledge in neuroscience requires a better understanding of the communication and processing mechanisms that take place in neuronal networks. Over the last few decades, a large number of researchers have made efforts to develop such a technology that can precisely monitor communication through a neuronal network down to a single-cell resolution. The development of such a technology would enable neuroscientists to better understand the mechanisms of neuronal networks that are responsible for human learning, memory, sending and functioning. The obtained understanding can then be utilised for treating neurological disorders such as Alzheimer’s disease [3], Parkinson’s disease [4], epilepsy [5], hypoxic ischemia [6] and stroke [7,8].

The complexity of the brain, as well as the limited accessibility and lack of freedom in the *in vivo* experiments, make *in vitro* experimentation more valuable [9]. *In vitro* experimentation simplifies the complexity of the process by running a controlled experiment on a brain slice or a culture of dissociated neurons. New devices/technologies for neuronal applications should primarily be evaluated *in vitro*. The *in vitro* studies can also yield valuable information about the physical configuration and biological environments for the interaction of the neurons with the devices [10]. The knowledge gained from the *in vitro* experiments can then be extended for solving *in vivo* problems. This work aims to develop a new device that allows neuroscientists studying neuronal networks at single-cell resolution *in vitro*.

The communication within the neuronal network *in vitro* can be monitored via various techniques that can mainly be categorised into intracellular [11–16] and extracellular [17–24] techniques. The conventional intracellular techniques insert an electrode/micropipette inside a neuron body for measuring the transmembrane voltage across the neuron. The intracellular techniques can record neuronal signals with high amplitudes in mV range from individual cells, but they are limited to short term monitoring of very few neurons due to their physical constraints and invasiveness to the neurons [25]. Extracellular techniques usually apply microelectrode arrays (MEAs) to measure ionic currents of a neuronal cell membrane that correspond to the action potential signals (APs). In contrast to the intracellular techniques, the extracellular techniques are non-invasive and allow long-term measurements on a large number of neurons [25]. However conventional extracellular techniques can only record neuronal signals at low amplitude (0.1–5 mVpp [25]) with a low signal-to-noise ratio (SNR), making them incapable of recording subthreshold synaptic potentials from neurons. Due to the current limitation of both intracellular and extracellular techniques, there is a need for further development of a device that allows monitoring of neuronal networks at a single-cell resolution for an extended time. Since MEAs are capable of monitoring a large number of neurons for a long time and have the potentials for high temporal and spatial resolutions, MEAs have been the main subject of research and development in neuroengineering over recent years.

There already exists a number of commercial devices that apply extracellular techniques for monitoring neuronal network communication *in vitro*. The CMOS-MEA5000-System from Multi Channel Systems [26], BioCam 4096 from 3Brain [27], and MED64 system from Alpha MED Scientific [28] are the most commonly used MEA systems for this purpose. Despite the ability of these devices to record from a large number of electrode sites (maximum of 4225), they require higher spatial and temporal resolutions to detect subthreshold synaptic potentials from neurons at single-cell resolution.

Recording AP signals from neuronal networks at single-cell resolution demands small microelectrodes comparable to the neuronal cells. However, as the size of the electrodes reduces, their impedance increases and their recording SNR decreases. Applying nanomaterials is revealed to significantly improve spatial and temporal resolutions of MEAs by increasing the surface area due to their 3D topology. Gold nanostructures [17,29–32], carbon nanotubes (CNTs) [33–35], silicon nanowires (Si-NWs) [12,36,37] and platinum nanowires (Pt-NWs) [15,38] are the most common nanomaterials that have been applied on MEAs to improve their electrical characteristics as well as the spatial and temporal resolutions for neuronal applications.

A more recent introduction to nanowire technology for neuronal applications has been the introduction of zinc oxide nanowires (ZnO-NWs), a natural n-type semiconductor, commonly used in light-emitting diodes (LEDs) [39], solar cells [40–42], biosensors [43–45] and piezoelectric devices [46–48] due to their excellent electronic and photoelectronic properties. Other favourable properties of ZnO nanowires are that they can be grown via hydrothermal synthesis, at a low temperature (below 100°C), with a low cost and high scalability. ZnO nanowires can also be grown on flexible substrates, by using the hydrothermal synthesis, that is ideal for both *in vitro* and *in vivo* biological applications [43]. Despite the great potentials of ZnO nanowires for integration with MEAs, Ryu *et al.* [49] are the only group that recently used MEAs with ZnO nanowires for recording signals from rat’s brain tissue (*in vivo*). Thus, it is desired to further study and develop the synthesis of ZnO nanowires on MEAs due to their novelty in neuronal applications

1.2 Thesis outline

This thesis consists of 7 chapters with 3 results and discussion chapters on hydrothermal synthesis of ZnO nanowires, the biocompatibility of ZnO nanowires with human hNT neurons, and characterisation of MEAs with ZnO nanowires. A breakdown of the thesis chapters is presented below to outline the thesis content.

Chapter 2: Microelectrode arrays (MEAs)

Chapter 2 introduces microelectrode arrays (MEAs) as a technique for monitoring the neuronal network *in vitro*. The literature of the MEAs are explored extensively to identify the strength and weakness of different MEAs. The microelectrode-cell interface is also modelled to determine the significant electrical parameters that need to be improved for recording signals from the neuronal cells with high signal-to-noise (SNR). Furthermore, the fundamental properties and synthesis approach of ZnO nanowires are explored that demonstrates their suitability for integration with MEAs for neuronal applications.

Chapter 3: Experimental details

Chapter 3 describes the experimental processes and the characterisation techniques that were applied throughout this thesis. The hydrothermal growth of ZnO nanowires and fabrication of MEAs in different configurations are described as were utilised in the results Chapters 4–6. Furthermore, the techniques that were applied for characterising the morphology, biocompatibility, electrical properties and robustness of the samples are introduced in details.

Chapter 4: Selective growth of ZnO nanowires

Chapter 4 investigates the hydrothermal synthesis approach to control the morphology and geometry of the ZnO nanowires. The influence of the hydrothermal growth parameters such as the precursor concentration, growth time and additive polyethylenimine (PEI) on the morphology of the nanowires are investigated. The geometry of the ZnO nanowires is governed by controlling the location and area of the ZnO seed layer on the substrates. The ZnO seed layer is also determined as a parameter that can control the morphology of the nanowires as well as their geometry. The theory behind the hydrothermal growth kinetics is also investigated to explain the influence of the hydrothermal growth parameters and the seed layer on the morphology of the ZnO nanowires.

Chapter 5: Human Neurons on ZnO nanowire florets

Chapter 5 examines the biocompatibility of ZnO nanowires in the form of floret arrays with human NTera2.D1 (hNT) neurons. The influences of the ZnO nanowire morphology and the array geometry on the adhesion and growth of the hNT neurons are investigated. The localisation of the hNT neurons within the ZnO nanowire arrays is also examined showing their interaction with individual ZnO nanowire florets. The adhesion and growth of the hNT neurons are shown to be promoted on the short nanowires with high densities. Furthermore, the hNT neurons are demonstrated to be functionally viable on the ZnO nanowire arrays as they respond to the glutamate stimulation.

Chapter 6: ZnO nanowire microelectrode arrays (ZnO-NW MEAs)

Chapter 6 investigates the integration of ZnO nanowires with microelectrode arrays (MEAs) and characterise their electrical properties and robustness for compatibility in neuronal applications. ZnO nanowires with different morphology are grown on MEAs, and their electrical characteristics are examined through electrochemical impedance spectroscopy. MEAs with ZnO nanowires reduced the electrochemical impedance as desired for recording neuronal signals with high SNR, in comparison to the control planar Cr/Au MEAs. An equivalent circuit is also applied to model the electrochemical impedance of the MEAs in different configurations. ZnO nanowires are also encapsulated with different metallic layers (Cr/Au, Ti and Pt) that further improved their electrochemical impedance as well as the robustness stability that make them ideal for long term neuronal applications.

Chapter 7: Conclusion and future work

Chapter 7 summarises the key results of this thesis to highlight the suitability of ZnO nanowires achieved in this work for neuronal applications. Future work extension of this work is also discussed herein.

Chapter 2

Microelectrode Arrays (MEAs)

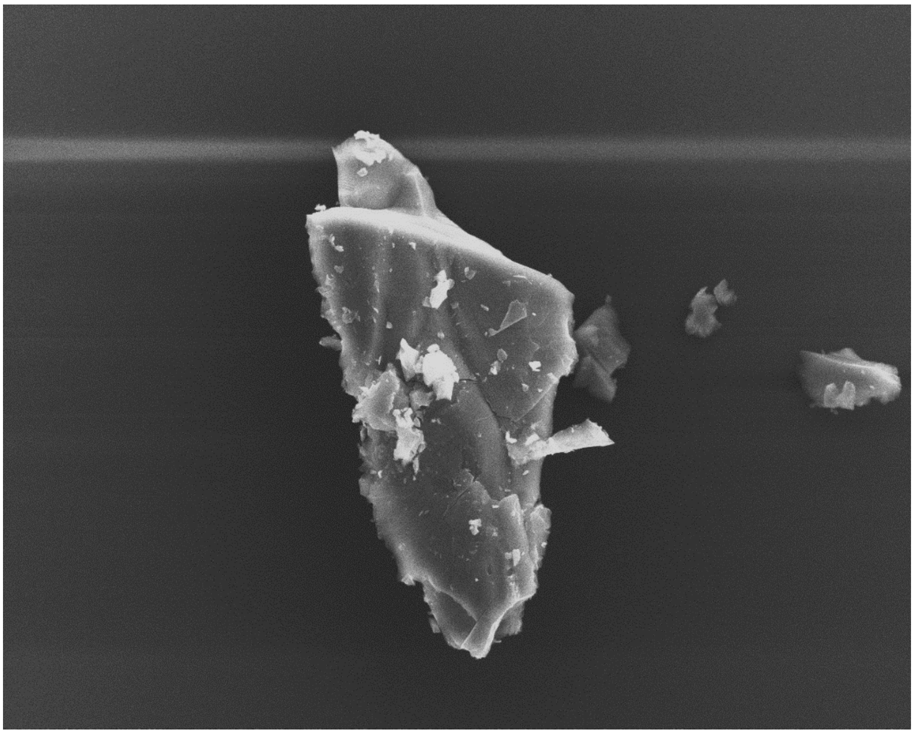

An unknown iceberg that is a thousand times smaller than a hair. Maybe that is why some politicians think that global warming is not very serious.

2.1 Introduction

This chapter studies the mechanisms that take place in the neuronal networks for the signal communication between the cells and introduces the techniques that have been used for recording these signals. The literature on the microelectrode arrays (MEAs) that have been used for recording neuronal signals *in vitro* are reviewed extensively to identify their weakness and strength. The interaction between the neuronal cell and the microelectrode is also modelled to show how the signal resolution of MEAs can be improved. The fundamental properties of zinc oxide nanowires (ZnO-NWs) are then studied, showing their potential for integration with MEAs for neuronal applications. Furthermore, the techniques in the synthesis of ZnO nanowires are studied that can be utilised in for the fabrication of MEAs with ZnO nanowires in this work.

2.2 Neuronal network communication

2.2.1 Fundamentals in neuronal network communication

The functionality of neuronal network communication is based on the propagation of signals, known as Action Potentials (APs). Intracellular and extracellular environments of a neuronal cell consist of abundant ions (mainly sodium (Na^+), potassium (K^+) and chloride (Cl^-)) [50], as shown in Figure 2.1 (a). When a neuronal cell is inactive, the concentration gradient of the ions across the cell membrane results in a potential difference, known as the resting potential (V_{rest}) [50]. The resting potential is typically in the range of −85 mV to −60 mV, e.g. −62 mV for pyramidal neurons [51] as shown in Figure 2.1 (b), where excessive negative charges exist inside the cell relative to the outside. Once an external stimulus is applied to a cell that is strong enough to raise the membrane potential over a threshold value (V_{thresh}, e.g. −53 mV for pyramidal neurons [51] as shown in Figure 2.1 (b)), a signal depolarisation takes place. The depolarisation causes ion channels of the cell membrane to open for the passage of specific ions, as shown in Figure 2.1 (a). As a result, the potential difference across the cell membrane rapidly rises to about +30 mV [25,52] and then falls back to the resting potential

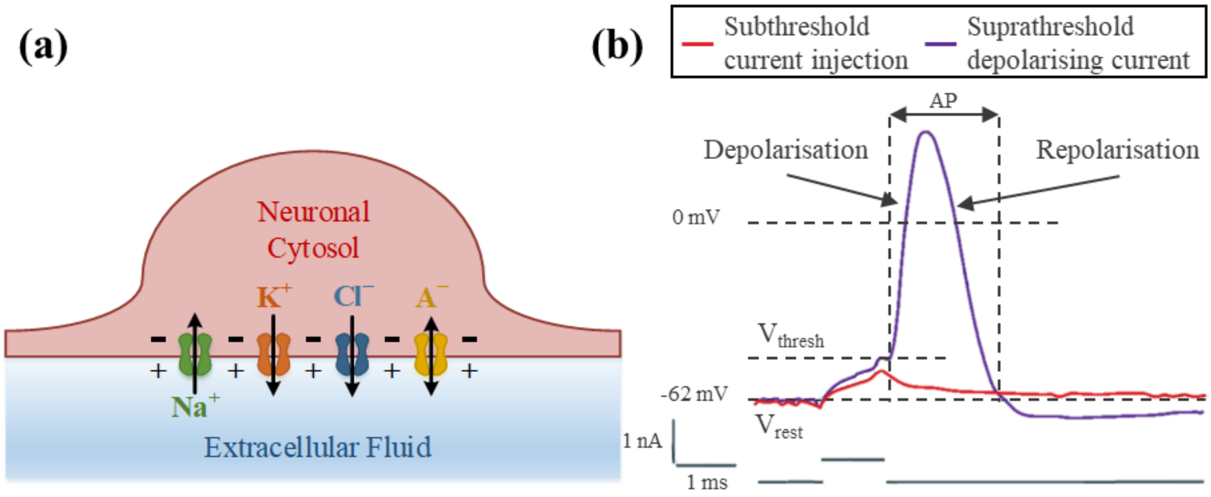

Figure 2.1. (a) Schematic showing the ion concentration inside and outside of the neuronal cells. The ion channels are embedded transmembrane proteins that allow selective passage of specific ions: sodium (Na^+), potassium (K^+), chloride (Cl^-), and other anions (A^-, e.g. phosphate). The intracellular of the neuron (cytosol) is negatively charged relative to the extracellular space at the inactive state (resting). (b) Action potential (AP) of a rat hippocampal pyramidal neuron that was evoked by the injection of a suprathreshold depolarising current (purple), while the subthreshold current injection (red) did not result in firing an action potential. The neuronal cell had a resting potential (V_{rest}) of −62 mV and a threshold potential (V_{thresh}) of about −53 mV. The figure (b) is modified from [51].

(repolarisation) at a frequency of 800-3000 Hz (typically at 1 kHz) [35], as shown in Figure 2.1 (b). The generated AP can then propagate along the neurites towards the other neurons for transmission of the signals within the neuronal network.

2.2.2 Intracellular vs Extracellular techniques

Monitoring of the neuronal communication can be conducted by various techniques that can be categorised into intracellular [11–16] and extracellular [17–24] approaches, as shown schematically in Figure 2.2. The conventional intracellular technique inserts an electrode or micropipette inside a neuron body to measure the transmembrane voltage across the neuronal cell, as shown in Figure 2.2 (a). The extracellular technique applies a device, e.g. microelectrode as shown in Figure 2.2 (b), to measure the variation in the ionic current of the cell membrane.

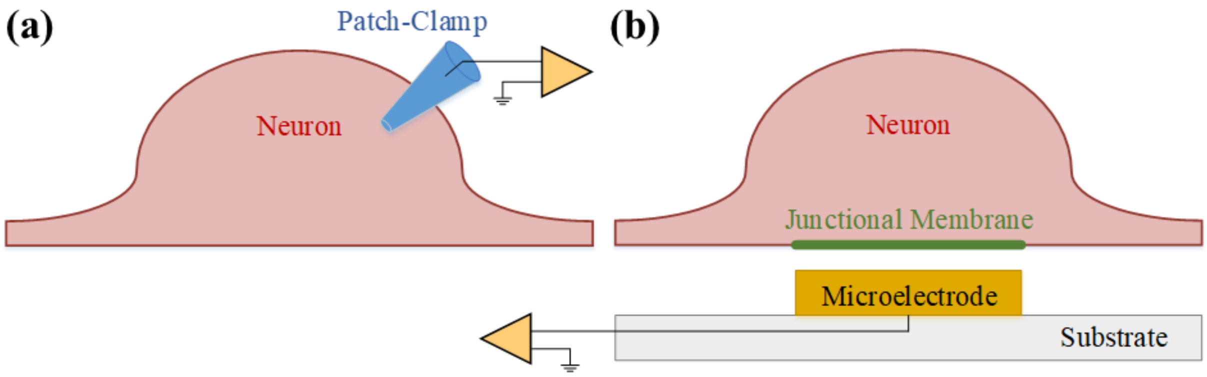

Figure 2.2. Schematics of intracellular and extracellular signal recording techniques. (a) Using a patch-clamp to measure the intracellular voltage variation of the neuron. (b) Using a microelectrode to measure the ionic current variation of the neuronal cell membrane. Reproduced from [25].

The intracellular techniques provide an excellent electrical coupling with the cells that can record signals with high accuracy, in tens of millivolt range [53]. However, the technique is limited to a very few individual neurons due to the physical constraints. Furthermore, the duration of the intracellular recording is limited by mechanical and biophysical instabilities [25]. In contrast, extracellular techniques such as microelectrode arrays (MEAs) can monitor a large number of cells for a long time. However, the AP signals that can be recorded from outside of the cells by the extracellular techniques are low in amplitude, typically in the microvolt range [25]. The extracellular techniques are, therefore, incapable of recording sub-threshold synaptic potentials from neurons due to the inaccessibility to the intracellular parts of the cells and the low signal-to-noise (SNR) ratio. Development of MEAs that enable signal recording of a large number of neurons at single-cell resolution with high SNR for a long period of time would be an ideal solution to allow further understanding of neuronal cells and their electrical signal propagation.

2.3 Microelectrode arrays (MEAs) in literature

In this section, a summary of the literature on microelectrode arrays that have been developed to date is reviewed extensively to determine the strengths and weaknesses of MEAs. The knowledge gained from this review is then used for the work conducted in this thesis. In this regard, MEAs with both planar configurations and with integrated nanomaterials are reviewed. An electrical model is also provided to understand how the coupling between a neuronal cell and a microelectrode can be improved to record signals with high SNR.

2.3.1 Planar MEAs

The first substrate integrated microelectrode array was created by Thomas *et al.* (1972) to measure signals from dissociated chick myocytes [54]. Eight years later, Pine *et al.* (1980) [55,56] reported the first successful recording from single neurons by using gold platinised microelectrodes. Since then, a large number of researchers and scientists were investigating MEAs for monitoring signal communication within neuronal networks. They have mostly applied silicon (Si) [12,17,33,37,57–63] and glass [15,21,35,54,64–66] substrates for the fabrication of MEAs. Gold (Au) [12,17,21,22,29,54,58,62,67–70], platinum (Pt) [18,61,65,71–73], titanium (Ti) [33,74], indium tin oxide (ITO) [64], and silver (Ag) [59] are the most common materials used as electrodes in MEAs due to their electrical characteristics, corrosion resistance and biocompatibility.

Table 2.1 summarises characteristics of literature that utilised planar MEA for recording signals from neurons. The planar MEAs were demonstrated to be capable of recording AP signals from neurons with signal amplitudes of up to 3 mV and SNR of 100 [70,75,76]. However, a coating layer of platinum black (Pt black) has typically been applied on the planar MEAs through a platinisation process to increase the effective surface area of the electrodes. Coating planar MEAs with Pt black has shown to reduce the impedance of microelectrodes by a factor of up to 150 [69] that subsequently improved the recording SNR. Reger *et al.* [64] showed that using ITO microelectrodes coated with PT black could record AP signals with a maximum SNR of 500 from large invertebrate neurons.

Table 2.1. Summary of planar MEA specifications in literature.

Year	Ref.	Substrate	Electrode material	Coating layer	No. electrodes	Impedance at 1 kHz	Recorded signal amplitude	Electrode area	SNR	Testing cells
1972	[54]	Glass	Au	Pt black	30	N/A	20−1000 µV	7 µm (sq)	N/A	Dissociated chick neurons
1977	[70]	N/A	Au	N/A	36	N/A	3 mV	10 µm (dia)	N/A	Isolated snail neurons
1980	[67]	Fibrous collagen	Au	Pt black	16	N/A	50 µV	10 µm (sq)	5−15	Rat superior neurons
1989	[64]	Glass	ITO	Pt black	61	500 kΩ	2–3 mV	12 µm (dia)	500	Invertebrate neurons
1990	[22]	N/A	Au	Pt black	64	0.1–1 MΩ	100–400 µV	8 µm (sq)	N/A	Chick myocytes
1994	[21]	glass	Au	Pt black	60	400 kΩ	N/A	10 µm (dia)	N/A	N/A
1999	[58]	Silicon	Au	Pt black	16	48 kΩ	144 µV	8 µm (sq)	35−70	Rat hippocampal neurons
2004	[24]	Fused silica	Au	Pt black	124	0.3−1.0 MΩ	50−250 µV	5 µm (sq)	10	Rat hippocampal neurons
2007	[77]	Glass	Au	Pt black	32	112 kΩ	50 µV	10 µm (sq)	5	Rat hippocampal neurons
2008	[69]	Si/SiO_2	Au	Pt black	60	25 ± 3 kΩ	15–75 µV	10 µm (dia)	5−25	Rat hippocampal neurons
2010	[75]	Flexible polymer, PDMS	Au	N/A	11	0.01−1 MΩ	5−100 µV	30 × 100 µm	N/A	Rat hippocampal slice
2012	[78]	Glass	ITO	Pt black	64	100 kΩ	50−150 µV	30 µm (sq)	5−15	Mouse cortical neurons
2014	[76]	Borosilicate glass	Pt	N/A	64	200 kΩ	3 mV	12 µm (dia)	100	HL-1 cells

(dia): diameter of the circular electrode, (sq): width of the square electrode, (N/A): not available/stated

The recording SNR of planar MEAs is often low due to the high impedance of the microelectrodes. Although some literature has shown the capability of recording AP signals with high SNR by planar MEAs, this can be attributed to the relatively large physical size of the cells that have been used in these studies and the fact that the neighbouring cells (i.e. of the brain slice/tissue) could have affected these measurements. While small microelectrodes are required for monitoring neuronal networks at single-cell resolution, the impedance of electrodes increases as the size reduces. The high impedance of the small planar microelectrodes makes them blind to the action potentials with low amplitudes. Advances in MEAs are, therefore, required to improve their electrical characteristics desired for monitoring signal communication within the neuronal networks at single-cell resolution with high SNR. In the next section, the coupling of a planar microelectrode with a neuronal cell is modelled to demonstrate how MEAs can be modified to record neuronal signals with high SNR.

2.3.2 Microelectrode-cell coupling

The interaction of a neuronal cell with a microelectrode for recording AP signals was modelled by a passive electrical circuit, as shown in Figure 2.3. The modelled microelectrode-cell configuration consists of three main sections; microelectrode, neuronal cell, and a gap of 40−100 nm (cleft) between the cell and the microelectrode made by the existing protein of the cell membrane [79]. The membrane of the neuronal cell can be separated as the junctional membrane that faces the microelectrode (represented by the green line in Figure 2.3) and the non-junctional membrane elsewhere (represented by the red line in Figure 2.3). The electrical behaviour of the cell membrane can subsequently be modelled as a parallel resistor and capacitor [25], where R_j and C_j represent the junctional membrane resistance and capacitance, respectively, and R_{nj} and C_{nj} represent the non-junctional membrane resistance and capacitance, respectively. The interface of the microelectrode in the solution (cell culture) can also be electrically modelled by a parallel resistor and capacitor, R_{ee} and C_{ee}, respectively [50]. The conduction through the metallic microelectrode is represented by a series resistor (R_e). The adhesion of the neuronal cell to the microelectrode can be modelled by a sealing resistance (R_{seal}) that is associated with the current leakage from the cell through the cleft to the culture solution. A high R_{seal} can represent a tight coupling between the cell and the microelectrode resulting in a low current leakage [80]. The signal loss from the cell through the cleft to the microelectrode can also be affected by the spread resistance of the solution (R_{spred}) [80].

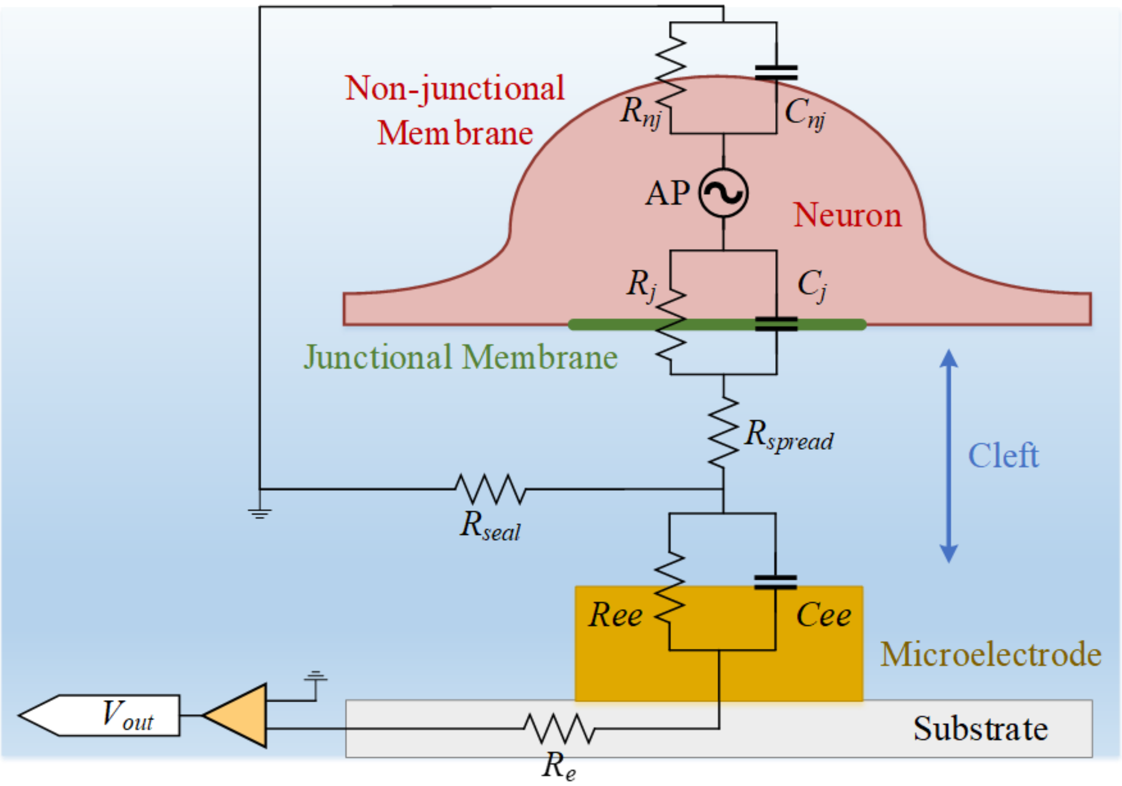

Figure 2.3. The equivalent electrical circuit of a planar microelectrode coupling with a neuronal cell. The electrical circuit comprised of passive components: microelectrode resistance (R_e), microelectrode-electrolyte resistance R_{ee} and capacitance (C_{ee}), spread resistance of the culture solution (R_{spread}), sealing resistance (R_{seal}), junctional membrane resistance (R_j) and capacitance (C_j), non-junctional membrane resistance (R_{nj}) and capacitance (C_{nj}), action potential signal (AP), and recording output signal (V_{out}). Cleft represents the gap between the cell and the microelectrode.

The influence of the critical electrical parameters associated with the coupling of the microelectrode and the cell (i.e. R_{ee}, C_{ee}, R_{spread}, and R_{seal}) can be simulated by varying their values individually while the other parameters are fixed to their typical values, as shown in Table 2.2. The values of all electrical parameters were defined from the literature; however, the values of the R_{ee}, C_{ee}, R_{spread}, and R_{seal} parameters were chosen in such a way that the influence of the simulating parameters became more apparent.

Table 2.2. Parameters used for electrical modelling of the microelectrode-cell coupling

AP signal	R_j	C_j	R_{nj}	C_{nj}	$R_{spread}{}^{b}$	$R_{seal}{}^{b}$	$R_{ee}{}^{b}$	$C_{ee}{}^{b}$	R_e
100 $mV_{pp}{}^{a}$	1 GΩ	0.1 pF	100 MΩ	100 pF	12 kΩ	100 MΩ	1 TΩ	1 nF	100 Ω
[50,51]	[25]	[25]	[25]	[25]	[80]	[25,80]	[25,81]	[25,81]	[81]

[a] Peak-to-peak amplitude of the action potential signal at the neuronal cell.

[b] Parameters that varied for the electrical simulation of the microelectrode-cell coupling.

Figure 2.4 (a)–(d) show the influence of the R_{ee}, C_{ee}, R_{spread}, and R_{seal} parameters on the recording signals by the microelectrode. The coupling factor was determined as the proportion of the signal amplitude recorded by the microelectrode to the action potential amplitude, i.e. 100 $mV_{\text{peak-to-peak}}$, of the neuronal cell. The action potential that was elicited at the neuronal cell consisted of a resting potential of −62 mV, a threshold potential of −53 mV, depolarisation to a peak of +30 mV, and repolarisation to −70 mV, as previously demonstrated for a rat hippocampal pyramidal neuron in Figure 2.1 (b).

Reducing the impedance of the microelectrode-electrolyte at the cleft, i.e. reducing R_{ee} or increasing C_{ee}, can increase the coupling factor by 8%, as shown in Figure 2.4 (a) and (b), respectively. The R_{ee} of less than 1 MΩ and the C_{ee} of higher than 1 nF are shown to allow recording signals with high SNR. The microelectrodes are therefore required to be fabricated from materials that have high charge transfer characteristics (low electrochemical R_{ee}) with high surface area (high C_{ee}).

The culture solution of the cells is required to have a high conductivity ($R_{spread} < 1$ MΩ) that allows passage of the AP signal current to the microelectrodes with minimum distortion, as shown in Figure 2.4 (c). Furthermore, the tightness of the contact between the cell and the microelectrode, as determined by R_{seal}, plays a vital role in the quality of recording signals. Figure 2.4 (d) shows that increasing the R_{seal} to 10 MΩ or higher can improve the coupling factor by 35%. As a tighter contact is provided between the cell and the microelectrode, the AP signal is less dissipated through the medium and therefore signals with higher amplitudes can be recorded by the microelectrodes. Thus, the microelectrode devices are required to be made of materials with a configuration that can adhere tightly to the neuronal cells (small cleft) for recording signals with high SNR.

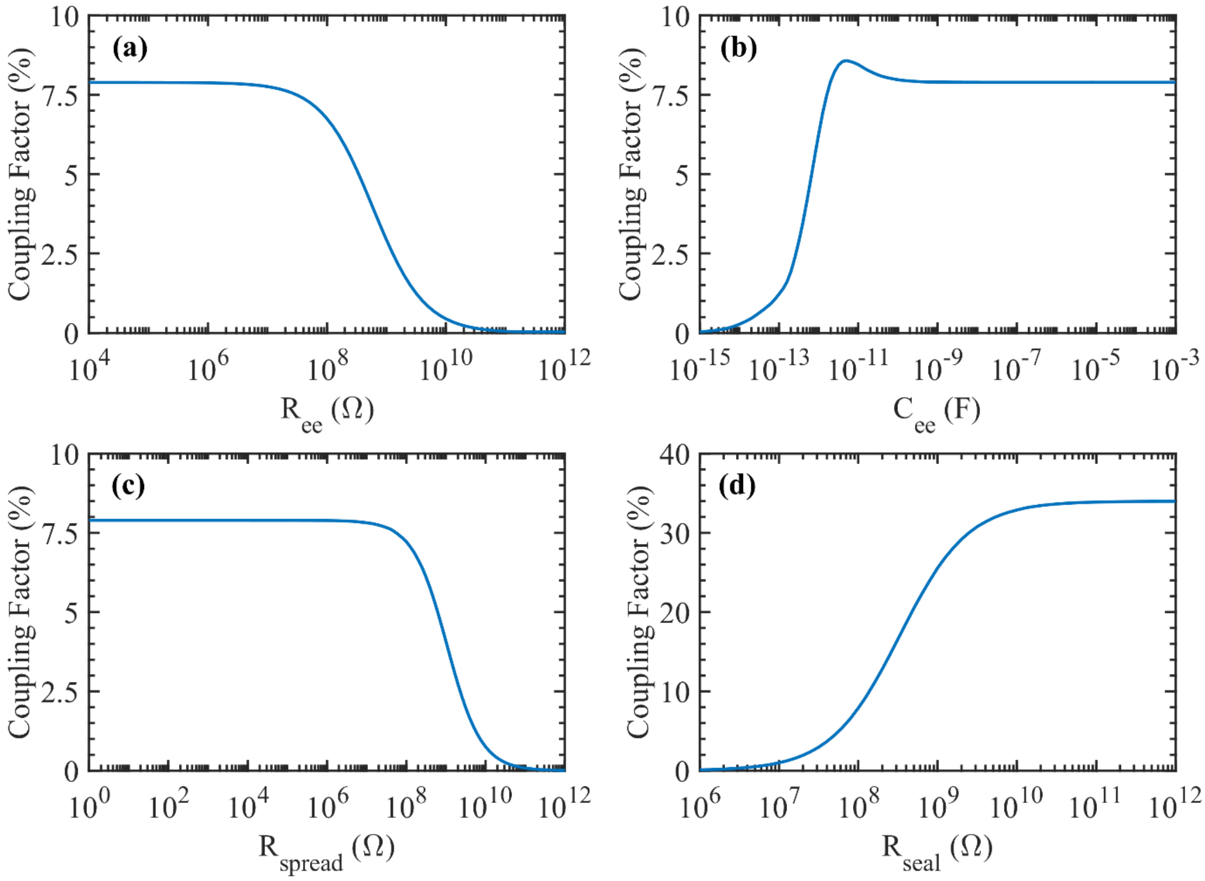

Figure 2.4. Electrical simulation of the microelectrode-cell coupling. The coupling factor was determined as the proportion of the signal amplitude recorded by the microelectrode to the action potential amplitude of the neuronal cell, i.e. 100 $mV_{peak\text{-}to\text{-}peak}$. (a)–(d) show the influence of the microelectrode-electrolyte resistance (R_{ee}) and capacitance (C_{ee}), spread resistance of the solution (R_{spread}), and sealing resistance (R_{seal}) on the coupling factor, respectively. The simulation has been done in LTspice (Linear Technology) simulation software using the circuit shown in Figure 2.3 and varying a single parameter at a time while the other parameters were maintained constant.

2.3.3 Nanomaterial MEAs

The idea of applying nanomaterials on planar microelectrodes for improving the microelectrode-cell coupling has attracted a lot of attention over recent years. Many researchers have made efforts on the synthesis of nanomaterials on microelectrodes in order to improve their electrical characteristics for recording signals from neuronal cells. Thus far, the common nanomaterials that have been utilised for this purpose are gold (Au) nanostructures [17,29–32,82,83], carbon nanotubes (CNTs) [33–35,61,66,84,85], silicon nanowires (Si-NWs) [12,36,37,63,86], platinum nanowires (Pt-NWs) [15,38], and ZnO nanowires (ZnO-NWs) [49,68]. The specifications of the significant nanomaterial MEAs in the literature are summarised in Table 2.3.

Table 2.3. Summary of nanomaterial MEA specifications in literature.

Nanomaterial	Year	Ref.	Substrate	Base electrode	Nanomaterial size[a]	Impedance at 1 kHz	Recorded signal	Electrode diameter[b]	SNR	Testing cells
Au nanowires	2007	[31]	Si/SiO$_2$, polymide	Au	Ø: 10–1,000 nm L: 5,000 nm	500 kΩ	N/A	50 µm (cir)	N/A	Brain tissue
Au microspine	2009	[30,62,82]	Si/SiO$_2$, glass	Au	Ø: 800–1,800 nm L: 1,500 nm	N/A	0.1–25 mV	0.75–1.25 µm (cir)	9 ± 5	Aplysia, NIH/3T3, CHO, PC-12, H9C2 cells
Au nanoflakes	2010	[32]	Glass	Au	Ø: 5,000–50,000 nm	26.7 kΩ	100–300 µV	5–50 µm (cir)	10–30	Rat hippocampal neurons
Au nanopillars	2011	[17]	Si/SiO$_2$	Au	Ø: 60 nm L: 300–400 nm	350 kΩ	1.5 mV	20 µm (cir)	223	Cardiac myocytes (HL-1)
Au nanopillars	2014	[29]	Glass	Au	Ø: 4–200 nm L: 4,000–22,500 nm	13–360 kΩ	0.1–1.2 mV	30 µm (cir)	N/A	Rat cortical neurons
Pt nanowires	2011	[38]	Silicon	Pt	600× increased surface area	2 kΩ	N/A	120 µm (cir)	N/A	Human neuroblastoma (SH-SY5Y)
Pt nanopillars	2012	[15]	Quartz	Pt	Ø: 150 nm L: 1,500 nm	6 MΩ	100–200 µV	5–10 µm (sq)	4.5–9	Cardiac myocytes (HL-1)
Si microprobes with Au tips	2004	[37]	Si/SiO$_2$	Ni/Si	Ø: 2,000 nm L: 60,000 nm	300–500 kΩ	100 µV	20 µm (cir)	N/A	Retinal ganglion cells
Si/SiO$_2$ nanowires with Ti/Au tips	2012	[12]	SOI	Au	Ø: 150 nm L: 3,000 nm	N/A	4 mV	50 µm (cir)	100	Rat cortical neurons, HEK93 cells
Vertically aligned	2006	[34]	Glass	P-doped	Ø: 30–50 nm	3–4 kΩ	N/A	30 µm (sq)	N/A	Rat hippocampal

Nanomaterial	**Year**	**Ref.**	**Substrate**	**Base electrode**	**Nanomaterial size[a]**	**Impedance at 1 kHz**	**Recorded signal**	**Electrode diameter[b]**	**SNR**	**Testing cells**
MW-CNTs				poly-silicon						neurons
MW-CNT islands	2007	[33]	Si/SiO$_2$	TiN	Ø: tens of nm	1.1–10 kΩ	1.2 mV	80 µm (cir)	135	Rat cortical neurons
SW-CNTs	2008	[65,85]	Glass	Pt	Ø: 10–25 nm L: 1,000–1,500 nm	20 kΩ	210 µV	40 µm (cir)	21	PC12, 42MG-BA, 3T3, HEK-293 cells
MW-CNTs functionlised with carboxylic acid	2014	[35]	Glass	Au	Ø: 9.5 nm L: 1,500 nm	19 kΩ	160 µV	50 µm (cir)	N/A	Rat cortical neurons
CNTs on 3D pyramid-shaped Si with tips of Ti/Pt	2016	[61]	Si	Pt	Ø: 25–30 nm L: 600 nm	14 kΩ	N/A	200 µm (sq) with tips of 2 µm (cir)	N/A	Mouse neuroblast cells
Carbon nanofiber (CNF)	2016	[66]	Quartz	Carbon film	Ø: 23,600 nm L: 20,700 nm	25 kΩ	50 µV	30 µm (cir)	N/A	Rat cortical neurons
ZnO nanowires with Cr/Au/PEDOT encapsulation	2017	[49,68]	Flexible polyimide	Au	Ø: 55 nm L: 3,500 nm	520 Ω	700 µV	800 µm (sq)	N/A	HEK293 cells, rat brain

[a] Ø: nanomaterial diameter, L: nanomaterial length/height

[b] (cir): diameter of the circular electrode, (sq): width of the square electrode

(N/A): not available/stated

Gold (Au) is the most common electrode material used in MEAs due to its high conductivity, corrosion resistance, chemical stability, non-oxidation properties, and biocompatibility making it ideal for neuronal applications [87–89]. However, the impedance of plain gold electrodes increases when gold microelectrodes with small size are made. Ganji *et al.* [90] previously demonstrated that reducing the diameter of gold microelectrodes from 2 mm to 2 µm resulted in a significant increase of the electrochemical impedance from 1 kΩ to 1 MΩ at 1 kHz of frequency. In this regard, gold nanostructures in the form of nanowires [31,87], nanopillars [17,29], nanoflakes [32], and microspines [30,62,82] were applied to increase the 3D surface of the gold microelectrodes. As a result, the impedance of MEAs was reduced by a factor of up to 89.5 when gold nanopillars with a high aspect ratio (> 100) were used, compared to plain gold microelectrodes with impedance of 1.17 MΩ at 1 kHz of frequency [29]. The impedance reduction can also reduce the thermal noise originating from the electrode impedance and increase the SNR of recording action potentials [32].

Silicon is one of the most common elements in the universe that can compound with many other elements (e.g. oxygen, hydrogen, carbon) and form in a diverse range of structures. Among various forms of silicon, silicon nanowires (Si-NWs) are ideal nanostructures for neuronal applications due to their high surface to volume ratio [91] and biocompatibility properties [92,93]. Kawano *et al.* [37] previously developed a silicon-microprobe by a vapour-liquid-solid (VLS) technique using catalytic-Au dots. The Si-probe was then encapsulated with a SiO_2 layer, and its tip was covered by a gold layer to reduce the probe impedance, 100–500 kΩ at 1 kHz. The achieved Si-probes were 2 µm wide and 60 µm long, which were able to penetrate a retinal tissue to record signals from the ganglion cells, 50 µm below the front surface of the tissue. A different design made by Robinson *et al.* [12] consisted of vertical Si nanowires encapsulated with SiO_2 shells and capped with Ti/Au tips. Nanowires with diameters of 150 nm and heights of 3 µm were achieved by using the top-down method that resulted in a tight sealing between the cells and the nanowires with a sealing resistnace of 100–500 MΩ. Consequently, action potentials with high amplitudes of 4 mV and SNR of 100 were achieved to be recorded from the rat cortical neurons.

Carbon nanotubes (CNTs) have been a nanomaterial of interest in nanotechnology applications since their discovery in 1991 [94], due to their outstanding physical and electrical properties. Over recent years, CNTs have been an attractive subject in the development of MEAs for neuronal applications due to their biocompatibility [34,65,66,84,95], physical properties (high strength and flexibility [34]) and electrochemical properties [34]. Gabriel *et al.* [85] found that synthesis of single-walled CNTs on MEAs can reduce the impedance of Pt and Pt-black microelectrodes from 600 kΩ and 200 kΩ to 20 kΩ at 1 kHz of frequency, respectively. Furthermore, Gabay *et al.* [33] demonstrated that an SNR as high as 135 could be achieved for recording action potentials from rat cortical neurons by applying CNTs as an island on the microelectrodes.

Thus far, Ryu *et al.* [49,68] are the only group who have applied ZnO nanowires on MEAs in 2017 for recording neuronal signals from a rat brain *in vivo*. They have fabricated Cr/Au microelectrodes with ZnO nanowires on top of flexible polyimide substrates. Since ZnO nanowires are semiconductors with relatively low conductivity, another layer of Cr/Au has been sputter coated on the nanowires that fused with the underlying Cr/Au microelectrodes. ZnO/Cr/Au nanowires were further coated with a layer of poly-(3,4ethylenedioxythiophene) (PEDOT) to improve their biocompatibility. Due to the porous surface structure of the PEDOT coating layer, the effective surface area and the charge capacity of the nanowires was increased that reduces their impedance furthermore. As a result, the impedance reduced from 17.9 kΩ of the planar gold microelectrode to 520 Ω at the frequency of 1 kHz and increased the charge capacitance from 0.016 µC to 18.048 µC [49].

In this work, ZnO nanowires are proposed as a good candidate for the active nanomaterial on MEAs for *in vitro* neuronal applications. While other nanowires have successfully been used in the neuronal applications, it is difficult to vary their morphology and topography over a wide range of parameters to study their influence in neuronal applications. In part this is due to the complexity of their fabrication processes such as chemical vapour deposition (CVD) including vapour-liquid-solid growth (VLS) [37] and vapour-solid-solid growth (VSS) [63,86], electrochemical deposition [17,31,32], electroplating [29,30,82,83] or dispersion [35,84,85]. All of those methods require fine tuning, sometimes complex hardware, and often need to be carried out at high temperatures, making integration with pre-existing MEA structures challenging. In contrast, ZnO nanowires can largely benefit from their hydrothermal growth, where ZnO nanowires with various morphology and topography can easily be grown and the fabrication process can easily be carried out on prefabricated MEAs with Au electrodes. Here, I am focusing on the techniques to grow and control the morphology of the ZnO nanowires to understand how they may be applied for recording neuronal signals from human neuronal cells. In the next section, the properties of the ZnO nanowires that make them suitable for neuronal application is studied, and the appropriate synthesis techniques that can be utilised for the fabrication of ZnO-NW MEAs are introduced.

2.4 ZnO nanowire MEAs

2.4.1 Fundamental properties of ZnO nanowires

Zinc oxide (ZnO) is a group II-VI semiconductor with a direct wide bandgap of 3.44 eV and a high free exciton binding energy of 60 meV at room temperature ideal for electronic and optoelectronic applications [96,97]. The wide bandgap of ZnO allows high temperature and high power operation with low noise generation [98]. The bandgap 3.44 eV also corresponds to the wavelength of 360 nm (ultraviolet) that makes ZnO transparent within the visible spectrum [97]. ZnO crystals are typically formed in a hexagonal wurtzite structure, as shown in Figure 2.5, although both rock-salt (or Rochelle-salt) and zinc-blende crystal structures are also possible to form if grown under high pressure [98,99]. The wurtzite crystal structure of ZnO involves planes of Zn^{2+} (0001) and O^{2-} $(000\bar{1})$ along the c-axis direction as polar faces (c-faces), $(10\bar{1}0)$ and $(11\bar{2}0)$ planes as non-polar faces (m-face and a-face). The lattice constants of ZnO crystal structure are a = 3.25 Å and c = 5.2 Å [100].

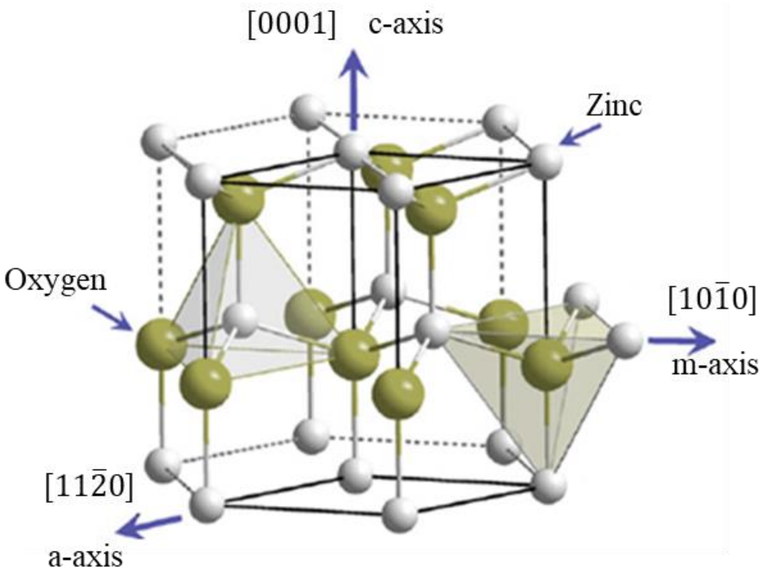

Figure 2.5. Wurtzite crystal structure of ZnO with lattice constants of a = 3.25 Å and c= 5.2 Å. Polar faces of Zn^{2+} and O^{2-} are along the c-axis [0001] and non-polar faces are along the m-axis $[10\bar{1}0]$ and a-axis $[11\bar{2}0]$. Modified from [100].

ZnO can be formed into one-dimensional (1D) nanostructures ranging from nanowires (or nanorods) to nanotubes and nanobelts [43]. In recent years, ZnO nanostructures have readily been used in light-emitting diodes (LEDs) [39], solar cells [40–42,101,102], biosensors [43–45] and piezoelectric devices [46–48] due to their excellent electronic and optoelectronic properties as well as ease of fabrication. Furthermore, ZnO is a biocompatible and biodegradable material that makes it ideal for medical and biological applications [103–105]. ZnO nanostructures are typically synthesised via a vapour phase transport (VPT) technique or a hydrothermal phase method [106]. The VPT technique applies a high temperature process, typically chemical vapour deposition (CVD), to grow ZnO nanostructures on a rigid substrate. In contrast, the hydrothermal approach benefits from its low cost, low temperature synthesis (below 100°C), scalability and the ability to grow on various substrates including inorganic and organic flexible substrates [43,107,108]. For these reasons, the hydrothermal approach is, therefore, chosen for fabrication of ZnO nanowires on microelectrodes in this work.

2.4.2 ZnO nanowire hydrothermal growth

The hydrothermal synthesis applies a solution of precursors at a low temperature (below 100ºC) that goes through a chemical reaction to form ZnO crystals. The morphology of the ZnO nanowires is typically governed by controlling the hydrothermal growth parameters such as ZnO seed layers [109–114], precursor concentration [43,115–117], growth time [115,118,119], growth temperature [118,120], solution pH [118,121], additive auxiliary agents [122] and polyethylenimine (PEI) [42,123]. The role of the hydrothermal growth parameters is discussed below to identify the significant parameters for controlling the morphology of ZnO nanowires through the hydrothermal growth in this work.

2.4.2.1 Role of the seed layer

An advantage of the hydrothermal method is the ability to apply ZnO seed layers for growing vertical ZnO nanowires on desired regions of a substrate. Without a ZnO seed layer, the ZnO crystallisation needs to undergo a nucleation step that can arbitrarily take place on the substrate and result in randomly oriented nanowires with various morphology. A ZnO seed layer can be deposited on a substrate via sputter coating [124,125] or spin coating methods [42,126] to bypass the nucleation process. The thickness [109–111] and the grain size of the seed layer [112–114] are demonstrated to affect the morphology of the ZnO nanowires. In general, a thick seed layer results in wide and short nanowires with a low density [43]. The density of the ZnO nanowires is also determined to vary significantly from 6.8×10^4 to 2.6×10^{10} NWs/cm^2 as the seed layer thickness varied from 1.5 nm to 3.5 nm [109]. The seed layers thicker than 3.5 nm were determined to confine the variation of the nanowire density. Increasing the seed layer thickness can also improve the crystallinity of the seed layer with increased grain size and decreased surface roughness that results in thicker nanowires with improved alignment [110]. Hsiao *et al.* [112] also reported that the large crystal size of the seed layer could increase the diameter of the nanowires and decrease their density. Thus, in this work ZnO seed layers are deposited via sputter coating with a thickness of 100 nm to allow the growth of well-aligned ZnO nanowires on defined regions of the substrates with the least variation of the nanowire morphology across the seed layer.

2.4.2.2 Role of the hydrothermal growth solution: precursor concentration, auxiliary agents and pH

The growth solution plays a vital role in the hydrothermal synthesis to control the morphology of the ZnO nanowires. Deionised (DI) water is the most common solvent that has been used for the hydrothermal synthesis [112,119,127]. Zinc nitrate ($Zn(NO_3)_2$) [43,46,106,107,116,119,124,128–130] or zinc chloride ($ZnCl_2$) [40,68] precursors have commonly been used to provide zinc ions, Zn^{2+}, for the ZnO crystallization. The secondary precursor of hexamethylenetetramine (HMT) has also been used in the solution to provide the hydroxyl ions, OH^-, necessary for the ZnO growth. The growth solution of zinc nitrate and HMT precursors in DI water is subsequently chosen to be used for growing ZnO nanowires in this work. The most significant parameter that should be considered in the growth of the ZnO nanowires is the amount of the precursors available in the solution. Increasing the precursor concentration is generally demonstrated to increase the diameter, length and density of the ZnO nanowires [43,115]. Wang *et al.* [117] previously reported that the equimolar ratio of zinc nitrate and HMT resulted in the highest aspect ratio of the nanowires, where the nanowire length increased and the diameter did not change with the precursor ratio [117]. Thus, varying the equimolar concentration of zinc nitrate and HMT precursors is selected as a technique to control the morphology of the ZnO nanowires for this work.

Vernardou *et al.* [121] and Chevalier-César *et al.* [118] demonstrated that the morphology of ZnO nanostructures could also vary by tuning the pH of the solution. Different morphologies of the nanowires varying from hexagonal and coned-tip nanorods to nanoprisms and nanoflowers were obtained by using growth solution with a pH of 7, 8, 10 and 12, respectively [121]. The neutral growth solution with a pH of 7.0 was determined to form ZnO hexagonal nanorods with excellent homogeneity.

Joo *et al.* [122] introduced a face-selective electrostatic method to control the aspect ratio of the ZnO nanowires within a range of 0.1–100 by applying non-zinc complexes at alkaline conditions. Introducing auxiliary complexes such as cadmium (Cd) and aluminium (Al) to the growth solution inhibited the nanowire growth in certain directions. Positively charged Cd ions were adsorbed on top faces of the ZnO nanowires that resulted in the growth of thick nanowires with low aspect ratios. In contrast, negatively charged Al ions were adsorbed on lateral faces of the ZnO nanowires and resulted in the growth of long nanowires with high aspect ratios.

Polyethylenimine (PEI) is an organic polymer commonly used in the hydrothermal synthesis to enhance the aspect ratio of the ZnO nanowires [41,123,131]. The PEI is determined to hinder the radial growth of ZnO nanowires by binding to the lateral faces of the nanowires [106,131]. Burke-Govey *et al.* [123] previously showed the effect of PEI concentration and molecular weight on the aspect ratio of the ZnO nanowires. Burke-Govey *et al.* reported that the PEI with Mw of 800 g/mol could result in growth of homogenous nanowires for a broader range of concentration, 2–8 mM, compared to the Mw of 2000 g/mol and 1300 g/mol that yielded homogeneous nanowires for 2 mM of concentration only [123]. The PEI with Mw of 800 g/mol is chosen to be used in this work as an additive precursor for enhancing the aspect ratio of the ZnO nanowires.

2.4.2.3 Role of the hydrothermal growth process: growth temperature and growth time

The crystallisation of ZnO occurs at a prolonged rate at room temperature, hence the temperature of growth solution needs to be raised to around 40–95°C [118,120] to speed up the crystallisation process. Increasing the growth temperature is found to increase the length of the nanowires while the diameter remains almost unchanged. The growth time has also shown to have a direct impact on both axial and radial growth of the nanowires, at which both the length and diameter of the nanowires can be increased. In addition, the growth of the nanowires is determined to undergo a two-phase procedure over the growth time, including a fast growth rate at the early stages, followed by a slow growth rate [115,118,119]. However, there are differences between axial and lateral growth trends depending on the growth regime and the other parameters that have been applied. The growth time is chosen as another parameter to control the morphology of the ZnO nanowires at a fixed growth temperature of 95°C.

The effects of the growth time, precursor concentration and the additive PEI will all be investigated in Chapter 4 to control the growth of the ZnO nanowires through the hydrothermal synthesis. The other parameters such as the growth temperature (95ºC), ZnO seed layer (via sputter coating with a thickness of 100 nm), the growth solvent (DI water) and the concentration ratio between the zinc nitrate and HMT precursors (1:1) will all be kept constant to not influence the outcomes.

2.5 Conclusion

Advances in microelectrode arrays (MEAs) is required to allow monitoring of neuronal networks with a large number of neurons at single-cell resolution and a high signal-to-noise ratio (SNR) for a long time. Using different nanomaterials have previously demonstrated to improve the electrical and biological characteristics of MEAs for neuronal applications. In this work, ZnO nanowires are proposed as the ideal nanomaterial on MEAs for recording action potential signals from neuronal networks *in vitro* due to their excellent electrical properties, biocompatibility and novelty.

The hydrothermal synthesis is determined as an ideal approach to grow ZnO nanowires on MEAs, due to the ease of fabrication, low cost, high scalability and the low temperature process that can be applied on various substrates including the flexible substrates. Furthermore, ZnO nanowires in different morphologies can be grown by controlling the hydrothermal growth parameters. The morphology of the ZnO nanowires is subsequently investigated by controlling the precursor concentration, growth time and additive polyethylenimine (PEI) in Chapter 4. In addition, Chapter 4 investigates how ZnO nanowires can be selectively grown on defined regions of the substrates. The biocompatibility of the resulting ZnO nanowires with different morphology and geometry are examined for human neurons in Chapter 5. Finally, the electrical characteristics and the robustness of the MEAs integrated with ZnO nanowires are investigated in Chapter 6, showing their compatibility for recording AP signals from human neuronal cells *in vitro*.

Chapter 3

Experimental Details

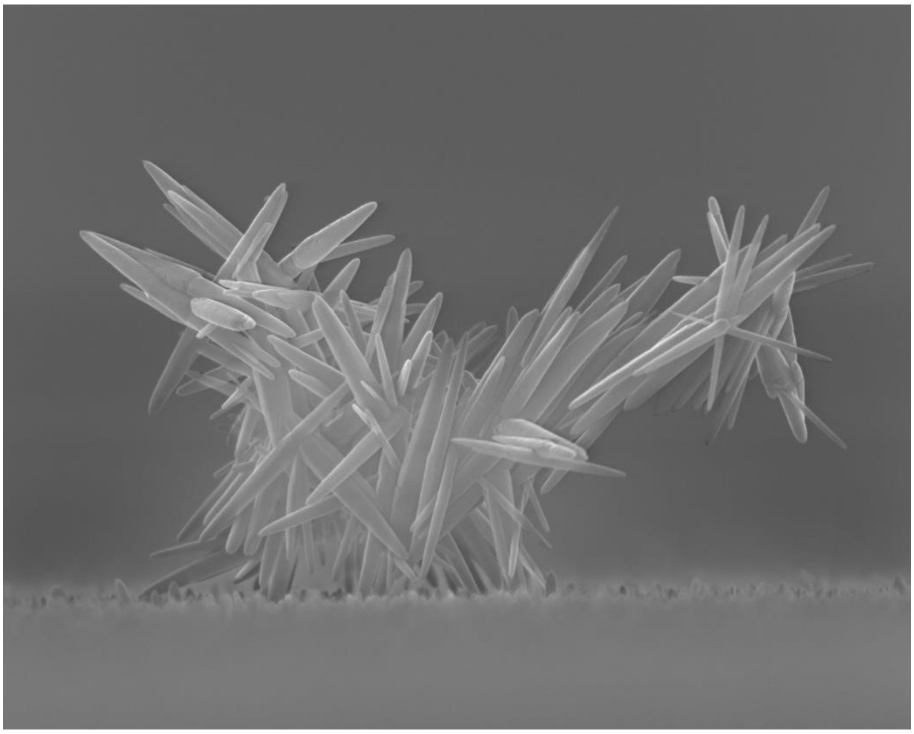

The ZnO Trojan Horse that Achaeans had in their minds to invade Troy.

3.1 Introduction

This chapter details the experimental procedures and characterisation techniques that have been carried out throughout the work presented in this thesis. The standard photolithography processes and the details of the hydrothermal synthesis of zinc oxide nanowires (ZnO-NWs) are initially introduced. Then, the fabrication processes of ZnO nanowire samples and microelectrode arrays (MEAs) that have been used in Chapters 4–6 for investigating the selective growth of ZnO nanowires, the biocompatibility of ZnO nanowires and electrochemical characteristics of ZnO-NW MEAs are described. The experimental details of the processes such as scanning electron microscopy (SEM), neuronal viability, electrochemical impedance spectroscopy (EIS) and robustness test that were carried out for characterising the morphology, biocompatibility, electrical properties and mechanical stability of the ZnO nanowires and MEAs are also described here.

3.2 Fabrication processes

3.2.1 Photolithography processes

Standard photolithography processes have been carried out in this work to control the location of ZnO nanowires on substrates and to pattern the MEAs. Figure 3.1 (1a)–(1f) and (2a)–(2f) schematically show the photolithography process for positive photoresists (AZ1518 and AZ5214E, MicroChemicals) and negative photoresists (SU8-2150, MicroChemicals), respectively.

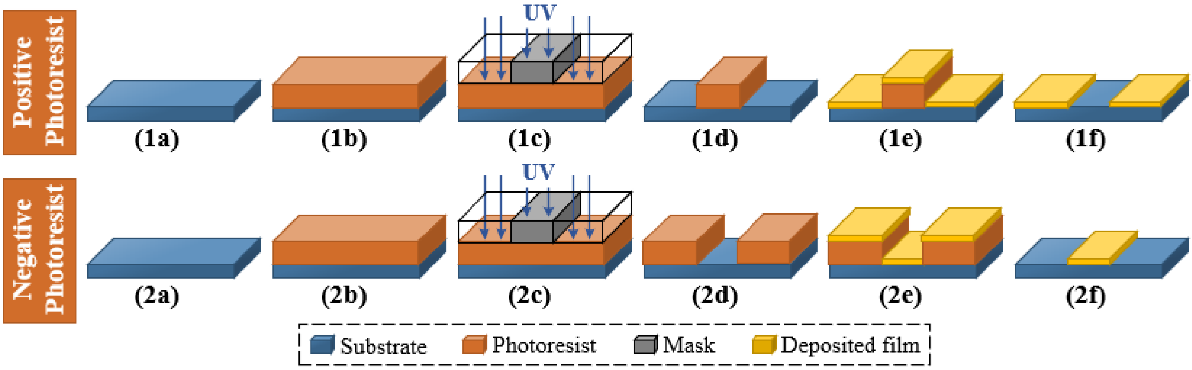

Figure 3.1. Schematics of the photolithography process for (1a)–(1f) positive photoresists and (2a)–(2f) negative photoresists. The photolithography process includes (a) substrate preparation; (b) photoresist spin coating; (c) exposing the photoresist to ultraviolet (UV) light using the mask aligner; (d) photoresist development; (e) film deposition; and (f) lift-off process.

The process started with cleaning the substrates (Si or Si/SiO_2 (100 nm oxide layer), University Wafer) thoroughly by 1 minute sonication in acetone, 1 minute sonication in isopropanol (IPA), rinsing in IPA and drying in a stream of clean nitrogen (N_2), as shown in Figure 3.1 (a). The substrates were then coated with a thin layer of photoresist (AZ1518, AZ5214E or SU8-2150) via spin coating followed by soft baking, as shown in Figure 3.1 (b). Karl Suss MJB3 mask aligner equipped with a USHIO 350W mercury vapour lamp (USH-350DS) was utilised to expose areas of the photoresist to ultraviolet light (UV, with the wavelength of 365 nm (i-line)) using a chrome stencil on a glass plate, as shown in Figure 3.1 (c). Upon the exposure of the positive photoresist to the UV, the exposed areas of the photoresist became soluble and could readily be removed by a development process, as shown in Figure 3.1 (1d). In contrast, the exposure of the negative photoresist to the UV made the exposed parts to cross-link and strengthen while the unexposed parts could be removed by the development process, as shown in Figure 3.1 (2d). The development process involved immersion with gentle agitation of the substrates in the developer solution, e.g. AZ351B and SU8 developers, followed by rinsing with deionised (DI) water (for AZ1518 and AZ5214E photoresists) or IPA (for SU8 photoresist) and drying with N_2.

Thin films of ZnO were deposited on the substrates with photoresist patterns via RF sputter coating (500 RF Magnetron, HHV Ltd) at a deposition rate of 0.1–0.2 Å/s, as shown in Figure 3.1 (e). A lift-off process was then carried out by immersion of the substrates in a solvent, i.e. acetone or N-Methyl-2-pyrrolidinone (NMP), until the photoresist dissolved and the upper ZnO film lifted-off, as shown in Figure 3.1 (f). The process was followed by sonication in acetone (1 minute) or NMP (2 minutes), 1–2 minutes sonication in IPA, rinsing in IPA and drying with N_2.

Metallic films were deposited on the substrates by thermal (Cr/Au) or e-beam (Ti and Pt) evaporation using Angstrom Engineering Nexdep Evaporator, as shown in Figure 3.1 (e). The lift-off process was then carried out by immersion in acetone until the photoresist dissolved and the upper metals lifted-off, as shown in Figure 3.1 (f). The process was followed by 1 minute sonication in acetone, 1 minute sonication in IPA, rinsing in IPA and drying with N_2 to ensure the substrates were clean of any debris.

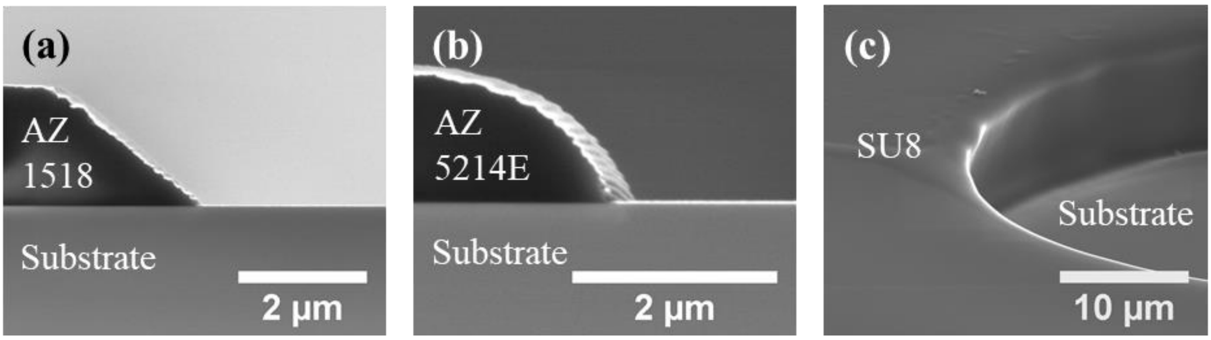

Figure 3.2. SEM images of the photoresist after the photolithography processes. (a) and (b) show SEM images of AZ1518 and AZ5214E positive photoresists from the cross-section view, respectively. The samples were coated by a layer of Cr/Au (2/20 nm) to reduce the charging effect of the photoresists for SEM imaging. (c) SEM image of SU8-2150 negative photoresist from 70° tilted view. The sample was coated by a 7 nm thin layer of carbon to reduce the charging effect of the SU8 for SEM imaging.

Figure 3.2 (a)–(c) show SEM images of AZ1518, AZ5214E and SU8-2150 photoresists after the photolithography processes, respectively. The SEM images show that the AZ1518, AZ5214E and SU8 photoresists produce patterns on the substrates with a thickness of 1.8 µm, 1.4 µm and 8 µm, respectively. The detailed photolithography recipes of AZ1518, AZ5214E and SU8-2150 photoresists are described below.

3.2.1.1 AZ1518 positive photoresist

1. AZ1518 photoresist is dropped onto the substrate using a glass micropipette to cover the entire substrate surface without any gaps or bubbles.
2. The substrate with the photoresist is spin-coated at 4000 rpm (with the acceleration of 7500 rpm/s) for 1 minute to spread the photoresist across the substrate with a thickness of 1.8 µm.
3. The sample is soft-baked on the hot-plate at 95°C for 2–3 minutes to evaporate the solvents and solidify the resist.
4. The sample is aligned to the pattern of the mask using the MJB3 mask aligner and exposed to the UV (with the power density of 18.7 mW/cm^2) for 15 seconds (280 mJ/cm^2).
5. The photoresist is developed by agitating in a 1:4 dilution of AZ351B developer to DI water for 15–20 seconds followed by 10 seconds rinsing in DI water and drying with N_2 to remove remaining developer and debris.

3.2.1.2 AZ5214E positive photoresist

1. AZ5214E photoresist is dropped onto the substrate using a glass micropipette to cover the entire substrate surface without any gaps or bubbles.
2. The substrate with the photoresist is spin-coated at 4000 rpm (with the acceleration of 7500 rpm/s) for 1 minute to spread the photoresist across the substrate with a thickness of 1.4 µm.
3. The sample is soft-baked on the hot-plate at 95°C for 2–3 minutes to evaporate the solvents and solidify the resist.
4. The photoresist is flash exposed to UV for 0.15 second (minimum exposure time available on the MJB3 mask aligner).
5. The photoresist is cross-linked by baking on the hot-plate at 110°C for 2 minutes.
6. The sample is aligned to the pattern of the mask using the MJB3 mask aligner and exposed to the UV (with the power density of 18.7 mW/cm^2) for 12 seconds (224 mJ/cm^2).

7. The photoresist is developed by agitating the sample in a 1:4 dilution of AZ351B developer to DI water for 15–20 seconds followed by 10 seconds rinsing in DI water and drying with N_2 to remove remaining developer and debris.

3.2.1.3 SU8 negative photoresist

1. SU8-2150 photoresist is mixed with cyclopentanone solvent at 4:1 ratio. The SU8-2150 is quite viscous that makes it hard to dilute. The mixed solution is sonicated at 50°C for a few hours to ensure that the solution is well mixed.
2. The diluted SU8 is dropped onto the substrate using a glass micropipette to cover the entire substrate surface without any gaps or bubbles.
3. The substrate with the SU8 is spin-coated at 500 rpm (with the acceleration of 500 rpm/s) for 10 seconds followed by spin-coating at 4000 rpm (with the acceleration of 7500 rpm/s) for 40 seconds to spread the SU8 across the substrate with a thickness of 8 µm.
4. The SU8 photoresist is soft-baked on the hot-plate at 55°C for 3 minutes, followed by 85°C for 3 minutes and 55°C for 3 minutes.
5. The sample is aligned to the pattern of the mask using the MJB3 mask aligner and exposed to the UV (with the power density of 18.7 mW/cm^2) for 10 seconds (187 mJ/cm^2).
6. The SU8 photoresist is post-baked on the hot-plate at 55°C for 3 minutes, followed by 85°C for 3 minutes and 55°C for 3 minutes
7. The SU8 is developed by agitating the sample in the SU8 developer for 30 seconds followed by 10 seconds rinsing in IPA and drying with N_2 to remove remaining developer and debris.
8. The SU8 is hard-baked on the hot-plate at 200°C for 15 minutes to improve its mechanical and chemical stability.

3.2.2 Hydrothermal growth of ZnO nanowires

ZnO nanowires were grown hydrothermally on the substrates with pre-deposited ZnO seed layers. The growth substrates were prepared by the deposition of ZnO seed layers on the substrates using RF sputter coater (500 RF Magnetron, HHV Ltd). The hydrothermal growth solution was prepared by mixing equimolar solution amounts of zinc nitrate hexahydrate (98%, Sigma Aldrich) and hexamethylenetetramine (HMT 99%, Sigma Aldrich) precursors in 100 mL of DI water (with the conductivity of 18.2 MΩ·cm and pH of 7.00). A diverse range of precursor concentration, 2.5–150 mM, was used to control the morphology of the ZnO nanowires. The precursor concentration of 25 mM was also used as the standard concentration, as it has commonly been used in the literature for growing ZnO nanowires [101,119,125,132,133]. Polyethylenimine (PEI, Mw = 800 g/mol, Sigma Aldrich) with varying concentrations could also be added to the solution to mediate the growth solution and enhance the aspect ratio of the ZnO nanowires. The PEI concentration of 2–8 mM was used in Chapter 4 to investigate the effect of the PEI concentration. In Chapter 5 and 6, the PEI concentration of 6 mM is used to grow ZnO nanowires with high aspect ratios.

The growth substrates were then attached to a stainless-steel rod facing downwards, using double-sided carbon tape, and placed at the height of 2 cm in a 100 mL Schott borosilicate glass bottle, as shown in Figure 3.3. The bottles were then placed in a preheated water-bath (GD100, Grant Instruments) at 95°C to begin the growth of the ZnO nanowires. The growth time was varied from 1 h to 35 h for controlling the morphology of the ZnO nanowires. The substrates were removed from the bottles after a certain amount of growth time and rinsed thoroughly in DI water. The substrates were finally sonicated in DI water, using a Sonorex Digitex DT31 ultrasound sonicator (35 kHz, 240 W, Bandelin), for 10–20 seconds to remove ZnO nanowire debris from the substrates followed by drying with N_2.

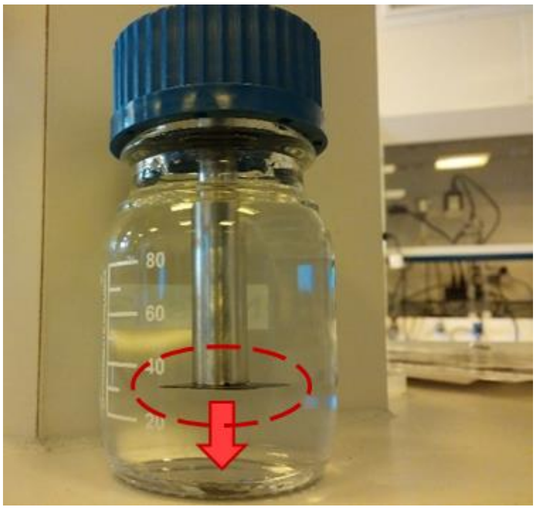

Figure 3.3. Position of the growth substrate in the hydrothermal growth solution. The substrate was attached to a stainless-steel rod facing downwards at the height of 2 cm in the growth solution.

3.2.3 Vertical ZnO nanowire (Chapter 4)

In Chapter 4, the hydrothermal growth of vertical ZnO nanowires is investigated to selectively control the morphology and geometry of the ZnO nanowires. In this regard, samples were made in two steps: first, fabrication of the growth substrates; and second, hydrothermal growth of the ZnO nanowires on the growth substrates. Three methods (Method 1, Method 2, and Method 3) were used for fabrication of the growth substrates, as shown in Figure 3.4.

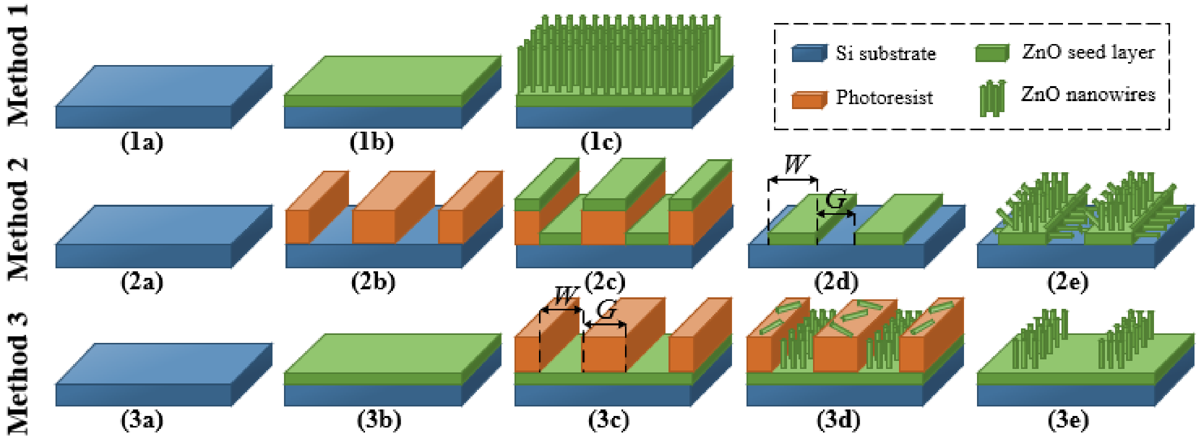

Figure 3.4. Three methods for fabrication of vertical ZnO nanowire samples as used in Chapter 4. Method 1: (1a) silicon (Si) substrate preparation; (1b) sputter deposition of ZnO seed layer over the entire substrate; (1c) hydrothermal growth of ZnO nanowires on the bulk ZnO seed layer. Method 2: (2a) Si substrate preparation; (2b) photolithography to define AZ5214E photoresist pattern on the substrate; (2c) sputter deposition of ZnO seed layer; (2d) lifting-off the photoresist to leave ZnO seed layer on defined regions; (2e) hydrothermal growth of ZnO nanowires. Method 3: (3a) Si substrate preparation; (3b) sputter deposition of ZnO seed layer over the entire substrate; (3c) photolithography to define AZ5214E photoresist pattern on the seeded substrate; (3d) hydrothermal growth of ZnO nanowires; (3e) lifting-off the photoresist to remove the ZnO nanowire debris. *W* indicates the seed layer width (the exposed area to the growth) and *G* indicates the seed layer gap (the unexposed area).

Method 1 was applied to fabricate the growth substrates with a bulk ZnO seed layer where vertical ZnO nanowires could grow all over the substrates, as shown in Figure 3.4 (1a)–(1c). 10 × 10 mm^2 silicon (Si) [100] substrates were initially cleaned with 1 minute sonication in acetone, 1 minute sonication in IPA, rinsing in IPA and drying in a stream of clean N_2. 100 nm thick ZnO seed layer was then deposited on the substrates using RF sputter coating (500 RF Magnetron, HHV Ltd). Different hydrothermal growth parameters were used for growing ZnO nanowires with different morphologies. Firstly, the equimolar concentration of zinc nitrate hexahydrate and HMT precursors varied from 2.5 mM to 150 mM for 4 h of growth time. Secondly, the growth time varied from 1 h to 20 h when standard 25 mM of precursor concentration was used. Lastly, the additive PEI precursor with concentrations of

2 mM–8 mM was added to 25 mM of the precursor concentration for the growth times of 4 h and 20 h.

Method 2 and Method 3 were utilised to pattern the growth of ZnO nanowires at controlled locations on the substrates and with highly controlled seed areas, using standard photolithography techniques, as shown schematically in Figure 3.4 (2a)–(2e) and (3a)–(3e), respectively. AZ5214E photoresist was used to form resist layers with linear patterns on the substrates before (Method 2) and after (Method 3) deposition of the ZnO seed layer, as seen in Figure 3.4 (2b) and (3c), respectively. A lift-off process was carried out in Method 2 to remove the excessive seed layer, leaving a pattern of ZnO seed areas on the substrate for the nanowire growth, as shown in Figure 3.4 (2d)–(2e). When using Method 3, the photoresist pattern was left on the bulk ZnO seed layer during the hydrothermal growth, as seen in Figure 3.4 (3d). The lift-off was applied post nanowire growth to remove ZnO nanowire debris, as shown in Figure 3.4 (3e).

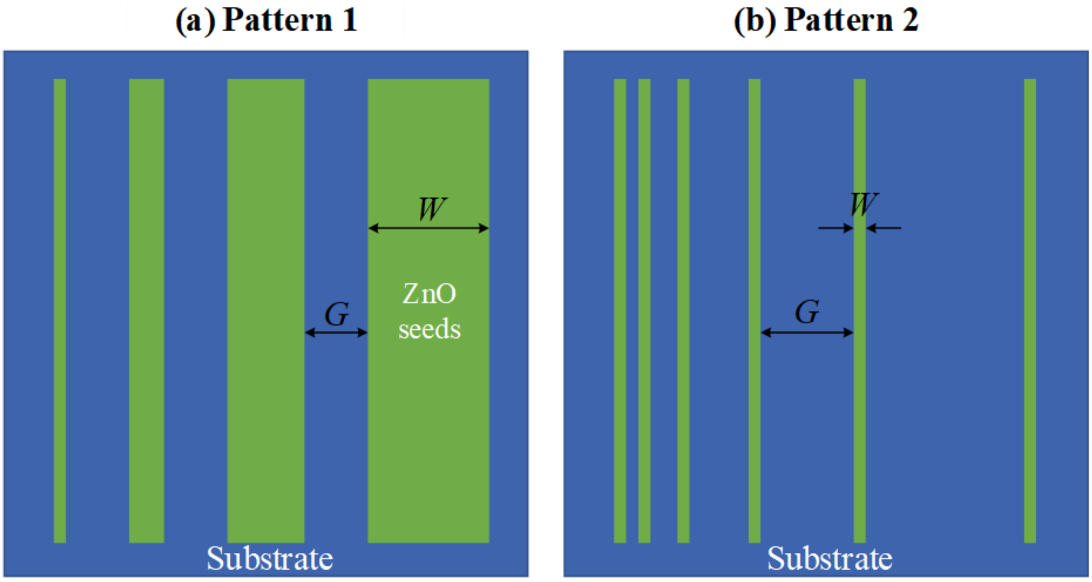

Figure 3.5. ZnO seed layer patterns used through Method 2 and Method 3 fabrication processes for the ZnO nanowire samples in Chapter 4. (a) Schematic of Pattern 1 with varying seed line width (*W*) and fixed seed line gap (*G*). (b) Schematic of Pattern 2 with varying seed line gap and fixed seed line width.

Two different seed area patterns were used in the fabrication of ZnO nanowires at controlled locations via Method 2 and Method 3 fabrication processes that were described above. Pattern 1 comprised of 7 mm long seed lines with the fixed seed line gaps (*G*) of 200 µm and the seed line widths (*W*) varying from 4 µm to 1 mm, as shown schematically in

Figure 3.5 (a). Pattern 2 comprised of 7 mm long seed lines similar to that of Pattern 1, but with the fixed seed line widths of 10 µm and the seed line gaps varying from 2 µm to 800 µm, as shown in Figure 3.5 (b). The exact values of the seed line widths and the gaps were measured from the scanning electron microscopy (SEM) images. The seed area ratio was subsequently calculated using Equation 3.1. The minimum adjacent gaps of the seed lines were used in the calculation of the seed area ratios.

$$\text{Seed area ratio} = \frac{W}{W+G} \qquad \text{Equation 3.1}$$

3.2.4 ZnO nanowire florets (Chapter 5)

Figure 3.6 shows the fabrication process of the ZnO nanowire florets as used in Chapter 5. 7 × 7 mm^2 Si substrates with 100 nm oxide layer on top (Si/SiO_2) were initially cleaned by 1 minute sonication in acetone, 1 minute sonication in IPA, rinsing in IPA and drying with N_2, as shown in Figure 3.6 (a). A photolithography process similar to Method 2, Section 3.2.3, was utilised to define a pattern of AZ5214E photoresist on the substrate, as shown in Figure 3.6 (b). A 100 nm thick ZnO seed layer was then deposited on the substrates via RF sputter coating, as shown in Figure 3.6 (c). A lift-off process was then applied by soaking in NMP at 60°C for 1 h followed by 2 h sonication in NMP at 60°C, 2 minutes sonication in IPA, rinsing in IPA and drying with N_2 to remove excessive seeds, as shown in Figure 3.6 (d). A hydrothermal growth process was carried out to grow ZnO nanowire florets from the deposited seed layers, as shown in Figure 3.6 (e). The nanowires were grown using 25 mM of zinc nitrate hexahydrate and HMT precursors with 6 mM of PEI for growth times of 1, 2, 4 and 8 h. The substrates were removed from the solution immediately after the growth, followed by rinsing in DI water, 1 minute sonication in DI water and drying with N_2.

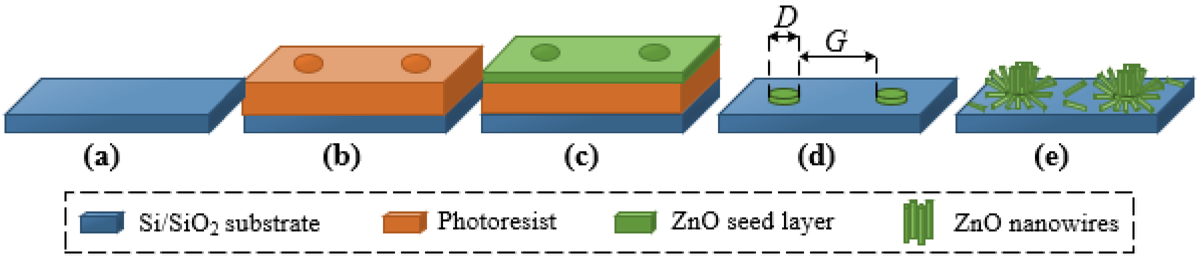

Figure 3.6. Fabrication process of ZnO nanowire florets for Chapter 5. (a) Si/SiO_2 substrate preparation; (b) photolithography to define AZ5214E photoresist pattern on the substrate; (c) sputter deposition of ZnO seed layer; (d) lifting-off the photoresist to leave ZnO seed layer on defined

regions; (e) hydrothermal growth of ZnO nanowires. *D* and *G* indicate the seed layer diameter and the gap between the seed layers, respectively, as shown in (d).

Figure 3.7 shows the photolithography mask pattern that was used for the fabrication of the ZnO nanowire florets for studying their biocompatibility with human hNT neurons. The pattern comprised of 9 arrays of circles with diameters of 15 µm, as shown in Figure 3.7 (a). Each of the arrays across the substrate has different inter-floret gaps of 5, 10, 20, 30, 40, 50, 75, 100 and 150 μm, as labelled by A–I in Figure 3.7 (a), respectively. Each array of the fixed diameter and the inter-floret gap was located within an area of 1 × 1 mm^2. Figure 3.7 (b) shows the magnified image of the “E” array with inter-floret gaps of 40 µm as an example.

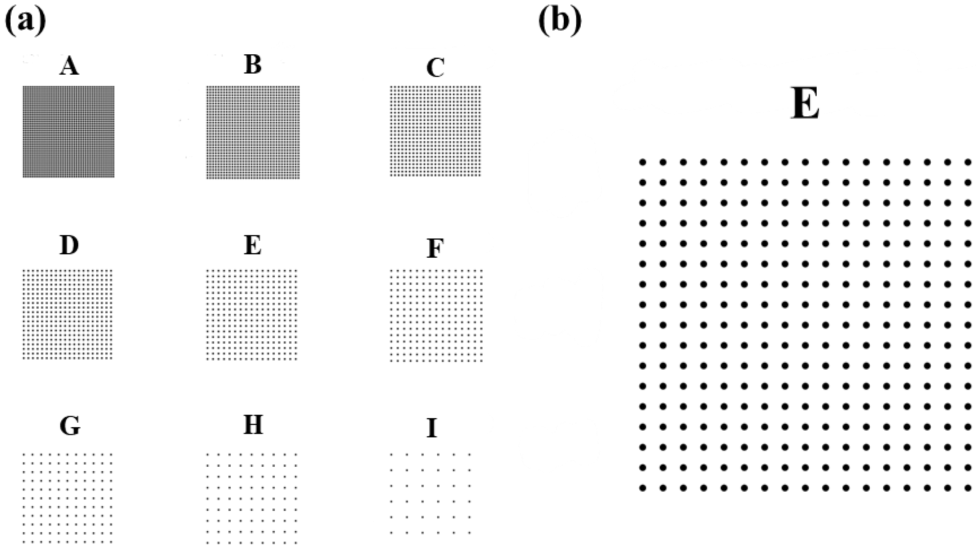

Figure 3.7. (a) Photolithography mask pattern used for fabrication of ZnO nanowire florets in Chapter 5. The pattern consists of 9 arrays of 15 μm wide circles with inter-floret gaps of 5, 10, 20, 30, 40, 50, 75, 100 and 150 μm as indicated by A–I, respectively. (b) Magnified view of the array with inter-floret gaps of 40 μm.

3.2.5 Microelectrode arrays (MEAs) (Chapter 6)

Microelectrode arrays (MEAs) were fabricated in three different configurations in Chapter 6: planar MEAs, MEAs with ZnO nanowires (ZnO-NW MEAs) and metal encapsulated ZnO-NW MEAs. MEAs were fabricated on 15 × 15 mm^2 Si substrates with 100 nm oxide layer in the layout shown in Figure 3.8. The MEA design comprised of 32 working microelectrodes and a single reference electrode within an area of 10.5 × 10.5 mm^2. The central working microelectrodes were placed in a 6–by–6 matrix within an area 4 × 4 mm^2. The central working microelectrodes were 200 µm in diameter with the gaps of 700 µm in between. The outer square electrode contact pads had an area of 600 × 600 µm^2 with the pitch gaps of 1100 µm. The electrode tracks that connected the outer electrodes to the central working microelectrodes had a minimum width of 50 µm wide. The designed photolithography mask also included four alignment markers (600 × 600 µm^2 and 500 × 500 µm^2 at the outer corners) to align different layers of the fabrication process.

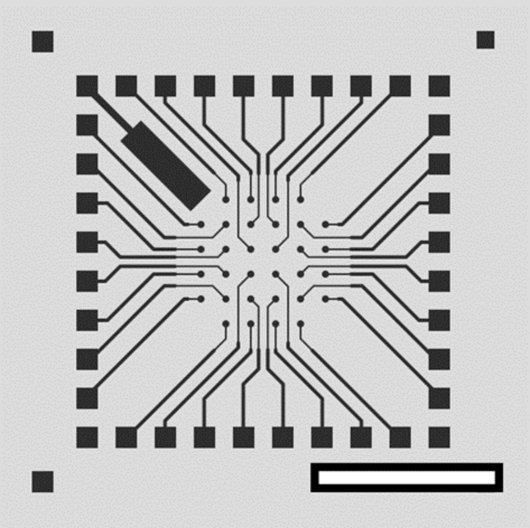

Figure 3.8. Photolithography mask design used for the fabrication of the microelectrode arrays (MEAs). Scale-bar is 5 mm.

3.2.5.1 Planar MEA

The fabrication of the planar MEAs is illustrated schematically in Figure 3.9. The Si/SiO$_2$ substrates were initially cleaned thoroughly by 1 minute sonication in acetone, 1 minute sonication in IPA, rinsing in IPA and drying with N$_2$, as shown in Figure 3.9 (a). Standard photolithography was applied to define a pattern of AZ1518 photoresist on the substrates, using Karl Suss MJB3 mask aligner, as shown in Figure 3.9 (b). Electrodes were deposited via thermal evaporation of 5 nm chrome followed by 50 nm of gold (Cr/Au) onto the Si/SiO$_2$ substrates, using Angstrom Engineering Nexdep Evaporator. A lift-process was then carried out by soaking in acetone for 1 h, 1 minute sonication in acetone, 1 minute sonication in IPA, rinsing in IPA and drying with N$_2$. Upon the lift-off process, the photoresist with the excessive Cr/Au was removed, leaving a pattern of Cr/Au electrodes on the substrates, as shown in Figure 3.9 (c).

The fabrication of planar MEAs was completed by the deposition of 8 µm thick SU8-2150 as a passivation layer through a photolithography process, as shown in Figure 3.9 (d).

The SU8 passivation layer covered the entire substrate except for the regions concentric with the working microelectrodes (with diameters of 50 µm) and the outer electrode contact pads to allow for electrical measurements of MEAs, as shown from top view in Figure 3.9 (e). The samples were finally hard-baked at 200°C for 15 minutes to heal any SU8 surface cracks and to improve the chemical and physical stability of the SU8 layer.

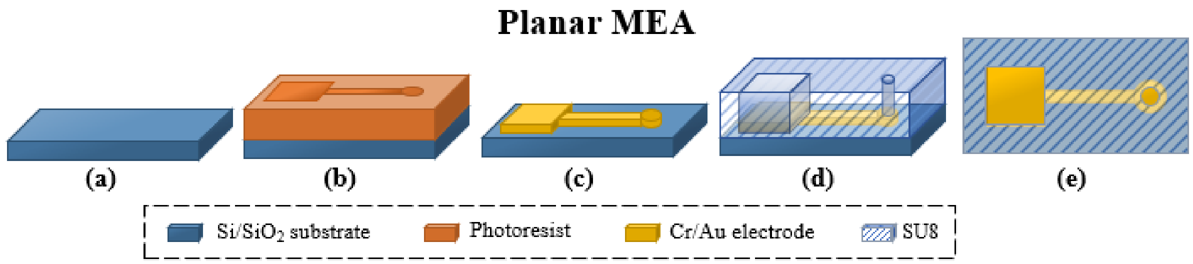

Figure 3.9. Fabrication process of planar microelectrode arrays (MEAs) for Chapter 6. (a) Si/SiO$_2$ substrate preparation; (b) photolithography; (c) deposition of Cr/Au layer by thermal evaporation followed by a lift-off process; (d) photolithography of SU8 passivation layer; (e) top view of the fabricated planar MEA.

3.2.5.2 ZnO nanowire MEA

Figure 3.10 illustrates the fabrication of MEAs with ZnO nanowires (ZnO-NW MEAs). The fabrication of ZnO-NW MEAs began from the fabricated planar MEAs as described above but without SU8 passivation layer. Photolithography was applied using AZ1518 photoresist to define circular gaps with diameters of 100 µm concentric with the central working microelectrodes, as shown in Figure 3.10 (b). A 100 nm thick ZnO seed layer was deposited by sputter deposition, using an HHV Auto 500 RF Sputter Coater, followed by a lift-off process to leave ZnO seeds on the central working microelectrodes, as shown in Figure 3.10 (c). Another photolithography step was applied using AZ5214E photoresist to define a pattern with 200 µm wide open areas concentric with the pre-deposited ZnO seeds, as seen in Figure 3.10 (d).

A hydrothermal synthesis, at 95°C, was used to grow ZnO nanowires from the pre-deposited ZnO seed layers, as described in Section 3.2.2 and shown in Figure 3.10 (e). The morphology of ZnO nanowires was controlled by varying the equimolar concentration of the zinc nitrate hexahydrate and HMT precursors within the range of 2.5–100 mM for 4 h of growth time and by varying the growth time from 4 h to 35 h when 25 mM of precursor concentration with 6 mM of PEI was used. A lift-off process was carried out after the growth of the nanowires by immersion in NMP for 2 h, 2 minutes sonication in NMP, 2 minutes sonication in IPA, rinsing in IPA and drying with N_2, as shown in Figure 3.10 (f). The SU8 passivation layer was then applied by the photolithography process to open a 50 µm wide circular window above the ZnO nanowires, as seen in Figure 3.10 (g).

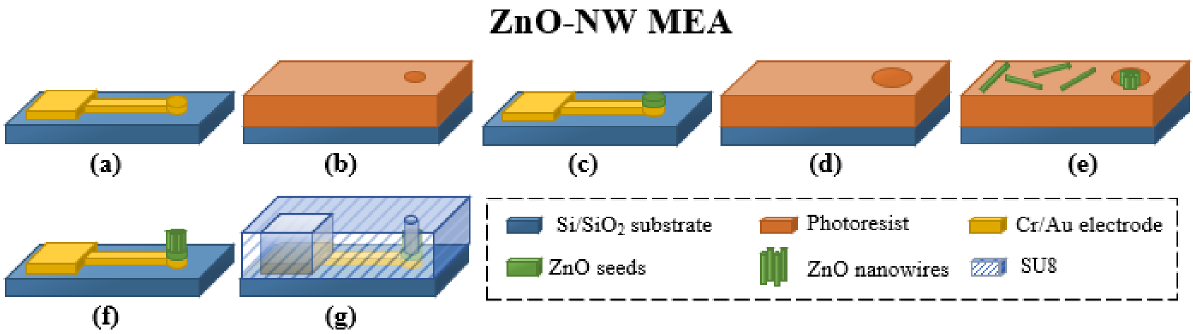

Figure 3.10. Fabrication process of microelectrode arrays with ZnO nanowires (ZnO-NW MEAs) for Chapter 6 that includes: (a) using a fabricated planar MEA without SU8 passivation layer; (b) photolithography; (c) sputter deposition of a ZnO seed layer followed by a lift-off process; (d) photolithography; (e) hydrothermal growth of ZnO nanowires; (f) lift-off; (g) photolithography of SU8 passivation layer.

3.2.5.3 Encapsulated ZnO nanowire MEA

MEAs with metal encapsulated ZnO nanowires were fabricated by an additional fabrication step on the ZnO-NW MEAs prior to the SU8 photolithography step, as illustrated schematically in Figure 3.11. Photolithography was applied using AZ1518 photoresist to define 200 µm wide open areas above the ZnO nanowires on the central working microelectrodes, as shown in Figure 3.11 (b). Different metal encapsulation layers of Cr/Au (2/20 nm) by thermal evaporation or titanium (Ti, 10 nm) and platinum (Pt, 10 nm) by e-beam evaporation were deposited on the substrates, using Angstrom Engineering Nexdep Evaporator. A lift-off process was then carried out, leaving a thin metallic layer coating the ZnO nanowires, as shown in Figure 3.11 (c). Finally, the SU8 photolithography step was carried out to complete the fabrication of the encapsulated ZnO-NW MEAs.

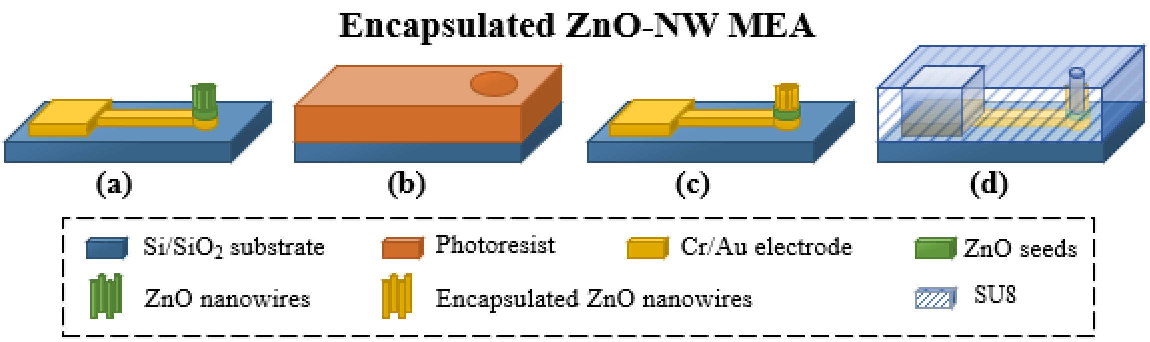

Figure 3.11. Fabrication process of microelectrode arrays with metal encapsulated ZnO nanowires (encapsulated ZnO-NW MEAs) for Chapter 6 that includes: (a) using a fabricated ZnO-NW MEA without SU8 passivation layer; (b) photolithography; (c) deposition of a metallic layer by thermal or e-beam evaporation followed by the lift-off process to encapsulate ZnO nanowires; (d) photolithography of SU8 passivation layer.

3.3 Characterisation

3.3.1 Scanning electron microscopy (SEM)

Scanning electron microscopy (SEM) and energy-dispersive X-ray spectroscopy (EDS) were performed by using either FEI NOVA NanoSEM 450 or JEOL 6500F for both imaging and elemental analysis of the fabricated samples. The SEM and EDS were operated at an accelerating voltage of 15 kV and 20 kV, respectively. The SEM images of ZnO nanowires were used to measure the diameter, length, aspect ratio and density of the nanowires using the ImageJ program. The diameter and density of ZnO nanowires were measured from the SEM images of each sample taken from the top view. The length of ZnO nanowires was measured from the SEM images taken from the cross-sectional view or at 70° tilted view. The nanowire aspect ratio was calculated as the ratio of the average length to the average diameter from the measurements.

The density of ZnO nanowires was determined by counting the number of nanowires within an area of 2–4 μm^2 of the SEM images, where only the distinguishable nanowires from the top view were used. This method could not define the exact density of the nanowires since any nanowires hidden underneath the upper layer of nanowires could not be counted. However, this method provided a reasonably good estimation of the nanowire density and is consistent across the samples. The method is also useful for studying the interaction of the

ZnO nanowires with the neuronal cells since the top area of the nanowires is the main part that interacts with the cells.

The error bars presented in the ZnO nanowire morphology graphs in Chapter 4–6 denoted one standard deviation (n > 30 NWs) for the diameter, length and aspect ratio, and 10 % standard deviation for the density. The standard deviation of the aspect ratio was calculated, assuming that the nanowire diameter and length were independent of each other. The human error and clarity of the SEM images were considered to affect the density measurements by 5–10 %. The data presented in the context of Chapter 4–6 were in the form of $\overline{\mathrm{X}} \pm \mathrm{SD}$, where $\overline{\mathrm{X}}$ was the mean value and SD was the one standard deviation, or 10% standard deviation (for nanowire density measurements).

3.3.2 Neuronal viability

Human NTera2.D1 cell line (hNT/NT2, ATCC CRL-1973) neurons were used for investigating the biocompatibility of ZnO nanowire samples with human neurons in Chapter 5. The biological experiments for the growth of hNT neurons have all been done by Brad J. Raos at the University of Auckland, as detailed in the Appendix A. In summary, human hNT neurons were differentiated from the NTera2.D1 embryonic carcinoma cell line following the previously introduced protocols [134–138]. After culturing NT2 cells for 4–5 weeks, hNT neurons were harvested by a selective trypsinisation and mechanical detachment procedure. The hNT neurons were then plated on the ZnO nanowire samples at approximately 1000 cells/mm^2. The ZnO nanowire samples were sterilised using Penicillin-Streptomycin-Glutamine (PSG, ThermoFisher Scientific), phosphate-buffered saline (PBS, Thermofisher Scientific), poly-D-lysine (PDL, Thermofisher Scientific) and Matrigel (Corning) before the cell plating.

Images of the hNT neurons on the samples were captured on an Olympus BX53 with an Olympus XC50 camera using a 20× magnification water immersion objective (UMPLFLNW 20×, NA 0.50). The functionality of neurons was measured by visualising free Ca^{2+} in the cytoplasm of neurons as a response to glutamate (Sigma Aldrich) stimulation after 2 DIV (days *in vitro*) by using Fluo-4 (green-fluorescent calcium indicator, ThermoFisher Scientific). The cytoplasm and nuclei of the neurons were then labelled by using fluorescent stains of CellTracker Green CMFDA (2 µM, ThermoFisher Scientific) and Blue Hoechst 33343 (1 drop per 500 µL media, ThermoFisher Scientific), respectively, as shown schematically in Figure 3.12. The cytoplasm area corresponded to the entire neuronal body, including the cell body (soma) and the neurites (dendrites and axons). Fluorescence images of each ZnO sample surface were captured over the entire substrate and stitched into a single image using CellSens Dimension software (Olympus).

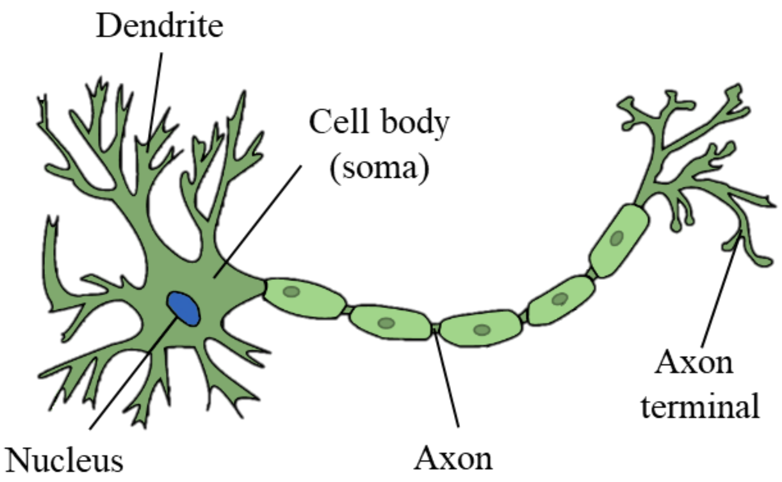

Figure 3.12. Schematic of a typical neuronal cell. The green regions represent the neuronal cytoplasm, including the cell body (soma) and neurites (dendrites and axons). The blue region represents the neuronal nucleus. Reproduced from [139].

The adhesion and patterning of the hNT neurons to the ZnO nanowire samples were quantified by measuring the area of the neuronal cytoplasm and nuclei on the defined regions of the substrate, using custom software in MATLAB for image processing. The area outside of the nanowire array region (plain Si/SiO_2 substrate), as shown in Figure 3.13 (a), was used as controls for neuronal growth. Figure 3.13 (b) shows the area of the nanowire array on the substrate. The neuronal adhesion was defined as the proportion of the neuronal cytoplasm and nuclei on the entire nanowire array, Figure 3.13 (b), relative to the control surrounding area, Figure 3.13 (a). Figure 3.13 (c) shows the area of the individual floret sites and 10 µm concentric bands at increasing distances from the florets. The localisation of the neurons to the nanowire florets was defined as a proportion of the neuronal nuclei area on the florets and the concentric surrounding bands, Figure 3.13 (c), relative to the control substrate area outside of the nanowire array, Figure 3.13 (a). In addition, the neurite growth was calculated as the proportion of the neuronal cytoplasm area to the nuclei area.

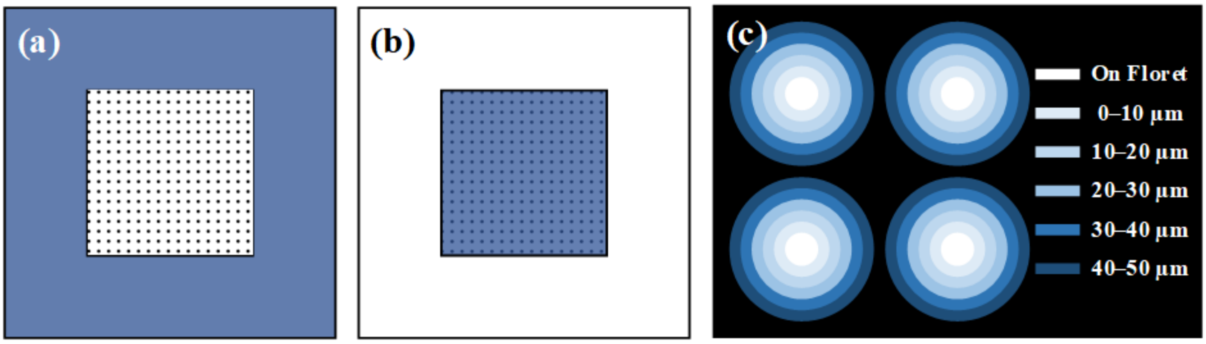

Figure 3.13. Schematics showing the areas of the ZnO nanowire samples used for quantification of neuronal adhesion and localisation in Chapter 5. (a) The plain substrate area outside of the nanowire array region for controls. (b) The area on the entire nanowire array for defining the neuronal adhesion and growth. (c) The area on the individual floret sites and 10 µm wide concentric band at increasing distances from the florets.

3.3.3 Electrochemical impedance spectroscopy (EIS)

The electrical characteristics of MEA devices were determined in Chapter 6 through electrochemical impedance spectroscopy (EIS) using Agilent 4294A precision impedance analyser in the configuration shown in Figure 3.14 (a). A frame made of polydimethylsiloxane (PDMS, Sylgard 184) was placed on the MEA to keep phosphate-buffered saline (PBS-1x) solution on the central working microelectrodes, and away from the outer electrode contact pads. The PBS-1x was prepared by dissolving a PBS tablet (2 g, Sigma Aldrich) in 200 mL of DI water. A 100 µL of PBS-1x (pH of 7.4 and conductivity of 13.2 mS/cm) was used for the EIS measurements as it is typically used for *in vitro* cell culture [140]. A two-point measurement configuration was applied, using tungsten electrode probes (14860-001, Rucker & Kolls), as shown in Figure 3.14 (b) and schematically in Figure 3.14 (c). The high potential (H_{pot}) and current (H_{cur}) terminals of the impedance analyser were connected to a tungsten electrode probe and placed in the PBS solution. The low potential (L_{pot}) and current (L_{cur}) terminals were connected to the outer electrode contact pads using a tungsten electrode probe. A potential of 100 mV was applied at high terminals by sweeping over a frequency range of 40 Hz to 10 MHz, and the impedance was recorded at the low terminals. These measurement parameters were chosen since neuronal cells typically transmit action potential signals (APs) with amplitudes of 100 mV_{pp} at a frequency of 1 kHz [25,51].

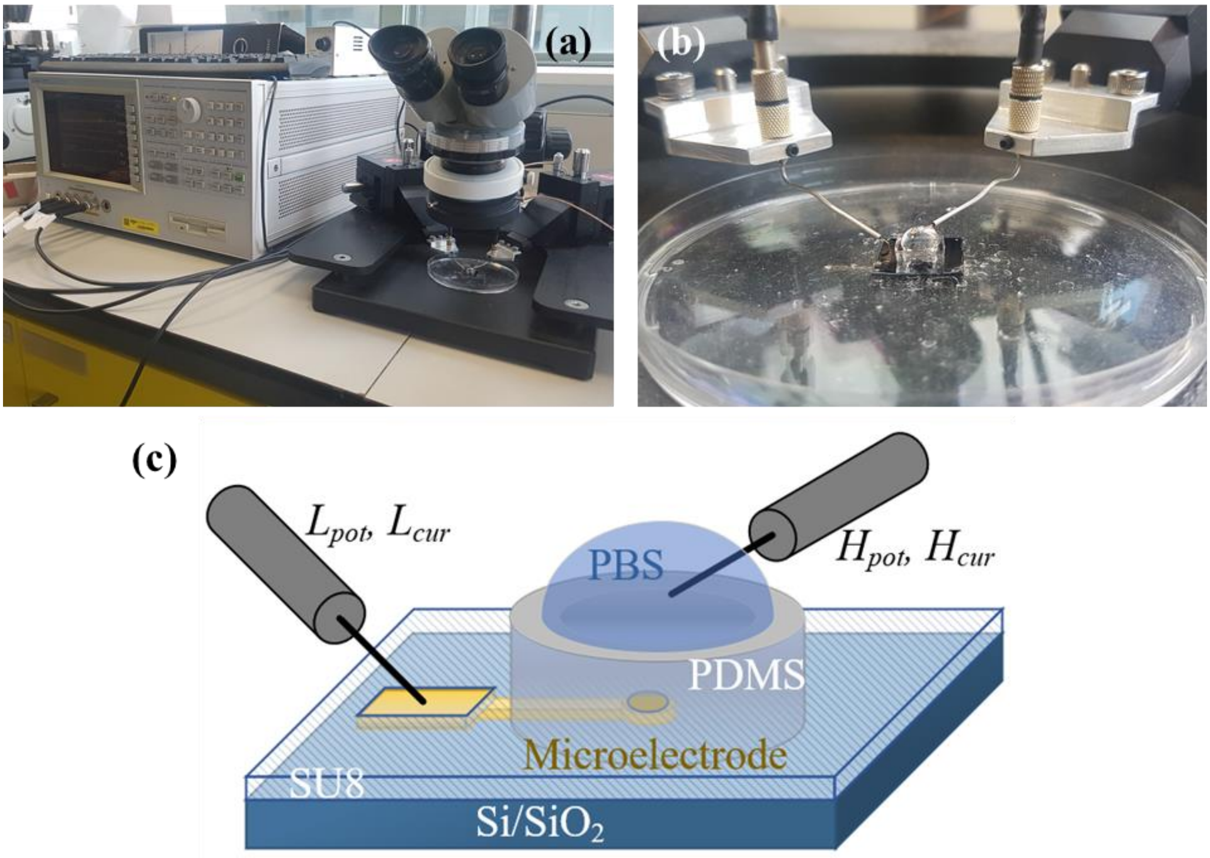

Figure 3.14. Electrochemical impedance measurement of microelectrode arrays (MEAs). (a) Measurement setup for the electrochemical impedance spectroscopy (EIS) of MEAs by using Agilent 4294A impedance analyser. (b) and (c) show an optical image and schematic of the two-point measurement connection used for the EIS, respectively. H_{pot} and H_{cur} represent the high potential and current terminals of the instrument connected to a tungsten electrode probe placed in phosphate-buffered saline solution (PBS). L_{pot} and L_{cur} represent the low potential and current terminals of the instrument connected to a tungsten electrode probe attached to the outer electrode contact pad of the MEA.

3.3.4 Mechanical stability

The mechanical stability of ZnO nanowires and metal encapsulated ZnO nanowires was determined by an ultrasound sonication, as previously described by Nick *et al.* [35] to study the mechanical stability of carbon nanotubes (CNTs) for neural interfaces. The ZnO nanowire and metal encapsulated ZnO nanowire samples were submerged in DI water and were sonicated for 24 h, using a Sonorex Digitec DT31 sonicator (240 W at 35 kHz, Bandelin). The ZnO nanowire samples were fabricated as ZnO nanowire florets with various inter-floret gaps, as described in Section 3.2.4. The ZnO nanowires were hydrothermally grown using 25 mM of precursor concentration with 6 mM of PEI for 1 h of growth time. The ZnO nanowires were also encapsulated with 10 nm Ti layer by e-beam evaporation normal to the entire substrate as an example of metal encapsulated ZnO nanowires. The SEM images of ZnO nanowires and Ti encapsulated ZnO nanowires before and after the sonication process were taken to determine their robustness for repeatable and long term neuronal applications.

3.4 Conclusion

The experimental procedures and characterisation techniques that were described in this chapter are all used in the following experimental results and discussion Chapters 4–6. In brief, Chapter 4 investigates the hydrothermal growth of ZnO nanowires to control the morphology and location of the nanowires. A wide range of growth parameters, such as precursor concentration of 2.5–150 mM, growth time of 1–20 h, and additive PEI concentration of 0–8 mM are used to control the morphology of the ZnO nanowires. Different fabrication processes of Method 1, Method 2, and Method 3 are also carried out to control the location of the ZnO nanowires. Different patterns of Pattern 1 and Pattern 2 are utilised through Method 2 and Method 3 fabrication processes to investigate the effect of the seed layer geometry (seed line width and gap) on the growth of ZnO nanowires. Scanning electron microscopy (SEM) is also used to characterise the morphology of the resulting ZnO nanowires.

In Chapter 5, the biocompatibility of ZnO nanowires with human hNT neurons is investigated. ZnO nanowires are grown as arrays of florets with various inter-floret gaps of 5–150 µm. The ZnO nanowire florets are grown on the patterned seed layers via Method 2 fabrication process. The morphology of the ZnO nanowires is varied by controlling the growth time from 1 h to 8 h, using the standard 25 mM of precursor concentration with 6 mM of PEI. The addition of PEI allows the active hydrothermal growth to be maintained for 8 h without refreshing the growth solution. SEM is used to characterise the morphology of the ZnO nanowires. The neuronal viability and image processing techniques described in this chapter are utilised to qualify the functionality as well as the adhesion and growth of the hNT neurons on the ZnO nanowire arrays.

In Chapter 6, the electrical properties of different microelectrode arrays (MEAs) are studied. MEAs are fabricated in form planar Cr/Au MEAs, ZnO-NW MEAs, and metal encapsulated ZnO-NW MEAs. The morphology of the ZnO nanowires on the MEAs is controlled by varying the precursor concentration from 2.5 mM to 100 mM for 4 h of growth time or by varying the growth time from 4 h to 35 h when standard 25 mM precursor concentration with 6 mM of PEI are used. The ZnO nanowires that are grown with 25 mM precursor concentration for 4 h are also encapsulated with a metallic layer of Cr/Au, Ti and Pt via the evaporation techniques. SEM is also used to characterise the morphology of the ZnO nanowires on the MEAs. The electrical properties of all MEAs are characterised via electrochemical impedance spectroscopy (EIS). Furthermore, the mechanical stability of the PEI ZnO nanowires and Ti encapsulated PEI ZnO nanowires are examined via the 24 h sonication process.

Chapter 4

Selective Growth of ZnO Nanowires

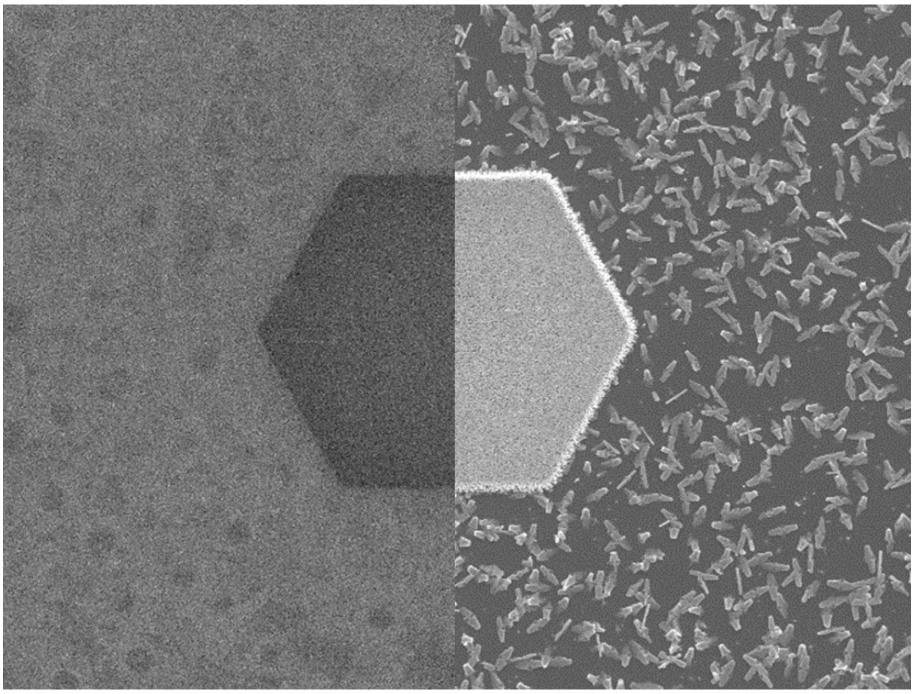

The dark side and bright side of the ZnO nanowires.

4.1 Introduction

Integration of microelectrodes with ZnO nanowires is proposed in this work to improve the performance of microelectrode arrays for recording signals from neuronal cells. ZnO nanowires have extensively been studied over the last decades, due to their excellent electronic and optoelectronic properties ideal for sensing applications [43–45]. Among different growth methods of ZnO nanowires, hydrothermal synthesis has received a lot of attention because of its low cost, low temperature (< 100°C), scalability and the ability to grow on various substrates including plastic substrates [43]. Vertical ZnO nanowires can easily be grown with high density on seeded substrates [107,123]. The variation in the morphology of the nanowires has been shown to alter their optical [141,142] and electronic properties [42,143]. The morphology and aspect ratio of ZnO nanowires grown via the hydrothermal synthesis have conventionally been controlled by varying growth parameters such as precursor concentration [43,115–117], growth time [115,118,119], growth temperature [118,120], solution pH [118,121] and ZnO seed layers [109,111,144].

In this chapter, the hydrothermal growth of ZnO that can later be applied to grow ZnO nanowires on microelectrode arrays is studied. The end goal is to improve their electronic properties and biocompatibility for integration with neuronal cells. The morphology and geometry of the ZnO nanowires are investigated, via control of the hydrothermal synthesis. I first study the influence of the critical growth parameters such as the precursor concentration, growth time and the addition of polyethylenimine (PEI) on the morphology of the ZnO nanowires grown on substrates with bulk seed layers. I then investigate how ZnO nanowires can grow on defined seed regions of the substrate and how the seed geometry influences the nanowire morphology. I finally study the theory behind the hydrothermal growth kinetics to explain the variations in nanowire morphology. The work presented in this chapter is drawn from the paper "Selective growth of ZnO nanowires with varied aspect ratios on an individual substrate" published in the Materials Research Express journal in October 2018 by Mohsen Maddah, Charles P. Unsworth and Natalie O.V. Plank [145]. The co-authors of this work have advised and commented on the manuscript of the published paper, but the thesis author has done all the experimental work and analysis.

4.2 ZnO nanowires growth on the bulk seed layer

In this section, the influence of zinc nitrate hexahydrate and hexamethylenetetramine (HMT) precursors, growth time and polyethylenimine (PEI) on ZnO nanowire growth are investigated. The effect of these parameters will later be applied to control the morphology of ZnO nanowires for the microelectrode array devices, Chapters 5 and 6. Method 1 fabrication process, as detailed in Section 3.2.3 of Chapter 3, was applied to prepare the growth substrates. $10 \times 10\ \mathrm{mm}^2$ silicon (Si) [100] substrates were initially cleaned by 1 minute sonication in acetone, 1 minute sonication in isopropanol (IPA), rinsing in IPA and drying in a stream of clean N_2. The substrates were then coated with a 100 nm thick bulk ZnO seed layer using RF sputter coating. The growth solution was prepared by mixing equimolar solution amounts of zinc nitrate hexahydrate and HMT precursors in 100 mL of deionised (DI) water. The growth substrates were placed in the growth solution at 95°C to begin the growth of ZnO nanowires, as shown in Figure 4.1. The substrates were removed from the growth solution after a certain amount of time and were cleaned thoroughly with 10 seconds sonication and rinsing in DI water followed by drying with N_2. The morphology of the resulting nanowires was then studied to determine the influence of the growth parameters.

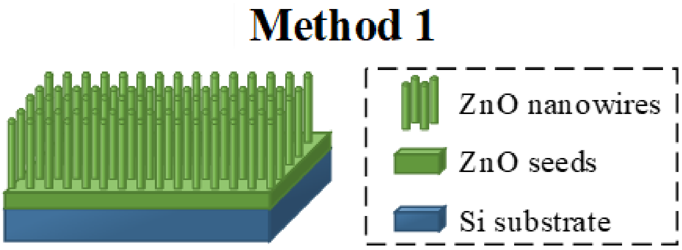

Figure 4.1. Schematic of ZnO nanowires grown on a Si substrate with a bulk ZnO seed layer, through Method 1 fabrication process, as detailed in Section 3.2.3 of Chapter 3.

4.2.1 Precursor concentration

Zinc nitrate hexahydrate, $Zn(NO_3)_2$, and hexamethylenetetramine (HMT), $(CH_2)_6N_4$, are the most common precursors that have been used in the hydrothermal growth of ZnO nanowires [43,115–117]. In this process, the zinc nitrate hexahydrate provides the Zn^{2+} ions and HMT provides the hydroxyl ions (OH^-) necessary for the formation of ZnO crystals. In the hydrothermal synthesis, the precursor concentration plays a vital role in the morphology of the resulting ZnO nanowires that can change their electrical characteristics and biocompatibility [117].

4.2.1.1 Results of the precursor concentration variation

Here, ZnO nanowires were grown on Si substrates with the bulk seed layers by varying the equimolar concentration of zinc nitrate hexahydrate and HMT precursors from 2.5 mM to 150 mM for the growth time of 4 h, as shown in Figure 4.2 (a)–(f), respectively. Figure 4.2 shows that increasing the precursor concentration resulted in longer and thicker ZnO nanowires, agreeing with previous work [116,117]. Figure 4.2 (f) shows a dramatic increase in the diameter for the 150 mM sample, compared to the 25 mM sample shown in Figure 4.2 (d). Furthermore, the SEM images in Figure 4.2 (a)–(f) show that the nanowire density decreased with increasing precursor concentration.

Increasing the precursor concentration from 2.5 mM to 150 mM decreased the pH of the solution from 7.2 to 5.2. Vernardou *et al.* [121] and Chevalier *et al.* [118] previously showed the influence of the growth solution pH on the morphology of ZnO nanowires. They reported that ZnO nanostructures grew in the form of hexagonal or cone-shaped nanowires at the pH of 7. Figure 4.2 shows the morphology of nanowires to be consistent with the hexagonal structure in the measured pH range of 5.2–7.2, although it is more apparent for the large nanowires that were grown by using a high precursor concentration, e.g. 150 mM with a pH of 5.2, as shown in Figure 4.2 (f).

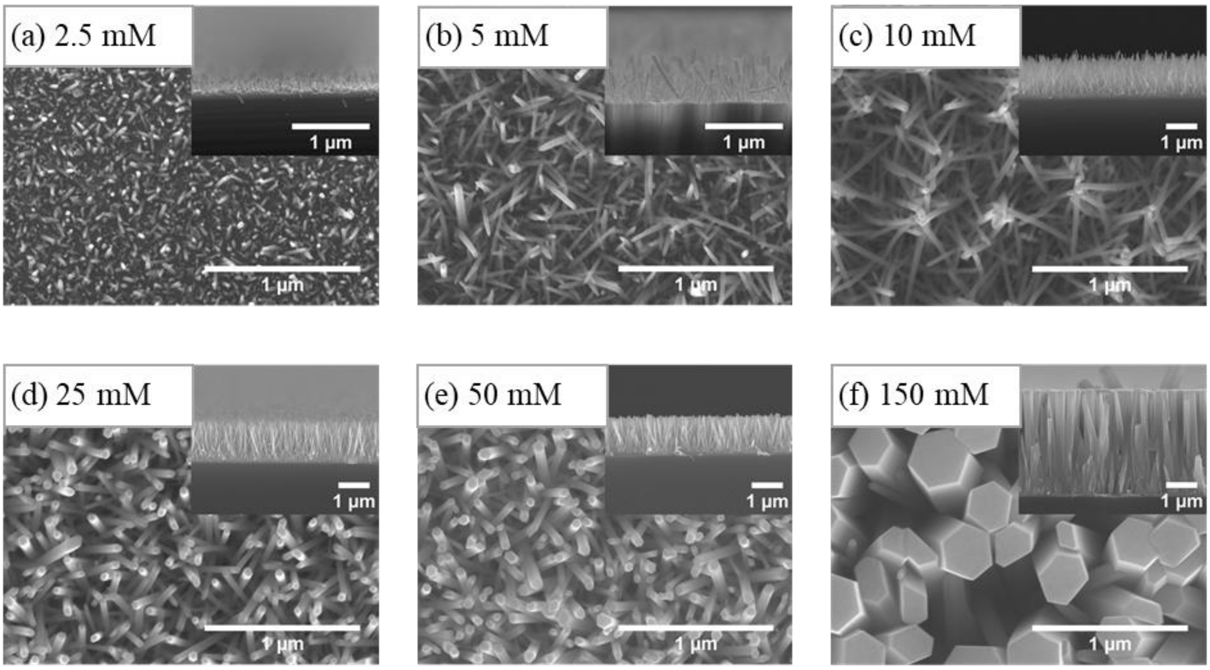

Figure 4.2. SEM images of ZnO nanowires grown on Si substrates with bulk ZnO seed layers that were grown for 4 h with equimolar precursor concentration of (a) 2.5 mM, (b) 5 mM, (c) 10 mM, (d) 25 mM, (e) 50 mM and (f) 150 mM. The SEM images of nanowires were taken from the top view and side view (insets).

Figure 4.3 (a) and (b) plot the diameter and length of the ZnO nanowires against the precursor concentration, respectively, grown for 4 h on Si substrates with the bulk seed layers. Increasing the precursor concentration from 2.5 mM to 150 mM increased both the diameter and the length of the nanowires. Subsequently, the nanowire length increased from 145 ± 100 nm to 3.33 ± 0.06 µm, and the diameter increased from 23 ± 2.5 nm to 290 ± 80 nm. For the concentrations of 2.5–15 mM, the nanowires predominantly grew longer rather than wider. Their length increased by a factor of 11× (0.145 ± 0.1 µm to 1.61 ± 0.2 µm) while their diameter only doubled (23 ± 2.5 nm to 45 ± 5 nm). For the precursor concentration of 15–50 mM, the length of the nanowires decreased, whereas the diameter increased. The length decreased from 1.61 ± 0.2 µm to 1.16 ± 0.1 µm while the diameter continued to increase from 45 ± 5 nm to 60 ± 10 nm. With precursor concentrations of 50-150 mM, both the diameter and the length of the nanowires increased from 60 ± 10 nm to 290 ± 80 nm and from 1.16 ± 0.1 µm to 3.33 ± 0.06 µm, respectively.

Figure 4.3 (c) shows the aspect ratio calculated from the data plotted in Figure 4.3 (a) and (b). The maximum aspect ratio of 36 ± 8 occurred at a concentration of 15 mM. Figure 4.3 (c) shows that increasing the concentration above 15 mM increased the nanowire diameter more quickly than the nanowire length. Consequently, the ZnO nanowire aspect ratio decreased beyond the concentration of 15 mM. The uncertainty bars in Figure 4.3 (a) show that the nanowire diameters were distributed over a broad range when a high precursor concentration was used. At a high precursor concentration of 150 mM, the nanowire diameters varied from 110 nm to 400 nm, agreeing with M. Gou *et al.* [120]. In contrast, the nanowire length distributed over a broader range when a low precursor concentration was used, e.g. 5 mM, as shown in Figure 4.3 (b).

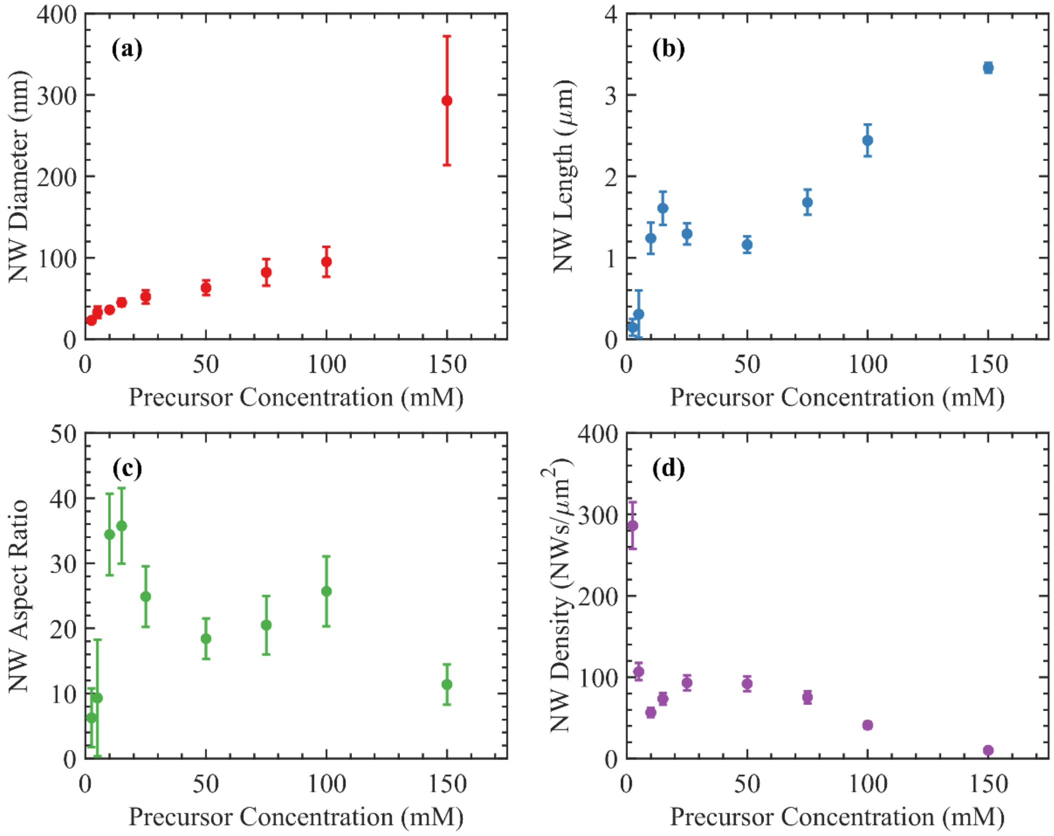

Figure 4.3. Morphological graphs of ZnO nanowires grown on Si substrates with bulk ZnO seed layers for various precursor concentrations using a growth time of 4 h. (a) Diameter, (b) length, (c) aspect ratio and (d) density of the ZnO nanowires were measured from SEM images. (c) The aspect ratios were calculated from data plotted in graphs (a) and (b). Error bars represent one standard deviation (n > 30 NWs) in (a)–(c) and 10% deviation in (d).

Figure 4.3 (d) plots the nanowire density for precursor concentrations in a range of 2.5–150 mM. At the lowest concentration of 2.5 mM, the density of the nanowires was highest at 285 ± 28 NWs/μm^2. Increasing the precursor concentration from 2.5 mM to 150 mM decreased the nanowire density by a factor of 28, to 10 ± 1 NWs/μm^2. Figure 4.3 (d) also shows a rapid decrease in the nanowire density from 285 ± 28 NWs/μm^2 to 55 ± 5 NWs/μm^2 when the precursor concentration increased from 2.5 mM to 10 mM. Within a concentration of 10–25 mM, the nanowire density increased from 55 NWs/μm^2 to 95 NWs/μm^2. Further increase of the precursor concentration above 25 mM continued to reduce the density from 95 ± 9 NWs/μm^2 to 10 ± 1 NWs/μm^2 at 150 mM of the concentration, which also agrees with Lopez *et al.* [116].

4.2.1.2 Influence on the precursor concentration

4.2.1.2.1 Low precursor concentration

The hydrothermal growth of ZnO nanowires on the seeded substrates underwent a mass transport limited growth [146]. In this mechanism, the number of reactant ions in the solution and their diffusion rate towards the seeds/nanowires control the growth rate of the nanowires. The presence of a thick ZnO seed layer (100 nm) on the Si substrate, as done with sputter deposition, is thought to result in a high reaction rate at the substrate surface [42]. A growth solution with a low precursor concentration, e.g. 2.5 mM, has a small number of ions in the bulk solution to diffuse towards the ZnO seeds/nanowires. Subsequently, there are fewer ions available at the nanowire surfaces during the growth that results in a slow nanowire growth.

4.2.1.2.2 Intermediate precursor concentration

Increasing the precursor concentration increases the diameter of the nanowires that grow from the seed layer. As there are more ions available near the seed layer surface, it is more likely for the ions to accumulate and begin the growth of wider nanowires. Furthermore, ZnO nanowires grow intrinsically at a faster rate along the c-axis of the nanowires than the lateral directions, as ions tend to be adsorbed more on the c-faces to reduce the overall nanowire surface energy [125]. As the precursor concentration increases to 15 mM, the growth rate along the c-axis increases faster than the growth rate in the lateral directions, resulting in increased nanowire aspect ratio. At the same time, the overall density of the nanowires decreases as the nanowires become longer and wider. As the diameter of the nanowires increases, the space between them becomes limited for new nanowires to grow. Furthermore, a selective competition takes place between the nanowires as they become longer and wider, limiting the number of nanowires for further growth.

The bulk seed layer deposited by the RF sputtering on Si substrates is a 100 nm thick polycrystalline layer with a surface roughness of 1.21 nm$_{\mathrm{rms}}$, as shown in Figure 4.4 (a). The seed layer comprises a high density of ZnO seeds that are randomly oriented on the substrate. The nanowires can, therefore, start growing from seeds in different orientations. As nanowires grow, the misaligned nanowires can collide with the neighbouring nanowires that either stops their further growth or changes their growth orientation, as shown in Figure 4.4 (b), [42,147]. The nanowires that were grown from the seeds with the c-axis perpendicular to the substrate have, therefore, more chance to survive and continue growing. As a result, the density of the nanowires decreases and their vertical alignment relative to the substrate improves as the nanowires grow longer.

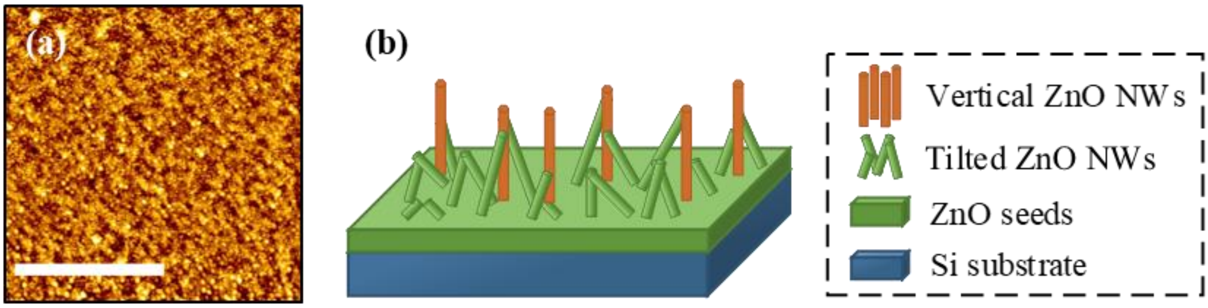

Figure 4.4. (a) Atomic Force Microscopy (AFM) image of sputter deposited ZnO seed layer on a Si substrate. The surface roughness of 100 nm thick seed layer was measured to be 1.21 nm_{rms}. Scale-bar = 1 µm. (b) Schematic shows the growth of ZnO nanowires on the seed layer in different directions. While tilted ZnO nanowires collided with the neighbouring nanowires, vertical ZnO nanowires could continue to grow longer.

At the precursor concentrations above 15 mM, both the diameter and the length of the nanowires increase. However, the lateral growth rate increases faster than the vertical growth that causes the aspect ratio to decrease. The growth rate along the c-axis is thought to reach a quasi-saturation point at 15 mM of concentration; the diffusion rate of the ions from the solution towards the nanowires equalises with the reaction rate at the growth surface [117,145]. Increasing the precursor concentration from 15 mM to 50 mM increases the radial growth of the nanowires more than the axial growth, resulting in the reduced aspect ratio. At a concentration of 50 mM, the lateral growth also reaches a quasi-saturation point, but since both vertical and lateral growth has reached their saturation points, the nanowires continue to grow both vertically and laterally.

4.2.1.2.3 High precursor concentration

Applying a substantially high precursor concentration, ≥ 150 mM, results in the growth of nanowires with large diameters that can fuse into each other, forming a dense layer of ZnO nanowires. The high precursor concentration supplies plenty of reactant ions at the nanowire surface that cannot solely be consumed by the existing nanowires. As a result, new clusters of ZnO nanowires can nucleate and start growing on top of the primarily grown nanowires, as shown in Figure 4.5. The newly nucleated nanowires have access to the ions in all directions that make them grow in the form of florets, as shown in Figure 4.5 (b). The ZnO florets are also surrounded by more ions as there is much free space around them for the diffusion of the ions. The ZnO florets, therefore, grow at a much faster rate in all directions compared to the previously grown nanowires.

By controlling the precursor concentration, it is possible to influence the morphology of the ZnO nanowires through the hydrothermal synthesis. The precursor concentration can, therefore, be used as a critical parameter to control the morphology of ZnO nanowires on microelectrode arrays for integration with neuronal cells. In the next section, I investigate the influence of growth time on nanowire growth.

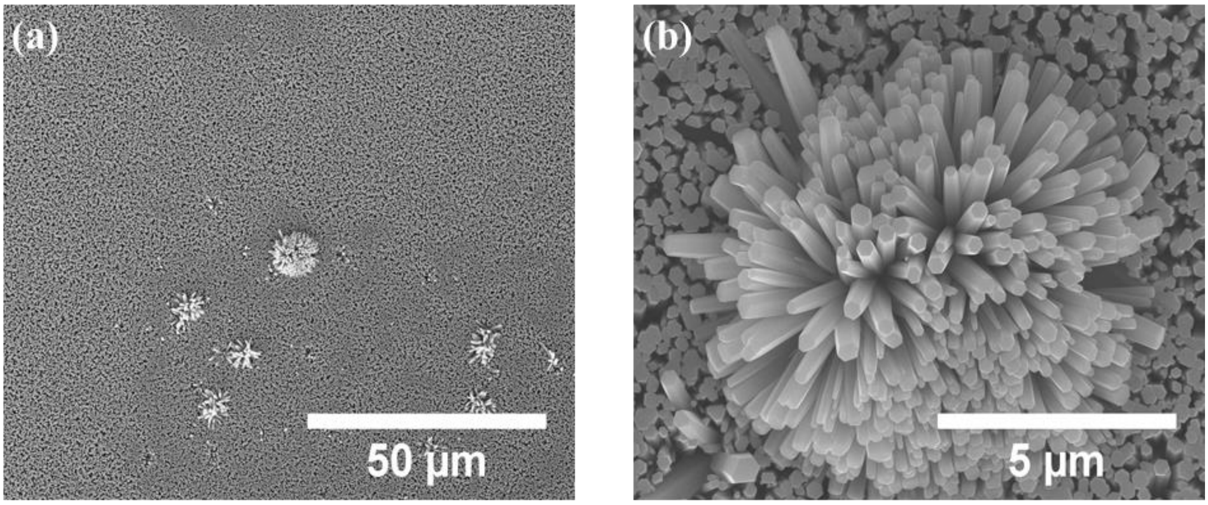

Figure 4.5. (a) SEM image of new ZnO nanowire clusters grown on primarily grown ZnO nanowires on a Si substrate with a bulk ZnO seed layer using 150 mM of precursor concentration and 4 h of growth. (b) The SEM image shows one of the new ZnO nanowire clusters at a higher magnification.

4.2.2 Growth time

The influence of the growth time on the nanowire growth was studied to further understand how to achieve the ZnO nanowire morphology required for my microelectrodes. ZnO nanowires were grown on Si substrates with the bulk ZnO seed layers using 25 mM of precursor concentration with the growth time varying from 1 h to 20 h. A concentration of 25 mM was used for studying the effects of the growth time, as it is commonly used in the literature [68,101,123,133] and has previously shown in Section 4.2.1 to produce nanowires with a reasonably high aspect ratio of 25–30.

4.2.2.1 Results of the growth time variation

Figure 4.6 (a)–(f) show scanning electron micrographs of ZnO nanowires grown after 1, 2, 4, 10, 15 and 20 h, respectively. The SEM images show both the top view and insets of the side view of the ZnO nanowires. The nanowires predominantly grew longer rather than getting wider as the growth time increased, agreeing with previous work [118,119]. The density of the nanowires also decreased by increasing the growth time. Furthermore, the variation in the nanowire morphology was more prominent in the early hours of the growth, 1–4 h, compared to the long growth times, 10–20 h.

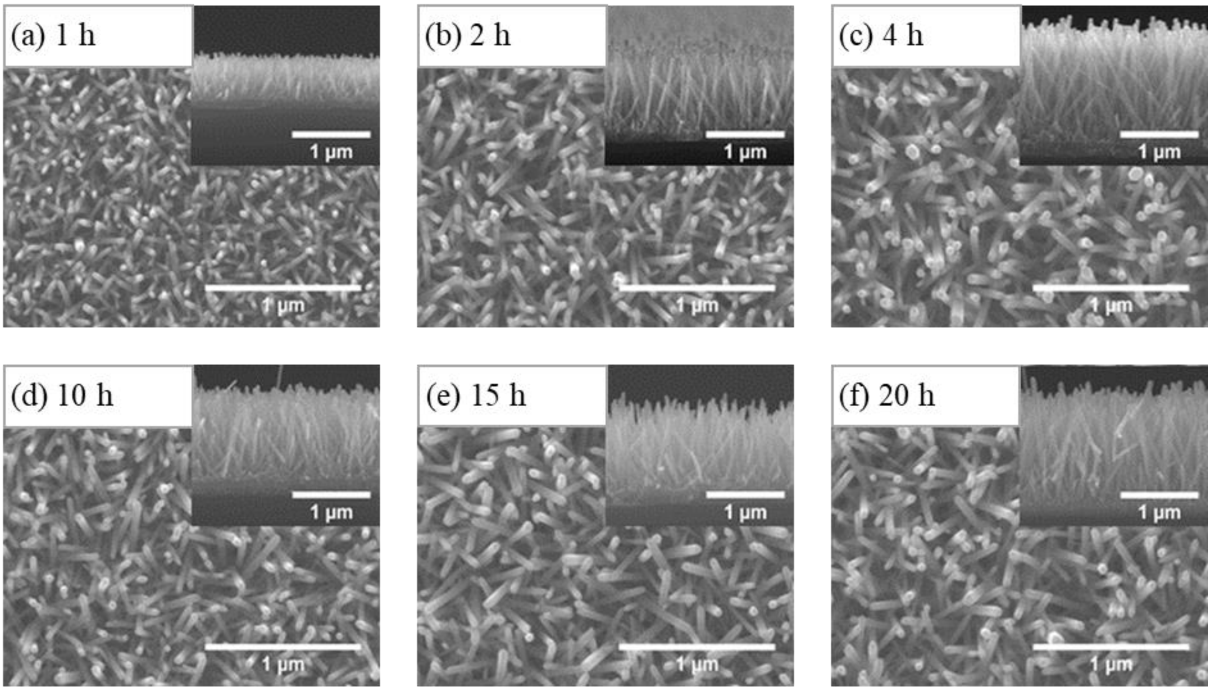

Figure 4.6. SEM images of ZnO nanowires grown on Si substrates with bulk ZnO seed layers using 25 mM of precursor concentration with a growth time of (a) 1, (b) 2, (c) 4, (d) 10, (e) 15 and (f) 20 hours. The SEM images of the nanowires were taken from the top view and the side view (insets).

Figure 4.7 (a)–(d) summarises the measurements taken from the SEM images for the nanowires grown with 25 mM of precursor concentration over the time periods of 1–20 h. The nanowires grew fastest within 1–4 h of growth. During the first 4 h of growth, the average length of the ZnO nanowires increased from 530 ± 50 nm to 1.38 ± 0.1 µm, while the average diameter only increased from 33 ± 4 nm to 50 ± 8 nm, as seen in Figure 4.7 (a) and (b), respectively. Consequently, the aspect ratio of the nanowires reached a maximum of

28 ± 6 within 4 h of growth and it remained nearly constant for any longer growth time, as shown in Figure 4.7 (c). After 4 h, the nanowire growth rate slowed down in both vertical and lateral directions, where the diameter and length did not change substantially any more.

Figure 4.7 (d) shows a plot of the nanowire density for the samples grown with 25 mM of precursor concentration for various growth times in the range of 1–20 h. For 25 mM of concentration, the density of the nanowires was maximum, 185 ± 18 NWs/µm^2, after 1 h of growth. The density of the nanowires approximately halved to 100 ± 10 NWs/µm^2 within 2 h of growth. For any longer growth time, ≥ 2 h, the average nanowire density remained approximately the same at 100 ± 20 NWs/µm^2.

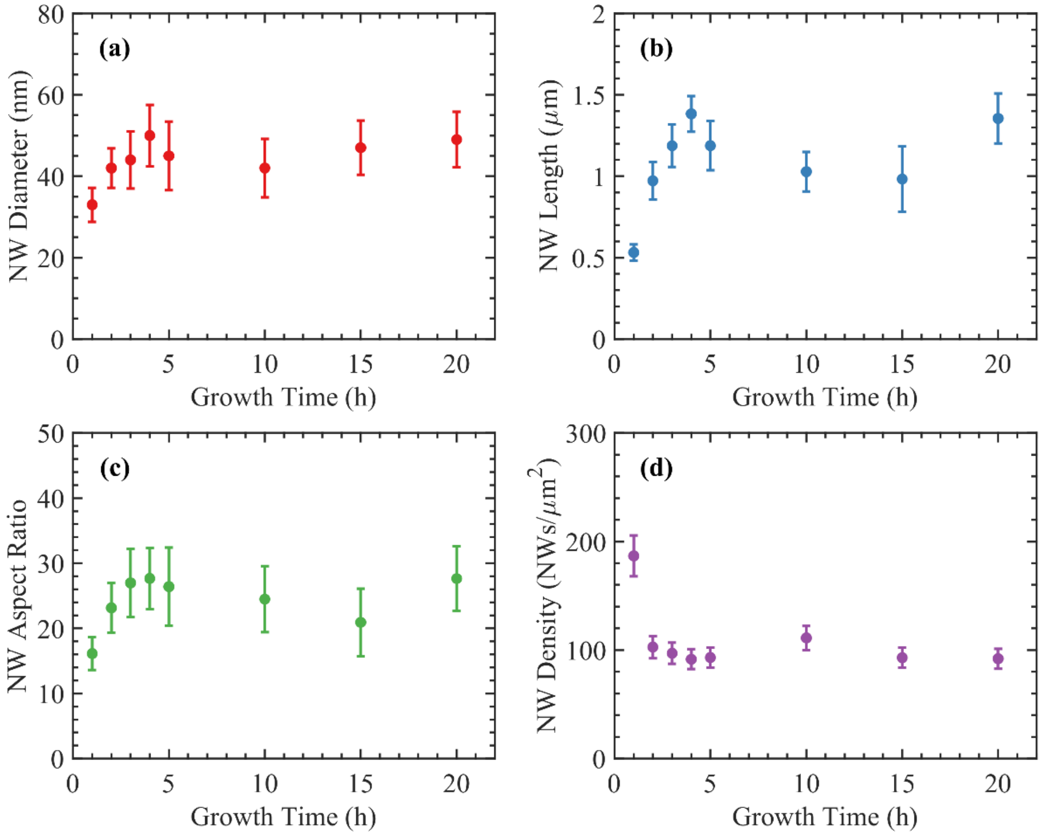

Figure 4.7. Morphological graphs of ZnO nanowires grown on Si substrates with bulk ZnO seed layers for various growth times using a precursor concentration of 25 mM. (a) Diameter, (b) length, (c) aspect ratio and (d) density of the ZnO nanowires were measured from SEM images. (c) The aspect ratios were calculated from data plotted in graphs (a) and (b). Error bars represent one standard deviation (n > 30 NWs) in (a)–(c) and 10% deviation in (d).

4.2.2.2 Influence of the growth time

4.2.2.2.1 Initial stages of the nanowire growth

At the beginning of the hydrothermal growth, the bulk solution concentration is at its maximum and provides the highest possible number of ions on the seed/nanowire surfaces [118]. Accordingly, the nanowires grow the fastest during the early stage of the growth. The density of the nanowires is also at its highest during the early stage of the growth as ZnO crystallisation takes place on the deposited seed layer with a high density of the seeds. Furthermore, due to the random orientation of the seeds, the nanowires grow in all directions [147].

4.2.2.2.2 During the nanowire growth

The concentration of the reactant ions decreases as the growth time increases due to the consumption of the ions by the ZnO nanowire growth and precipitation of ZnO in the growth bottle. The reducing ion concentration results in lower diffusion rates and therefore, a lower nanowire growth rate. Despite that the growth rate is reduced, nanowires continue to grow preferentially along the c-axis rather than the lateral directions [125]. The nanowires reach the maximum aspect ratio of 28 ± 6 within 4 h of growth. For growth times longer than 4 h, the nanowire diameter and length stay at a plateau of 45 ± 5 nm and 1 ± 0.2 μm, respectively, since very few ions have remained in the solution.

The density of the nanowires almost halves, from 185 ± 18 to 100 ± 10 NWs/μm^2, after 2 h of growth. As the nanowire length approximately doubles, from 530 nm to 970 nm, a selective competition takes place between the nanowires. As discussed in Section 4.2.1, an increase of the nanowire diameter and length can reduce the nanowire density. As the nanowires grow longer and wider, they can collide and stop further growth or coalesce with each other and continue their growth. For the growth times longer than 2 h, the nanowire density stays reasonably unchanged at 100 ± 10 NWs/μm^2, because most of the misaligned nanowires that started growing from the seeds have already been affected by the selective competition at earlier stages of the growth.

The effect of the growth time can vary significantly depending on the initial precursor concentration and the position of the substrate in the growth medium. The pH of the solution with 25 mM precursor concentration is measured to be stable at 6.1 ± 0.1 during 20 h of growth. However, the pH variation by the growth time is expected to be more noticeable when a higher precursor concentration, e.g. 100–150 mM, is used. For the high precursor concentration, there are more reactant ions in the solution at the beginning of the growth and the reduction of the ion concentration can be more significant during the nanowire growth.

4.2.2.2.3 The extreme growth of nanowires

In Section 4.2.1.2.3, using a high precursor concentration of 150 mM was determined to result in the growth of wide and long ZnO nanowires within 4 h of growth. Extending the growth time to 19 h, as shown in Figure 4.8, allows further growth of primarily grown nanowires both axially and radially, in such that the nanowires coalesce with each other and form a dense layer of ZnO nanowires with a thickness of 8.2 ± 0.1 μm, as seen in Figure 4.8 (b) and (c). As the ZnO nanowires coalesce, the room for radial growth reduces and the nanowires continue their axial growth as a layer.

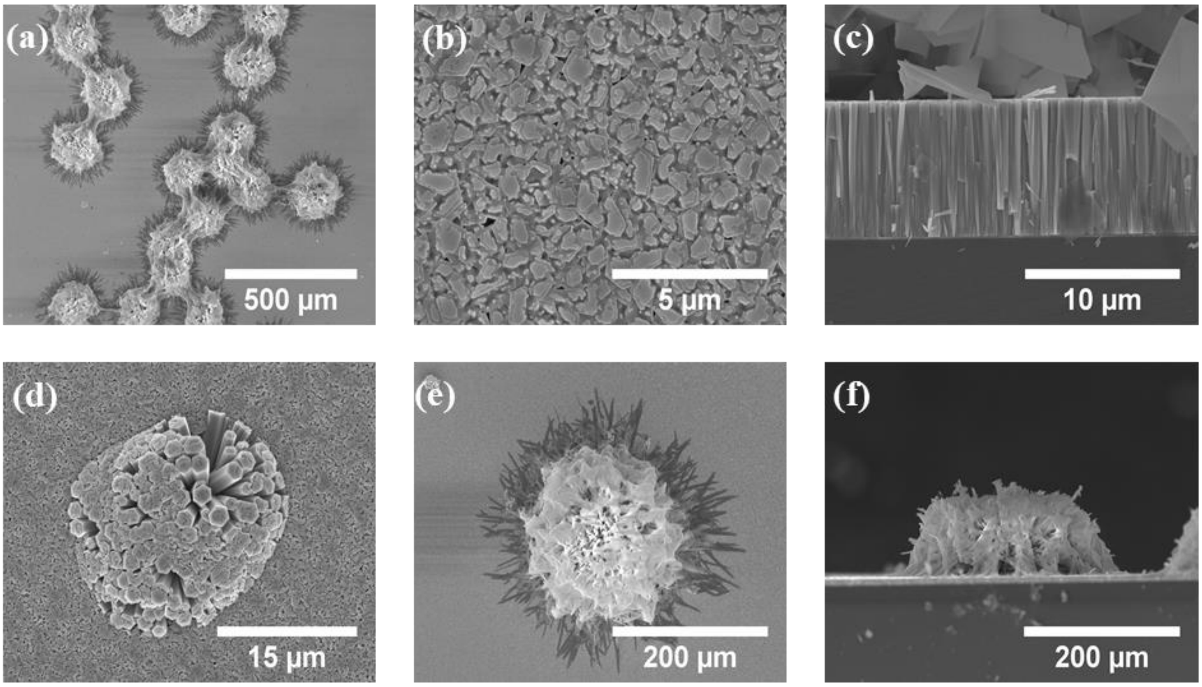

Figure 4.8. SEM images of ZnO nanowires grown on a Si substrate with a bulk seed layer using 150 mM of precursor concentration and 19 h of growth. (a) A topside overview of the ZnO structures grown on the substrate. (b) Top view and (c) side view of the primarily grown ZnO nanowires on the seeded substrate that were coalesced with each and formed a dense layer. (d) New nucleation of a ZnO cluster on top of the primarily grown ZnO nanowires. (e) Top view and (f) side view SEM images show extended growth of a new ZnO nucleation that formed into a large ZnO floret on top of the underlying grown ZnO nanowires.

Figure 4.5 previously showed that new nucleation of ZnO clusters could be formed on top of the primarily grown ZnO nanowires when a growth time of 4 h is applied using a precursor concentration of 150 mM. Figure 4.8 (d) also shows the new ZnO nucleation on top of the primarily grown nanowires for 19 h of growth. The longer growth time has also allowed new ZnO nucleation to continue their growth forming large ZnO florets, as seen in Figure 4.8 (e) and (f), with an average diameter of 240 ± 30 μm and an average height of 74 ± 11 μm. The ZnO florets are thought to undergo a faster growth rate compared to the underlying nanowires below as more ions are available around the ZnO florets. The fast diffusion of the ions around the ZnO florets is also considered to shape their morphology that consists of ZnO ribbons rather than nanowires. In the meantime, the depletion of the ions as consumed by the ZnO florets limits the growth of the ZnO layer underneath.

Applying ZnO nanowires on microelectrode arrays for electrical interaction with neuronal cells is thought to be affected by the morphology of the nanowires. Studying the influence of the nanowire morphology on the biocompatibility of the ZnO nanowires and the electrical properties of the microelectrodes requires the ability to control the morphology of the ZnO nanowires within a broad range. Increasing the growth time is expected to be an effective way of controlling the aspect ratio of the nanowires [115,118]. However, the nanowire growth is determined to be limited to 4 h when a growth solution with 25 mM of precursor concentration is used. Although a precursor concentration higher than 25 mM can be applied to continue the nanowire growth for a longer time, this can lead to the formation of undesired ZnO clusters. A multi-step growth can subsequently be applied by changing the growth solution after a certain time to ensure that the growth continuously takes place in the solution [119,132]. A continuous flow system can also be applied to provide a stable growth solution that controls the precursor concentration available in the solution for the entire growth time [148]. Such a system can minimise the variation of growth rate over time, allowing the nanowires to grow for a longer time to achieve high aspect ratios. In the next section, I investigate the effect of the additive PEI to mediate the growth of the nanowires within a long growth time as an alternative to applying a complicated multi-steps growth or a continuous flow system.

4.2.3 Polyethylenimine (PEI)

Polyethylenimine (PEI) is a polymer commonly used in the hydrothermal synthesis of ZnO nanowires to enhance the aspect ratio of the nanowires, which is now investigated here. Previous work by C. Burke-Govey *et al.* [123] showed that PEI with a molecular weight (Mw) of 800 g/mol is successful in controlling the morphology of ZnO nanowires in comparison to the other PEI. ZnO nanowires were grown using a precursor concentration of

25 mM with PEI (Mw of 800 g/mol) concentration varying from 2 mM to 8 mM. The ZnO nanowires were grown for 4 h and 20 h on Si substrates with bulk seed layers.

4.2.3.1 Results of the PEI variation

Figure 4.9 (a)–(c) show scanning electron micrographs from both top view and side view (insets) of ZnO nanowires grown by using 25 mM precursor concentration with PEI concentrations of 0, 6 and 8 mM, respectively, for 4 h of growth. The nanowire length decreased when a PEI concentration of 6 mM or lower was used compared to the nanowires grown with no PEI, as shown in Figure 4.9 (b) and (a), respectively. As the PEI concentration increased to 8 mM, as shown in Figure 4.9 (c), the nanowires became longer than the nanowires grown with no PEI. Furthermore, the nanowire diameter remained unchanged when different concentrations of PEI was applied, except 8 mM. Increasing the PEI concentration to 8 mM also resulted in reducing the density of the nanowires.

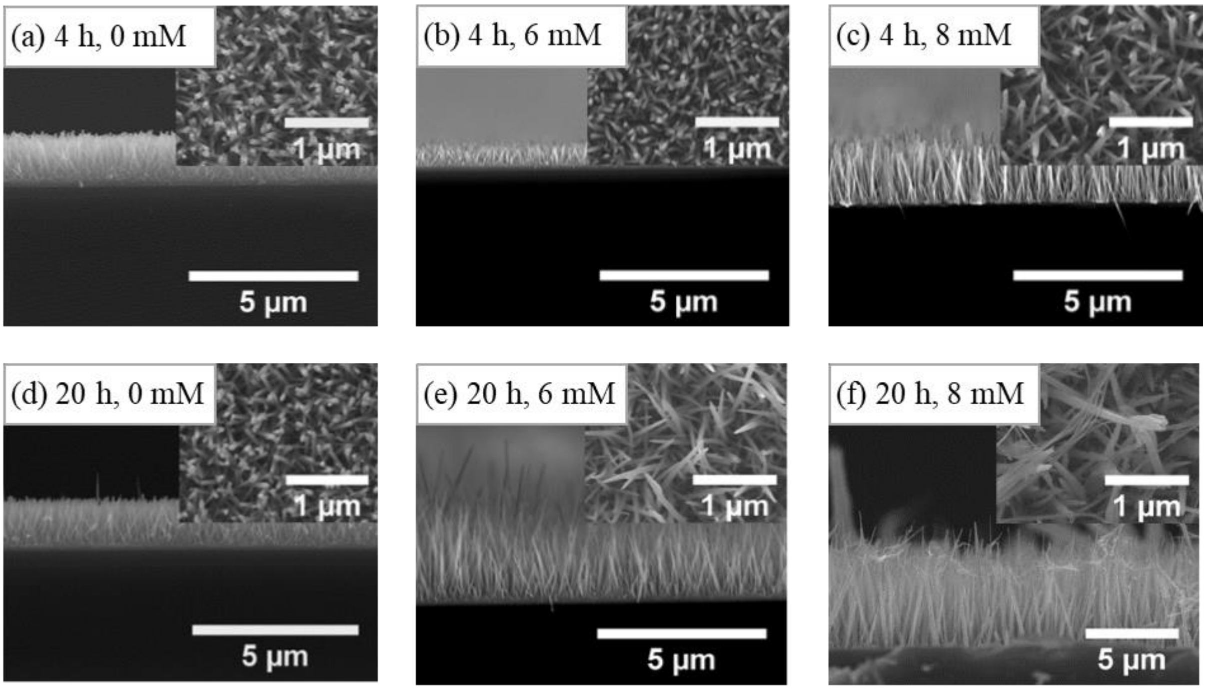

Figure 4.9. SEM images of ZnO nanowires grown on Si substrates with bulk ZnO seed layers using 25 mM of precursor concentration and additive PEI with a concentration of (a, d) 0 mM, (b, e) 6 mM and (c, f) 8 mM for 4 h and 20 h of growth, respectively. The SEM images of the nanowires were taken from side view and top view (insets).

Figure 4.9 (d)–(f) show SEM images of ZnO nanowires grown using 25 mM precursor concentration with PEI concentrations of 0, 6 and 8 mM, respectively, for 20 h growth. The nanowire length increased when 6 mM and 8 mM PEI concentrations were used, as shown respectively in Figure 4.9 (e) and (f), compared to the nanowires grown with no PEI, Figure 4.9 (d). The nanowire diameter also increased when 8 mM PEI concentration was used, whereas not much changes could be observed for PEI concentration ≤ 6 mM. The density of the nanowires decreased using 6 mM and 8 mM PEI concentration, compared to the nanowires grown with no PEI.

Figure 4.10 (a)–(d) plot the diameter, length, aspect ratio and density of ZnO nanowires grown on Si substrates with the bulk seed layers using 25 mM precursor concentration with various PEI concentrations 0–8 mM for 4 h and 20 h of growth. Figure 4.10 (a) shows that the nanowires had an average diameter of 45 ± 10 nm that did not change substantially with the PEI concentration and the growth time. However, at 20 h of growth, 8 mM PEI concentration exceptionally resulted in the growth of large nanowires with an average diameter of 65 ± 45 nm. The nanowires were also grown with a broad range of diameters, varying from 13 nm to 210 nm, when 8 mM PEI was used for 20 h of growth.

Introducing a low concentration of PEI to the growth solution was found to shorten the length of the nanowires, as seen in Figure 4.10 (b). For the growth time of 4 h, the addition of 4 mM PEI reduced the length from 1.4 ± 0.1 µm of no PEI to 0.53 ± 0.08 µm. Applying the PEI concentration of more than 4 mM increased the length of the nanowires to a maximum of 1.7 ± 0.4 µm for 8 mM. As discussed in Section 4.2.2, a growth time longer than 4 h did not affect the morphology of the nanowires without using PEI. Figure 4.10 (b) shows that in contrast to the samples grown without PEI, the addition of PEI to the solution resulted in the growth of nanowires to take place for a longer time, 20 h. However, using a low PEI concentration of 2 mM reduced the nanowire length from 1.25 ± 0.15 µm to 0.81 ± 0.15 µm, even after 20 h of growth. Applying a higher PEI concentration, 4–8 mM, to the solution allowed the nanowires to grow for the much longer growth time of 20 h. At 8 mM PEI the nanowire length was enhanced by a factor of 5×, to 6.2 ± 2.5 µm, after 20 h of growth. The nanowires that were grown with 8 mM PEI for 20 h also had a broad range of lengths that varied from 3.5 µm to 14 µm.

The aspect ratio of the nanowires varied with PEI concentration, as shown in Figure 4.10 (c). Since the diameter of the nanowires did not change substantially, as seen in Figure 4.10 (a), the aspect ratio followed the trend of the nanowire length, Figure 4.10 (b). When no PEI was applied, the nanowires had an average aspect ratio of 28 ± 7 for both 4 h and 20 h of growth. Adding 2 mM PEI concentration to the solution reduced the aspect ratio to 19 ± 6.

Increasing the PEI concentration to 4–6 mM continued to reduce the aspect ratio to 12 ± 3 for 4 h of growth time. However, for 20 h of growth, the aspect ratio began to increase when a PEI concentration of 4 mM or higher was used. At 8 mM PEI, the aspect ratio reached its maximum of 36 ± 14 for 4 h and 95 ± 75 for 20 h. Figure 4.10 (c) also shows a large uncertainty for the nanowires that were grown with 8 mM PEI for 20 h due to their broad range of diameters and lengths, as seen in Figure 4.10 (a) and (b) respectively.

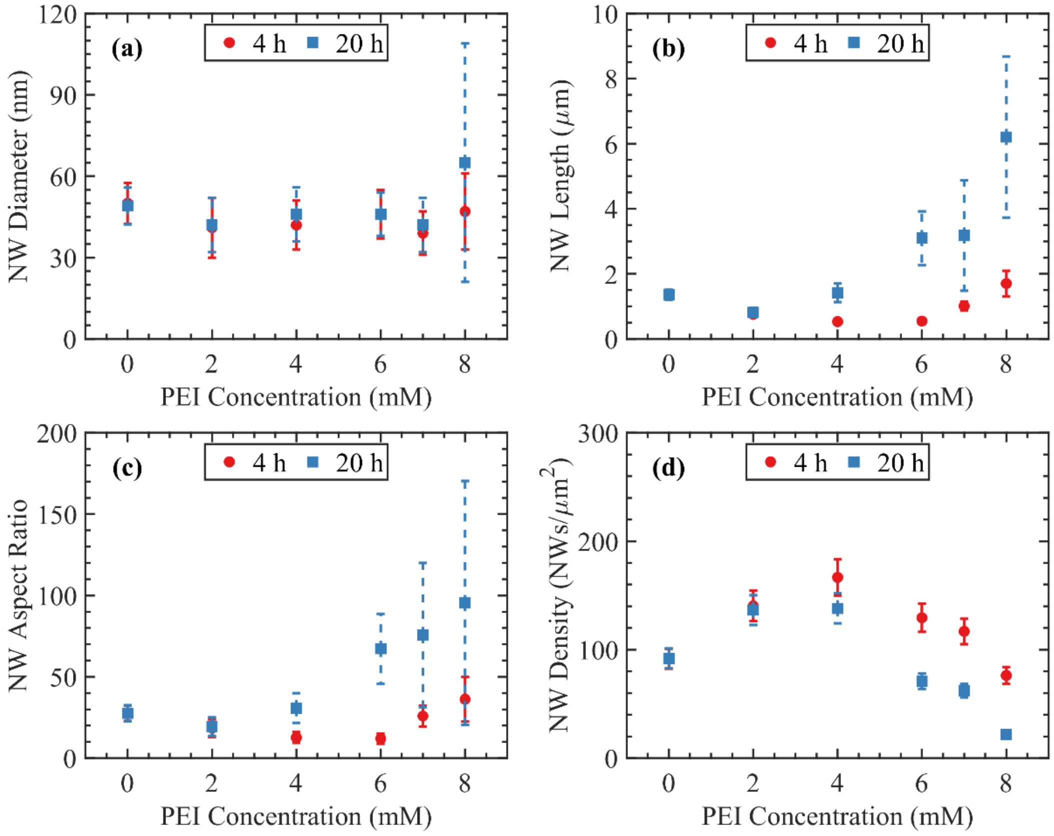

Figure 4.10. Morphological graphs of ZnO nanowires grown on Si substrates with the ZnO seed layers for various PEI concentrations, using 25 mM of precursor concentration with the growth time of 4 h (red circles) and 20 h (blue squares). (a) Diameter, (b) length, (c) aspect ratio and (d) density of the ZnO nanowires were measured from SEM images. (c) The aspect ratios were calculated from data plotted in graphs (a) and (b). Error bars represent one standard deviation (n > 30 NWs) in (a)–(c) and 10% deviation in (d).

Figure 4.10 (d) shows that the density of the nanowires inversely followed the trend of the nanowire length and the aspect ratio. The average density was about 92 ± 9 NWs/μm^2 for both 4 h and 20 h of growth when no PEI was used. The density reached a maximum of 167 ± 17 NWs/μm^2 for 4 h and 138 ± 14 NWs/μm^2 for 20 h at 4 mM PEI concentration. Increasing the PEI concentration beyond 4 mM reduced the density to a minimum of

76 ± 8 NWs/μm^2 and 22 ± 2 NWs/μm^2 for 4 h and 20 h of growth, respectively, when 8 mM PEI was used. Since the diameter of the nanowires did not vary significantly for various PEI concentrations, a selective competition between the nanowires was expected to take place as the nanowires were growing longer, which reduced the nanowire density.

4.2.3.2 Influence of PEI

PEI allows ZnO nanowires to grow for a longer time, e.g. from 4 h to 20 h, as shown in Figure 4.7 and Figure 4.10, respectively. ZnO crystallisation is thought to be taken heterogeneously and homogenously during the hydrothermal synthesis. In the heterogeneous growth, ZnO crystallisation takes place on a substrate and grow into ZnO nanostructures [149,150]. The homogenous growth comprises ZnO formation in the growth solution that precipitates to the bottom of the growth bottle [151]. Using a growth solution without PEI, the homogeneous growth is the dominant mechanism that quickly consumes the reactant ions available in the solution. The solution also changes becoming cloudy as a result of the ZnO formation in the bulk solution that precipitates as white powders. Adding PEI to the solution slows the homogenous nucleation in the solution and enhances the heterogeneous growth on the substrates. The solution colour also appears to be clear yellow, due to less ZnO precipitate in the solution. The colour change is also determined to originate from the $–N=CH_2$ groups produced by a Mannich reaction taken between HCHO compounds and NH_2 groups of PEI during the hydrothermal chemical reaction that results in the continuous growth of ZnO nanowires over a long growth [131].

PEI increases the aspect ratio during the hydrothermal synthesis of ZnO nanowires [123,125]. The PEI molecules can attach to the lateral (non-polar) faces of the nanowires that confine their lateral growth [106,131]. The limited lateral growth can also be seen in my results, as previously shown in Figure 4.10 (a), where nanowires with small diameters were grown despite the variation in PEI concentration and growth time. Subsequently, PEI encouraged the growth of nanowires along the c-axis that enhanced their aspect ratio.

Adding a PEI concentration of 8 mM to the growth solution spoils the pre-deposited ZnO seed layer that was partially removed during growth. The attachment of the sputter deposited seed layer to the substrate was weakened during nanowire growth; post-growth sonication could remove the entire seed layer with the attached nanowires from the substrate. The delamination of the seed layer can be associated with an increased pH level of the solution to 8.5 when 8 mM PEI is used compared to a pH of 6.1 for the growth solution with no PEI.

Varying the precursor concentration (2.5–150 mM), growth time (1–20 h) and PEI concentration (0–8 mM) controls the morphology of the ZnO nanowires within a broad range. As a result, ZnO nanowires with a diameter of 20–300 nm, length of 0.15–6.2 µm, aspect ratio of 6–95 and density of 10–285 NWs/µm^2 can be grown. The understanding taken from the influence of the growth parameters can later be applied to control the morphology of ZnO nanowires on microelectrodes for integration with neuronal cells.

The nanowires presented above were grown on the entire substrate. However, sometimes nanowires must be grown on defined regions, e.g. microelectrodes. Furthermore, varying the growth parameters as above will affect the nanowires similarly, requiring different samples for different nanowire morphologies. Although this technique can be applied to grow uniform nanowires on microelectrode arrays, nanowires with different morphologies across the same substrate are sometimes required.

In the next section, two different patterning techniques will be introduced that allow growing nanowires on defined regions. Furthermore, the influence of the seed layer geometry on the morphology of the nanowires will be investigated that paves the way to grow nanowires with different morphologies on a single substrate. The patterning technique will then be applied in Chapter 5 to minimise the difficulties and constraints associated with studying the integration of neuronal cells with ZnO nanowires of various morphology and geometry.

4.3 ZnO nanowires growth on the patterned seed layer

In this work, the aim is to achieve as simple a process as possible to create controlled variation in the morphology of ZnO nanowires on a single substrate at defined locations. The process will then be applied for fabricating samples with nanowires in various morphologies to study their interaction with neuronal cells. Furthermore, the patterning process will be applied to selectively grow ZnO nanowires on the microelectrodes for integration with the neuronal cells. The hydrothermal synthesis takes places at a low temperature (95°C) that allows a standard photolithography technique for controlling the regions of the nanowire growth. Two different processes, Method 2 and Method 3, as shown in Figure 4.11 (a) and (b) and detailed in Section 3.2.3 of Chapter 3, were applied for fabrication of the samples in this section. 10 × 10 mm^2 silicon (Si) [100] substrates were initially cleaned thoroughly by 1 minute sonication in acetone and then in IPA, followed by rinsing in IPA and drying with N_2. The photolithography process (using AZ5214E photoresist) was applied to define linear patterns on the substrates before (Method 2) and after (Method 3) deposition of ZnO seed layers, as shown in Figure 4.11 (a1) and (b1), respectively. The lift-off process was subsequently applied in Method 2 to remove any undesired seeds, leaving a pattern of ZnO seed lines on the substrate for the nanowire growth, as shown in Figure 4.11 (a2). In Method 3, a photoresist pattern remained on the substrates with bulk seed layers. The lift-off process was applied after the nanowire growth to remove ZnO nanowire debris, leaving vertical nanowires on defined regions, as shown in Figure 4.11 (b2).

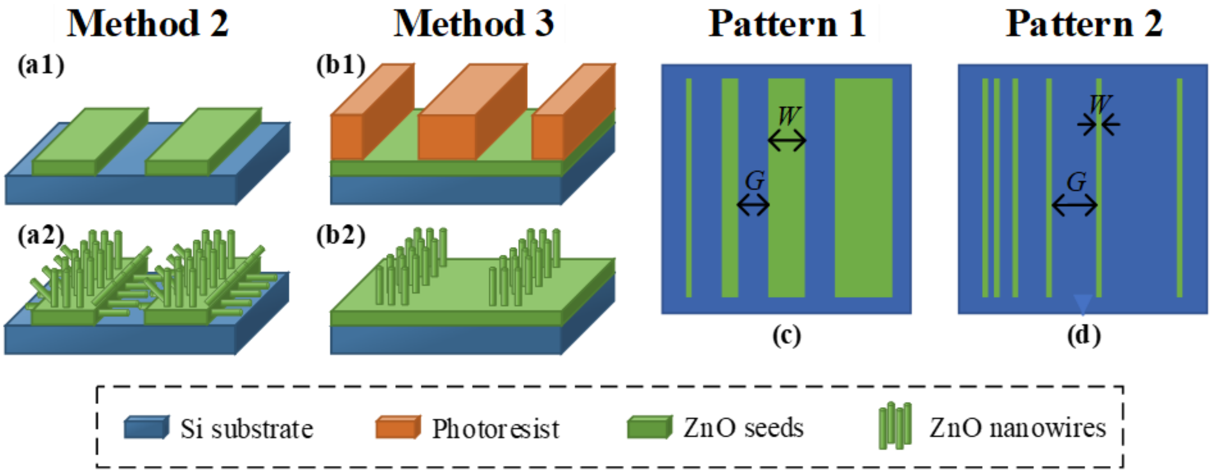

Figure 4.11. Fabrication processes for patterning ZnO nanowire growth. (a1)–(a2) Schematic of Method 2 fabrication process before and after the growth of ZnO nanowires, respectively. (b1)–(b2) Schematic of Method 3 fabrication process before and after growth of ZnO nanowires, respectively. The complete fabrication processes of Method 2 and Method 3 were detailed in Section 3.2.2 of Chapter 3. (c)–(d) Schematics of Pattern 1 with varying seed line width, *W*, and Pattern 2 with varying seed line gap, *G*, respectively.

Two patterns, Pattern 1 and Pattern 2, were used to investigate the effect of the ZnO seed layer geometry on the morphology of the resulting ZnO nanowires, as shown in Figure 4.11 (c)–(d), respectively. Pattern 1 comprised 7 mm long seed lines with their widths varying from 4 µm to 1 mm and a fixed gap of 200 µm between the seed lines. Pattern 2 comprised 7 mm long seed lines with a fixed width of 10 µm and seed line gaps varying from 2 µm to 800 µm. The nanowires were grown for 4 h using a precursor concentration of 25 mM without PEI. In this work, the influence of the seed line width (*W*) through Pattern 1 and the seed line gap (*G*) through Pattern 2 on the morphology of the nanowires are first investigated by applying Method 2. The nanowires grown by Method 2 are then compared with Method 3 to discuss the influence of the patterning process in the morphology of the resulting nanowires.

4.3.1 ZnO seed line width (Pattern 1)

A pre-deposited seed layer can bypass the nucleation stage of the nanowire growth, enhancing the heterogeneous growth during the hydrothermal synthesis [107]. The seeds can, therefore, behave as adsorbent targets to the reactant ions available in the growth solution to form ZnO nanowires. Here, the influence of the ZnO seed line width on the morphology of ZnO nanowires is investigated by growing ZnO nanowires using Pattern 1 via Method 2. A precursor concentration of 25 mM with 4 h of growth was used for growing ZnO nanowires.

4.3.1.1 Results of the ZnO seed line width variation

ZnO nanowires were grown on the seed lines with varying widths of 4 µm to 1 mm, where a fixed gap of 200 µm was provided, as shown in Figure 4.12. Figure 4.12 (a) shows a portion

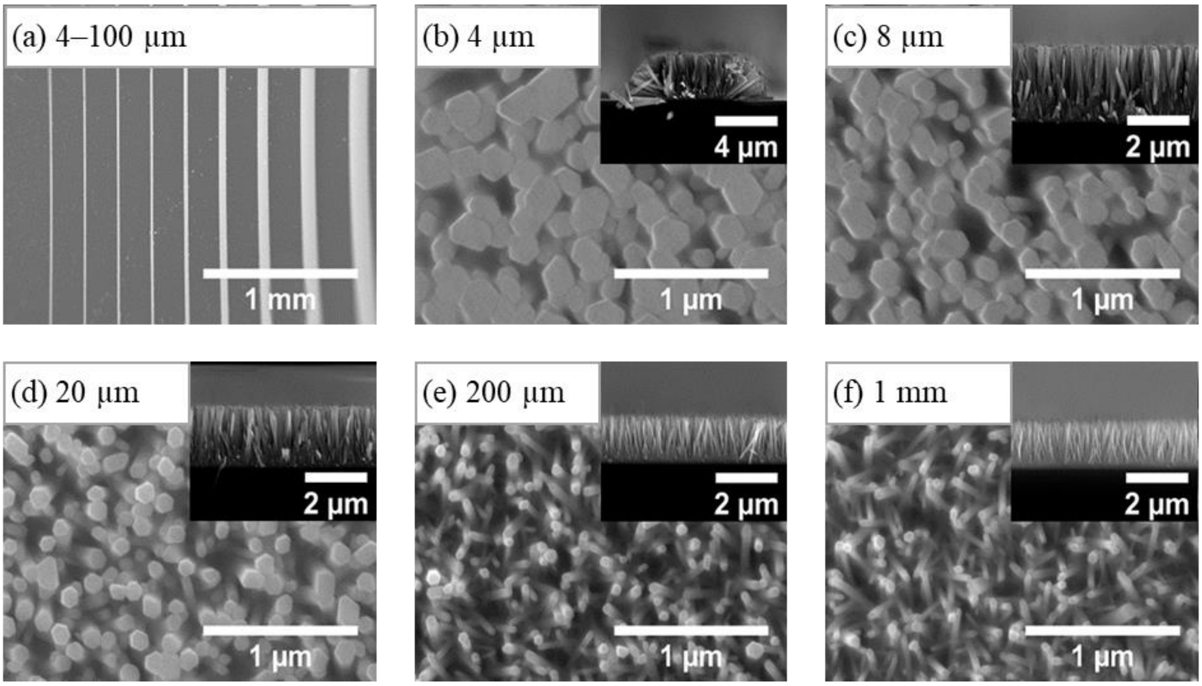

Figure 4.12. SEM images of ZnO nanowires grown on a Si substrate with patterned ZnO seed lines that vary in width from 4 µm to 1 mm, using a precursor concentration of 25 mM for 4 h of growth. The ZnO seed lines were patterned as Pattern 1 via Method 2 as detailed in Section 3.2.3 of Chapter 3. (a) The SEM image shows a topside overview of the patterned substrate that includes ZnO nanowires grown on seed lines with the width varying from 4 µm to 100 µm and a gap of 200 µm. (b)–(f) The SEM images of ZnO nanowires grown on the seed lines with a width of 4, 8, 20, 200 and 1000 µm, respectively. The SEM images of the nanowires were taken from the top view and the side view (insets).

of the patterned substrate, where the seed lines varied in widths from 4 µm to 100 µm. The SEM images in Figure 4.12 (b)–(f) show both top view and side view (insets) of the ZnO nanowires grown on 4, 8, 20, 200 and 1000 µm wide seed lines on the same substrate, respectively. The SEM images show that the variation in the ZnO seed line width affected the morphology of the nanowires. Increasing the seed line width resulted in the nanowire diameter and length to decrease and the density to increase.

Figure 4.13 plots ZnO nanowire morphology as a function of the ZnO seed line width. The seed line width varied from 4 µm to 1000 µm on the same substrate, where the gaps between the seed lines were kept fixed at 200 µm. Figure 4.13 (a) plots the ZnO nanowire diameters against the seed line widths. The nanowires had a maximum diameter of 220 ± 55 nm on the seed line with a width of 4 µm. The diameter decreased, almost halved, to 115 ± 20 nm as the seed line width increased to 20 µm. Further extension of the seed line width to 200 µm continued to reduce the diameter to 57 ± 13 nm, but at a slower pace. For the seed line widths in the range of 200–1000 µm, the diameters remained unchanged at 50 ± 9 nm.

Figure 4.13 (b) shows the influence of the varying ZnO seed line width on the length of the ZnO nanowires. Like the ZnO nanowire diameters shown in Figure 4.13 (a), the length of the nanowires was at a maximum of 2.54 ± 0.1 µm for the minimum seed line width of 4 µm. The nanowire length rapidly decreased to 1.49 ± 0.08 µm as the seed line width increased to 40 µm. Increasing the seed line width to 200 µm reduced the nanowire length to 1.28 ± 0.1 µm. Further increase of the seed line width to 200–1000 µm reduced the nanowire length to its minimum of 1.25 ± 0.2 µm.

Figure 4.13 (c) shows the aspect ratio of the ZnO nanowires for the varying ZnO seed line widths. The aspect ratio was determined to be at its minimum of 11.5 ± 3.0 for the narrowest seed line width of 4 µm. Increasing the seed line width to 10 µm slightly increased the aspect ratio to 13.3 ± 3.5. The aspect ratio continued to increase more rapidly to 22.5 ± 7.0 as the seed line width approached 200 µm. As a result, the length of the nanowires increased with a much faster rate compared to the diameter when the seed line width increased from 10 to 200 µm. The aspect ratio reached a maximum of 25.5 ± 7.5 at 400 µm wide seed line and remained approximately the same for any further increase of the seed line width to 1000 µm.

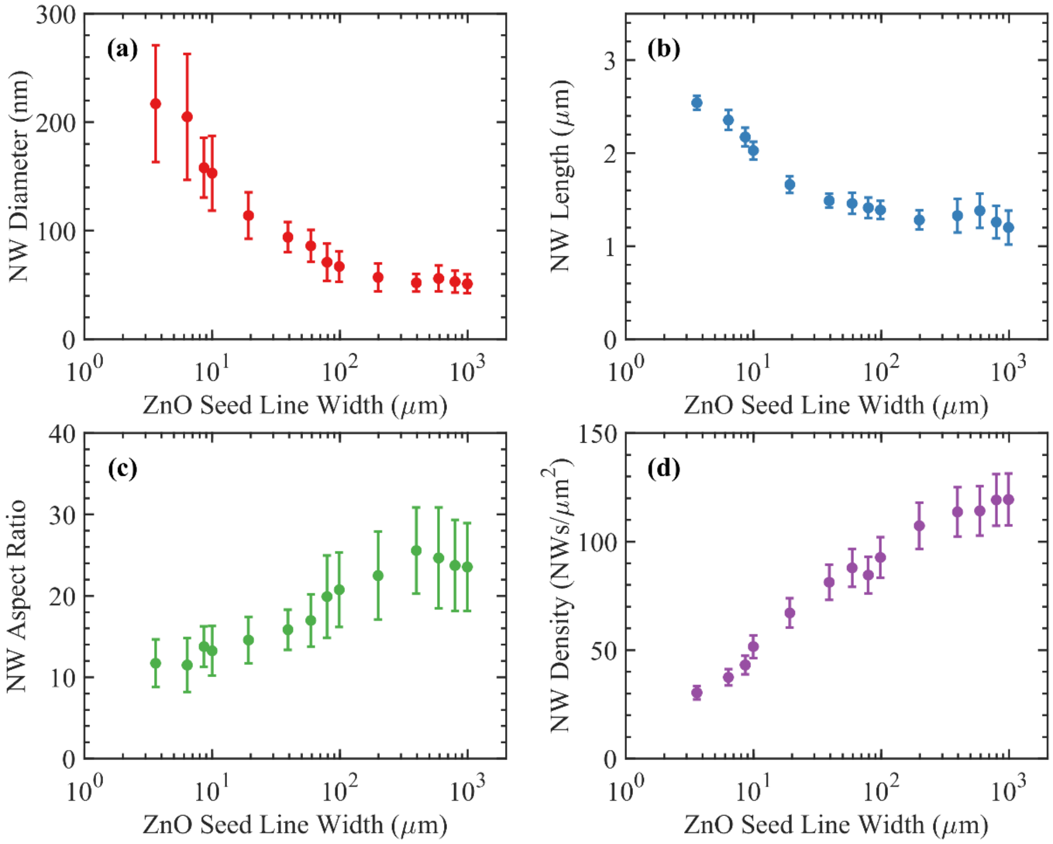

Figure 4.13. Morphological graphs of ZnO nanowires grown on a Si substrate with patterned ZnO seed lines that vary in width, using a precursor concentration of 25 mM for 4 h of growth. The ZnO seed lines were patterned with Pattern 1 via Method 2 as detailed in Section 3.2.3 of Chapter 3. (a) Diameter, (b) length, (c) aspect ratio and (d) density of the ZnO nanowires were measured from SEM images. The aspect ratios in (c) were calculated from data plotted in graphs (a) and (b). Error bars represent one standard deviation (n > 30 NWs) in (a)–(c), and 10% deviation in (d).

Figure 4.13 (d) plots the density of the ZnO nanowire against the seed line widths. Nanowires were grown with the lowest density of 30 ± 3 NWs/μm^2 when a seed line width of 4 μm was applied. Increasing the seed line width resulted in more individual nanowires to grow on the seeded regions. As the seed line width was increased to 20 μm, the density of the nanowires almost doubled to 67 ± 7 NWs/μm^2. The nanowire density rapidly increased to 107 ± 11 NWs/μm^2 as the seed line width approached 200 μm. Further increase of the width to 1000 μm slightly increased the density. At the maximum width of 1000 μm the density was found four times higher, 120 ± 12 NWs/μm^2, compared to 30 ± 3 NWs/μm^2 for the 4 μm wide seed line.

4.3.1.2 Influence of the ZnO seed line width

Figure 4.12 and Figure 4.13 showed that the nanowire morphology varied across the same substrate by varying the seed line width, even when the same growth parameters were applied to the entire substrate. Using a bulk seeded substrate with precursor concentration of 25 mM and 4 h of growth resulted in ZnO nanowires with an average diameter of 50 ± 7.5 nm, length of 1.38 ± 0.11 µm, aspect ratio of 27.7 ± 6.4 and density of 92 ± 9 NWs/µm^2. The 200 µm wide seed line with a gap of 200 µm achieved the same morphology as the bulk seeded substrates, with an average diameter of 57 ± 13 nm, length of 1.28 ± 0.1 µm, aspect ratio of 22.5 ± 7.0 and density of 107 ± 11 NWs/µm^2. The patterned ZnO seed lines can, therefore, be determined to behave as a bulk seed layer when an equal or larger seed line width than the seed line gap is provided.

ZnO seeds act as adsorption points for the reactant ions during the hydrothermal growth. The seeds on a small seed region are thought to attract more ions compared to those on a bulk seed layer. Subsequently, the diffusion rate of the ions towards the small seed areas is relatively faster that results in a faster growth rate of the nanowires. Due to the faster growth rate, the nanowires can grow longer and wider when a narrow seed line is provided compared to a bulk seed layer.

As discussed in Section 4.2, the aspect ratio of the nanowires was maximum when a precursor concentration of 15 mM was applied for 4 h of growth. The vertical growth of the nanowires was subsequently determined to be quasi-saturated. Increasing the precursor concentration beyond 15 mM, e.g. 25 mM, resulted in the nanowire aspect ratio decreasing, where the nanowires grew more laterally than vertically. Reducing the seed area is thought to increase the diffusion rate of the ions towards the seeds in the same manner as increasing the precursor concentration for the bulk seed layers. Accordingly, the nanowire aspect ratio reduces when a small seed area is provided, as nanowires grow more laterally than vertically.

The density of the nanowires reduces by shrinking the seed line width. As the nanowires grow longer and wider, selective competition takes place that reduces the nanowire density. In this respect, nanowires either coalesce with each other to continue their growth or eliminate each other from further growth, resulting in fewer nanowires reaching the top surface for observation by scanning electron microscopy.

4.3.2 ZnO seed line gap (Pattern 2)

The variation of the seed layer geometry by the seed line width is determined to affect the morphology of ZnO nanowires across the same substrate. Below we investigate the influence of the gap between the seed lines on the morphology of nanowires.

4.3.2.1 Results of the ZnO seed line gap variation

ZnO nanowires were grown on a single substrate, using Pattern 2 via Method 2, with 25 mM of precursor concentration and 4 h of growth. The gaps between the patterned seed lines were varied from 2 µm to 800 µm while the seed line widths were fixed at 10 µm. Figure 4.14 (a) shows both top view and side view (inset) of a portion of the substrate that includes ZnO nanowires grown on 10 µm wide seed lines with gaps of 2–400 µm. The SEM images in Figure 4.14 (b)–(f) show a top view of the gap between the seed lines and an inset of the ZnO nanowires grown on 10 µm wide seed lines with the gaps of 2, 4, 10, 100 and 800 µm, respectively. Despite that identical 10 µm wide ZnO seed lines were applied on the substrate

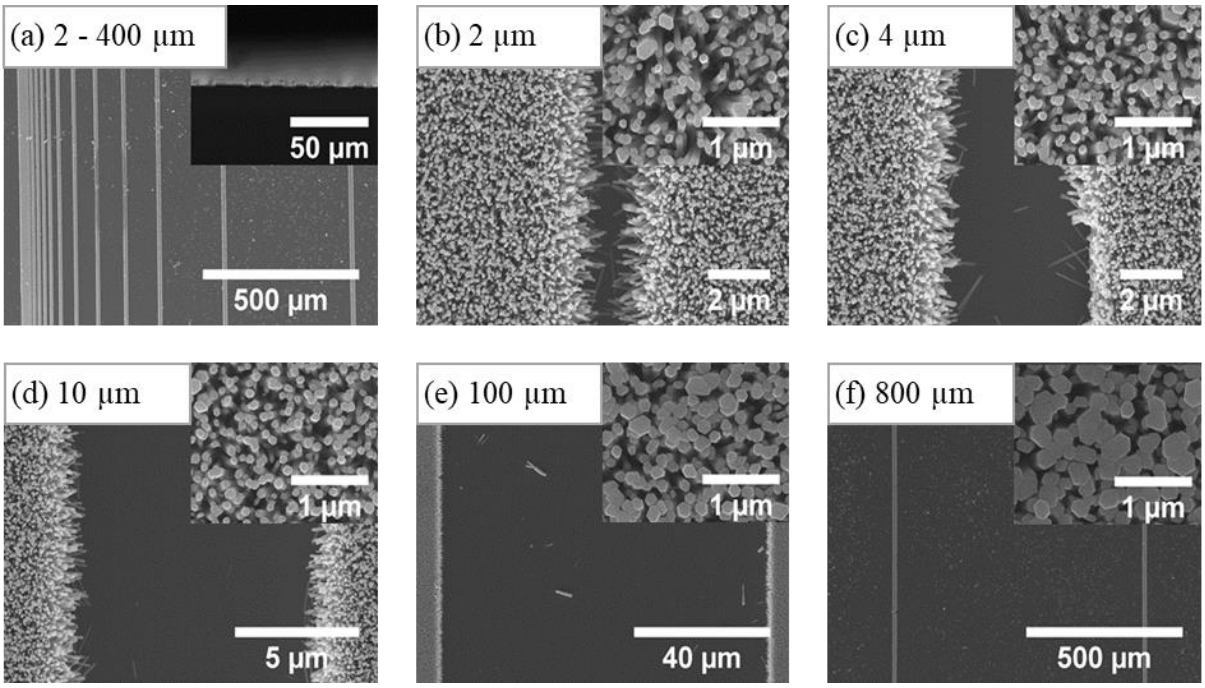

Figure 4.14. SEM images of ZnO nanowires grown on a Si substrate with 10 µm wide patterned ZnO seed lines where the gaps from 2 µm to 800 µm, using a precursor concentration of 25 mM for 4 h of growth. The ZnO seed lines were patterned as Pattern 2 via Method 2 as detailed in Section 3.2.3 of Chapter 3. (a) The SEM image shows a top view and a side view (inset) of the patterned substrate with ZnO nanowires grown on 10 µm wide seed lines with gaps varying from 2 µm to 400 µm (2 µm to 20 µm for the inset). (b)–(f) The SEM images of ZnO nanowires grown on the seed lines with gaps of 2, 4, 10, 100 and 800 µm, respectively.

and the same growth conditions were used, the grown ZnO nanowires altered in morphology. The nanowire diameter and length increased, and the density decreased as the gap between the seed lines increased.

Figure 4.15 plots the morphology of the resulting ZnO nanowires for various seed line gaps that were provided between 10 μm wide seed lines. Figure 4.15 (a) shows the diameter of the resulting nanowires for the varying seed line gaps. The nanowires had the lowest diameter of 102 ± 16 nm when a seed line gap of 6 μm was provided. Within the gap range of 2–20 μm, the diameter of the nanowires remained unchanged with an average diameter of 107 ± 25 nm. Increasing the gap from 20 μm to 800 μm increased the nanowire diameter to a maximum of 235 ± 48 nm.

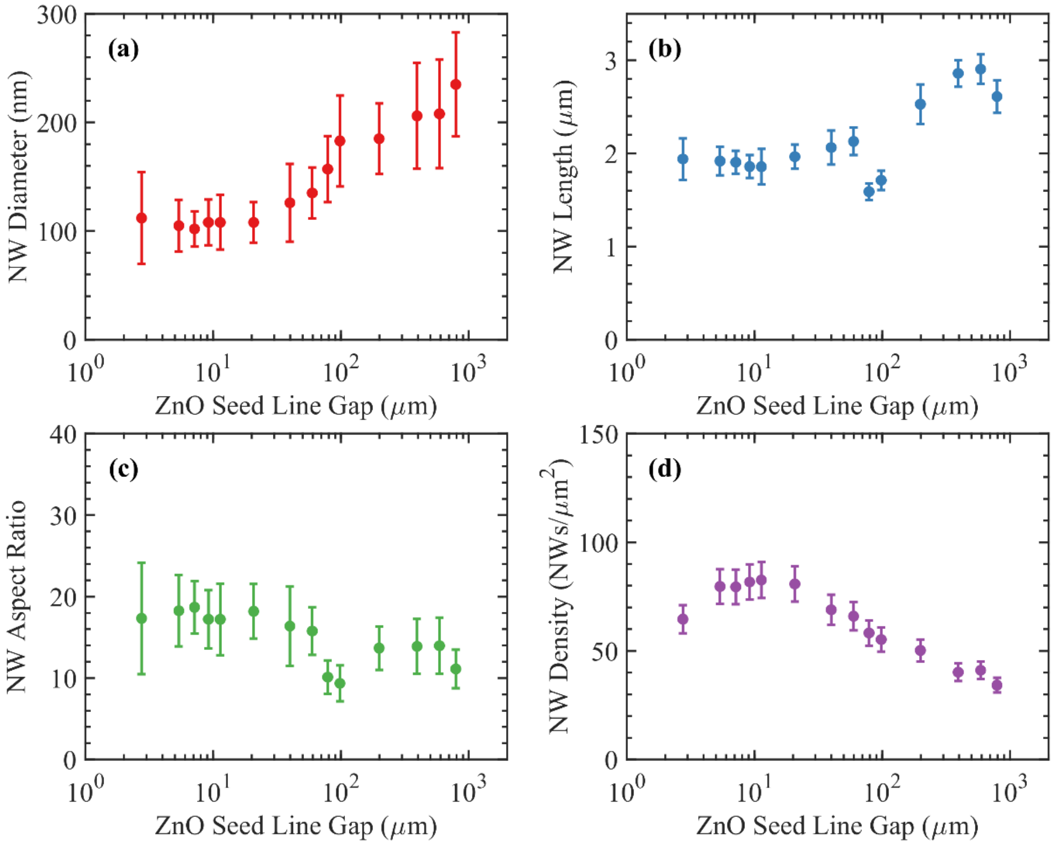

Figure 4.15. Morphological graphs of ZnO nanowires grown on patterned 10 μm wide ZnO seed lines with various gaps. The nanowires were grown on a Si substrate using 25 mM of precursor concentration and 4 h of growth and were patterned using Pattern 2 via Method 2 as detailed in Section 3.2.2 of Chapter 3. (a) Diameter, (b) length, (c) aspect ratio and (d) density of the ZnO nanowires were measured from SEM images. (c) The aspect ratios were calculated from data plotted in graphs (a) and (b). Error bars represent one standard deviation (n > 30 NWs) in (a)–(c), and 10% deviation in (d).

Figure 4.15 (b) shows the effects of the seed line gap variation on the resulting nanowire length. The nanowires had a minimum length of 1.9 ± 0.2 μm when a gap range of 2–20 μm was provided. Increasing the gap from 20 μm to 600 μm resulted in the nanowire length to reach 2.9 ± 0.2 μm. For the seed line gaps of 80–100 μm, the length of the nanowires were found to be shorter, 1.65 ± 0.1 μm, compared to what was expected from the trend. These outliers are thought to be a result of the possible damage made to the nanowires during the mechanical preparation process that had been taken for SEM imaging at the cross-section view.

The relationship between the length and diameter of the grown nanowires is shown as the aspect ratio in Figure 4.15 (c) for various seed line gaps. The nanowires had a maximum aspect ratio of 17.3 ± 8.6 when a minimum gap of 2 μm was provided. The aspect ratio of the nanowires stayed unchanged for 2–20 μm gaps as their vertical and lateral growth did not change substantially. Beyond 20 μm of the gap, the nanowires generally grew faster in lateral directions than the c-axis direction that slightly reduced the aspect ratio to 11.1 ± 3 for a maximum seed line gap of 800 μm.

Figure 4.15 (d) shows the density of the nanowires as a function of the seed line gap. The nanowire density was maximum of 80 ± 8 NWs/μm^2 when 4–10 μm gaps were provided. As the seed lines moved further apart from each other, the density of the nanowires decreased due to a selective competition that took place between the nanowires. The nanowire density almost halved to 34 ± 3 NWs/μm^2 when a maximum seed line gap of 800 μm was provided.

4.3.2.2 Influence of the ZnO seed line gap

The nanowire morphology is affected by varying the gap between the seed lines. With gaps > 10 μm, increasing the gap results in increased length and diameter of the nanowires despite the identical growth conditions being applied. The diameter is also affected more than the length by the seed line gap. Consequently, the aspect ratio reduces as the gap increases. The nanowire density also reduces as the gap widens. The nanowire morphology is reasonably stable for the gap ≤ 10 μm. A threshold of 10 μm can, therefore, be defined for the seed line gap, at which the nanowire morphology begins to change by increasing the gap beyond the threshold.

The gap between the seed lines provides an area around the seeds that allows lateral diffusion to take place during the hydrothermal growth of ZnO nanowires. The reactant ions can, therefore, diffuse faster towards the ZnO seeds to enhance the growth rate of the nanowire. Besides, the by-products that are produced by the chemical reaction at the nanowire surface act as a growth rate limiting factor [152]. Providing a gap between the seed lines can also increase the removal rate of the by-products, to diffuse away from the seed lines, and further boost the growth of the nanowires.

ZnO nucleation can randomly take place on Si substrates without any seed layer and grow into randomly oriented nanowires. The random nanowires can similarly grow on unseeded regions between the seed lines. The number of random nanowires that grow between the seed lines varies by applying different gaps between the seed lines, as shown in Figure 4.14. Providing a small gap between the seed lines, e.g. 2–10 µm as shown in Figure 4.14 (b)–(d), respectively, is determined to reduce the number of random nanowires that grow on unseeded regions in comparison to a large gap, e.g. 100 µm and 800 µm as shown Figure 4.14 (e) and (f), respectively. When a small gap is provided, most of the reactant ions available above the unseeded regions can be consumed by the neighbouring seeds that prevent any growth of the random nanowires on the plain substrate surface. Expanding the gap between the seed lines allows more reactant ions to remain above the unseeded regions that can eventually grow into random ZnO nanowires.

4.3.3 Patterning process

Varying the seed line width and gap, by using Pattern 1 and Pattern 2 through Method 2, are determined to alter the morphology of the resulting nanowires. In this section, the difference in the fabrication processes of Method 2 and Method 3, as detailed in Section 3.2.3 of Chapter 3, is investigated by growing ZnO nanowires on patterned seed lines that vary in either the seed line width, Pattern 1, or the seed line gap, Pattern 2. Nanowires were grown with a precursor concentration of 25 mM and 4 h of growth. The morphology of the resulting nanowires is then examined as a function of the seed area ratio, defined as the proportion of the seed line width to the sum of the seed line width and the gap.

4.3.3.1 Method 2 vs. Method 3

Figure 4.16 shows SEM images of nanowires grown on the patterned ZnO seed lines via Method 2 in (a) and (c), and via Method 3 in (b) and (d). Figure 4.16 (a) and (b) show top view of the patterned ZnO seed lines that vary in the gap within a range of 2–400 µm with the insets showing the 200 µm gaps. ZnO randomly nucleated on a plain substrate surface and grew into undesired nanowires. A high number of random nanowires were grown on the substrate surface when a large gap, e.g. 200 µm, between the seed lines was provided, as shown in Figure 4.16 (a). The number of undesired randomly grown nanowires was minimised by applying a gentle cleaning process in DI water; however, they could not be thoroughly removed. Since the nanowire growth took place at a low temperature (95°C), a photoresist pattern could be left on the substrates during the growth via Method 3. Lifting-off the photoresist after the nanowire growth subsequently removed any unwanted nanowires and left vertical nanowires on the defined regions only, as shown in Figure 4.16 (b).

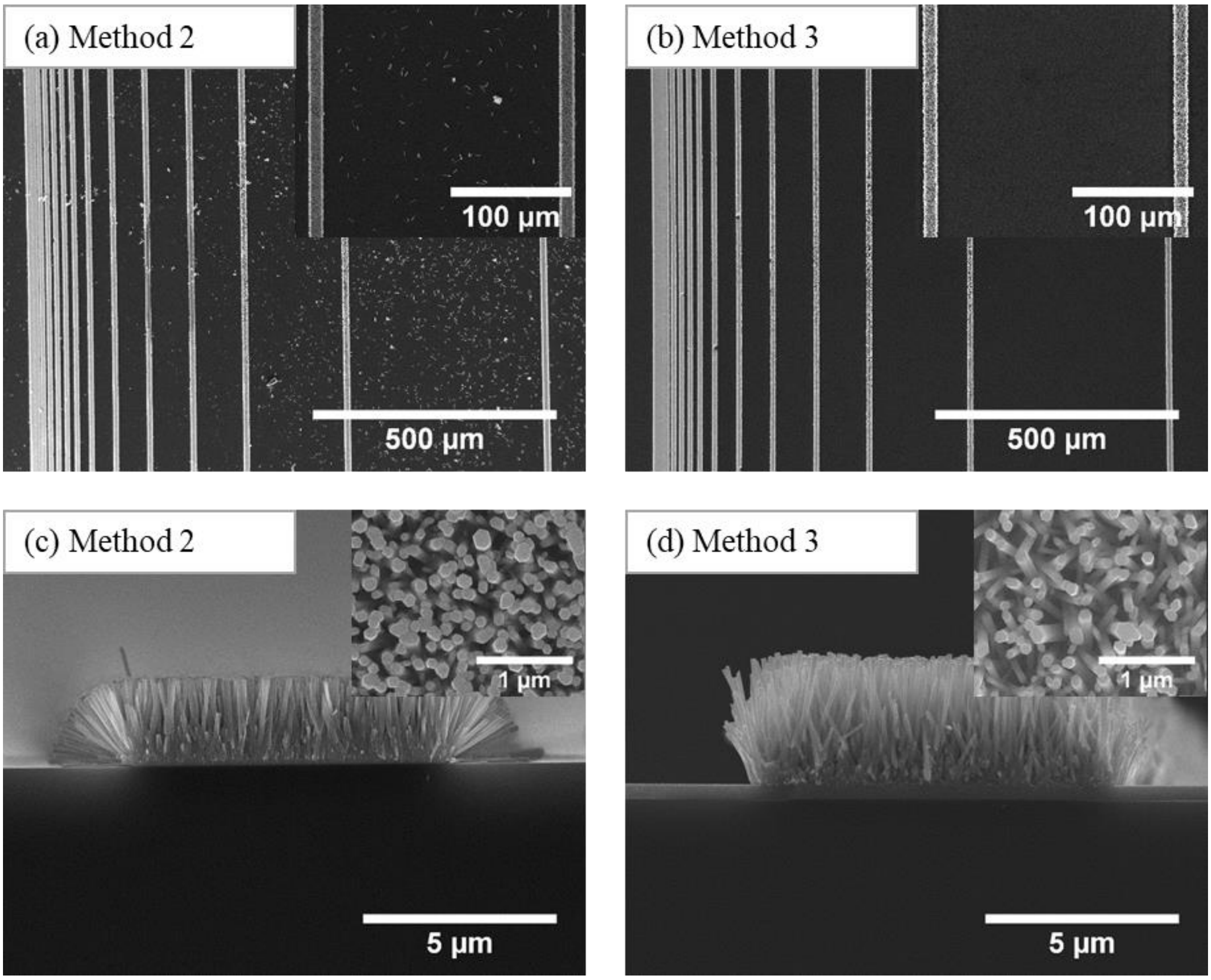

Figure 4.16. Arrays of ZnO nanowires grown on ZnO seed lines patterned by Pattern 2 using Method 2 shown in (a) and (c), and via Method 3 shown in (b) and (d). (a) and (b) show top view SEM images of a portion of the samples with 10 μm wide seed lines that vary in the gap from 2 μm to 400 μm (200 μm gaps for the insets). (c) and (d) show SEM images of nanowires grown on 10 μm wide seed lines with an adjacent gap of 60 μm from side view and top view (insets).

Figure 4.16 (c) and (d) show SEM images from side view and top view (insets) of the nanowires grown on 10 μm wide seed lines with an adjacent gap of 60 μm via Method 2 and Method 3, respectively. Figure 4.16 (c) shows that Method 2 resulted in the lateral growth of the nanowires at the edges of the seed region. In contrast, Figure 4.16 (d) shows that

Method 3 blocks the lateral growth and resulted in the growth of vertical nanowires only. Furthermore, the length of the resulting nanowires was found to be longer when Method 3 was applied compared to the nanowires that were grown by Method 2, even though their diameters did not change significantly.

4.3.3.2 The seed area ratio

The seed area ratio was defined as the proportion of the seed line width to the sum of the seed line width and the minimum adjacent gap, *W/(W + G)*, as illustrated in Figure 4.11. The seed area ratio was controlled by varying the seed line width and the seed line gap. Figure 4.17 shows the morphology of the nanowires that were grown via Method 1, Method 2 and Method 3 as a function of the seed area ratio. Figure 4.17 also shows the morphology of the nanowires that were grown on different seed layer patterns; Pattern 1 with varying seed line width labelled as “-W” and Pattern 2 with varying seed line gap labelled as “-G”.

Figure 4.17 (a) shows that the diameters of the nanowires that were grown on the patterned seed lines closely matched with each other despite their differences in the patterning process—Method 2 or Method 3. However, the diameter of the nanowires that were grown on the seed lines with various gaps was slightly larger than the nanowires that were grown on the seed lines with the various widths. The nanowires had a maximum diameter of 235 ± 48 nm and 195 ± 38 nm for Method 2 and Method 3, respectively, at the lowest seed area ratio of 1%. Increasing the seed area ratio to 83% reduced the diameter to 57 ± 8.5 nm for both Method 2 and Method 3 that approached the diameter of the nanowires that were grown on the bulk seed layer, 50 ± 7.5 nm.

Figure 4.17 (b) shows the influence of the seed area ratio on the length of the ZnO nanowires. The nanowires grown by Method 3 were longer than the nanowires grown by Method 2. Moreover, the nanowires that were grown on the seed lines with various gaps were longer and thicker compared to those grown using various seed line widths. At 1% of the seed area ratio, nanowires were the longest with an average length of 2.90 ± 0.16 µm and 4.60 ± 0.49 µm for Method 2 and Method 3, respectively. The nanowire length reduced as the seed area ratio increased. The nanowire length almost halved, from 2.90 ± 0.16 µm to 1.20 ± 0.18 µm, by increasing the seed area ratio from 1% to 83% by using Method 2. The length of the nanowires grown via Method 3 decreased by a factor of 3, from 4.60 ± 0.49 µm to 1.58 ± 0.20 µm, as the area ratio increased from 1% to 83%. The length of the nanowires grown at the maximum seed area ratio of 83% for both Method 2 and Method 3 was close to

1.38 ± 0.11 µm, which was measured as the average length of the nanowires grown on the bulk seed layer.

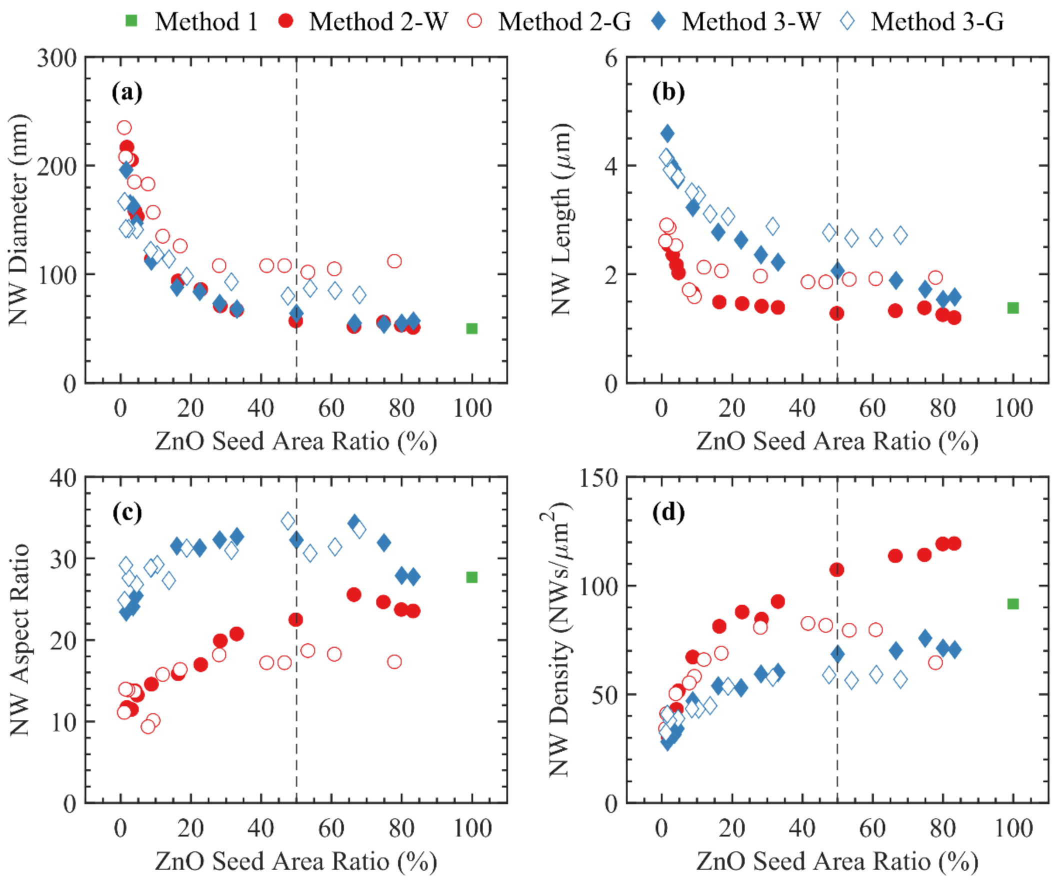

Figure 4.17. Morphological graphs of ZnO nanowires grown on Si substrates with patterned ZnO seed lines using a precursor concentration of 25 mM and 4 h of growth. (a) Diameter, (b) length, (c) aspect ratio and (d) density of ZnO nanowires were measured using SEM images. (c) The aspect ratios were calculated from data plotted in graphs (a) and (b). The ZnO seed lines were patterned via Method 1 (bulk seed layer), Method 2 and Method 3 as indicated by the legends. The suffix "-W" and "-G" correspond to the patterned seed lines that vary in width (Pattern 1) and gap (Pattern 2), respectively. The dashed line indicates the unity seed line width-to-gap ratio, where the seed area ratio is at 50%.

Figure 4.17 (c) shows the aspect ratio plotted against the seed area ratio. The nanowires grown via Method 2 and Method 3 can be distinguished from each other using the aspect ratio. Method 2 resulted in nanowires with aspect ratios of 9–26 compared to Method 3 that resulted in higher aspect ratios of 23–34. At the seed area ratio of 1%, the nanowires grown by Method 2 had an aspect ratio of 11.1 ± 3.0. The aspect ratio increased to 23.5 ± 7.6 by increasing the seed area ratio to 83%. The nanowires had a minimum aspect ratio of 23.4 ± 6.7 at 1% of the seed area ratio when Method 3 was used. The aspect ratio reaches a maximum of 34.6 ± 7.9 at the seed area ratio of 50%. Further increase of the seed area ratio from 50% to 83% reduced the aspect ratio to 27.8 ± 7.7, which was similar to the aspect ratio of 27.7 ± 6.4 measured for the nanowires grown on the bulk seed layer.

Figure 4.17 (d) shows the density of the nanowires as a function of the seed area ratio. The seed lines with a minimum seed area ratio of 1%, for both Method 2 and Method 3, consisted of the least number of the nanowires, 30 ± 3 NWs/μm^2. Increasing the seed area ratio increased the nanowire density on the seed lines. The density of the nanowires that were grown via Method 2 increased faster by the seed area ratio in comparison to the nanowires that were grown via Method 3. The nanowires reached a maximum density of 120 ± 12 NWs/μm^2 and 76 ± 7 NWs/μm^2 at a seed area ratio of 83% for Method 2 and Method 3, respectively. The nanowires grown on the seed lines with various widths and gaps followed the same trend line when Method 3 was used. However, this was not the case for Method 2, where they started to diverge at the seed area ratio of 30%.

The seed area ratio of 50% is marked in Figure 4.17 that represents the unity ratio between the seed line width and the gap, $W/G = 1$. A threshold of 50% can be defined for the seed area ratio that influenced the nanowire morphology. The nanowire morphology was affected the most within the initial 50%, where the width of the seed line was smaller than the surrounding gap. The nanowires grew longer and thicker as the seed area ratio decreased. M. Coltrin *et al.* [152] previously showed that the nanowire growth enhancement was notable when a small fraction of the surface was exposed to the growth, where organic molecules were used to cover the unexposed areas. As the seed area ratio approached 50%, the seed layer behaved more like a bulk seed layer for the nanowire growth. The nanowire growth remained reasonably steady when the seed area ratio was increased beyond 50%.

4.4 Growth kinetics

Controlling the parameters of the growth solution, such as the precursor concentration, the growth time and the PEI concentration have conventionally been applied to alter the morphology of ZnO nanowires through the hydrothermal synthesis. However, the results in Section 4.3 showed that the morphology of the nanowires could also be governed by controlling the seed layer geometry. In this section, the growth kinetics are discussed to understand why the morphology of the nanowires is influenced by varying the seed layer geometry.

4.4.1 Hydrothermal growth

During the hydrothermal growth of ZnO nanowires, zinc nitrate hexahydrate and HMT precursors go through a chemical reaction that provides Zn^{2+} and OH^- ions required for ZnO crystallisation. The ions can nucleate on the substrate surface and form ZnO crystals. A ZnO seed layer can be applied to bypass the nucleation step, where ZnO crystallisation can take place directly on the deposited seed layer. ZnO nanowires are formed as the ions are generally adsorbed on polar surfaces along the c-axis [0001] due to the tendency of the ions to minimise the surface energy of the ZnO crystals [125]. In the meantime, ZnO nanowires can also grow in the lateral directions $[10\bar{1}0]$ and $[11\bar{2}0]$—a-axis and m-axis, respectively—to produce thicker nanowires [153].

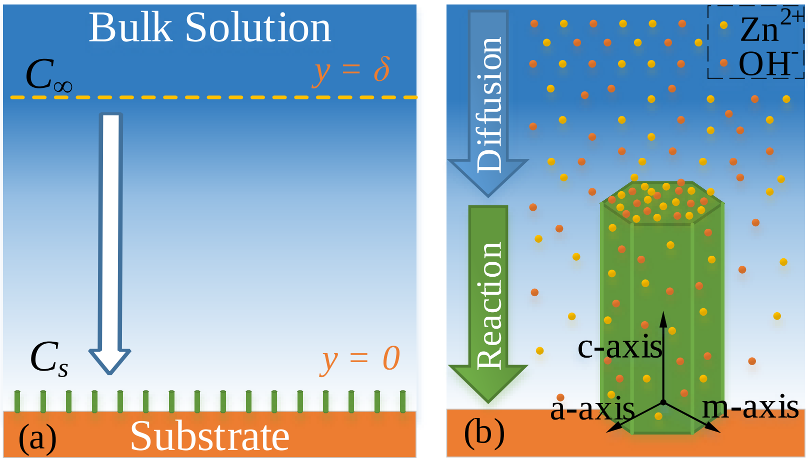

Figure 4.18. Schematics of ZnO nanowire growth kinetics in the growth solution. (a) Schematic showing the reactant ions concentration above the nanowire array, where the concentration is maximum (C_∞) in the bulk solution at $y = \delta$ and minimum (C_S) near the substrate at $y = 0$. (b) Schematic showing diffusion of the ions from the bulk solution towards the nanowires and the reaction at the nanowire surface. Most of the ions adsorb on the c-face (0001) along the c-axis direction that has the highest surface energy compared to the lateral non-polar faces along a-axis and m-axis, $[10\bar{1}0]$ and $[11\bar{2}0]$.

The deposited ZnO seeds can be used as adsorption targets for the Zn^{2+} and OH^- ions to guide the growth of ZnO nanowires onto defined areas. Upon the adsorption of the ions by the seeds, the ions diffuse from the bulk solution, C_∞ at $y = \delta$, towards the seed surface, C_s at $y = 0$, as shown in Figure 4.18 (a). At the surface of the seeds/nanowires, the ions are involved in a chemical reaction that results in the growth of the nanowires. The growth rate of the ZnO nanowires mainly depends on the reaction rate happening on the nanowire surface and the diffusion rate that supplies the reactant ions from the solution to the surface, as shown in Figure 4.18 (b). The reaction rate is a rate at which ZnO crystallisation takes place on the nanowire surface and can be defined as:

$$Reaction\ rate = \frac{d(NWs)}{dt} = N\, k\, A_{NWs}\, \delta \qquad \text{Equation 4.1}$$

where N is the number of nanowires; k is the kinetic coefficient (cm/min) on ZnO nanowire/seed surfaces; A_{NWs} is the nanowire surface area, and δ is the distance between the bulk solution region and the nanowire surface. Furthermore, the reaction rate for the nanowire growth can be defined distinctly for vertical surface (0001) and lateral surfaces $(10\bar{1}0)$ $(11\bar{2}0)$ as

$$\frac{d(NWs)}{dt} = N\,(\frac{1}{4} k_z\, \pi\, D_{NW}{}^2 + k_r\, \pi\, D_{NW}\, H_{NW})\, \delta \qquad \text{Equation 4.2}$$

where D_{NW} and H_{NW} are the average diameter and height of the nanowires, respectively; k_z and k_r are the kinetic coefficients for vertical and lateral surfaces, respectively.

Due to the consumption of the reactant ions by the ZnO nanowires on the substrate, the concentration of the ions diminishes near the substrate. The deficiency of the ions near the substrate creates a concentration gradient in the boundary layer, $y = [0, \delta]$, and the ions diffuse from the bulk solution towards the substrate surface. The diffusion rate can be defined as a rate at which reactant ions move from the highly concentrated region (C_∞ at $y = \delta$) towards the low concentrated region (C_s at $y = 0$). Furthermore, the concentration of the ions is considered to drop linearly with distance in the boundary layer [146] as

$$C_s = \frac{C_\infty}{1 + \Phi} \qquad \text{Equation 4.3}$$

where Φ is the Thiele modulus [146,154,155] defined as the ratio between the surface reaction rate and the diffusion rate (Q, cm^2/min):

$$\Phi = \frac{Reaction\ rate}{Diffusion\ rate} \qquad \text{Equation 4.4}$$

$$= \frac{d(NWs)/dt}{Q}$$

$$= \frac{N\,(\frac{1}{4} k_z\, \pi\, D_{NW}{}^2 + k_r\, \pi\, D_{NW}\, H_{NW})\, \delta}{Q}$$

The hydrothermal growth mechanism of ZnO nanowires can subsequently be categorised as a reaction rate limited growth ($\Phi \ll 1$) and a diffusion rate limited growth ($\Phi \gg 1$), as shown in Figure 4.19 (a) and (b) respectively.

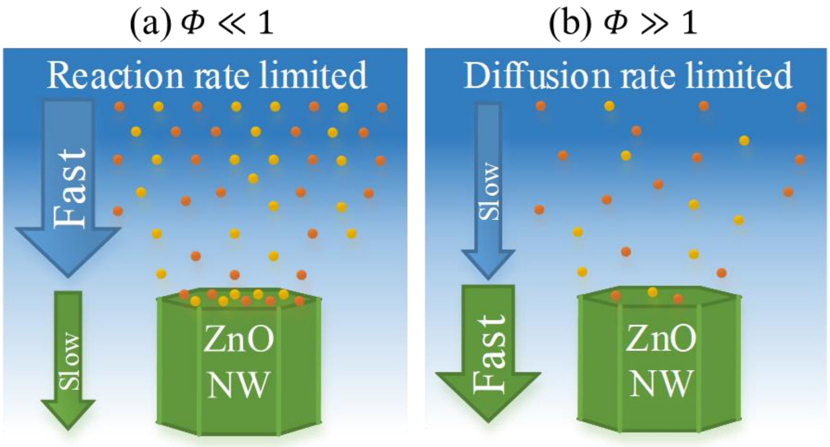

Figure 4.19. (a) Reaction rate limited and (b) diffusion rate limited growth mechanisms trough the hydrothermal synthesis. (a) The high number of the reactant ions that diffuse from the solution towards the ZnO nanowires resulted in the relatively fast diffusion rate and slow reaction rate on the surface of the nanowires with the small Thiele modulus ($\Phi \ll 1$). (b) The small number of the reactant ions provide a slower diffusion rate towards the nanowires, where the reaction rate takes place on the nanowire surface relatively faster ($\Phi \gg 1$).

In the case of $\Phi \ll 1$, as shown in Figure 4.19 (a), the diffusion rate is the dominant factor that results in the reaction rate limited growth. Due to the high diffusion rate of the reactant ions, the growth rate of ZnO nanowires is relatively fast, resulting in the formation of long and thick nanowires. Since the diffusion rate is much faster than the reaction rate, there are more reactant ions available at the surface than required for the controlled growth of nanowires on defined regions. Random nucleation of ZnO can, therefore, take place that results in the growth of random nanowires on a plain substrate.

In the case of $\Phi \gg 1$, as shown in Figure 4.19 (b), the nanowire growth is diffusion rate limited (mass transport limited) implying a high reaction rate at the nanowire surface. Many nanowires can grow heterogeneously on the substrate with limited precipitation forming in the growth solution. Applying a seed layer of ZnO on the substrate can enhance the reaction rate of the nanowire growth by eliminating the nucleation step, as ZnO nanowires can grow directly on the pre-deposited ZnO seed layer. Many nanowires can grow vertically on the seed layer while limited random nanowires grow elsewhere. Due to a high density of the nanowires on a small seed region, the depletion rate of the reactant ions is much faster near the nanowire surface, resulting in a deficiency of the ions near the substrate. Subsequently, the nanowires grown on the seed regions are short and narrow compared to the nanowires grown via a reaction rate limited growth mechanism.

4.4.2 Influence of the growth kinetics on the nanowire growth

Figure 4.20 shows ZnO nanowires that were grown on Si substrates when a different portion of the substrate was covered by the ZnO seed layer, using the same growth parameters; 25 mM of precursor concentration without PEI and 4 h of growth. The introduced Thiele modulus can explain the variation in the growth of the nanowires by the seed area ratio, as was demonstrated in Section 4.3.3. Figure 4.20 (a) shows nanowires that were randomly grown on a plain substrate, with no ZnO seed layer. The resulting nanowires were enormous, with an average diameter of 660 ± 100 nm and length of 6.3 ± 1.5 μm, and very low in density, 0.23 NWs/μm^2. The resulting nanowire morphology agrees with the case of small Thiele modulus, $\Phi \ll 1$, where nanowire growth is reaction rate limited.

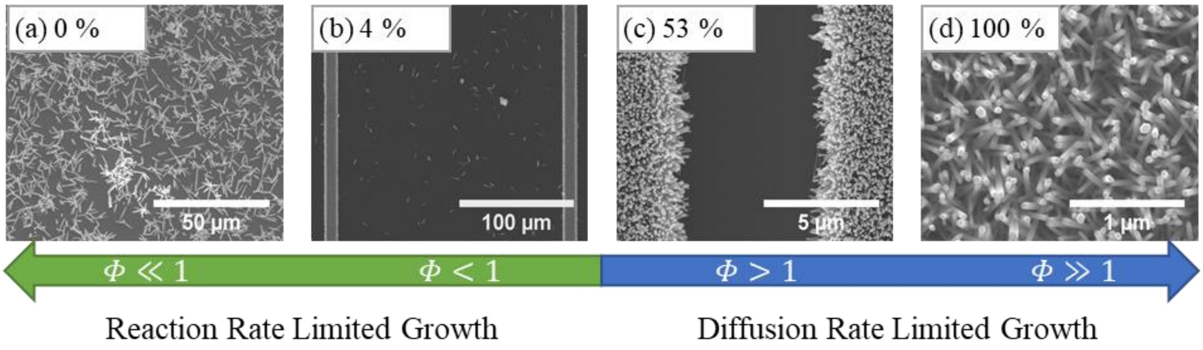

Figure 4.20. Influence of dominant hydrothermal growth mechanisms on the growth of ZnO nanowires for various seed layer geometry. (a)–(d) show top view SEM images of ZnO nanowires grown on a plain Si substrate (0%), patterned seed layer with a seed area ratio of 4%, patterned seed layer with a seed area ratio of 53% and a bulk seed layer (100%), respectively. Thiele modulus value, Φ, and the dominant growth mechanism are labelled below the SEM images.

Applying a small area of the seed layer, e.g. 4% as shown in Figure 4.20 (b), increased the Thiele modulus and results in nanowire growth less influenced by the diffusion rate. As a result, fewer and smaller nanowires grew on the substrate with a high density of the small nanowires grown on the seed layer. When a larger area of the seed layer was used, e.g. 53% as shown in Figure 4.20 (c), all nanowires were grown on the seed layer with no random nanowires on the substrate surface. As the seed area ratio increased to 100%, a bulk seed layer as shown in Figure 4.20 (d), the surface reaction rate became the dominant factor (diffusion rate limited growth mechanism) that resulted in the maximum density of the nanowires with the narrowest and shortest nanowires.

Figure 4.21 (a) and (b) show SEM images of ZnO nanowires grown at the centre and the edges of a bulk seed layer, respectively. The ZnO nanowires grown at the edges were larger in both diameter and length, 166 ± 49 nm and 2.96 ± 0.35 μm, respectively, compared to the nanowires grown at the centre with an average diameter of 42 ± 5 nm and length of 0.97 ± 0.115 μm. The nanowires grew both vertically and laterally at the edges of the seed layer, forming a brush-head configuration as shown in Figure 4.21 (b) inset, at which the alignment degrees of the nanowires varied from 0° to 90° with respect to the substrate.

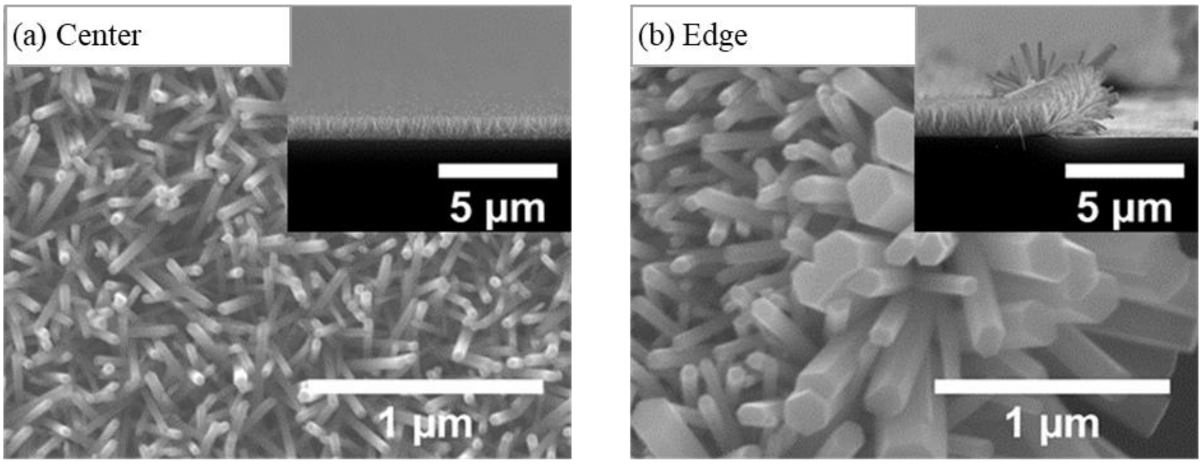

Figure 4.21. SEM images of ZnO nanowires grown (a) at the centre and (b) at the edge of a seed layer. The SEM images were taken from the top view and side view (insets). The nanowires were grown on a 10 × 10 mm^2 bulk ZnO seed layer using 25 mM of precursor concentration and 2 h of growth.

The Thiele modulus can describe the variation in morphology of the ZnO nanowires across the seed layer. The diffusion of the ions from the solution to the seeds could only take place vertically for the central region of the seed layer. By moving towards the unseeded region, approaching the seed layer edges, the diffusion could occur laterally as well as vertically. Upon the increased diffusion pathways at the seed layer edges, more reactant ions were available for the growth of the nanowires compared to the central region of the seed layer, as shown in Figure 4.22 (a). Similarly, the by-products that formed by the chemical reaction at the seed layer surface could desorb much faster from the edges compared to the central region. The Thiele modulus could subsequently be lower at the edges of the seed layer compared to the centre. The nanowires grew with a much faster rate at the edges that resulted in wider and longer nanowires in comparison to the nanowires that were grown at the centre, as shown in Figure 4.22 (b), which also agrees with J. Boercker *et al.* [146].

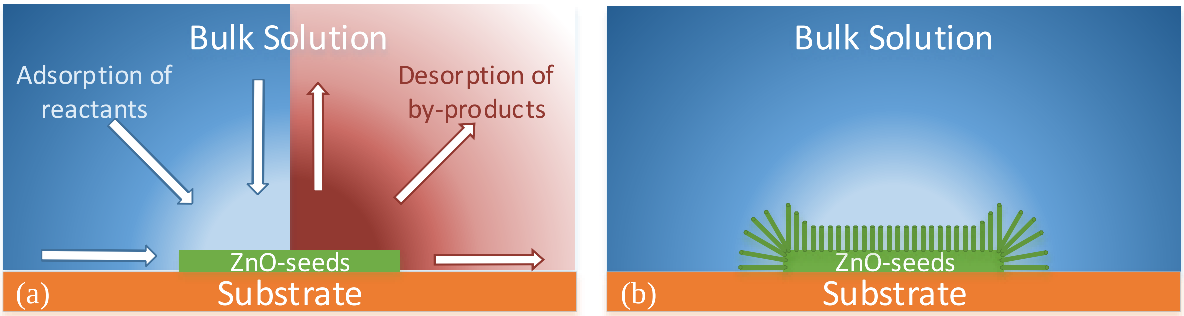

Figure 4.22. Schematics of the ZnO nanowire growth across the seed layer. (a) Diffusion of reactant ions around the seeded area, where blue represents the adsorption of Zn^{2+} and OH^- ions towards the seeds and red represents the desorption of by-products from the seeds. The paler the colour is, the lower the concentration of the corresponding ions are. (b) shows growth of the nanowires on the seed layer with larger nanowires grown at the edges.

4.5 Summary

Figure 4.23 shows morphological graphs of the ZnO nanowires grown in this work by varying the growth parameters and the seed layer geometry. Figure 4.23 (a) and (c) plot morphology of ZnO nanowires grown on Si substrates with bulk seed layers (Method 1) by varying the precursor concentration (2.5–150 mM), growth time (1–20 h), and PEI concentration (2–8 mM). Controlling the precursor concentration and the growth time resulted in the morphology of the nanowires to change within a range of 20–300 nm of diameter, 0.15–3.3 µm of length, 6–36 of aspect ratio and 10–285 NWs/µm^2 of density. Adding PEI to the growth solution changed the aspect ratio of the resulting nanowires to 12–36 and 19–95 when 4 h and 20 h of growth were used, respectively. The diameter of the nanowires remained reasonably constant at 45 ± 10 nm for various PEI concentrations; however, the growth along the c-axis of the nanowires was affected the most that varied the nanowire length.

Figure 4.23 (b) and (d) show the morphology of the ZnO nanowires grown by varying the seed line width from 4 µm to 1 mm with a fixed gap of 200 µm (Pattern 1) and varying the seed line gap from 2 µm to 800 µm with a fixed width of 10 µm (Pattern 2) via Method 2 and Method 3. Morphology of the nanowires across a single substrate varied within a range of 50–240 nm of diameter, 1.2–2.9 µm of length, 9–26 of aspect ratio and 30–120 NWs/µm^2 of density by using Method 2. The length of the nanowires substantially increased to 1.5–4.6 µm with a similar diameter range of 50–200 nm when Method 3 was used, in comparison to Method 2. The aspect ratio of the nanowires that were grown by Method 3 was subsequently higher, 23–34, with a lower density of 28–76 NWs/µm^2, compared to Method 2.

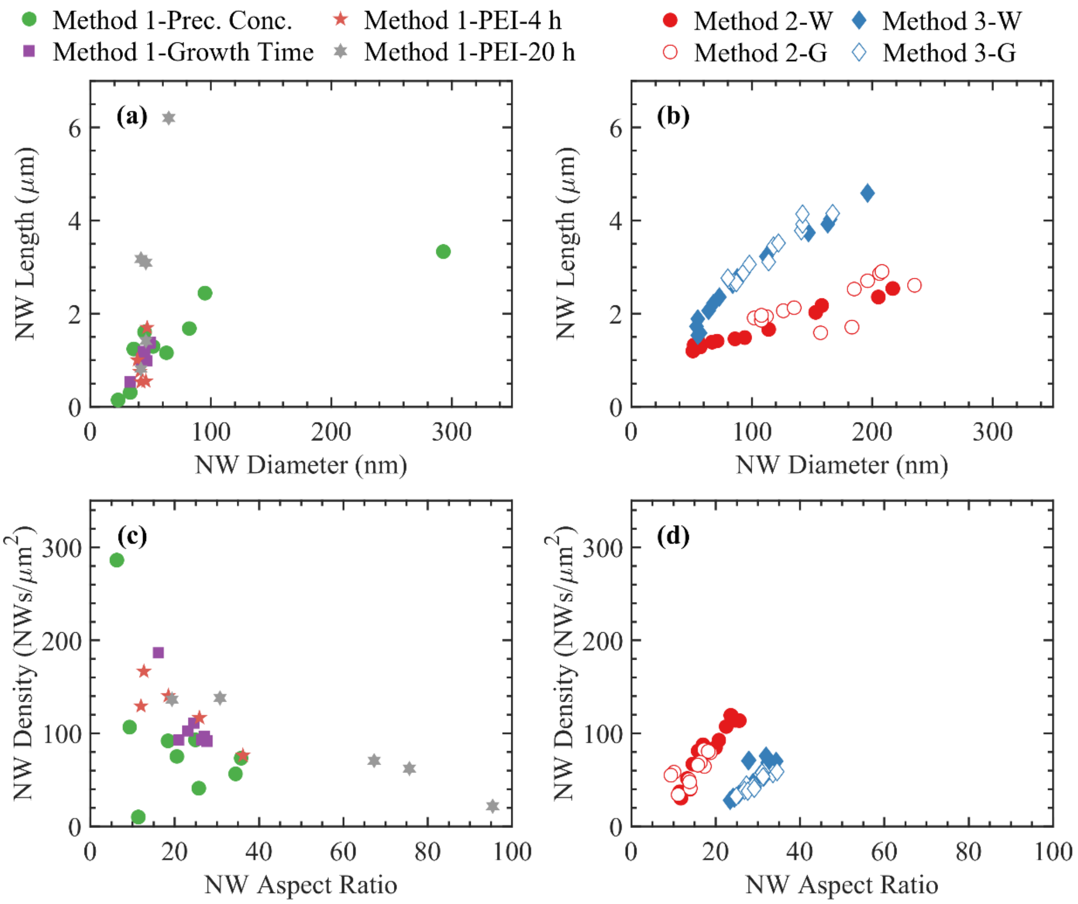

Figure 4.23. Morphological graphs of ZnO nanowires that were grown via Method 1–3. (a) and (c) show morphology of ZnO nanowires grown by varying the growth parameters such as precursor concentration (2.5–150 mM), growth time (1–20 h), PEI concentration (2–8 mM) for 4 h and 20 h of the growth time on the bulk seeded substrates, using Method 1. (b) and (d) show morphology of ZnO nanowires grown by varying the seed layer geometry using Method 2 and Method 3 with Pattern 1 (varying in the seed line width, "-W") and Pattern 2 (varying in the seed line gap, "-G").

4.6 Conclusion

This chapter demonstrates that a hydrothermal synthesis can successfully be applied for growing ZnO nanowires on microelectrode arrays. ZnO nanowires with different morphologies can be grown on Si substrates with seed layers by controlling the precursor concentration and the growth time. The growth time parameter was useful for controlling nanowire growth within the 1-4 h. The nanowires cannot grow further beyond 4 h of growth due to the depletion of the reactant ions in the growth solution when 25 mM of precursor concentration is used. The addition of PEI to the growth solution can mediate the growth such that the growth can be maintained for a longer time, e.g. 20 h. Furthermore, the aspect ratio of the resulting nanowires can be increased by growing for a longer time when PEI is applied, because PEI molecules attach to the lateral faces of the nanowires that confine their lateral growth and promote their growth along the c-axis.

Two different processes are introduced in this chapter that can pattern the growth of ZnO nanowires at defined locations. The geometry of the nanowires can subsequently be patterned using a standard photolithography technique through introduced processes, Method 2 and Method 3. The processes can later be used for fabrication of microelectrode arrays with ZnO nanowires grown at the top.

The seed layer geometry is introduced as a new parameter that can control the morphology of ZnO nanowires through hydrothermal synthesis. Increasing the seed area ratio as was done by decreasing the seed layer area or increasing the surrounding area can enhance the growth rate of the ZnO nanowires. ZnO nanowires with various morphologies can be grown across a single substrate by applying this technique. The difficulties and time constraints associated with studying the influence of the nanowire morphology on their characteristics, e.g. electrical properties and biocompatibility, can be minimised by reducing the number of samples through this technique.

Taking the understanding of how the growth parameters such as the precursor concentration, growth time, additive PEI and the seed layer geometry can influence the morphology of ZnO nanowires through the hydrothermal synthesis, new samples can be produced for integration with cells. In the next chapter, the influence of the ZnO nanowire morphology and geometry with human NTera2.D1 (hNT) neurons will be investigated.

Chapter 5

Human Neurons on ZnO Nanowire Florets

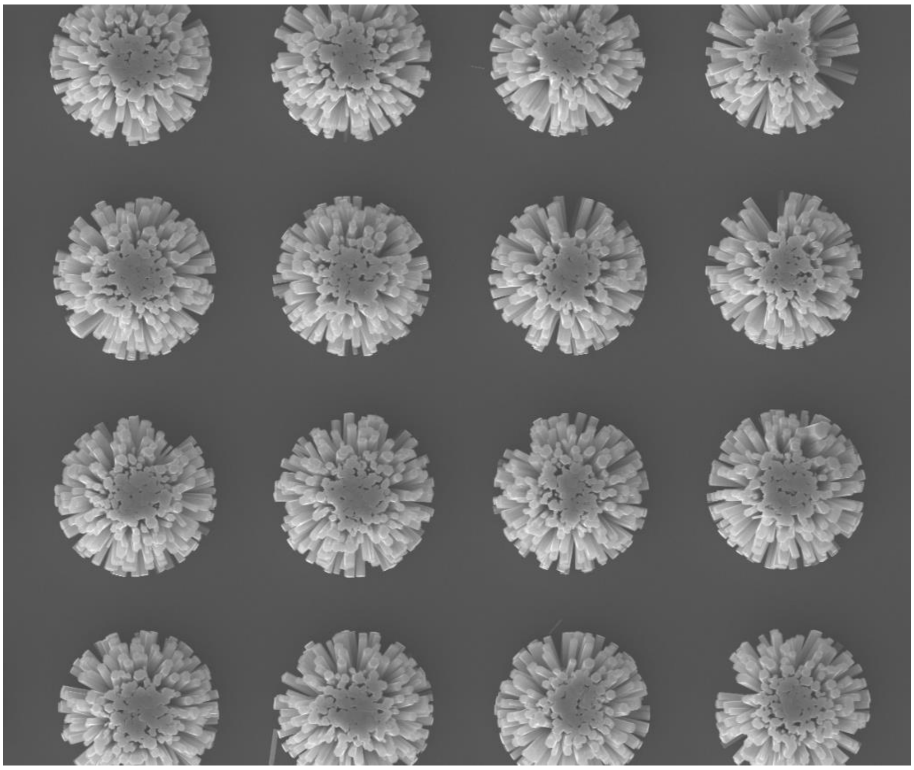

Botanic garden of ZnO dahlia flowers. The only flowers that can grow in cleanroom laboratories.

5.1 Introduction

1-dimensional (1D) nanowires have widely been used in biological applications for cell guidance and spatial patterning [156,157], electrical recording [12,15,158,159], mechanical sensing [160] and biomolecule transportation [161,162]. Nanowires benefit from their high aspect ratio (long axial dimensions with nanometre cross-section comparable to the micrometre size of cells) and large surface areas that can improve the interaction of the devices with the cells [163–169]. ZnO nanowires are proposed in this work as an ideal nanomaterial to be grown on microelectrode arrays for interaction with neuronal cells. ZnO nanowires can also be grown via a low temperature hydrothermal synthesis (at 95°C) with a low cost and high scalability on various substrates, including flexible substrates [43,107,119]. However, the biocompatibility of ZnO nanowires is not very well defined as it varies depending on the application and cell type. While ZnO nanowires have demonstrated to be biocompatible for H9c2, HEK293 cells and PC12 neurons [49,105], they have shown to reduce the viability of 3T3 fibroblasts, human umbilical cord vein endothelial cells, bovine capillary endothelial cells and hippocampal neurons [170,171].

The NTera2.D1 cell line (hNT) is a human embryonic carcinoma cell line that can be differentiated into neurons that express ubiquitous neuronal markers and provide a close model to adult human neuronal tissue [172,173]. The hNT cells are widely available and raise no ethical concerns as they are differentiated from a cancer stem cell line rather than a primary tissue [134]. Although to date, no study of human neurons has been reported on pristine ZnO nanowires. Varying the morphology and geometry of the ZnO nanowires have also been demonstrated to change the adhesion and viability of cells [174–177]. In this chapter, the biocompatibility of ZnO nanowires on human neurons is investigated for the first time. The influences of the ZnO nanowire morphology and geometry on adhesion and viability of hNT neurons are studied by applying the techniques developed in Chapter 4 for the growth of ZnO nanowires.

The work presented in this chapter is drawn from the paper “ZnO nanowire florets promote the growth of human neurons” that is published in the Materialia journal by Brad J. Raos, Mohsen Maddah, E. Scott Graham, Charles P. Unsworth and Natalie O.V. Plank [178]. The co-authors of this work have advised and commented on the manuscript of the published paper, but the majority of the work has been taken by Brad J. Raos and the thesis author. The work on fabrication and characterisation of the ZnO nanowire samples have been taken by the thesis author at Victoria University of Wellington, while the biological experiments have been done by Brad J. Raos at The University of Auckland. The analysis of the data presented in the paper was a collaborative work between the thesis author and Brad J. Raos. The thesis author has done all the work presented in this chapter unless it has been stated.

5.2 ZnO nanowire morphology

In this section, the morphology of the ZnO nanowire samples is characterised, before investigating the adhesion and viability of human hNT neurons on the ZnO nanowires. In Section 4.2 of Chapter 4, the morphology of the ZnO nanowires was demonstrated to be controlled by varying the precursor concentration and the growth time through the hydrothermal synthesis. Adding 6 mM of PEI to the growth also increased the duration of the growth time that resulted in the growth of the nanowires with high aspect ratios. The growth of the nanowires onto the defined locations was achieved by providing a patterned ZnO seed layer on the substrate (Method 2) through a standard photolithography process, as detailed in Section 3.2.4 of Chapter 3. The morphology of the ZnO nanowires was also changed by varying the geometry of the seed layer, as shown in Section 4.3.2 of Chapter 4. The samples and growth recipes were chosen in such a way to minimise the total number of the samples required for investigating the interaction of the hNT neurons with the ZnO nanowires. ZnO nanowires were grown as arrays of florets (islands), so the effect of the ZnO nanowire geometry and morphology on the adhesion and growth of the hNT neurons to both the entire arrays and the individual nanowire florets could be examined independently. We understood this method to have promises due to previous work by Du *et al.* [179] that demonstrated patterning poly(ε- caprolactone) (PCL) nanowires as an array of islands to improve the adhesion and growth of human MG-63 cells, compared to the substrates with flat films or bulk nanowires of PCL.

The samples here were made on 7 × 7 mm^2 silicon substrates with a 100 nm oxide layer (Si/SiO$_2$). The substrates were initially cleaned by 1 minute sonication in acetone, 1 minute sonication in isopropanol (IPA), rinsing in IPA and drying with nitrogen (N$_2$). Method 2 was applied using a standard photolithography technique to define a pattern of AZ5214E photoresist on the substrates, as detailed in Section 3.2.4 of Chapter 3. A 100 nm thick layer of ZnO seeds was then deposited on the patterned substrates, using RF sputter coating. A lift-off process was then applied to remove the photoresist, leaving 9 arrays of circular seed layers with diameters of 15 µm and inter-floret gaps of 5–150 µm on the substrates. The lift-off process consisted of soaking in N-Methyl-2-pyrrolidinone (NMP) at 60°C for 1 h followed by 2 h sonication in NMP at 60°C, 2 minutes sonication in IPA and drying with N$_2$. The ZnO nanowires were then grown on the patterned substrates using the hydrothermal synthesis. The growth solution was prepared by mixing 25 mM of zinc nitrate hexahydrate and hexamethylenetetramine (HMT) precursors with 6 mM of polyethylenimine (PEI with Mw of 800 g/mol) in 100 mL of deionised (DI) water. The growth substrates were placed in the growth solution at 95°C to grow nanowires for 1, 2, 4 and 8 h. The substrates were then removed from the solution and rinsed thoroughly in DI water with 60 seconds sonication and dried with N$_2$. Figure 5.1 (a) shows a ZnO nanowire sample that comprised of

9 arrays with inter-floret gaps of 5, 10, 20, 30, 40, 50, 75, 100 and 150 µm. The magnified brightfield image of the nanowire array with an inter-floret gap of 40 µm is shown in Figure 5.1 (b) as an example of the arrays.

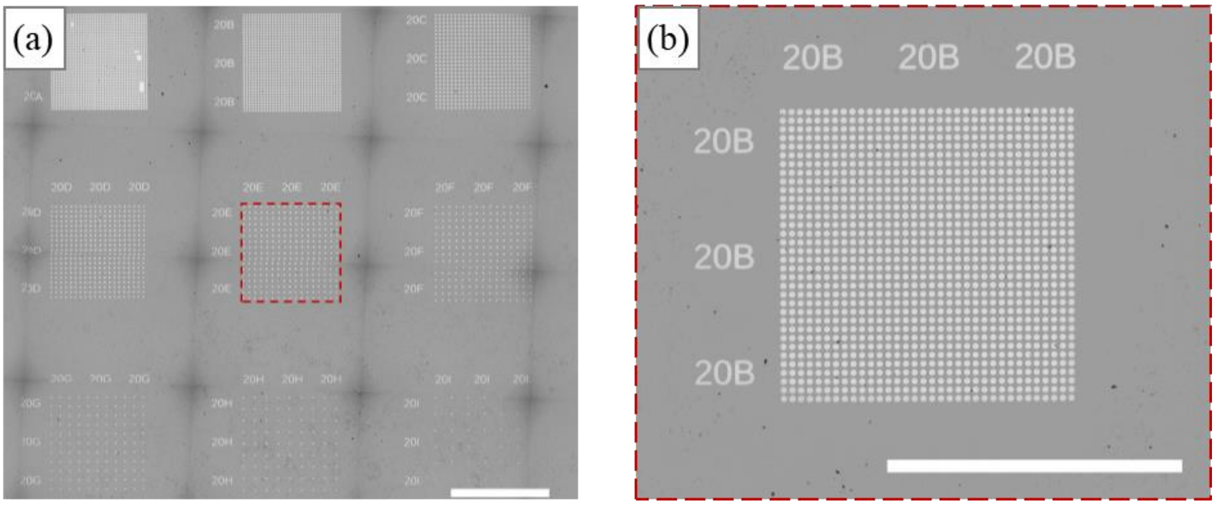

Figure 5.1. Brightfield images of ZnO nanowire arrays. (a) Brightfield image of a ZnO nanowire sample comprised of 9 arrays of nanowire florets with inter-floret gaps of 5, 10, 20, 30, 40, 50, 75, 100 and 150 µm. (b) Magnified brightfield image of the nanowire array with an inter-floret gap of 40 µm as depicted with a red square in (a). Scale-bars are 1 mm.

5.2.1 Varying the ZnO nanowire inter-floret gaps

Figure 5.2 shows scanning electron microscopy (SEM) of ZnO nanowires that were grown as arrays of florets on the same Si/SiO_2 substrate. Figure 5.2 (1a)–(4a) shows top view SEM images of ZnO nanowire arrays that were grown on 15 µm wide circular seed layers with inter-floret gaps of 5, 20, 50 and 150 µm, respectively. Despite applying the same growth conditions, 25 mM of precursor concentration with 6 mM of PEI for 8 h of growth, the nanowire morphology across the same substrate varied between the arrays with different inter-floret gaps, agreeing with the previous results shown in Section 4.3 of Chapter 4. Figure 5.2 (1b)–(4b) and (1c)–(4c) show SEM images from the top view and 70° tilted view of the ZnO nanowire florets, respectively. The size of the florets increased as a larger inter-floret gap was provided within the array despite each seed layer being 15 µm wide. The florets that were grown in the arrays with small gaps, e.g. 5 µm as shown in Figure 5.2 (1b) and (1c), comprised vertical nanowires only. As a larger inter-floret gap was provided, e.g. 50 µm as shown in Figure 5.2 (3b) and (3c), lateral nanowires started to grow around the florets. The diameter and height of the nanowire florets increased as longer nanowires were grown both laterally and vertically on the seeds with large inter-floret gaps, e.g. 150 µm as shown in

Figure 5.2 (4b) and (4c). Furthermore, Figure 5.2 (1d)–(4d) shows that increasing the gap between the florets also resulted in the diameter of the nanowires to increase and the density to decrease. These details will be further explained in Section 5.2.3.

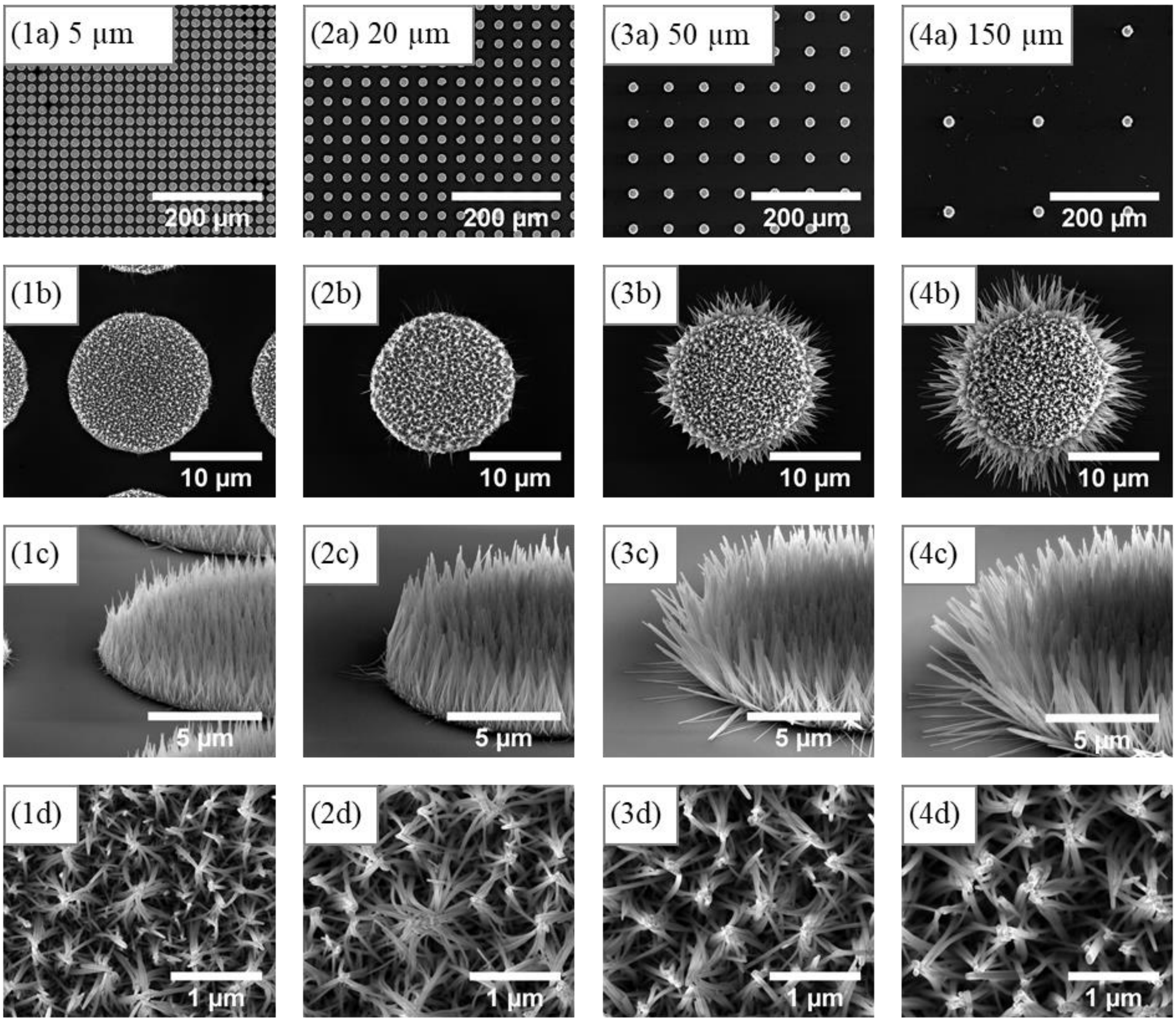

Figure 5.2. SEM images of ZnO nanowire arrays with various inter-floret gaps of (1a–d) 5 µm, (2a–d) 20 µm, (3a–d) 50 µm and (4a–d) 150 µm. The nanowires were grown on circular seed layers with diameters of 15 µm, using 25 mM of precursor concentration with 6 mM of PEI for 8 h of growth on the same Si/SiO_2 substrate. SEM images were taken from the top view (a, b, d) and 70º tilted view (c).

5.2.2 Varying the ZnO nanowire growth time

Figure 5.3 shows SEM images of ZnO nanowire arrays on 15 µm wide circular seed layers with inter-floret gaps of 150 µm, that were grown for 1, 2, 4 and 8 h of growth time using 25 mM of precursor concentration and 6 mM of PEI. The morphology of the nanowires varied with the growth time as before; however, Section 4.2.2 of Chapter 4 previously showed that the precursor ions in the growth solution ran out after 4 h of growth. In contrast, the addition of 6 mM PEI to the solution mediated the growth and resulted in the nanowire growth to be maintained for 8 h without refreshing the growth solution, agreeing with the results shown in Section 4.2.3 of Chapter 4. Fewer precipitates were also formed on the plain substrate (unseeded regions) due to the PEI coordination of the growth, as expected [107], than without using PEI.

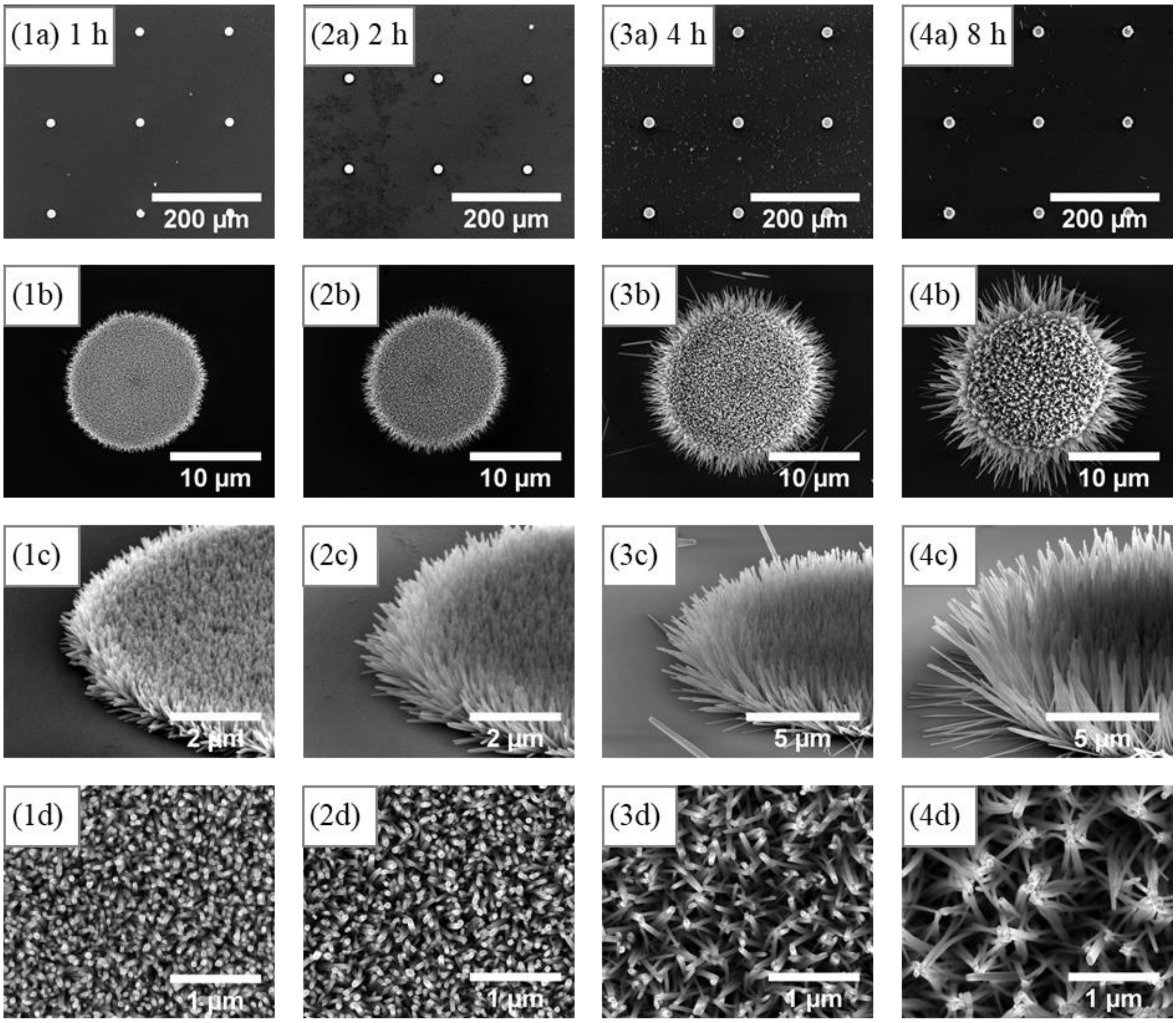

Figure 5.3. SEM images of ZnO nanowire arrays that were grown for different growth times of (1a–d) 1 h, (2a–d) 2 h, (3a–d) 4 h and (4a–d) 8 h. The nanowires were grown on circular seed layers with diameters of 15 µm and inter-floret gaps of 150 µm, using 25 mM of precursor concentration with 6 mM of PEI on different Si/SiO_2 substrates. SEM images were taken from the top view (a, b, d) and 70º tilted view (c).

Figure 5.3 (1a)–(4a) and (1b)–(4b) show the top view SEM images of ZnO nanowire arrays with inter-floret gaps of 150 µm that were grown for 1, 2, 4 and 8 h, respectively. Increasing the growth time from 1 h to 8 h resulted in larger florets to grow on the seeds. The length of the nanowires that were grown vertically and laterally from the seeds increased with the growth time, as shown in Figure 5.3 (1c)–(4c). Furthermore, the nanowire diameter slightly increased while the density decreased when the growth time increased from 1 h to 8 h, as shown in Figure 5.3 (1d)–(4d).

5.2.3 Characterisation of the ZnO nanowire morphology

Figure 5.4 plots the morphology of the ZnO nanowires that were grown as florets on 15 µm wide circular seed layers with inter-floret gaps of 5–150 µm, and growth times of 1, 2, 4 and 8 h. Figure 5.4 (a) shows that the average diameter of the resulting nanowires was within a range of 20–75 nm when different inter-floret gaps and growth times were used. The average diameter of the nanowires increased from 27 ± 6 nm to 46 ± 8 nm as the inter-floret gap increased from 5 µm to 50 µm using 1 h of growth time. The nanowire diameter stayed unchanged for any further increase of the gap beyond 50 µm. Increasing the growth time from 1 h to 8 h slightly elevated the average diameter by 5–15 nm.

Figure 5.4 (b) shows the variation of the nanowire length for different inter-floret gaps and growth times. Increasing the gap from 5 µm to 50 µm for 1 h of growth time resulted in the length of the nanowires increasing from 360 ± 25 nm to 750 ± 70 nm. As the growth time was increased from 1 h to 8 h, the average length of the nanowires for all arrays significantly increased from 600 ± 180 nm to 3.4 ± 0.7 µm. The nanowire lengths for all growth times also increased by increasing the inter-floret gap from 5 µm to 50 µm; however, the length did not change for the gaps greater than 50 µm.

The proportion of the nanowire length to the diameter, defined as the aspect ratio, is shown in Figure 5.4 (c). The average aspect ratio increased from 14 ± 2 to 70 ± 6 by increasing the growth time from 1 h to 8 h. The aspect ratio enhancement with increased growth time agreed with the results shown in Section 4.2.3 of Chapter 4 and the previous work [123,125] that showed PEI as an aspect ratio enhancing agent. The influence of the inter-floret gap on the aspect ratio was more noticeable within the range of 5–50 µm, as the nanowire length increased more than the diameter. The aspect ratio remained at a plateau for the inter-floret gaps larger than 50 µm, since the nanowire diameter and length did not change considerably, as seen in Figure 5.4 (a) and (b), respectively.

Figure 5.4 (d) plots the density of the nanowires that were grown on the seed patterns for various inter-floret gaps and growth times. The density of the nanowires was estimated by counting the number of nanowires within an area of 2–4 μm^2 of the SEM images from the top view. The smallest inter-floret gap of 5 μm with 1 h of growth time resulted in the maximum density of 450 ± 45 NWs/μm^2. Increasing the inter-floret gap from 5 μm to 50 μm resulted in the density of the nanowires decreasing from 450 ± 45 NWs/μm^2 to 220 ± 20 NWs/μm^2. The density stayed unchanged when the inter-floret gap increased beyond 50 μm. The density also decreased as a longer growth time was applied. The nanowire density range for all arrays reduced from 200–450 NWs/μm^2 to 40–120 NWs/μm^2 as the growth time increased from 1 h to 8 h.

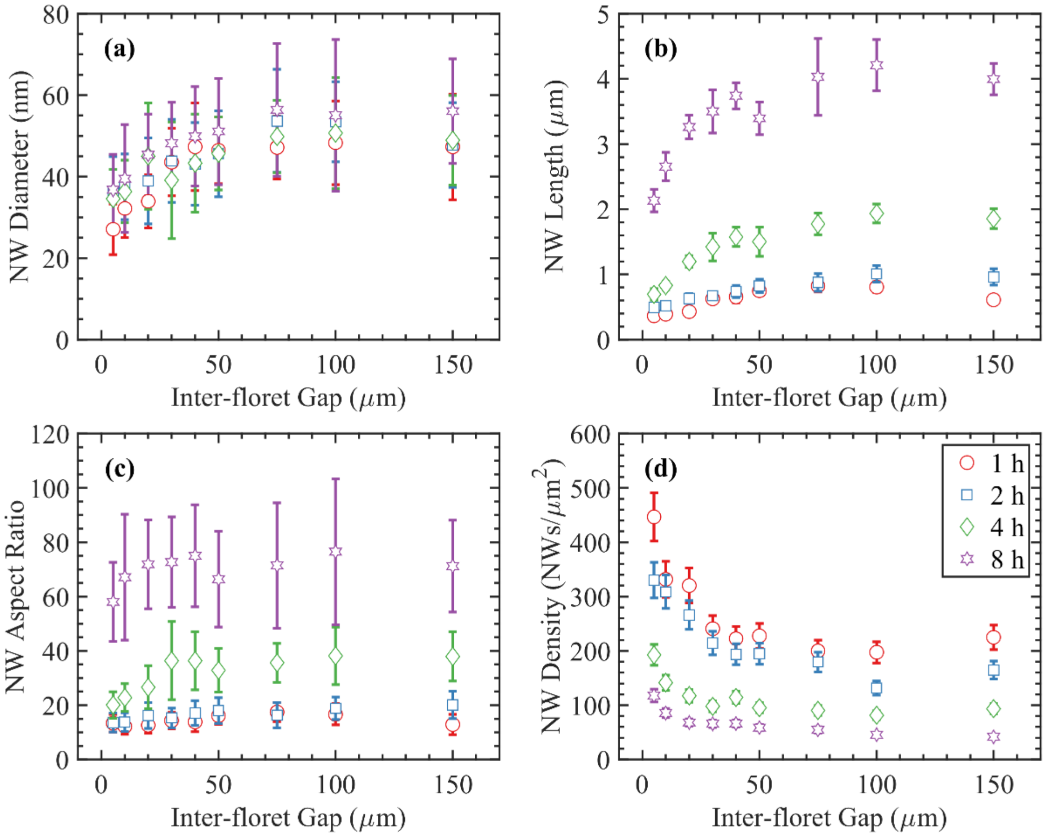

Figure 5.4. Characterisation of the nanowire morphology as (a) diameter, (b) length, (c) aspect ratio and (d) density for various inter-floret gaps of 5–150 μm, and growth times of 1–8 h. ZnO nanowires were grown as florets on 15 μm wide seeds using 25 mM of precursor concentration with 6 mM of PEI. Error bars represent one standard deviation (*n* > 30 NWs) in (a)–(c) and 10% deviation in (d).

Figure 5.4 showed that the morphology of the nanowire florets varied across the same substrate due to the variation of the inter-floret gaps within the arrays. The length and density of the nanowires varied significantly between the arrays with inter-floret gaps of 5–50 μm. Furthermore, a broader range of the nanowire morphology was achieved by using different growth times, 1–8 h. The nanowires that were grown for a long time, i.e. 8 h, were determined to have high aspect ratios and low densities compared to the nanowires that were grown for a short time, i.e. 1 h. The morphology of the nanowires that were grown in this work agreed with the results demonstrated in Chapter 4. The resulting ZnO nanowires provide a broad range of morphology and geometry that are comparable to the micrometre size of the neuronal cells and are ideal for biocompatibility studies as well as integration with microelectrode arrays.

5.3 hNT neurons on ZnO nanowires

In this work, hNT neurons were used to investigate the compatibility of the ZnO nanowires for integration with human neurons. hNT neurons can provide a close model to adult human neuronal tissues, while they are widely available with no ethical concern because they can be differentiated from cancer stem cell lines [134]. All of the cell growth experimentation work, including the neuron differentiation and plating, fluorescence labelling and image processing were taken by Brad J. Raos at The University of Auckland, as detailed in Appendix A. In short, human hNT neurons were differentiated from the NTera2.D1 (hNT/NT2) cell line following the previously introduced protocols [134–138]. After culturing neurons for 4–5 weeks, the hNT neurons were plated on the ZnO nanowire substrates at approximately 1000 cells/mm^2. The Ca^{2+} functionality of neurons on the ZnO nanowires was measured after 2 days *in vitro* (DIV) to visualise free Ca^{2+} in the cytoplasm using an Olympus BX53 microscope. The cytoplasm and the nuclei of the neurons were labelled by using green CMFDA and blue Hoechst 33343 fluorescent stains, respectively. The individual fluorescence images taken over the entire ZnO sample chip were then stitched into a single image using CellSens Dimension (Olympus). Image processing was finally performed using custom software in MATLAB to study the growth of hNT neurons on ZnO nanowires.

In this section, the adhesion of the hNT neurons to the entire ZnO nanowire arrays with various geometry and nanowire morphology is studied first. The localisation of the neurons to the individual nanowire florets within the array is then investigated to demonstrate the influence of the nanowires on the growth of the neurons. Lastly, the functionality of the neurons is examined by stimulation with glutamate, showing that hNT neurons are functionally viable on ZnO nanowires.

5.3.1 Neuronal adhesion to the entire ZnO nanowire array

Figure 5.5 shows fluorescence images of hNT neurons on ZnO nanowire arrays that are outlined with red squares. The inset of Figure 5.5 shows the growth time (hours) and the inter-floret gaps (µm) of the ZnO nanowire arrays. The fluorescence images show the neuronal cytoplasm that was labelled by the green stains and the nuclei by the blue stains. The cytoplasm shown in Figure 5.5 corresponds to the entire neuron body, including the cell body (soma) as well as the neurites (dendrites and axons). The neuronal nuclei were measured to have an average diameter of 11 ± 2 µm. The soma was also measured to be approximately 15–25 µm wide.

Figure 5.5 (1a–c) and (2a–c) show ZnO nanowires that were grown for 1 h and 8 h with inter-floret gaps of 5, 40 and 150 µm, respectively. Although hNT neurons were grown on the entire sample, the density of the neurons placed within the ZnO nanowire arrays was different compared to the substrate areas surrounding the arrays that were used as controls. Furthermore, the neuron density was determined to be different between the arrays that were grown with different growth times and inter-floret gaps.

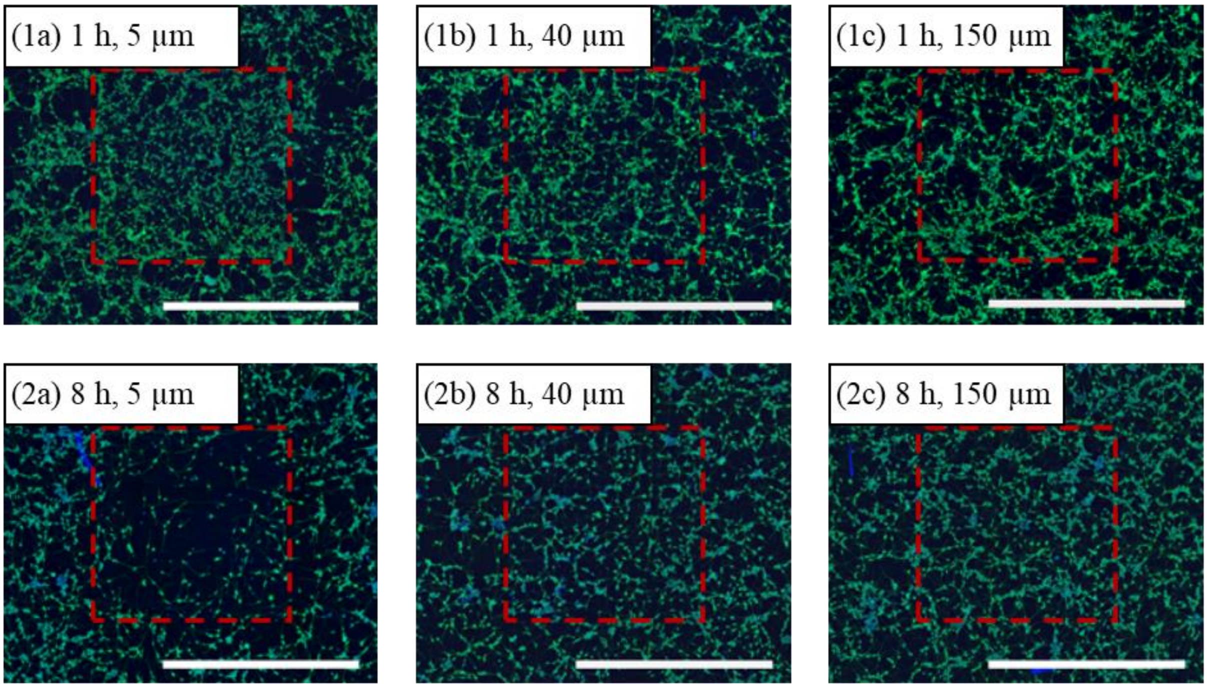

Figure 5.5. Fluorescence images of hNT neurons on ZnO nanowire arrays that were grown for (1a–c) 1 h, and (2a–c) 8 h. Fluorescence images show cytoplasm (green) and nuclei (blue) of the hNT neurons. The red squares outline the regions of the nanowire arrays with inter-floret gaps of (a) 5 µm, (b) 40 µm and (c) 150 µm. Scale-bars are 1 mm.

The adhesion and growth of the hNT neurons to the ZnO nanowire arrays are demonstrated in Figure 5.6. Figure 5.6 (a) and (b) show the brightfield image of a ZnO nanowire array and the fluorescence image of hNT neuronal cytoplasm and nuclei on the nanowire array, respectively. The neuron density ratio was subsequently defined as the area of the neurons within the nanowire array, the white regions of Figure 5.6 (c), relative to the area of the neurons on the control substrate surface surrounding the array, the white regions of Figure 5.6 (d). The adhesion and growth of both neuronal nuclei and cytoplasm on the ZnO nanowire arrays with inter-floret gaps of 5–150 µm and growth times of 1–8 h were investigated. Figure 5.6 (e) represent the neuronal nuclei density ratio that accounts to the adhesion of the neurons to the entire ZnO nanowire arrays when neuronal cells were plated on the sample. Figure 5.6 (f) represents the neuronal cytoplasm density ratio that corresponds to the adhesion of the entire neuronal body (cell body and neurites) and growth of the neurites (dendrites and axons) on the entire ZnO nanowire arrays after cell plating. The colour maps in Figure 5.6 (e) and (f) indicate the level of the neuron growth on the nanowire arrays with blue regions indicating the promotion, grey colours indicating no effect and red colours indicating inhibition of the neuron growth.

Figure 5.6 (e) and (f) show that both nuclei and cytoplasm density ratios were similarly influenced by the nanowire array geometry and growth time. The variation of the neuron density ratios could be categorised into two trends. First, the neuron density ratio reduced by increasing the growth time of the nanowires. Second, as the inter-floret gap within the nanowire array increased from 5 µm to 150 µm, the neuron density ratio approached unity; the adhesion and growth of the neurons on and off the nanowire array equalised.

ZnO nanowire arrays promoted the adhesion and growth of the neurons when 1 h and 2 h of growth time were used, as indicated by blue regions in Figure 5.6 (e) and (f). The greatest promotion of the neuron growth was achieved on the ZnO nanowire arrays that were grown for 1 h. The neuronal nuclei and cytoplasm density increased by 33% and 30%, respectively, on the ZnO nanowire arrays with inter-floret gaps of 20 µm. In contrast, growing ZnO nanowires for 4 h and 8 h, the adhesion and growth of the neurons were inhibited, as shown by red regions in Figure 5.6 (e) and (f). The neuronal nuclei density ratio reduced by 65% on the ZnO nanowire arrays with inter-floret gaps of 5 µm that were grown for 8 h. The neuronal cytoplasm density ratio reduced by 55% on the ZnO nanowire arrays with inter-floret gaps of 10 µm that were grown for 4 h.

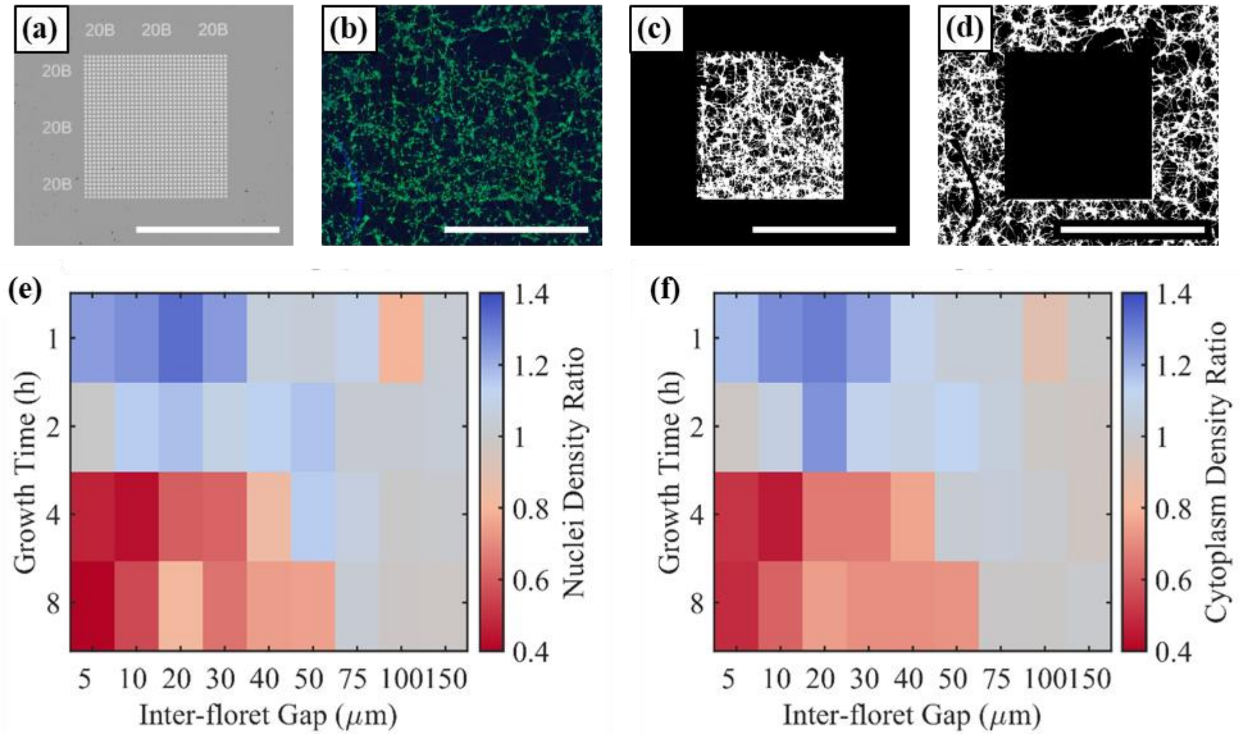

Figure 5.6. Adhesion and growth of the hNT neurons on the entire ZnO nanowire arrays. (a) Brightfield image of a ZnO nanowire array. (b) Fluorescence image of the hNT neuronal cytoplasm (green) and nuclei (blue) on the nanowire array shown in (a). (c) The neuronal nuclei and cytoplasm area within the nanowire array (white regions). (d) The neuronal nuclei and cytoplasm area on the control substrate area surrounding the array (white regions). Scale-bars are 1 mm. (e) Neuronal nuclei density ratio and (f) cytoplasm density ratio of the hNT neurons that were grown within the nanowire array, e.g. (c), relative to the control substrate area, e.g. (d), for various inter-floret gaps and growth times. The blue regions indicate promotion; the grey regions indicate no effect and the red regions indicate inhibition of the neuron growth on the nanowire arrays relative to the control substrate areas.

Increasing the inter-floret gap of the nanowire arrays from 5 μm to 150 μm faded the influence of the ZnO nanowire array on promotion/inhibition of the neuron adhesion and growth. The variation of the neuron density for different growth times was most distinguishable on the ZnO nanowire arrays with inter-floret gaps of 5–30 μm. Despite the promotion of neurons on 1 h and 2 h arrays and the inhibition on 4 h and 8 h arrays, the neuron density ratio approached unity as the inter-floret gap increased from 30 μm to 150 μm. The unity density ratio determined that the hNT neurons adhered and grew on the entire ZnO nanowire arrays with large inter-floret gaps (> 30 μm) similarly to the control substrate area.

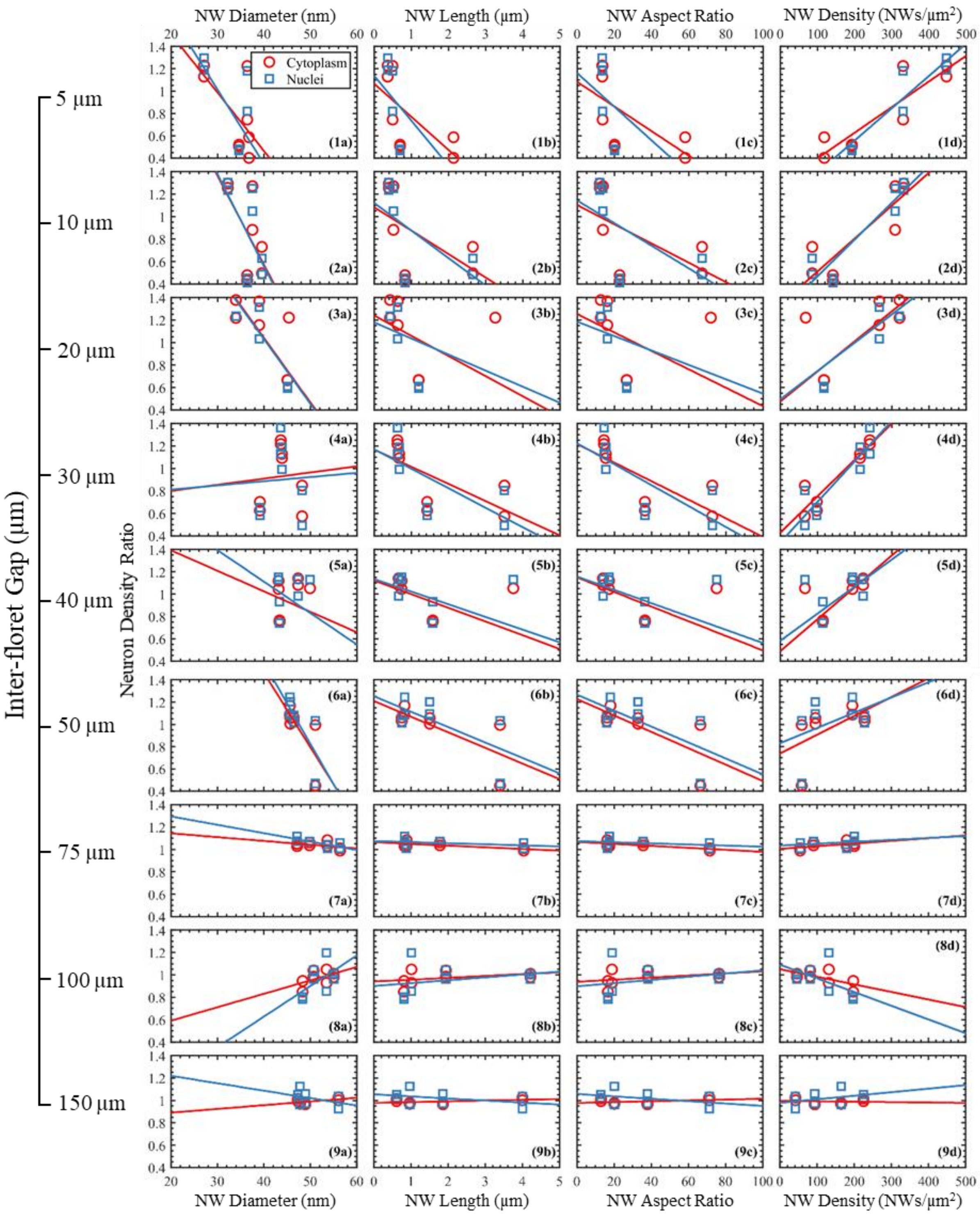

Figure 5.7. Influence of the nanowire array geometry on the variation of the neuron density ratio with the nanowire morphology. The neuronal cytoplasm density ratio (red) and nuclei density ratio (blue) are plotted against the (a) diameter, (b) length, (c) aspect ratio and (d) density of the nanowires, respectively. The geometry of the nanowire array varied with the inter-floret gaps of 5, 10, 20, 30, 40, 50, 75, 100 and 150 μm in (1–9), respectively. The linear trendlines are shown to guide the eye.

The understanding of the hNT neuron adhesion and growth to the ZnO nanowire arrays can be deepened by analysing the nanowire morphology, which I previously discussed in Section 5.2.3. Figure 5.7 shows the influence of both nanowire array geometry (inter-floret gaps) and the nanowire morphology (diameter, length, aspect ratio and density) on the neuron density ratio for the entire nanowire arrays. ZnO nanowires with average diameters of 27–37 nm, lengths of 0.36–2.13 µm, aspect ratios of 13–58, and densities of 120–450 NWs/µm^2 were grown on the nanowire arrays with small inter-floret gaps of 5 µm and growth times of 1–8 h, as shown in Figure 5.7 (1a–d). The neuronal cytoplasm and nuclei density ratio changed within a range of 0.50–1.23 and 0.36–1.30, respectively, due to the variation of the nanowire morphology.

The slope of the linear trendlines in Figure 5.7 (1)–(6) determined that the nanowire morphology had the greatest effect on the neuron adhesion and growth when arrays with inter-floret gaps of 5–50 µm were provided. As the inter-floret gap was increased to the 75–150 µm range, the variation of the neuronal cytoplasm and nuclei density ratios reduced, as shown in Figure 5.7 (7)–(9). Increasing the growth time from 1 h to 8 h for the arrays with inter-floret gaps of 75–150 µm resulted in the ZnO nanowires with diameters of 47–56 nm, lengths of 0.61–4.2 µm, aspect ratios of 13–77, and densities of 42–225 NWs/µm^2 to grow, as discussed in Section 5.2.3. Despite the variation in the nanowire morphology, the neuron density ratio did not change significantly. The neuronal cytoplasm and nuclei density ratios were measured to be 0.99 ± 0.06 and 0.98 ± 0.09, respectively, across all samples produced in this range.

As well as considering the effect of the inter-floret gap on the nanowire morphology, it is crucial to consider the proportion of the substrate region that is covered by the ZnO nanowires. The ZnO nanowire arrays with small gaps of 5 µm between 15 µm wide circular seed layers implied that 44% of the nanowire array region was covered by the ZnO nanowires and the remaining 56% was plain Si/SiO$_2$ substrate surface. The neuron adhesion and growth were, subsequently, influenced the most by the nanowires when a small inter-floret gap was used. As the inter-floret gap increased to 50 µm, only 4.2% of the array region was covered with the ZnO nanowires, significantly diminishing the effect of the ZnO nanowires on the neuron density variation. Further increase of the inter-floret gaps to 75–150 µm resulted in only 2.2% down to 0.6% of the array regions to include ZnO nanowires. The nanowire arrays appeared more like a plain substrate to the neurons, regardless of the changes in the nanowire morphology when large inter-floret gaps were used. As a result, the promotion and inhibition of neuron adhesion and growth on the ZnO nanowire arrays were less prominent compared to the control substrate areas surrounding the arrays. ZnO nanowires are, therefore, required to cover more than 4% of the sample area, e.g. microelectrode surface in this work, to promote the growth of hNT neurons.

The neuronal cytoplasm and nuclei density ratios on the ZnO nanowire arrays decreased with increasing the nanowire diameter, length and aspect ratio, as shown in Figure 5.7 (1a–c), respectively. The adhesion and growth of the hNT neurons on the nanowire array was promoted when nanowires shorter than 500 nm were grown. Zaveri *et al.* [174] previously determined that ZnO nanowires with diameters of 50 nm and lengths of 500 nm can pierce the cell membrane of primary mouse macrophages that can lead to cell death. The neuronal cytoplasm and nuclei density ratios also increased when more nanowires were grown on the seeds, as shown in Figure 5.7 (1d). The nanowires with densities higher than 350 NWs/µm^2 were shown to promote the adhesion and growth of the hNT neurons on the entire nanowire arrays. Bonde *et al.* [164] demonstrated that high-density nanowires ($\geq$ 30 NWs/µm^2) could support the growth of adherent cells, where cells could grow on top of the nanowires without sinking down. However, the promotion and inhibition in the growth and adhesion of the cells on high-density nanowires largely depend on the geometry and the material of the nanowires. Here, ZnO nanowires with lengths shorter than 500 nm and densities higher than 350 NWs/µm^2 are shown to promote the growth and adhesion of human hNT neurons on the entire ZnO nanowire arrays. These ZnO nanowires can, therefore, be integrated with microelectrode array devices to record extracellular signals from the hNT neurons.

5.3.2 Localisation of hNT neurons to the individual ZnO-NW florets

In the previous section, the adhesion and growth of hNT neurons on the ZnO nanowire arrays were demonstrated to vary with the geometry of the nanowire array and the morphology of the nanowires. In this section, the localisation of the hNT neurons to the individual nanowire florets within the nanowire array is investigated. Figure 5.8 shows the fluorescence images of hNT neurons, with the nuclei labelled by the blue stains and the cytoplasm labelled by the green stains, on the ZnO nanowire florets that are outlined with white circles. The ZnO nanowire florets were grown for 1 h and 8 h with the inter-floret gaps of 5, 40, and 100 µm, as shown in Figure 5.8 (1a–c) and (2a–c), respectively.

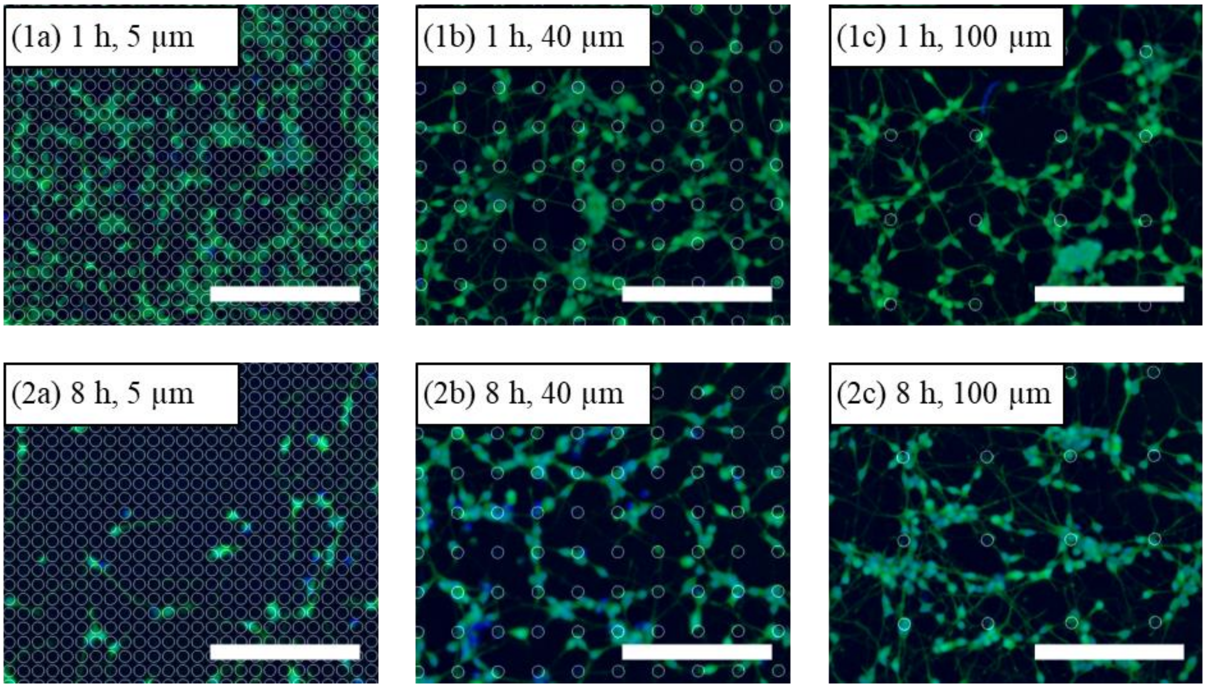

Figure 5.8. Fluorescence images of hNT neurons on ZnO nanowire arrays that were grown for (1a–c) 1 h, and (2a–c) 8 h. Fluorescence images show cytoplasm (green) and nuclei (blue) of the hNT neurons. The locations of ZnO nanowire florets are outlined with white circles. The ZnO nanowire arrays have inter-floret gaps of (a) 5 µm, (b) 40 µm and (c) 100 µm. Scale-bars are 200 µm.

The localisation of hNT neurons within the array was investigated by measuring the density of the neuronal nuclei on the individual ZnO nanowire florets and around the florets in proportion to the neuronal nuclei density on the control substrate area. Figure 5.9 shows the area of the 15 µm wide florets and 10 µm concentric bands at increasing distance from the florets that were used for investigating the localisation of the neurons. The plain substrate area surrounding the nanowire array was used as the control area to calculate the neuron density ratio.

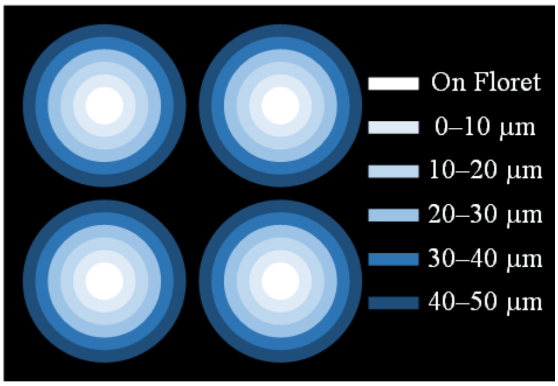

Figure 5.9. Schematic diagram of the nanowire florets and 10 µm wide concentric bands that show the distance from the florets.

Figure 5.10 shows the neuronal nuclei density ratio on the nanowire florets and the 10 µm concentric bands around the florets. ZnO nanowires were grown for 1, 2, 4, and 8 h, as shown in Figure 5.10 (a)–(d), respectively. The inter-floret gaps of 5–100 µm were used in this analysis. The 150 µm gap samples were not included since the localisation of neurons to the exact location of the individual nanowire florets with 150 µm gap was challenging and not entirely reliable. The neuronal nuclei density on the entire nanowire array, as previously shown in Figure 5.6 (e), is also repeated at the top row of Figure 5.10 (a)–(d) for comparison. The neuron density presented in here comprised the neuronal nuclei only, not the cytoplasm, for simplicity in the analysis as they both followed a similar trend. The white regions in Figure 5.10 represent no information since the gap between the florets was smaller than the indicated concentric bands. The blue and red regions in Figure 5.10 indicate the increasing and decreasing population of the neurons that resided on the florets and the concentric bands relative to the control substrate area, respectively.

Two general trends can be seen in the localisation of the hNT neurons to the individual ZnO nanowire florets within the array, as shown in Figure 5.10 (a)–(d). Firstly, the neuron density ratio on the florets increased for all growth times of 1–8 h, as the inter-floret gap within the array increased. This trend can be seen by moving from left to right in Figure 5.10. Secondly, the neuron density ratio reduced in the areas that were further away from the floret sites. The trend can be seen by moving from top to bottom in Figure 5.10.

The nanowire florets with small inter-floret gaps of 5 µm were demonstrated to have neuron density ratios of 1.16 and 1.01 when nanowires were grown for 1 h and 2 h, respectively. In contrast, the 4 h and 8 h nanowire florets reduced the neuron density ratio to 0.47 and 0.49, respectively. The nanowire florets with the inter-floret gaps of 5 µm comprised a high density of nanowires, 120–450 NWs/µm^2, for 1–8 h of growth times, as characterised in Figure 5.4 (d). Persson *et al.* [168] previously determined that a high density of gallium phosphide (GaP) nanowires acted as a bed-of-nails to the mouse fibroblasts, at which cells could reside on top of the nanowires and be fully motile. Here, growing florets for a short time of 1–2 h resulted in the nanowires with high densities of 390 ± 60 NWs/µm^2 and low aspect ratios of 13.5 ± 0.1. The same population of hNT neurons resided on these nanowires as the control Si/SiO$_2$ substrate surface, where neuronal density ratios of 1.16 and 1.01 were measured for 1 h and 2 h samples, respectively. In contrast, growing florets for 4–8 h resulted in nanowires with a relatively lower density of 155 ± 35 NWs/µm^2 and a higher aspect ratio of 40 ± 20. The hNT cells tended not to reside on the sparse nanowires with high aspect ratios (narrow and long nanowires). The neuron density ratio subsequently reduced to 0.47 and 0.49, for 4 h and 8 h grown nanowires, respectively. Lee *et al.* [170] previously demonstrated that, although NIH 3T3 fibroblasts and human umbilical cord vein endothelial cells could initially adhere on ZnO nanowires, cells could not spread if the spacing between the nanowires were more than 70 nm. For the ZnO nanowires with a large inter-spacing, the focal adhesion of the cells on the nanowires could not assemble as required for the formation of lamellipodia (cytoskeletal actin that allows cells to spread) [180]. In this work, using a long growth time of 4–8 h resulted in the nanowire density to decrease and subsequently, the spacing between the nanowires to increase. Here, the reduced viability and growth of hNT neurons on 4 h and 8 h ZnO nanowires could be associated with the low focal adhesion assembly on the sparse ZnO nanowires.

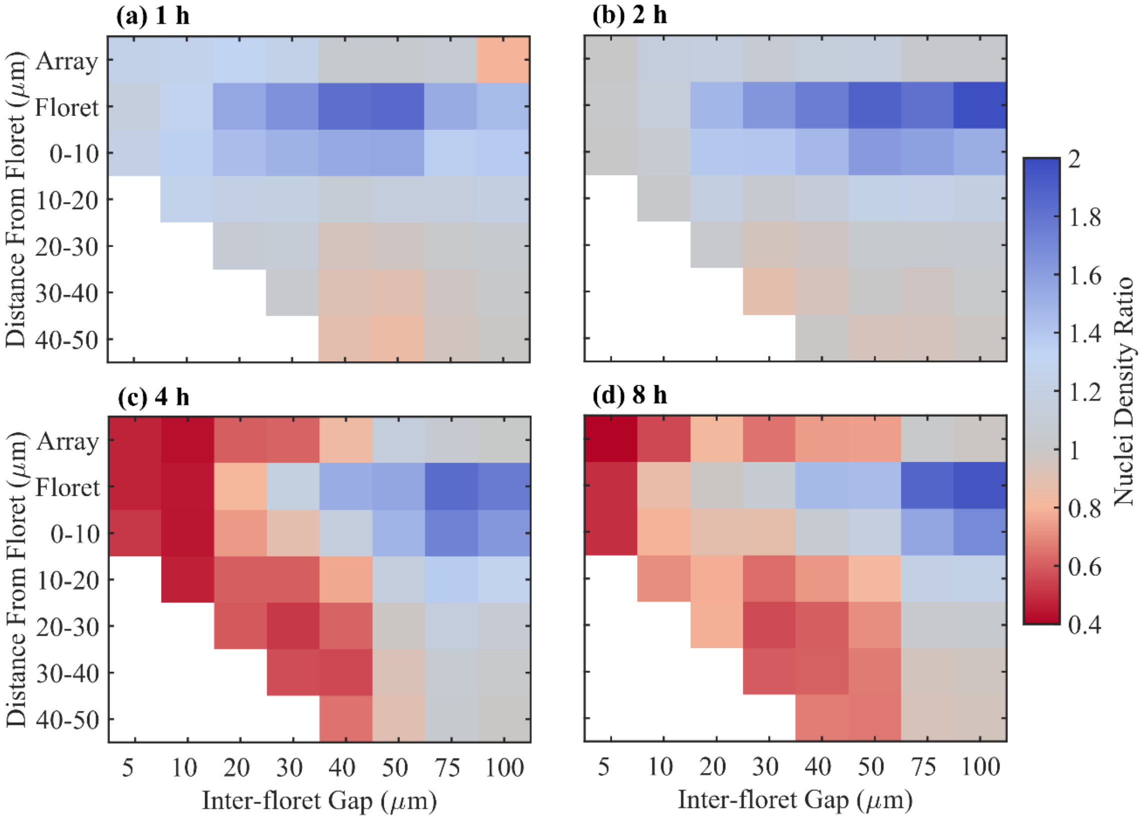

Figure 5.10. The density ratio of human hNT neurons on the nanowire florets and 10 µm concentric bands around the florets. The density ratio was calculated as the density of the neuronal nuclei on florets or within the concentric bands in proportion to the nuclei density on the control substrate area surrounding the array. The nuclei density ratio over the entire nanowire array, as previously shown in (b), is repeated here and labelled as “Array”. The ZnO nanowires were grown for (a) 1 h, (b) 2 h, (c) 4 h and (d) 8 h with inter-floret gaps of 5–100 µm.

As the inter-floret gaps increased to 100 µm, the neuron density ratio on all florets increased to 1.45–1.98 for growth times of 1–8 h. Despite that providing a large inter-floret gap increased the aspect ratio of the nanowires, 16–76 for growth times of 1–8 h as shown in Figure 5.4 (c), more hNT cells resided on the florets in comparison to when a small inter-floret gap was provided. Hanson *et al.* [181] and Buch-Månson *et al.* [166] previously demonstrated that cell membranes could deform and wrap around sparse vertical InAs and SiO_2 nanowires. Here, the hNT neurons with approximated 15–25 µm wide cell body (soma) could have deformed and adhered tightly to the florets (with diameters of 15–20 µm) that were located sparsely from each other (e.g. inter-floret gap of 100 µm).

The localisation of the hNT neurons on the floret sites was considerably varied by the growth times and inter-floret gaps, as shown in Figure 5.10. The population of the neurons decreased by increasing the distance from the floret sites. The reduced neuron density is shown in Figure 5.10 as the colour of the regions changed from blue to grey and from grey to red by increasing the diameters of the concentric bands (moving from top to bottom). Although hNT neurons did not physically contact the ZnO nanowire florets, their viability was reduced, particularly for 4–8 h grown nanowires, as shown in Figure 5.10 (c) and (d). This behaviour can be attributed to the possible effects of the ZnO nanowires to the culture medium.

ZnO has been defined as a biocompatible material when it has been used in bulk (above the micrometre range) as commonly used in healthcare and biomedical products [182]. However, as the size of ZnO is reduced to the nanoscale, the cytotoxicity of ZnO nanowires could be observed due to the release of Zn^{2+} ions [175]. Although Zn^{2+} is determined as an essential ion for many biological processes; a high concentration of Zn^{2+} can lead to cell death [183]. Racca *et al.* [183] found ZnO ions to be cytotoxic at concentrations above 10 µg/mL due to phagocytosis and subsequent dissolution of free-floating ZnO ions within the cytoplasm of the cells. Although the ZnO nanowires grown in this work were physically attached to the substrates, and it was not possible for the cells to phagocytose the ZnO nanowires, there is a possibility that ZnO nanowires could be dissolved partially in the culture media, as demonstrated by Zaveri *et al.* [174]. The reduced growth of neurons even at a distance away from the florets could, therefore, be a result of the released ZnO ions from the ZnO nanowires.

Figure 5.10 (c) and (d) show that the growth of the neurons between the florets was significantly reduced when nanowires were grown for 4–8 h. The reduced neuron density could be attributed to an increased concentration of the Zn^{2+} ions released from the ZnO nanowires, although I have no direct evidence of this. Using a growth time of 4–8 h resulted in longer ZnO nanowires to grow in comparison to a growth time of 1–2 h, as demonstrated in Figure 5.4. As a result, it is possible that a higher amount of Zn^{2+} ions could be released by the large nanowires, impacting the viability of hNT cells around the florets.

Another method of investigating the biocompatibility of the ZnO nanowires is to assess the growth of the neurites (neuronal axons and dendrites). The neurite growth was calculated by measuring the total area of the neuronal cytoplasm, representing the neuronal cell bodies and neurites, relative to the total area of the neuronal nuclei across the entire substrate. Ciofani *et al.* [105] previously demonstrated that the neurite growth could also be inhibited on ZnO nanowires due to the release of Zn^{2+} ions in the culture solution. Figure 5.11 shows the neurite growth on the ZnO nanowire substrates that were grown for 1, 2, 4, and 8 h. Here, the neurite growth was measured to be maximum at 3.94 ± 0.77 when ZnO nanowires were grown for 1 h. Increasing the growth time of the nanowires from 1 h to 8 h reduced the overall neurite growth on the sample. The neurite growth reached a minimum of 2.76 ± 0.29 when ZnO nanowires were grown for a maximum of 8 h. The neurite growth that decreased with increasing the ZnO nanowire growth time from 1 h to 8 h can further contribute to the possible dissolution of the ZnO nanowires in the culture solution; however, more investigation is required to confirm this hypothesis.

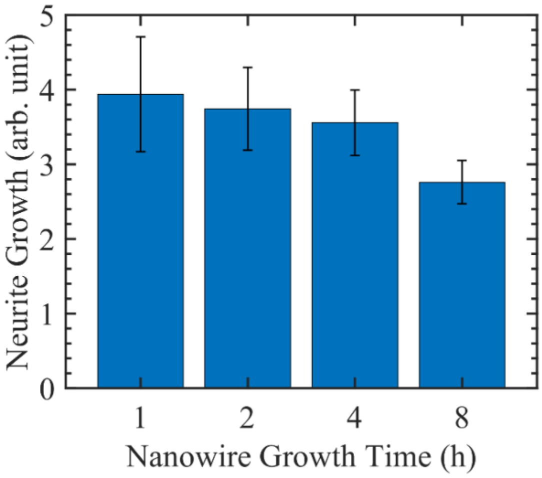

Figure 5.11. Neurite growth on ZnO nanowire substrates for growth times of 1, 2, 4, and 8 h. Neurite growth was calculated as the total area of the neuronal cytoplasm across the whole substrate, relative to the total neuronal nuclei area. Error bars represent one standard deviation.

5.3.3 hNT neuron functionality

The functionality of hNT neurons on ZnO nanowires was examined by measuring their responses to glutamate stimulation. Glutamate is an amino acid that is commonly used as a neurotransmitter for transmission of signals between neuronal cells [184]. The cytoplasmic Ca^{2+} concentration of the hNT neurons was increased when stimulated with glutamate; however, only about 40% of hNT neurons are expected to respond to the glutamate stimulation since hNT neurons contain a heterogeneous subpopulation of dopaminergic, cholinergic, GABAergic and glutamatergic neurons [185,186].

Figure 5.12 (a)–(d) shows the viability of the hNT neurons located on the ZnO nanowire arrays that were grown for 1, 2, 4, and 8 h, respectively. Figure 5.12 (1) shows the Fluo-4 fluorescence images of hNT neurons inside and outside of the nanowire arrays. Fluo-4 is a calcium (Ca^{2+}) indicator that exhibits a large fluorescence intensity when it binds Ca^{2+} molecules that were induced from the cells for neurotransmissions [34]. Figure 5.12 (2) shows the selected hNT neurons inside and outside of the nanowire arrays for tracing the Fluo-4 fluorescence intensity as a response to the glutamate stimulation.

The fluorescence traces of the hNT neurons inside and outside the ZnO nanowire array are shown in Figure 5.12 (3) and (4), respectively. The cytoplasmic Ca^{2+} concentration of hNT neurons within the ZnO nanowire arrays and on the control substrate area increased after stimulation with glutamate. The hNT neurons were, subsequently, determined to be alive and functionally viable, inside and outside of all ZnO nanowire arrays. In Section 5.3.1, the 4–8 h nanowires were demonstrated to reduce the adhesion and growth of the hNT neurons on the entire nanowire arrays; however, Figure 5.12 (3a–d) shows that the remaining hNT neurons on all nanowire arrays are alive and functional. The resulting ZnO nanowires are, therefore, determined to be biocompatible for human hNT neurons, and the adhesion and growth of the hNT neurons can be controlled by the morphology and geometry of the ZnO nanowires.

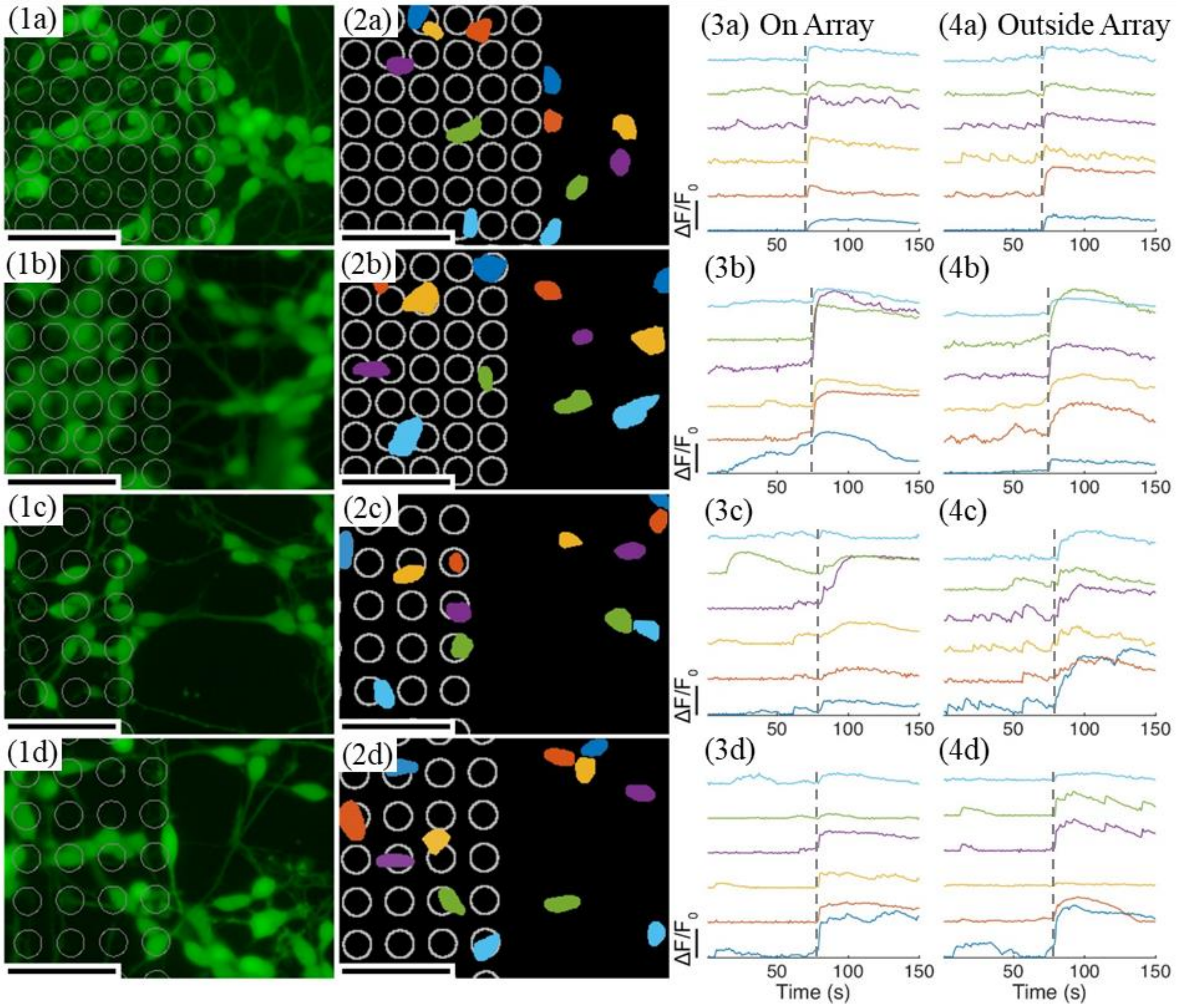

Figure 5.12 Viability test of hNT neurons on ZnO nanowires by measuring their response to the glutamate stimulation. (1) Fluo-4 (green) fluorescence images of hNT neurons inside and outside of the nanowire arrays. (2) The colour-coded neurons that were selected inside and outside of the nanowire arrays for tracing the changes in the intensity of the Fluo-4 fluorescence as responses to the glutamate stimulation. (3, 4) Fluo-4 fluorescence traces of neurons inside and outside of the nanowire arrays that were coloured with reference to the neurons shown in (2), respectively. The dashed lines indicate the glutamate stimulation time in (3, 4). (a–d) ZnO nanowire arrays were grown for 1, 2, 4, and 8 h, respectively. ZnO nanowire florets were outlined by white circles in (1–2) with scale-bars of 100 µm. (3–4) $\Delta F/F_0$ scale-bars = 0.2.

5.4 Conclusion

ZnO nanowires are demonstrated to be a biocompatible nanomaterial for human NTera2.D1 (hNT) neurons. The promotion and inhibition in growth of hNT neurons on ZnO nanowire arrays are shown to be influenced by both the geometry and the morphology of the nanowires. The ZnO nanowires are required to cover at least 4% of the substrate area for controlling the adhesion and growth of the neurons, either to promote or to inhibit. In this chapter, the growth of the hNT neurons on the ZnO nanowire arrays was increased by 30% compared to the control Si/SiO_2 substrate surface when ZnO nanowires with lengths of less 500 nm and densities of higher than 350 NWs/μm^2 were provided. The promotion of the hNT neuron growth demonstrated the biocompatibility of the ZnO nanowires and the favourable surface roughness for the neurons to reside.

Growing ZnO nanowires for a long time, 4–8 h, resulted in narrow and long nanowires (high aspect ratio) with a low density that reduced the adhesion and growth of the neurons on the entire nanowire arrays. The sparse and sharp nanowires can pierce the cell membrane and cause cell death. Furthermore, ZnO nanowires may also dissolve into Zn^{2+} ions in the culture media to reduce cell viability. Although Zn^{2+} ions are essential ions for many biological processes, an excessive concentration of Zn^{2+} that could be released from the large ZnO nanowires may be cytotoxic to the hNT neurons, causing cell death.

The increase of the inter-floret gaps reduces the ability of ZnO nanowire morphology for controlling the hNT neuron growth. However, the hNT neurons can be immobilised on the sparse nanowire florets due to the possible deformation of the cell membrane around the nanowires. The localisation of the hNT neurons on the ZnO nanowire florets can, therefore, be increased by providing a larger inter-floret gap within the array.

By tracing the fluorescence intensity of the hNT neurons, the cytoplasmic Ca^{2+} concentration of the neurons was increased after stimulation with glutamate. The hNT neurons are determined to be alive and functionally viable both inside and outside of all ZnO nanowire arrays. I propose that ZnO nanowires can be applied as a biocompatible nanomaterial on microelectrode arrays (MEAs) for interaction with human hNT neurons. The ZnO nanowires on the MEAs are ideally required to be short in lengths (i.e. < 500 nm for diameters of 30 nm) with a high density (i.e. ≥ 350 NWs/μm^2) to support the growth of hNT neurons. In the next chapter, the MEAs will be integrated with ZnO nanowires, and their electrochemical impedance will be investigated to characterise their electrical properties required for neuronal applications.

Chapter 6

ZnO Nanowire Microelectrode Arrays (ZnO-NW MEAs)

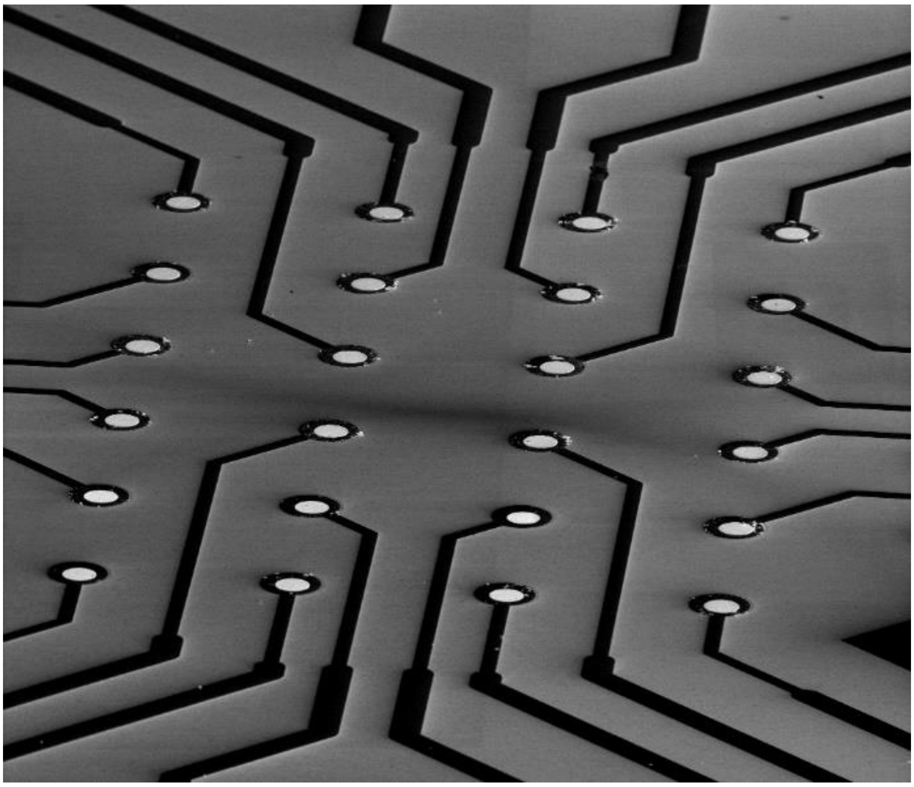

Fury roads to the ZnO towns for a mad neuroscientist to study neurons.

6.1 Introduction

Microelectrode arrays (MEAs) have conventionally been applied in recording electrical signals from neuronal cells to understand the communication and processing that take place within the neuronal networks [187]. Advances in neuroscience demand MEAs with small microelectrodes that can record electrical signals from neuronal cells at single-cell resolution. However, as the microelectrodes reduce in size, their electrical impedance increases proportionally to their surface area that degrades the signal-to-noise ratio (SNR) of the recording signals [25,90]. In this regard, researchers have made efforts to fabricate small MEAs comparable to the micrometre size of the neuronal cells [164] with low impedance

(< 2 MΩ) [188] that are capable of recording action potential (AP) signals with a high SNR at single-cell resolution.

Gold [17,21,29–32,69], platinum [65,71,72], titanium [33,74] are the most common materials that have been used as microelectrodes in MEAs due to their excellent electrical characteristics, corrosion resistance and biocompatibility. Platinum black (Pt black) coating has also been commonly applied by covering the planar microelectrodes of different materials through a platinisation process to reduce the impedance [21,58,64]. Similarly, conductive polymers such as polypyrrole (PPy) [189–191] and poly(3,4ethylenedioxythiophene) (PEDOT) [90,192,193] have been utilised as a coating layer to improve the electrical properties and biocompatibility of the MEAs. However, polymer microelectrodes can be mechanically unstable for long term neuronal applications [194,195].

While small planar surface areas are required for recording AP signals from neuronal cells at single-cell resolution, the SNR of the recording signals reduces with the microelectrode size due to the increased impedance. One way to keep the impedance of the microelectrodes low with small planar surface areas is to increase the total surface area by the introduction of 3D topological structures. 3D nanomaterials have previously been exploited to reduce the impedance of microelectrodes with Gold (Au) nanostructures [17,29–32], carbon nanotubes (CNTs) [33–35], vertical silicon nanowires (Si-NWs) [12,36,37], and vertical platinum nanowires (Pt-NWs) [15,38] being the most common nanomaterials that have been applied on MEAs to increase the surface area for integration with neuronal cells.

A more recent introduction to the nanowire technology for cell applications has been the introduction of vertical zinc oxide nanowires (ZnO-NWs), natural n-type semiconductors, commonly used in light-emitting diodes (LEDs) [39], solar cells [40–42], biosensors [43–45] and piezoelectric devices [46–48] due to their excellent electronic and photoelectronic properties. ZnO nanowires can be grown via a hydrothermal synthesis at a low temperature (at 95°C) with low cost and high scalability, as demonstrated in Chapter 4. Using the hydrothermal synthesis, ZnO nanowires can be grown on flexible substrates that are ideal for biological applications [43]. The morphology of ZnO nanowires can also be controlled by the hydrothermal growth parameters such as precursor concentration, growth time, ZnO seed layers, and additive polyethylenimine (PEI), as demonstrated in Chapter 4. Furthermore, Section 4.3 of Chapter 4 showed that ZnO nanowires could be grown on defined regions of a substrate using standard photolithography techniques [145]. In Chapter 5, ZnO nanowires were shown to be a suitable biocompatible nanomaterial for human NTera2.D1 (hNT) neurons; however; their biocompatibility could alter depending on the morphology and geometry of the nanowires. The short ZnO nanowires (< 500 nm for diameters of 30 nm) with a high density (> 350 NWs/µm^2) were also demonstrated as an ideal morphology that promoted the growth of hNT neurons.

Despite the great potential of ZnO nanowires for integration with MEAs in neuronal applications, Ryu *et al.* [49] are the only group that recently utilised MEAs with ZnO nanowires for recording neuronal signals from rat's brain *in vivo*. Ryu *et al.* also demonstrated that encapsulation of ZnO nanowires with Cr/Au and PEDOT layers could improve their electrical characteristics as well as their biocompatibility. The impedance of MEAs can also be influenced by the morphology of the nanomaterials, as Nick *et al.* [29] demonstrated improved impedance of MEAs when high aspect ratio gold nanopillars were used.

In this chapter, the electrical characteristics of MEAs in different configurations are investigated to define their electrical compatibility for neuronal applications. The electrical properties of MEAs are characterised by electrochemical impedance spectroscopy (EIS). To do so, planar MEAs are initially fabricated and characterised as a benchmark to identify any improvement in the electrical properties of the nanostructured MEAs. The electrochemical impedance of MEAs with ZnO nanowires in different morphology is then investigated, using a modified Randles equivalent circuit. Finally, the impedance of MEAs is studied when ZnO nanowires are encapsulated with different metals (Cr/Au, Ti, and Pt). In addition to the electrical characteristics, the robustness of ZnO nanowires and metal encapsulated ZnO nanowires are investigated to determine their compatibility for long term measurements in neuronal applications. The work presented in this chapter is drown from the paper "Ti and Pt encapsulated ZnO nanowire microelectrodes for neural applications" by Mohsen Maddah, Yi Wang, Gideon J. Gouws, Charles P. Unsworth, and Natalie O. V. Plank that has recently been submitted. The co-authors of this work have advised and commented on the manuscript of the paper, but the thesis author has done all the experimental work and analysis.

6.2 Planar MEAs

In this section, the electrical properties of planar MEAs are investigated through EIS measurements. Planar MEAs were fabricated using a standard photolithography technique, as detailed in Section 3.2.5.1 of Chapter 3. MEAs were fabricated on 15 mm × 15 mm silicon substrates with a 100 nm oxide layer (Si/SiO_2). The substrates were initially cleaned thoroughly by sonication in acetone (1 minute), sonication in isopropanol (IPA) (1 minute), rinsing in IPA and then drying in a stream of clean nitrogen (N_2). Standard photolithography was applied to define a pattern of AZ1518 photoresist on the substrates. Electrodes were deposited via thermal evaporation of 5 nm chrome followed by 50 nm of gold (Cr/Au) onto the Si/SiO_2 substrates. A lift-process was then applied using acetone and IPA to remove photoresist with the excessive Cr/Au, leaving a pattern of Cr/Au electrodes with central working microelectrodes (200 µm in diameters) on the substrates to create planar MEAs. The fabrication of planar MEAs was completed by photolithography of 8 µm thick SU8-2150 as a passivation layer. The SU8 layer covered the entire substrate except for the regions above the working microelectrodes (with diameters of 50 µm) and the outer electrode contact pads to allow for the electrical measurements. The samples were finally hard-baked at 200°C for 15 minutes to heal any surface cracks of the SU8 layer and to improve the chemical and physical stability of the SU8 layer.

6.2.1 MEA configuration

Figure 6.1 (a) shows an optical image of a fabricated planar MEA. The fabricated planar MEA was comprised of 32 Cr/Au working microelectrodes and one reference electrode on the Si/SiO_2 substrate. The central working microelectrodes were placed in a 6 × 6 matrix within an area of $4 \times 4\ mm^2$, which were connected to the outer electrode contact pads, as shown in Figure 6.1 (b). The microelectrodes were 200 µm in diameters with spacings of 700 µm in between. Figure 6.1 (c) and (d) show a planar microelectrode before and after the SU8 photolithography process, respectively. The SU8 photolithography defined 50 µm wide open windows concentric with the central microelectrodes for EIS measurements.

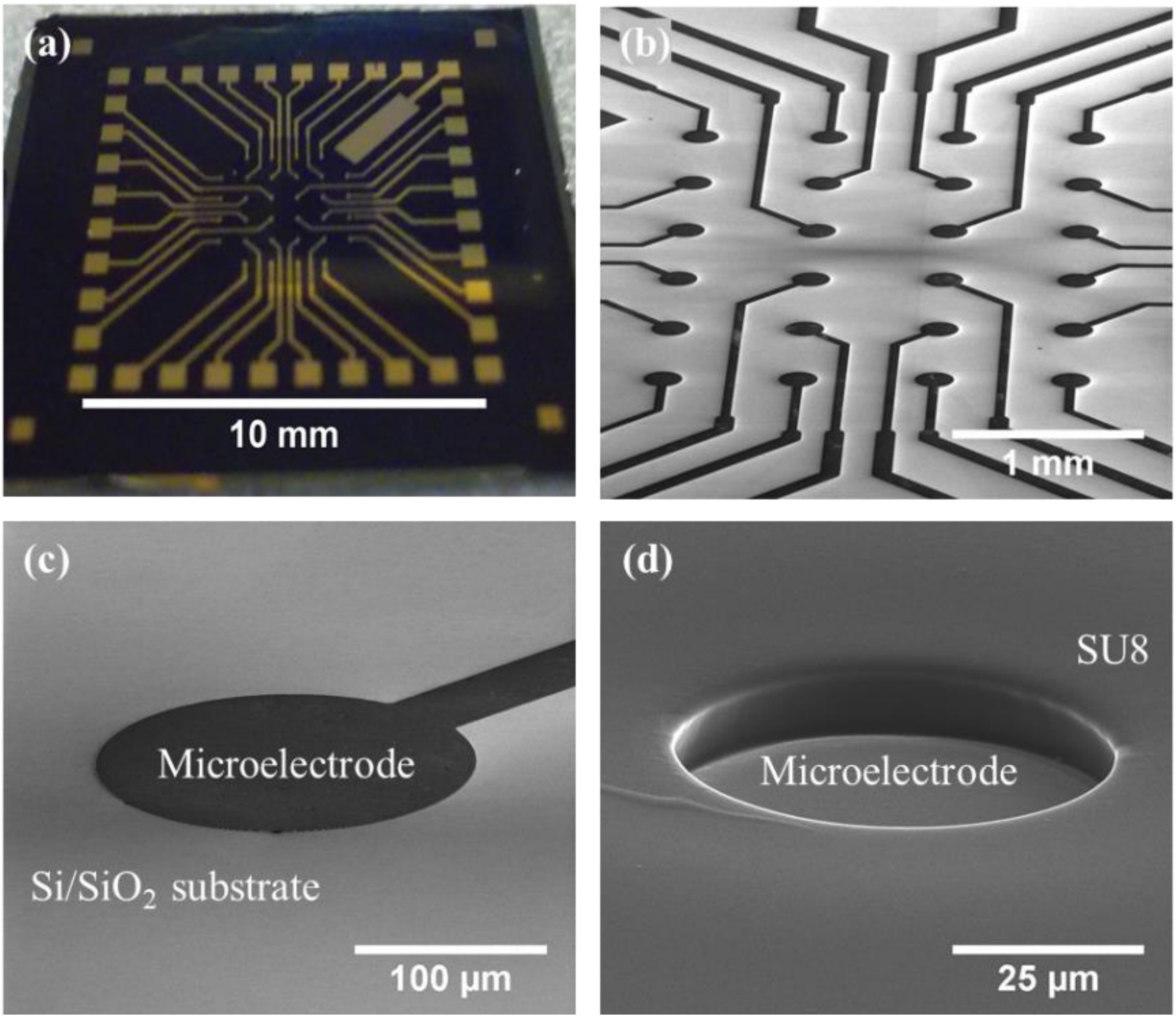

Figure 6.1. Planar microelectrode array. (a) and (b) show optical image and SEM image of a fabricated planar MEA without SU8 passivation layer, respectively. (c) and (d) show SEM images of a planar microelectrode before and after SU8 photolithography process, respectively. SEM images were taken at 70° tilted view.

6.2.2 EIS of planar MEAs

Electrochemical impedance spectroscopy of the MEAs was measured using the Agilent 4294A precision impedance analyser in the configuration shown in Figure 6.2. A frame made of polydimethylsiloxane (PDMS) was used to keep 100 µL of the phosphate-buffered saline solution (PBS-1x) on the central region of the MEA excluding the outer electrode contact pads. The high potential and current terminals of the impedance analyser were connected to a tungsten electrode probe and placed in the PBS solution. The low potential and current terminals were connected to the MEA electrode contact pads using a tungsten electrode probe. A potential of 100 mV (with 0 V_{bias}) was applied at high terminals by sweeping over a frequency range of 40 Hz to 10 MHz, and the impedance was recorded at the low terminals.

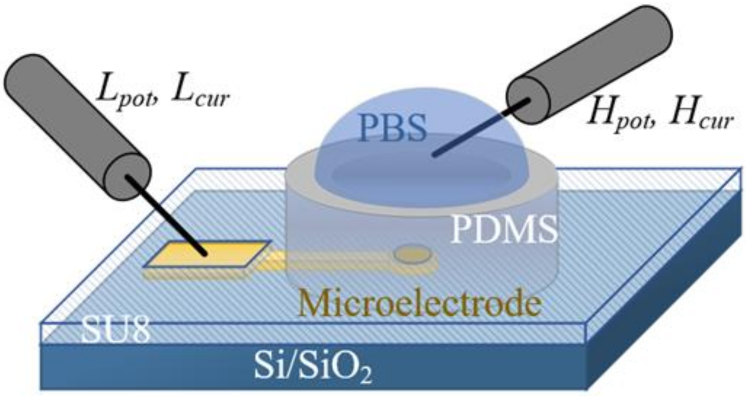

Figure 6.2. Measurement setup for the electrochemical impedance spectroscopy of MEAs. Two-point measurement connection, where H_{pot} and H_{cur} represent the high potential and current terminals of the instrument connected to a tungsten electrode probe placed in phosphate-buffered saline solution (PBS-1x), and L_{pot} and L_{cur} represent the low potential and current terminals of the instrument connected to a tungsten electrode probe attached to the outer electrode contact pad of MEA.

The EIS measurements included the impedance of the MEA as well as all auxiliary connections used between the impedance analyser terminals and the MEA, e.g. coax cables, adapters, probe electrodes and the PBS solution. An open/short compensation was applied to correct the impedance measurements, defining the true characteristics of the MEAs. The open-circuit impedance was measured by opening the circuit at the electrode probe ends. The short-circuit impedance was measured by placing both electrode probes in the PBS solution. The corrected impedance was calculated by

$$Z_{MEA} = \frac{Z_M - Z_S}{Z_O - Z_M} Z_O \qquad \text{Equation 6.1}$$

where Z_{MEA} is the true impedance of the MEA, Z_M is the measured impedance of the MEA, Z_O is the impedance of the open-circuit and Z_S is the impedance of the short-circuit. All of the impedance data presented in this work are the average impedance measurements taken from more than 20 microelectrodes ($n > 20$) on multiple samples with the same microelectrode configuration. The measurements have all been corrected by applying the open/short compensation described above.

Figure 6.3 (a) and (b) show the electrochemical impedance Bode plots, impedance magnitude and phase vs frequency, of planar MEAs that were averaged over multiple samples with the same microelectrode configuration, respectively. The impedance of the MEAs before and after the open/short compensation were presented in Figure 6.3. Figure 6.3 also shows the impedance of the open-circuit and the short-circuit that were used for the open/short compensation procedure. The open-circuit impedance magnitude was measured to be 20 GΩ that decreased to 5 MΩ as the frequency increased from 40 Hz to 10 MHz. The impedance phase of the open-circuit was determined to alter within −90° to 90°, particularly for the frequencies below 10 kHz, since an auto-balancing bridge method was used in the Agilent 4294A precision impedance analyser. The measured short-circuit had an impedance magnitude of 10 kΩ that decreased to 300 Ω as the frequency increased from 40 Hz to 10 MHz. The impedance phase of the short-circuit was at −60° at 40 Hz that increased to 30° at 10 MHz. The short-circuit impedance represented the impedance of the auxiliary connections and the PBS solution that were used in the EIS measurement of MEAs.

Figure 6.3 (a) shows that the impedance magnitude of the planar MEA decreased with increasing frequency from 40 Hz to 10 MHz. The impedance phase was determined to be stable at about −90° (capacitive behaviour) for the frequency range of 40 Hz to 100 kHz, as shown in Figure 6.3 (b). Increasing the frequency beyond 100 kHz resulted in the measured impedance phase to increase to 0° (ohmic behaviour), however, due to the applied open/short compensation the true phase of the planar MEA reached a maximum of −70° at 2 MHz. The transition of the impedance behaviour from capacitive to ohmic at high frequencies was, therefore, determined as an influence of the auxiliary connections or the PBS solution, not the characteristics of the MEAs.

A frequency of 1 kHz has commonly been used in neuronal applications [25,90], as neuronal action potentials typically take place at this frequency. Therefore, it is useful to investigate the electrical characteristics of different MEAs by comparing their impedance at a frequency of 1 kHz. Ganji *et al.* [90] previously determined that the impedance of MEAs substantially varied from 1 kΩ to 1 MΩ as the diameter of planar gold electrodes decreased from 2 mm to 20 µm. In this thesis, the fabricated planar MEAs were measured to have an average impedance magnitude of 835 ± 40 kΩ with a phase of −89° ± 0.5° at the frequency of 1 kHz. The measured impedance is slightly higher than the average impedance of 500 kΩ that Ganji *et al.* [90] measured for 50 µm wide gold microelectrodes, but lower than 1.17 ± 0.24 MΩ that Nick *et al.* [29] measured for 40 µm wide gold microelectrodes. Furthermore, Ganji *et al.* [90] determined that the microelectrodes with diameters smaller than 100 µm have capacitive-like behaviour with a phase spectra close to −90° for the frequency range of 1 Hz to 10 kHz that agrees with the measured impedance phase in this work.

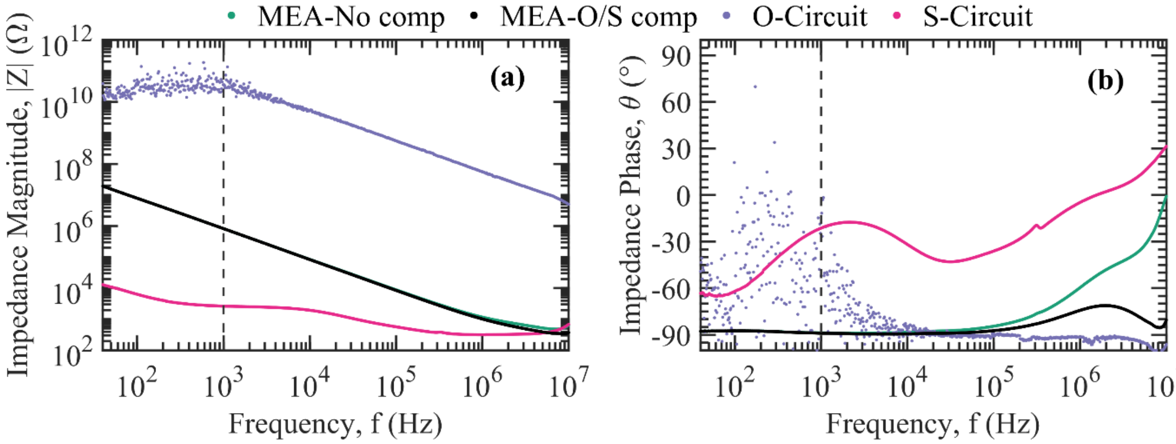

Figure 6.3. Electrochemical impedance spectroscopy Bode plots (a) impedance magnitude vs frequency and (b) impedance phase vs frequency of planar MEAs. The average impedance of planar MEAs before and after the open/short compensation are indicated by 'MEA-No comp' and 'MEA-O/S comp', respectively. The measured impedance of the open-circuit 'O-Circuit' and the short-circuit 'S-Circuit' that were used for the open/short compensation are also plotted in (a) and (b). Dashed lines indicate the frequency of 1 kHz.

6.3 ZnO-NW MEAs

MEAs with ZnO nanowires were then fabricated by directly growing the ZnO nanowires onto the planar MEAs without SU8 passivation layer, as detailed in Section 3.2.5.2 of Chapter 3. Photolithography was carried out using AZ1518 photoresist to define a circular gap with a diameter of 100 µm concentric with the central working microelectrodes. A 100 nm thick ZnO seed layer was then deposited by sputter deposition followed by a lift-off process to leave ZnO seeds on the central working microelectrodes. Further photolithography was then carried out using AZ5214E photoresist to define a pattern with 200 µm wide open areas concentric with the pre-deposited ZnO seeds. The hydrothermal synthesis was carried out at 95°C to grow ZnO nanowires from the pre-deposited ZnO seed layers, as described in Chapter 4 [145]. The morphology of the ZnO nanowires was controlled by varying the equimolar concentration of the zinc nitrate hexahydrate and hexamethylenetetramine (HMT) precursors within the range of 2.5–100 mM for 4 h of growth time. The growth of nanowires with high aspect ratios was controlled through the addition of 6 mM polyethylenimine (PEI, Mw = 800 g/mol) as an auxiliary precursor to the "standard" 25 mM of precursors for various growth time within the range of 4–35 h. Post nanowire growth lift-off was carried out via immersion in n-methyl-2-pyrrolidinone (NMP) for 2 h followed by 2 minutes sonication in NMP, 2 minutes sonication in IPA, rinsing in IPA and drying with N_2. The SU8 passivation layer was then applied by a photolithography process to open a 50 µm wide circular window concentric with the ZnO nanowire microelectrodes. The SU8 passivation layer allowed only ZnO nanowires of the microelectrodes to be exposed to the electrolyte solution during the electrochemical impedance characterisation.

6.3.1 ZnO-NW morphology

Figure 6.4 (a) and (b) show SEM images of ZnO nanowires that were grown on MEAs by using 2.5 mM and 100 mM precursor concentrations for 4 h of growth, respectively. Increasing the precursor concentration is shown to increase the nanowire diameter and length while their density decreased, agreeing with the previous work demonstrated in Section 4.2.1 of Chapter 4 [145]. The nanowires were also demonstrated to have a flat top surface for the high precursor concentration compared to the tapered nanowires for the low concentration. Figure 6.4 (c) and (d) show SEM images of ZnO nanowires that were grown by using 25 mM of precursor concentration with 6 mM of PEI for 4 h and 35 h of growth time, respectively. The addition of PEI to the growth solution allowed mediation of the precursors within the hydrothermal growth solution and extended the active growth time compared to the standard growth without PEI. The ZnO nanowires were subsequently grown with high aspect ratios, as previously demonstrated in Section 4.2.3 of Chapter 4. The PEI molecules attached to the lateral faces of the nanowires that confined their radial growth and enhanced the axial growth over time [106,131]. As a result, nanowires grew longer when the growth time increased with PEI presented during the growth, in contrast to the growth without PEI that resulted in the nanowires to grow thicker and longer. The density of the nanowires also reduced as the nanowires grew for a longer time, agreeing with the results shown in Section 4.2.3 of Chapter 4.

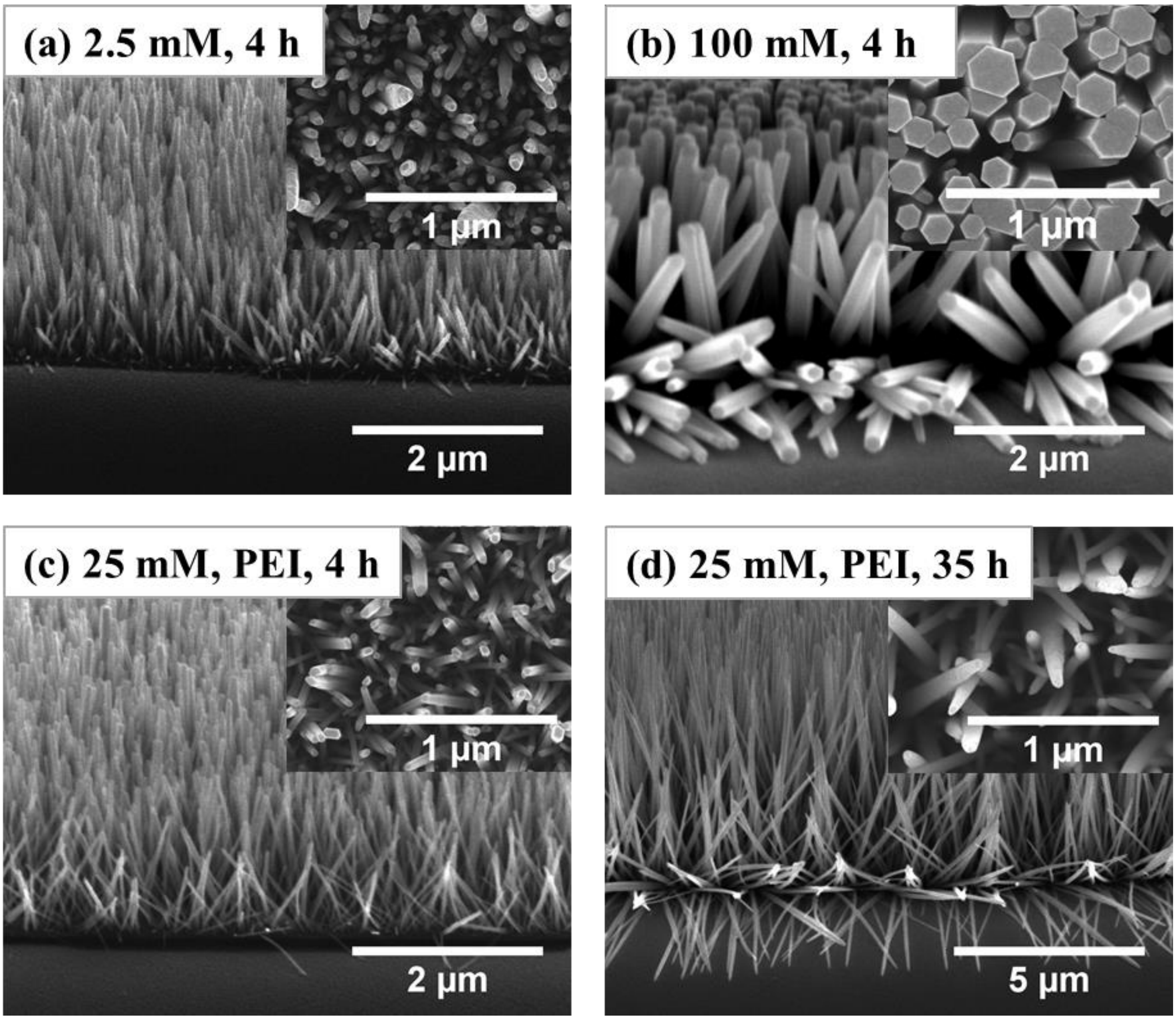

Figure 6.4. SEM images of ZnO nanowires grown on Cr/Au MEAs via the hydrothermal synthesis with varying growth parameters: ZnO nanowires were grown with equimolar precursor concentration of (a) 2.5 mM for 4 h, (b) 100 mM for 4 h, (c) 25 mM with 6 mM of PEI for 4 h and (d) 25 mM with 6 mM of PEI for 35 h. The SEM images of nanowires were taken at 70° tilted view and top view (insets).

Figure 6.5 (a)–(d) plot diameter, length, aspect ratio and density of the ZnO nanowires, respectively, that were grown on MEAs by either varying zinc nitrate hexahydrate and HMT concentrations for 4 h of growth or by varying the growth time when 25 mM of precursor concentration with 6 mM of PEI was used. The aspect ratio of the nanowires was calculated as the ratio of the measured nanowire length to the diameter from the SEM images. The density of the nanowires was estimated by counting the number of nanowires within an area of 2–4 µm^2 of the SEM images from the top view.

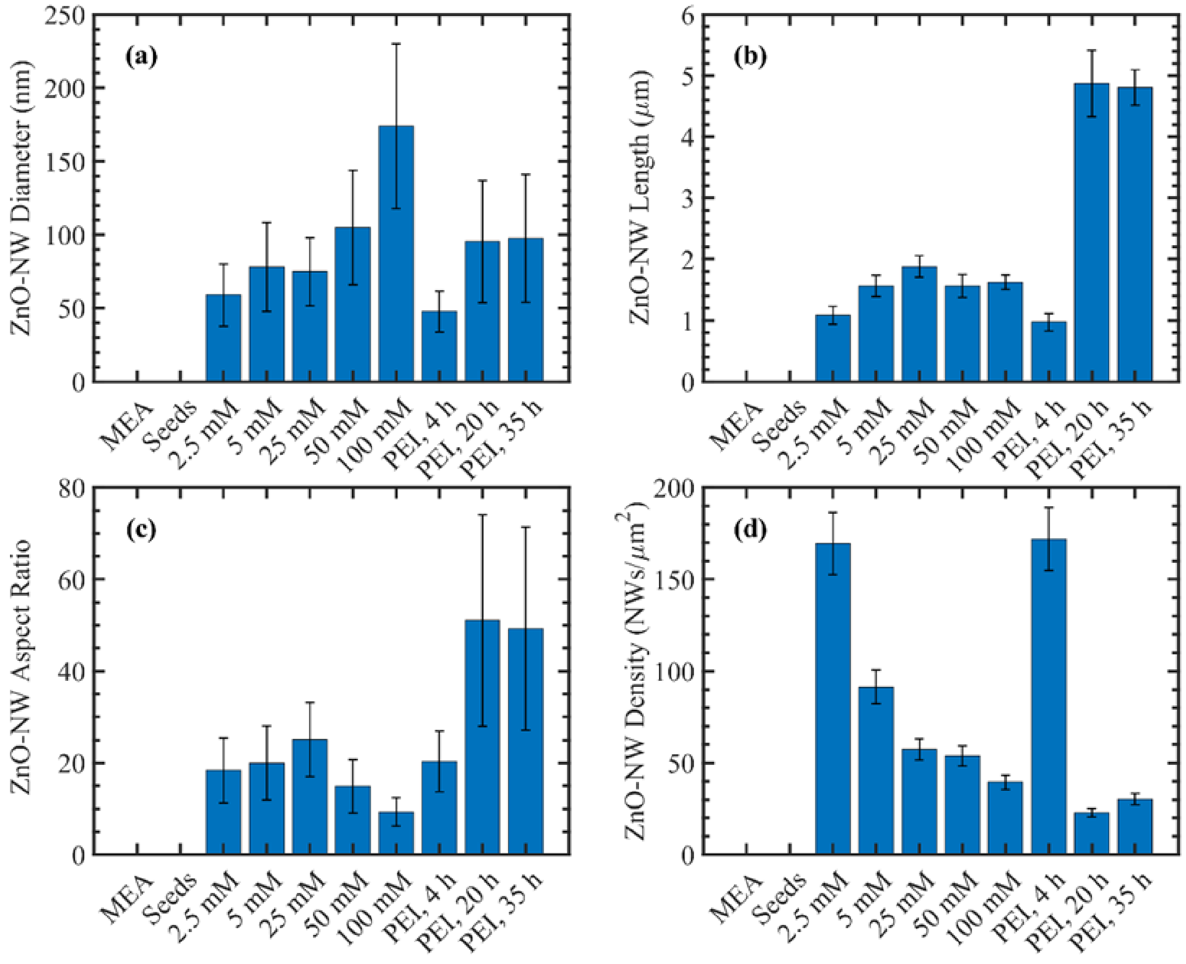

Figure 6.5. Morphological graphs of ZnO nanowires grown on MEAs, measured as nanowire (a) diameter, (b) length, (c) aspect ratio, and (d) density. The aspect ratios were calculated from data plotted in (a) and (b). Error bars represent one standard deviation (*n* > 30 NWs).

Varying the precursor concentration from 2.5 mM to 100 mM increased the nanowire diameter from 60 ± 20 nm to 175 ± 55 nm and decreased the density from 170 ± 17 NWs/μm^2 to 40 ± 4 NWs/μm^2. The nanowire length varied within the range of 1–2 μm for different precursor concentrations, with a maximum of 1.88 ± 0.18 μm at the precursor concentration of 25 mM. Subsequently, the aspect ratio of the nanowires was at its maximum of 25 ± 8 when 25 mM of precursor concentration was used for 4 h of growth time.

Adding 6 mM of PEI to the growth solution reduced the growth rate of the ZnO nanowires. When 6 mM of PEI was added to 25 mM of precursor concentration for 4 h of growth, the nanowire diameter and length reduced from 75 ± 23 nm to 48 ± 14 nm and from 1.88 ± 0.18 μm to 0.97 ± 0.14 μm, respectively. The density of the nanowires also increased from 57 ± 6 NWs/μm^2 without PEI to 172 ± 17 NWs/μm^2 with PEI. Increasing the growth time from 4 h to 35 h significantly increased the nanowire length by a factor of 5×, from

0.97 ± 0.14 µm to 4.8 ± 0.3 µm, and doubled the aspect ratio from 20 ± 7 to 49 ± 22. The diameter of the nanowires also increased from 48 ± 14 nm to 98 ± 43 nm while the density reduced by a factor of 6, from 172 ± 17 NWs/µm^2 to 30 ± 3 NWs/µm^2.

6.3.2 EIS of ZnO-NW MEAs

The ZnO nanowires were hydrothermally grown from a pre-deposited ZnO seed layer island on the microelectrodes, as shown in Figure 6.6 (a). The nanowires grew vertically from the seed layer with some residual scattered nanowires that either grew elsewhere on the microelectrodes or nucleated in the growth solution and were deposited onto the outer microelectrode area during removal from the growth solution. The MEAs were enclosed within an 8 µm thick layer of SU8, as shown in Figure 6.6 (b), to ensure that only the vertical nanowires within a 50 µm defined window contributed to the EIS measurements.

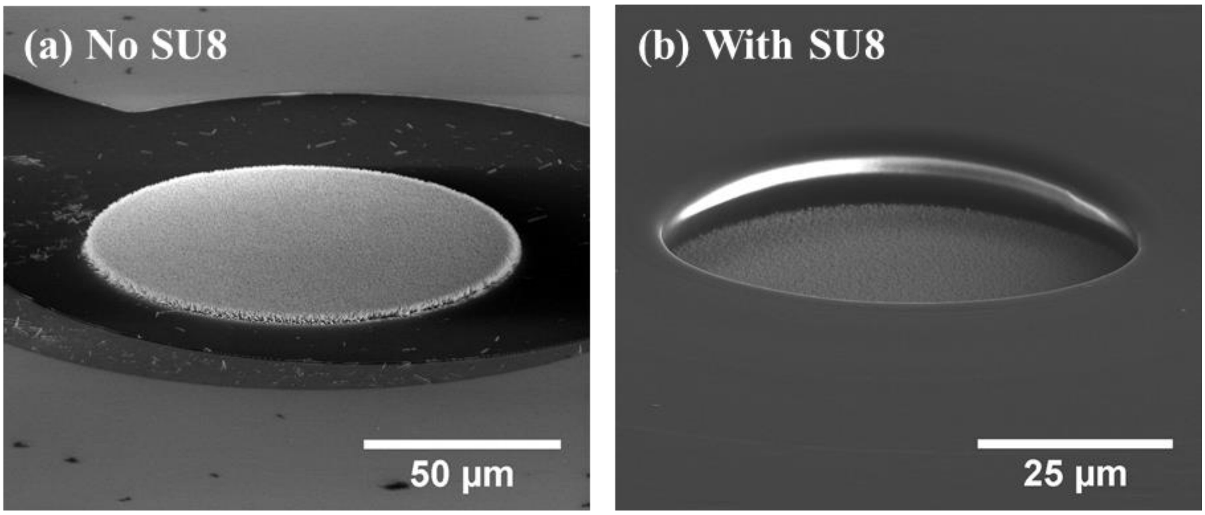

Figure 6.6. ZnO nanowire microelectrode before and after SU8 photolithography. (a) The SEM image of ZnO nanowires that were grown as an island on a microelectrode with a pre-deposited ZnO seed layer. ZnO nanowires were hydrothermally grown using a precursor concentration of 25 mM and growth time of 4 h. (b) The SEM image shows successful photolithography of SU8 passivation layer with 50 µm wide open window. The SEM images were taken at 70° tilted view.

Figure 6.7 shows the SEM image and energy-dispersive X-ray spectroscopy (EDS) of a ZnO-NW microelectrode with the SU8 passivation layer. The EDS shows silicon (Si) of the Si/SiO_2 substrate and gold (Au) of the deposited Cr/Au microelectrode in Figure 6.7 (b) and (c), respectively. The microelectrodes were 200 µm in diameter that attributed to the appearance of gold everywhere within the Figure 6.7 (c) window. Zinc (Zn) and oxygen (O) of ZnO nanowires are shown in Figure 6.7 (d) and (e), respectively, although oxygen also attributed to the Si/SiO_2 substrate. Figure 6.7 (c) shows carbon (C) mapping on the MEA that defined the successful photolithography patterning of the SU8 passivation layer on the ZnO-NW microelectrode without any defects or debris. The SU8 passivation layer ensured that only the ZnO nanowires of the microelectrodes were exposed to the electrolyte solution during the EIS measurements.

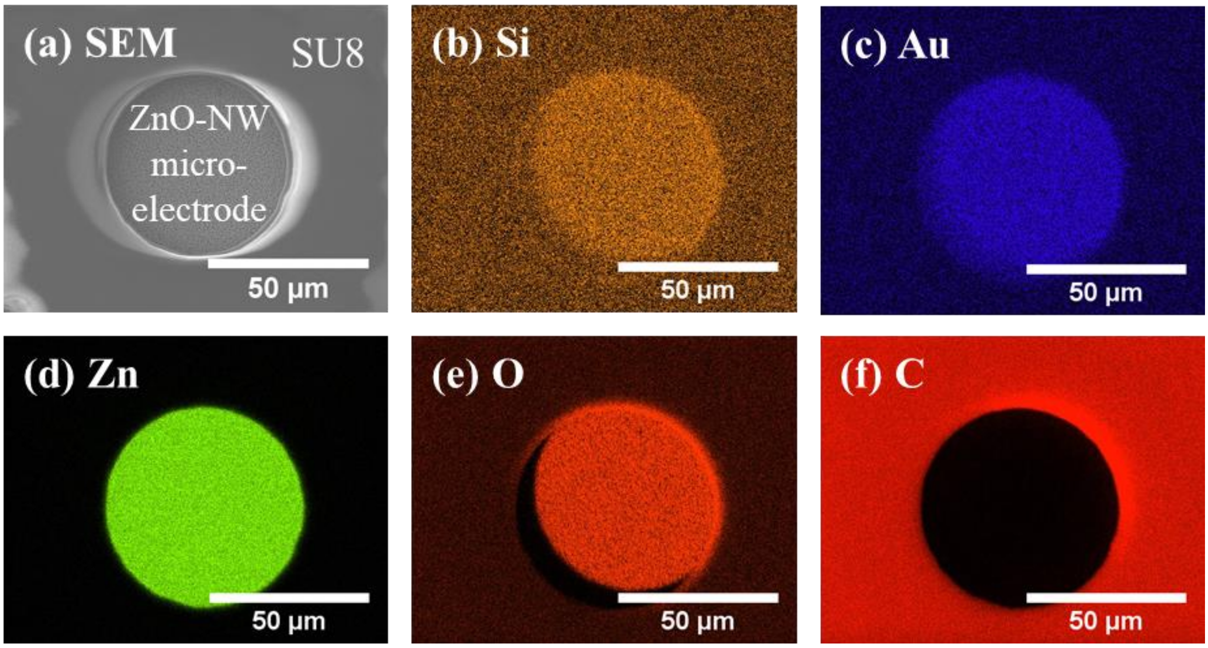

Figure 6.7. SEM and Energy-dispersive X-ray spectroscopy (EDS) of ZnO nanowire microelectrode. (a) SEM image of a ZnO-NW microelectrode enclosed with the SU8 passivation layer. (b)–(f) EDS mapping of the ZnO-NW microelectrode shown in (a). The EDS mapping shows (b) silicon (Si) of the Si/SiO_2 substrate; (c) gold (Au) of the underlying Cr/Au microelectrode; (d) zinc (Zn) of ZnO nanowires; (e) oxygen (O) of ZnO nanowires and the Si/SiO_2 substrate; and (f) carbon (C) of the SU8 passivation layer.

The EIS Bode plots of MEAs with ZnO nanowires in different morphologies are shown in Figure 6.8 (a)–(d). Figure 6.8 (a) and (b) show the impedance magnitude and phase of MEAs for a broad range of frequency, 40 Hz–10 MHz, respectively. Figure 6.8 (c) and (d) show the impedance magnitude and phase of MEAs at low frequencies, 40 Hz–2 kHz in linear scale, respectively, where neuronal action potential signals typically take place [25,51]. Figure 6.8 (a) shows that the impedance magnitude of all MEAs decreased with increasing frequency. Figure 6.8 (b) shows that the impedance phase of all MEAs generally remained constant around −90° for the frequency of lower than 100 kHz, corresponding to the capacitive behaviour of the MEAs. The dominant capacitive behaviour indicates that the impedance is significantly influenced by the surface areas of the microelectrodes that are exposed to the electrolyte. Hence, variation in the microelectrode surface area as done by controlling the ZnO nanowire morphology is the reason that changed the impedance of the MEAs. Furthermore, texturising the nanowire surface can improve the impedance of the microelectrodes by increasing the total surface area.

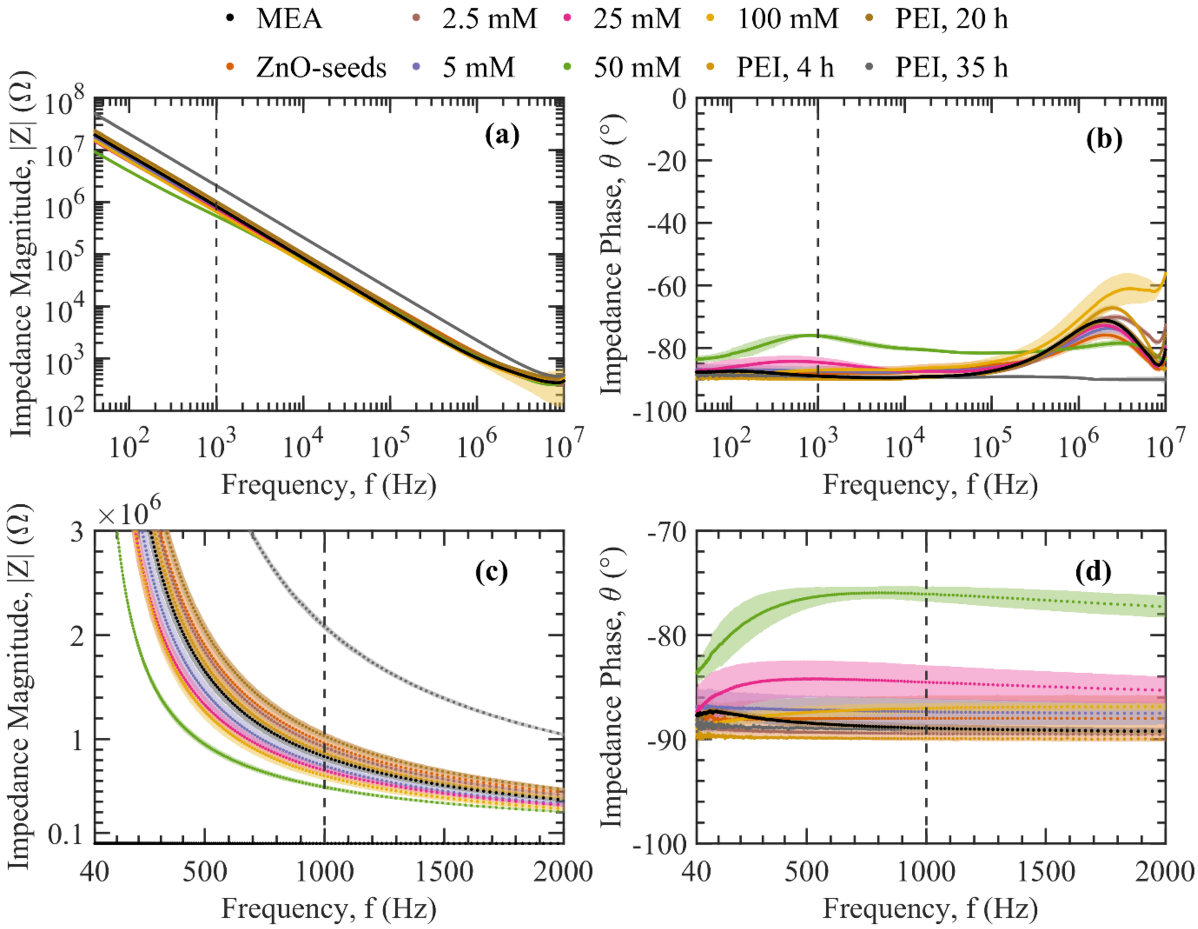

Figure 6.8. Electrochemical impedance spectroscopy of MEAs with ZnO nanowires that vary in morphology compared to the planar MEAs. (a) and (b) plot the average impedance magnitude and phase of MEAs for the frequency of 40 Hz–10 MHz in logarithmic scale, respectively. (c) and (d) plot the average impedance magnitude and phase of MEAs for the frequency of 40 Hz–2 kHz in linear scale, respectively. The dashed lines presented in (a)–(d) indicate the frequency of 1 kHz. The ZnO nanowires were hydrothermally grown with varying precursor concentration within the range of 2.5–100 mM for a growth time of 4 h, or with varying growth time within the range of 4–35 h for 25 mM of precursor concentration and 6 mM of PEI. Error shades represent one standard deviation ($n > 20$ microelectrodes).

The impedance of the MEAs with ZnO nanowires varied with the morphology of the nanowires where it was seen to be lower, the same, or even higher than the impedance of the planar MEAs. The variation of the impedance magnitude for ZnO-NW MEAs with different morphologies was more evident at low frequencies, as shown in Figure 6.8 (c). The MEAs with ZnO nanowires that were grown by using a precursor concentration of 50 mM for 4 h of growth improved the impedance the most by reducing the impedance magnitude. In contrast, the MEAs with ZnO nanowires that were grown by using 25 mM of precursor concentration with 6 mM of PEI for 35 h increased the impedance magnitude.

The 1 kHz impedance magnitude and phase of MEAs with different morphologies of ZnO nanowires are plotted in Figure 6.9 (a) and (b), respectively. Applying a 100 nm thick layer of ZnO seeds on MEAs resulted in a slight increase of the 1 kHz impedance magnitude, 965 ± 100 kΩ, compared to 835 ± 40 kΩ of planar Cr/Au MEAs. Growing ZnO nanowires on the seeds, using precursor concentrations within the range of 2.5–100 mM for 4 h of growth reduced the impedance magnitude, at which a minimum impedance of 540 ± 20 kΩ was achieved for the precursor concentration of 50 mM. The 50 mM nanowires were determined to have an average diameter of 105 ± 40 nm, length of 1.56 ± 0.18 µm, aspect ratio of 15 ± 6 and density of 54 ± 5 NWs/µm^2. The overall surface area (S) of the microelectrode with ZnO nanowires was calculated by

$$S = (\frac{1}{4} D^2 + D\ L)\ \sigma_{NWs}\ \pi^2\ R^2 \qquad \text{Equation 6.2}$$

where D and L were the diameter and length of the nanowires, respectively, σ_{NWs} was the density of the nanowires, and R was the radius of the hole (25 µm) in the SU8 passivation layer concentric with the ZnO-NW microelectrode. The overall surface area was increased by a factor of 28×, to 55,320 ± 29,750 µm^2, compared to the average surface area of 1,960 µm^2 for the planar MEAs. Furthermore, an average impedance phase of −88° ± 2° at the frequency of 1 kHz was measured for all MEAs, except the 50 mM ZnO-NW MEA with a phase of −76° ± 1°, showing that the capacitive behaviour as affected by the surface area was dominant in the electrochemical characteristics of the MEAs.

The addition of 6 mM PEI into the growth solution for 4 h of growth resulted in an increase of the impedance to 870 ± 35 kΩ, in comparison to 700 ± 40 kΩ of the 25 mM ZnO nanowires with no PEI. The PEI addition has caused the nanowires to grow smaller and shorter since PEI molecules slowed the growth rate of the ZnO nanowires by chelating Zn^{2+} ions in the growth solution [131]. The diameter and length of ZnO nanowires were reduced from 75 ± 23 nm and 1.88 ± 0.18 µm of no PEI to 48 ± 14 nm and 970 ± 140 nm with additive PEI, respectively. The density of the nanowires was also increased from

57 ± 6 NWs/μm^2 to 172 ± 17 NWs/μm^2 by adding PEI to the growth solution. Although, the overall surface area was similar for the nanowires grown with and without PEI, 49,820 ± 22,170 μm^2 and 50,400 ± 22,730 μm^2, respectively, the impedance of MEAs was found to be different. The high impedance of PEI nanowires could be associated to the PEI molecules that were attached to the lateral surfaces of the nanowires during the hydrothermal growth and had possibly changed the electrochemical characteristics of the nanowire surfaces.

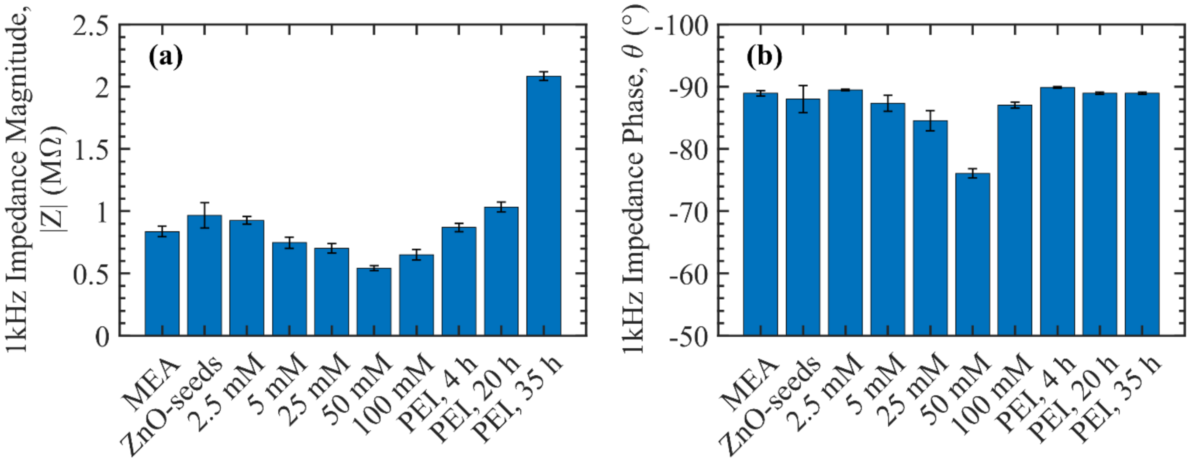

Figure 6.9. Impedance magnitude (a) and phase (b) at the frequency of 1 kHz for MEAs with ZnO nanowires in various morphology. ZnO nanowires were grown with varying precursor concentration for 4 h of growth, or with varying growth time when 25 mM of precursor and 6 mM of PEI were applied. Error bars represent one standard deviation (n > 20 microelectrodes).

PEI is a nonpolar polymer with side amino-groups ($-NH_2$), which can be protonated and positively charged [107,196]. The positively charged PEI were adsorbed to the negatively charged lateral surfaces of the ZnO nanowires that could partially passivate the surface states [196]. The passivation layer on the ZnO nanowires could subsequently increase the total impedance of ZnO-NW MEAs as the electrochemical charge transfer that took place at the surface of the nanowires was limited. However, the effect of different passivation layers such as polymethyl methacrylate (PMMA) [197], tin oxide (SnO_2) [198], aluminium oxide (Al_2O_3) and hydrogen (H) [199] were previously demonstrated to change the optical and electrical properties of the ZnO nanowires, no studies have been taken yet on characterisation of the ZnO nanowires with PEI as the passivation layer.

As the ZnO nanowires were grown with additive PEI for a longer time, the impedance continued to increase, reaching a maximum of 2.085 ± 0.035 MΩ for 35 h of growth. Despite the increase of the nanowire overall surface area from 49,820 ± 22,170 µm^2 at 4 h of growth to 88,130 ± 54,670 µm^2 at 35 h of growth, the impedance has unexpectedly increased to become even larger than the impedance of the planar Cr/Au MEAs, 835 ± 40 kΩ. Increasing the growth time from 4 h to 35 h resulted in the length of the nanowires to significantly increase by a factor of 5× and reduce the density by a factor of 6, while the diameter only doubled, as discussed in Section 6.3.1. Subsequently, the total top surface area of the nanowires (not including the lateral surfaces) reduced from 605 ± 255 µm^2 of 4 h to 445 ± 285 µm^2 of 35 h. These results show the possibility of the PEI behaving as a passivation layer at the lateral faces of the ZnO nanowires, which can limit the electrochemical conduction paths from the solution to the nanowire surfaces. The PEI was expected to reduce the impedance of the microelectrodes by growing ZnO nanowires with high surface areas and aspect ratios, but the EIS results showed that the PEI increased the impedance of microelectrodes. Although these MEAs with PEI ZnO nanowires can still be useful for AP signal recording as they have previously been shown in Chapter 5 to be biocompatible with human hNT neurons, they are not ideally optimised due to their electrical properties.

6.3.3 EIS modelling of ZnO nanowire MEAs

The electrochemical impedance of MEAs was examined by using a modified Randles equivalent circuit model [90,200,201], as shown in Figure 6.10. The equivalent circuit comprised series resistor (R_s), charge transfer resistor (R_{ct}), adsorption capacitor (C_{ad}), and constant phase element (CPE). The series resistor (R_s) represented all series resistance in the measurement, including the resistance of the auxiliary connections, PBS solution, and underlying metal electrodes. The charge transfer resistance (R_{ct}) or the redox reaction resistance represented the resistance for the charges transferring from the solution to the microelectrode surface. The adsorption capacitor (C_{ad}) accounted for the adsorption of the transferred species through the double-layer interface onto the microelectrode surface that participated in the redox reaction. The faradaic impedance, Z_f, was defined as a series combination of the charge transfer resistance and the adsorption capacitance by

$$Z_f = R_{ct} + jX_{Cad} \qquad \text{Equation 6.3}$$

where X_{Cad} was the reactance associated with the adsorption capacitance. The reactance of the adsorption capacitance was calculated by

$$X_{Cad} = \frac{1}{2\pi f C_{ad}} \qquad \text{Equation 6.4}$$

where f was the signal frequency used in the EIS. The constant phase element (*CPE*) accounted for the double-layer capacitance at the interface of the microelectrode and the electrolyte solution that behaved as a non-faradaic pseudo-capacitance. The reactance of the *CPE* was defined as

$$X_{CPE} = \frac{1}{Q\,(2\pi f)^{\alpha}} \qquad \text{Equation 6.5}$$

where α was the constant exponent, $0 \leq \alpha \leq 1$, with 1 representing an ideal capacitor and 0 representing an ideal resistor, and Q was a constant coefficient with the unit of $\mathrm{F{\cdot}cm^{-2}{\cdot}s^{n-1}}$ that represented the double-layer capacitance at the angular frequency of 1 rad/s.

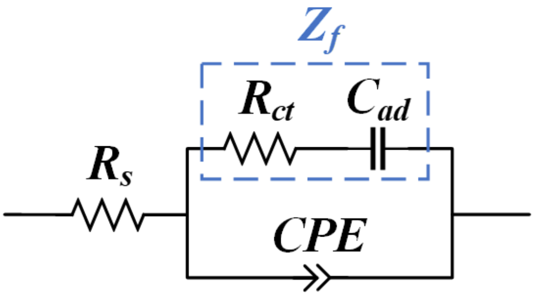

Figure 6.10. Modified Randles equivalent circuit model of MEAs for electrochemical impedance simulation. The equivalent circuit comprises series resistor (R_s), charge transfer resistor (R_{ct}), adsorption capacitor (C_{ad}), and constant phase element (*CPE*). Z_f represents the faradaic impedance of the circuit as a series combination of R_{ct} and C_{ad} impedance.

The obtained impedance of MEAs was fitted to the equivalent circuit by using the Palmsens PSTrace software to extract the electrochemical parameters of the MEA impedance. A Chi-Squared test was applied to evaluate the goodness of the fit, ensuring that the average error of the fit was less than 1%. Figure 6.11 (a)–(d) shows the charge transfer resistance, the adsorption capacitance, 1 kHz faradaic impedance, and 1 kHz non-faradaic impedance of the planar MEAs and ZnO-NW MEAs, respectively. The series resistance was also determined to be negligible (1 nΩ), demonstrating the successful impedance correction achieved by the open/short circuit compensation, where the influence of the solution and auxiliary connections on the impedance measurements were minimised.

Figure 6.11 (a) and (b) show the simulated R_{ct} and the C_{ad} parameters of the MEAs associated with the faradaic impedance (Z_f), respectively. The obtained values of R_{ct} for the

MEAs varied in the range of 0.76–6.43 kΩ, while C_{ad} varied from 10 pF to 120 pF. The reactance of the C_{ad} was calculated, using Equation 6.4, to be greater than the R_{ct} for all MEAs at frequencies below 100 kHz. The faradaic impedance was subsequently determined to be influenced the most by the C_{ad} than the R_{ct} at low frequencies. To understand the electrochemical behaviour of the MEAs, the simulated faradaic impedance magnitude ($|Z_f|$ as a combination of R_{ct} and C_{ad}), and the non-faradaic impedance magnitude ($|X_{CPE}|$) at 1 kHz of frequency, as shown in Figure 6.11 (c) and (d), respectively, are discussed below.

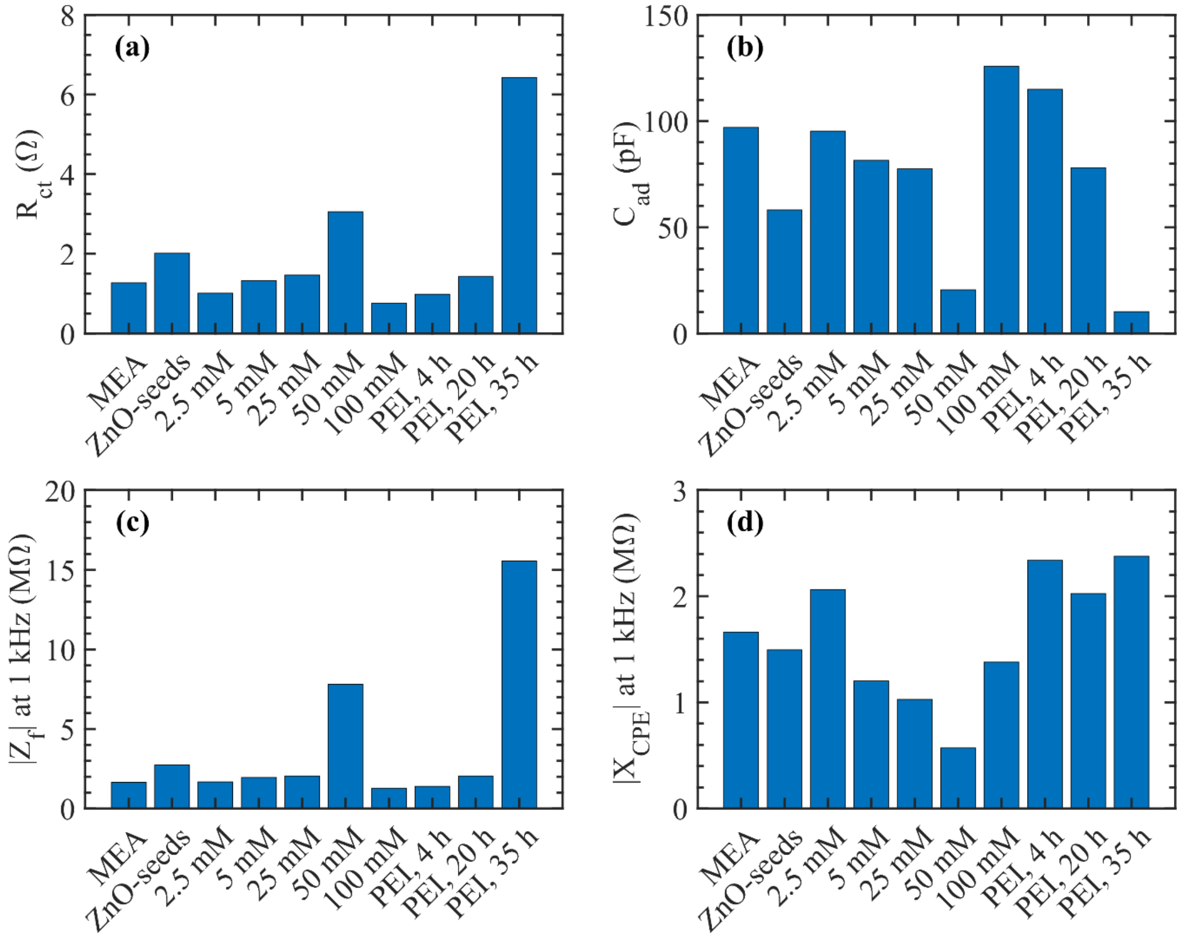

Figure 6.11. Electrochemical impedance analysis of MEAs with ZnO nanowires in various morphology. (a)–(d) Electrochemical parameters of charge transfer resistance (R_{ct}), adsorption capacitance (C_{ad}), faradaic impedance magnitude at 1 kHz ($|Z_f|$), and non-faradaic impedance magnitude at 1 kHz ($|X_{CPE}|$) of MEAs, respectively, which are simulated by fitting the experimental impedance data to the modified Randles equivalent circuit.

The electrochemical impedance of the planar MEA was determined to be equally influenced by $|Z_f|$ and $|X_{CPE}|$ parameters, with the respective fitted values of 1.64 MΩ and 1.66 MΩ at 1 kHz. As a ZnO seed layer was deposited on the planar MEA, the faradaic impedance increased to 2.74 MΩ at 1 kHz due to its semiconductive characteristics, while the non-faradaic impedance stayed about the same, 1.50 MΩ at 1 kHz. The overall impedance of the MEAs with ZnO seeds was subsequently higher than the planar MEAs.

Growing ZnO nanowires from the seed layer on MEAs enhanced the capacitive coupling of the EIS due to the reduced $|X_{CPE}|$ associated with the increased surface area. The capacitive coupling of the MEAs with the 50 mM ZnO nanowires was reduced to 570 kΩ, in comparison to 1.64 MΩ of planar MEAs. The $|Z_f|$ of the 50 mM ZnO-NW MEA increased to 7.80 MΩ due to the weak redox reaction (high R_{ct} and low C_{ad}) and long nanowires that made ions less accessible to the microelectrode surface [202]. Although the faradaic impedance was high at 50 mM compared to the other precursor concentrations, the non-faradaic impedance was relatively low that provided the dominant conduction pathway in the EIS of the ZnO-NW MEAs.

Growing ZnO nanowires for 4 h with additive PEI reduced the $|Z_f|$ from 2.05 MΩ to 1.38 MΩ and increased the $|X_{CPE}|$ from 1.03 MΩ to 2.34 MΩ, compared to when 25 mM precursors without PEI were used. The faradaic impedance of 4 h PEI nanowires reduced as the R_{ct} decreased and the C_{ad} increased that were associated with the redox reaction on the nanowires. The redox reaction is typically expected to take place at the top surface of the nanowires than the lateral sides since it is the closest surface to the electrolyte where ions can diffuse quickly, particularly when a high density of nanowires are provided and a fast reaction is carried out for a high frequency of 1 kHz. The total top surface area was increased from 500 ± 225 μm^2 to 605 ± 255 μm^2 when PEI was utilised in the growth of 25 mM ZnO nanowires for 4 h that subsequently reduced R_{ct} and increased C_{ad} associated with the redox reaction. Despite decreasing the faradaic impedance $|Z_f|$, the non-faradaic impedance $|X_{CPE}|$ was increased since PEI passivated the lateral faces of the nanowires that reduced the total surface area for the double-layer capacitance (CPE). As a result, the overall impedance was increased to 870 ± 35 kΩ, in comparison to 700 ± 40 kΩ of no PEI nanowires.

When ZnO nanowires were grown for 35 h with using PEI, both faradaic and non-faradaic impedances reached the maximum of 15.55 MΩ and 2.38 MΩ, respectively. The faradaic impedance $|Z_f|$ significantly increased from 1.38 MΩ to 15.5 MΩ, as the nanowire growth time was increased from 4 h to 35 h. The resulting nanowires were observed to have a small top surface area, 445 ± 285 μm^2, compared to 605 ± 255 μm^2 of 4 h since the density of the nanowires that could be seen by SEM from the top view was reduced. The decreasing top surface area limited the redox reaction on the nanowires that resulted in the $|Z_f|$ to increase. In addition, the increased length of the nanowires from 1.8 ± 0.18 µm to 4.8 ± 0.3 µm could have increased the $|Z_f|$ since the PBS electrolyte ions became less accessible to the surface of the planar gold microelectrodes underneath of the nanowires [202]. The non-faradaic impedance $|X_{CPE}|$ of the PEI nanowires was approximately similar, 2.25 ± 0.2 MΩ, despite the difference in the total surface area of the nanowires, 49,820 ± 22,170 μm^2 of 4 h compared to 88,130 ± 54,670 μm^2 of 35 h. The adsorption of PEI molecules on the lateral faces of the nanowires could, therefore, restrict the double-layer capacitance, where the top surfaces of the nanowires were the only surfaces responsible for the non-faradaic impedance.

ZnO nanowires with PEI were shown in Chapter 5 to be biocompatible with human hNT neurons. In Chapter 5, short nanowires with a high density were grown with additive PEI that promoted the growth of hNT neurons. In contrast, no studies have confirmed the biocompatibility of the pristine ZnO nanowires without PEI for hNT neurons. The EIS measurements showed that the ZnO nanowires that were grown with additive PEI are not suitable for MEAs since the adsorption of PEI on the lateral faces of the nanowires forms a passivation layer that increases the impedance of the ZnO-NW MEAs. Subsequently, the PEI ZnO nanowires are not expected to improve the electrical characteristics of MEAs for recording AP signals with high SNR from neuronal cells. In the next section, the pristine ZnO nanowires with no PEI are encapsulated with different metallic layers to further improve their electrical characteristics.

6.4 Metal encapsulated ZnO-NW MEAs

MEAs with metal encapsulated ZnO nanowires were fabricated by an additional fabrication step on the ZnO-NW MEAs without SU8 passivation layer, as detailed in Section 3.2.5.3 of Chapter 3. Photolithography was carried out using AZ1518 photoresist to define 200 µm wide open areas concentric with the central working microelectrodes with ZnO nanowires. Different encapsulation layers of Cr/Au (2/20 nm), Ti (10 nm) and Pt (10 nm) were deposited on the ZnO nanowires by thermal (Cr/Au) or e-beam (Ti and Pt) evaporation perpendicular to the substrate plane. A lift-off process was then applied to remove the excessive deposited materials, leaving a metallic layer on the ZnO nanowires. Finally, the SU8 photolithography process was carried out to complete the fabrication of the encapsulated ZnO-NW MEAs.

The ZnO nanowires on the MEAs were previously grown using the standard 25 mM of precursor concentration with 4 h of growth time since they resulted in a low impedance of 700 ± 40 kΩ at 1 kHz with a stable phase of −84° ± 4° for the entire frequency range of 40 Hz to 10 MHz. Figure 6.12 (a) and (b) show top view SEM images of ZnO nanowires before and after Cr/Au encapsulation, respectively. The metallic layer was deposited perpendicular to the substrate plane, resulting in the tops of the nanowires being fully encapsulated by the metallic layer, whereas the lower regions were only partially covered. Since the metallic encapsulation layer did not cover the entire nanowires, the conduction could not be taken directly by the metallic layer to the underlying microelectrodes. The ZnO nanowires that were encapsulated with Cr/Au, Ti and Pt, were therefore thought to behave differently from the pristine Cr/Au, Ti and Pt metallic nanowires.

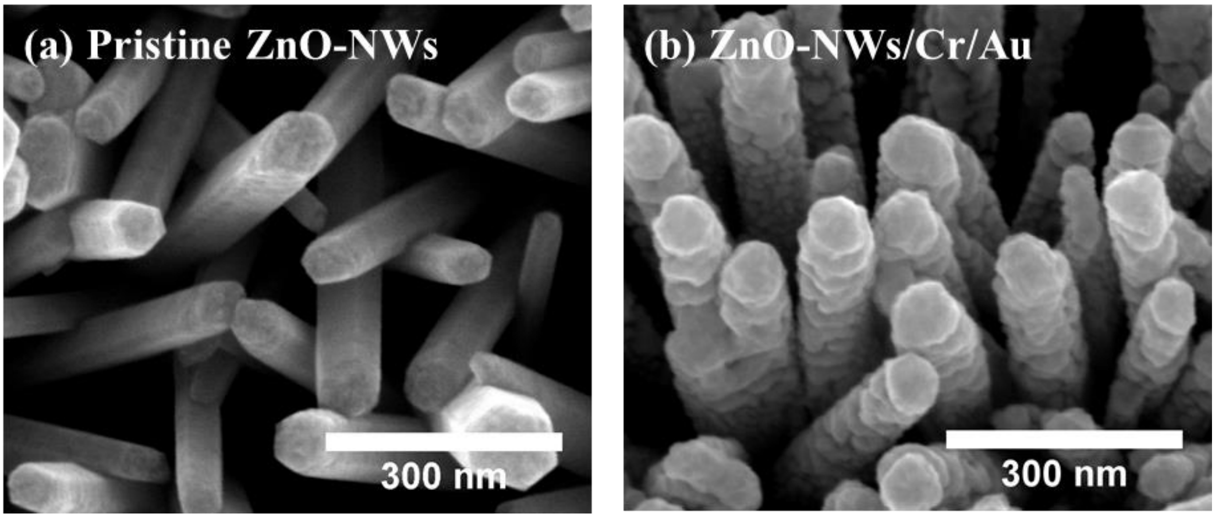

Figure 6.12. SEM images of (a) pristine ZnO nanowires and (b) Cr/Au encapsulated ZnO nanowires. The SEM images were taken from the top view.

6.4.1 EIS of metal encapsulated ZnO nanowires

Figure 6.13 (a)–(d) show the EIS Bode plots of MEAs with ZnO nanowires that were encapsulated with the different metallic layers of Cr/Au, Ti, and Pt. Figure 6.13 (a) and (b) show the impedance magnitude and phase of MEAs for a broad frequency range of 40 Hz–10 MHz, respectively. Figure 6.13 (c) and (d) show the impedance magnitude and phase at low frequencies, 40 Hz–2 kHz in linear scale, respectively, where neuronal action potentials take place. Figure 6.13 (a) and (c) show that the impedance magnitude of the MEAs with Ti and Pt encapsulated nanowires decreased, particularly at low frequencies, compared to the planar MEAs and pristine ZnO-NW MEAs. The impedance phase of the Ti and Pt encapsulated nanowires appeared to be higher for frequencies below 100 kHz compared to the other MEAs, as shown in Figure 6.13 (b) and (d). While Ti and Pt coating resulted in improved impedance, the impedance of Cr/Au encapsulated nanowires was similar to the pristine ZnO nanowires.

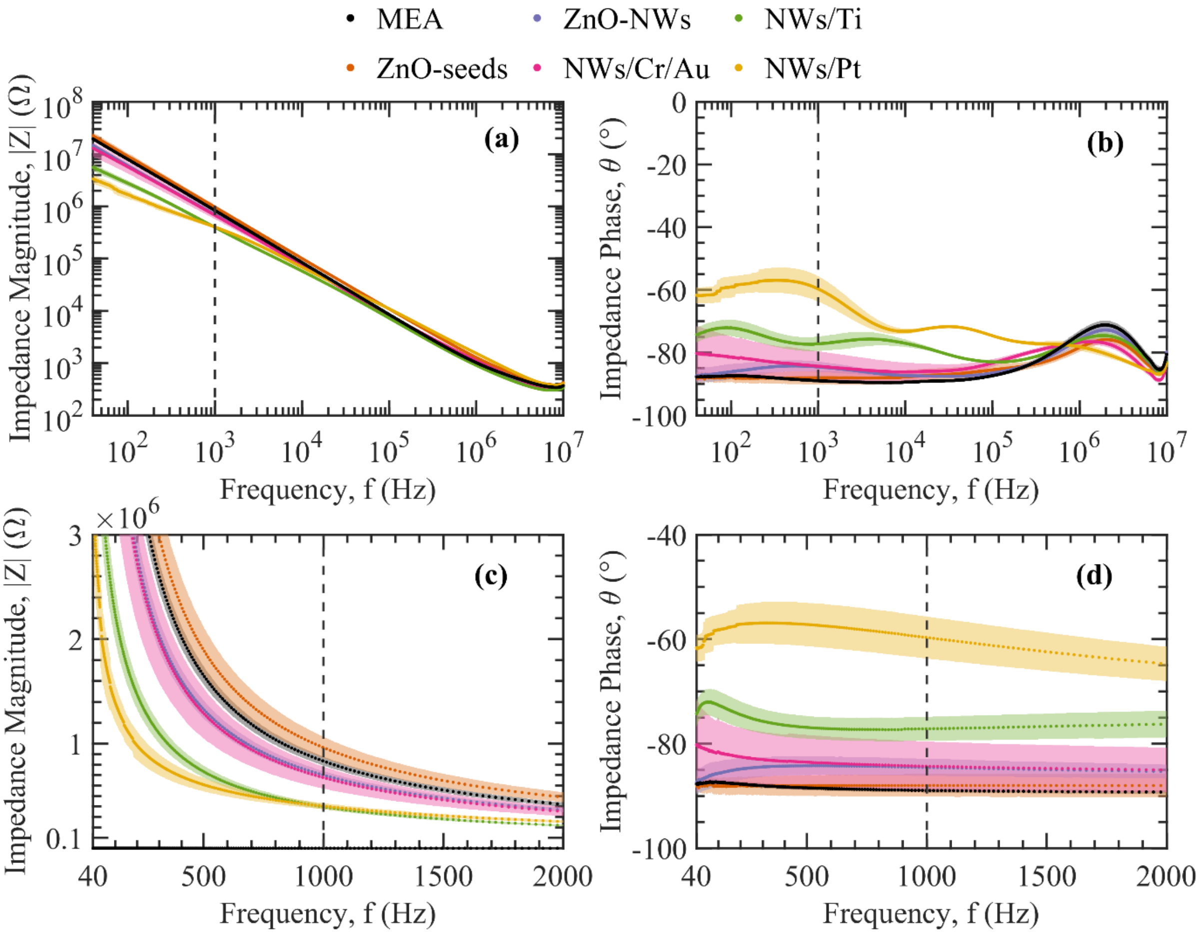

Figure 6.13. Electrochemical impedance spectroscopy of MEAs with metal encapsulated ZnO nanowires. (a) and (b) plot the average impedance magnitude and phase of MEAs for the frequency of 40 Hz–10 MHz in logarithmic scale, respectively. (c) and (d) plot the average impedance magnitude and phase of MEAs for the frequency of 40 Hz–2 kHz in linear scale, respectively. The dashed lines presented in (a)–(d) indicate the frequency of 1 kHz. The ZnO nanowires were hydrothermally grown with 25 mM of precursor concentration for 4 h of growth time. Error shades represent one standard deviation (*n* > 20 microelectrodes).

Figure 6.14 (a) and (b) show the impedance magnitude and phase of MEAs with encapsulated nanowires at the frequency of 1 kHz, respectively. Encapsulating ZnO nanowires with a 10 nm thin layer of Ti and Pt reduced the impedance magnitude from 835 ± 40 kΩ of the planar Cr/Au MEAs to an average impedance of 400 ± 25 kΩ at the frequency of 1 kHz. The impedance phase of Ti and Pt also increased to −77° ± 2° and −60° ± 4° at 1 kHz, respectively, showing the increased ohmic behaviour that contributed to their electrochemical impedance. The impedance of Cr/Au encapsulated ZnO-NW MEAs, with an average impedance magnitude of 680 ± 10 kΩ and phase of −84° ± 5°, was very similar to the pristine ZnO-NW MEAs, with an average impedance magnitude of 700 ± 40 kΩ and phase of −85° ± 2° at 1 kHz. Although Ti and Pt encapsulation of the ZnO nanowires improved the electrochemical characteristics of the microelectrodes by reducing the impedance, the Cr/Au encapsulation did not make any significant changes to the electrochemical impedance of the ZnO-NW MEAs.

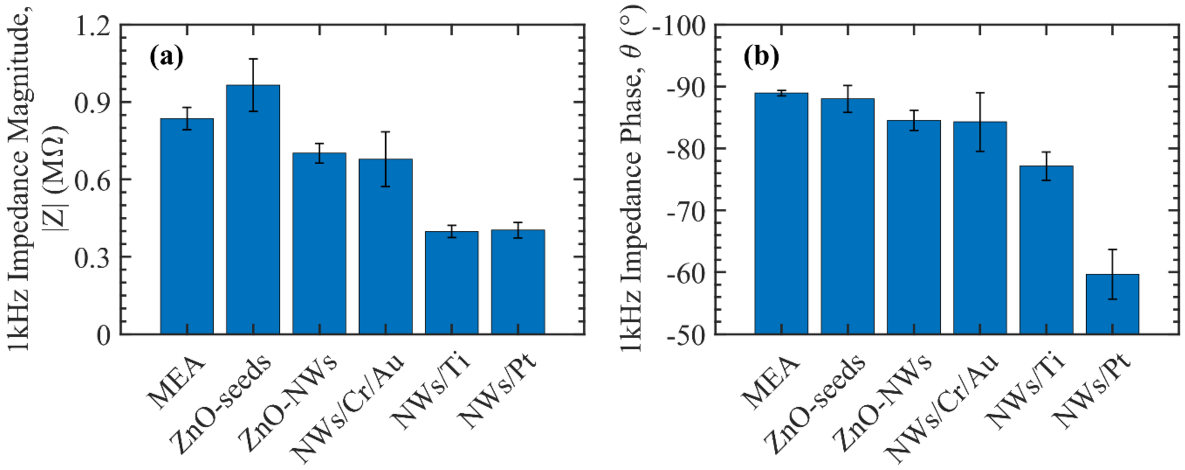

Figure 6.14. (a) Impedance magnitude and (b) phase at the frequency of 1 kHz, for MEAs with metal encapsulated ZnO nanowires compared to the planar MEAs and ZnO-NW MEAs. ZnO nanowires were grown with a precursor concentration of 25 mM for 4 h of growth time. Error bars represent one standard deviation ($n > 20$ microelectrodes).

6.4.2 EIS modelling of encapsulated ZnO nanowires

Figure 6.15 shows the electrochemical impedance parameters of the metal encapsulated ZnO-NW MEAs, obtained by fitting the measured impedance to the modified Randles circuit model that was presented in Figure 6.10 in Section 6.3.3. Figure 6.15 (a) and (b) show the charge transfer resistance (R_{ct}) and the adsorption capacitance (C_{ad}) that correspond to the redox reaction at the surface of the metal encapsulated ZnO-NW MEAs. Figure 6.15 (c) and (d) show the faradaic impedance magnitude ($|Z_f|$ as a series combination of R_{ct} and C_{ad} impedances), and the non-faradaic impedance magnitude ($|X_{CPE}|$) of metal encapsulated ZnO-NW MEAs at the frequency of 1 kHz, respectively.

The encapsulation of the ZnO nanowires with the metallic layers of Cr/Au, Ti and Pt, increased the charge transfer resistance (R_{ct}) from 1.46 kΩ of pristine ZnO nanowires to 3.04 kΩ, 2.27 kΩ and 1.85 MΩ, respectively. Despite the increase of the R_{ct}, the faradaic impedance $|Z_f|$ was mainly influenced by the C_{ad} at low frequencies, ≤ 1 kHz (e.g. ZnO-NW MEAs with $|X_{Cad}|$ = 2.05 MΩ for C_{ad} of 77.5 pF). The variation in the R_{ct} and C_{ad} of the ZnO nanowires that were encapsulated with different metals is attributed to the electrochemical properties of the metals for the redox reaction and the morphology (e.g. porosity) of the encapsulation layer that appeared on the nanowires.

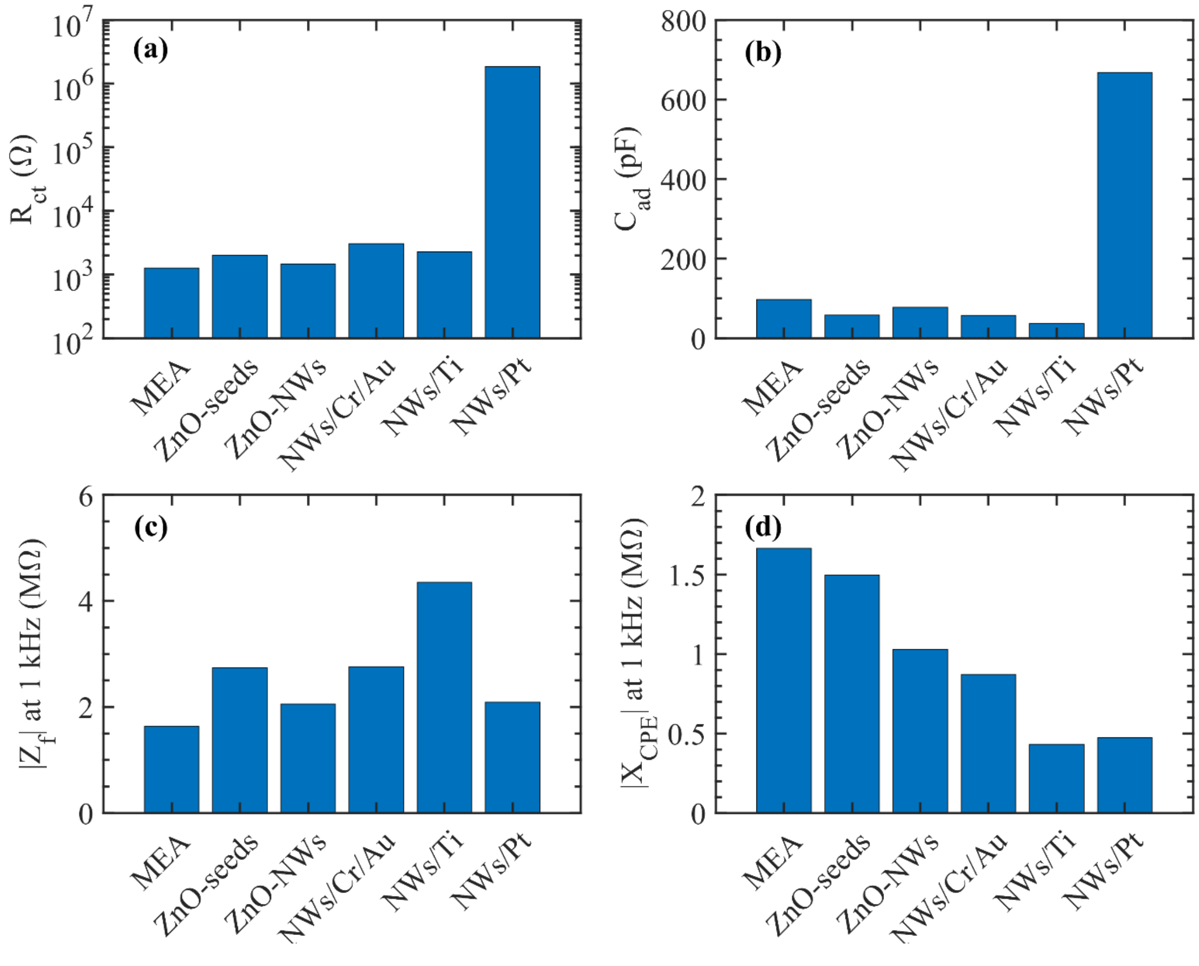

Figure 6.15. Electrochemical impedance analysis of MEAs with metal encapsulated ZnO nanowires. (a)–(d) Simulated electrochemical parameters of charge transfer resistance (R_{ct}), adsorption capacitance (C_{ad}), faradaic impedance magnitude at 1 kHz ($|Z_f|$), and non-faradaic impedance magnitude at 1 kHz ($|X_{CPE}|$), respectively, by fitting the experimental impedance data to the modified Randles equivalent circuit.

The non-faradaic impedance of the encapsulated nanowires was the dominant factor that affected the electrochemical impedance of the MEAs. Applying Ti and Pt encapsulation on the ZnO nanowires reduced the 1 kHz non-faradaic impedance from 1.03 MΩ of pristine ZnO nanowires to 430 kΩ and 470 kΩ, respectively, which improved their overall electrochemical impedance. The 10 nm thin encapsulation layers of Ti and Pt were observed to form as a porous structure (non-uniform layer) that texturised the surface of the ZnO nanowires. As the surface roughness of the nanowires increased, the overall surface area increased that reduced the non-faradaic impedance. The Cr/Au encapsulation of ZnO nanowires also reduced the non-faradaic impedance to 871 kΩ, but with a lower impact than the Ti and Pt encapsulation. As a thick layer was deposited for the Cr/Au encapsulation (2/20 nm), the encapsulation layer on the nanowires were more uniform (with less porosity) compared to the Ti and Pt encapsulation. Moreover, the thick Cr/Au encapsulation layer partially fused the adjacent nanowires, particularly at the top regions, which could reduce the overall surface area of the encapsulated nanowires.

6.4.3 Mechanical stability

Growing ZnO nanowires on MEAs was shown in Section 6.3 to improve the electrochemical characteristics of the microelectrodes by reducing the impedance. Encapsulation of the ZnO nanowires with a thin layer of Ti and Pt layers further reduced the electrochemical impedance of the ZnO-NW MEAs that can record high SNR action potentials from neuronal cells. In Chapter 5, the dissolution of ZnO nanowires into ZnO ions was hypothesised as a limiting factor in the biocompatibility of the ZnO nanowires for hNT neurons, where an excessive amount of ZnO ions could result in cell death. Although the short ZnO nanowires with a high density were shown to promote the growth of hNT neurons, the ZnO nanowires were grown with additive PEI. The adsorption of PEI on the lateral faces of the nanowires could have limited the dissolution of the ZnO nanowires into ZnO ions that improved their biocompatibility. In this section, the mechanical stability of the PEI ZnO nanowires is investigated in comparison to the PEI ZnO nanowires that were encapsulated with Ti, as an example of the metal encapsulated ZnO nanowires. The mechanical stability of the ZnO nanowires is examined by submerging ZnO nanowires in DI water and applying an ultrasound sonication (240 W at 35 kHz) for 24 h, as previously carried out by Nick *et al.* [35].

Figure 6.16 (a)–(c) show SEM images of PEI ZnO nanowires before and after the robustness test, respectively. The ZnO nanowires were grown on the seed layer array patterns that were used in Chapter 5. The ZnO nanowires were grown using 25 mM of precursor concentration with 6 mM of PEI for 1 h, as detailed in Section 3.2.4 of Chapter 3. The ZnO nanowires were grown as ZnO florets with different morphologies (diameters of 27–47, lengths of 360–800 nm, aspect ratios of 12–17, and densities of 200–450 NWs/µm^2) for arrays with different inter-floret gaps, 5–150 µm, on the Si/SiO$_2$ substrates. While ZnO nanowires with lengths shorter than 700 nm and densities higher than 220 NWs/µm^2 were found to be stable during the sonication, the longer nanowires with lower densities were damaged by the sonication, as shown in Figure 6.16 (b) and (c). The determined length of < 700 nm and density of > 220 NWs/µm^2 for the mechanical stability is comparable to the length of < 500 nm and density of > 350 NWs/µm^2 that were defined for the optimum biocompatibility in Chapter 5. Moreover, the ZnO nanowires that were grown laterally at the edges of the seed layers appeared to be more fragile, as shown in Figure 6.16 (c), compared to the vertical nanowires that were grown at the centre, as shown in Figure 6.16 (b).

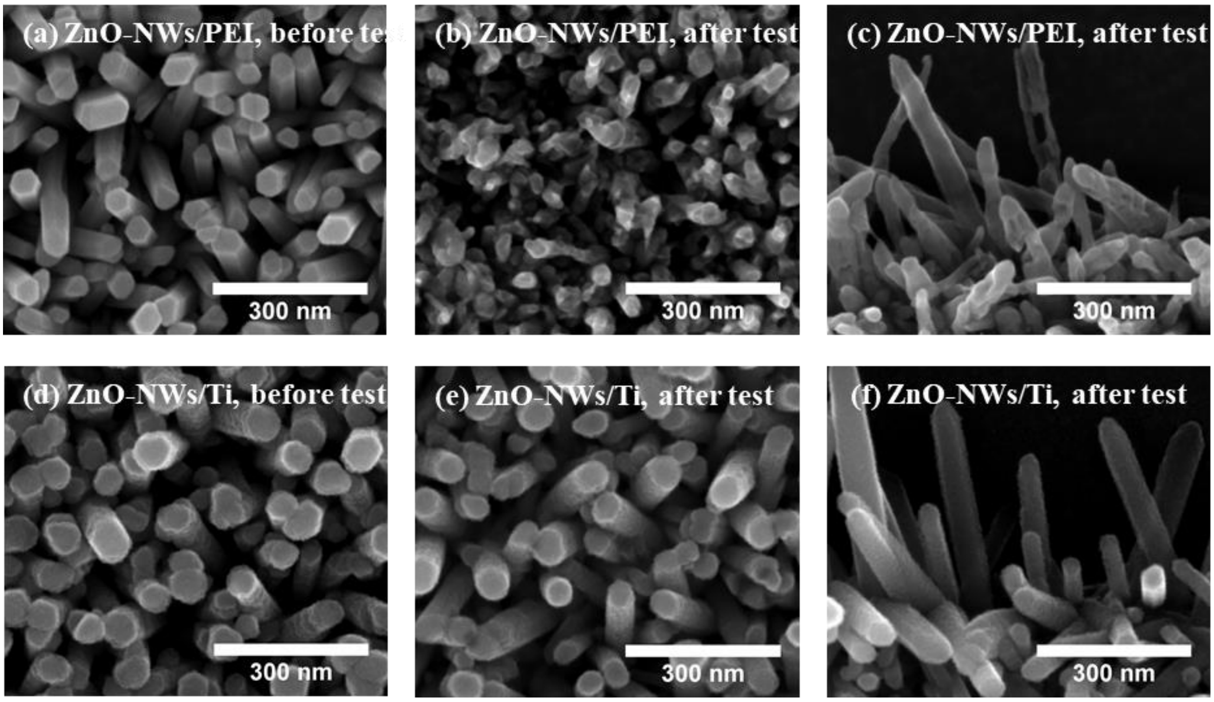

Figure 6.16. Robustness test of PEI ZnO nanowires and Ti encapsulated PEI ZnO nanowires are shown in (a)–(c) and (d)–(f), respectively. Top view SEM images of PEI ZnO nanowires before (a) and after (b, c) the robustness test are shown, respectively. Top view SEM images of Ti encapsulated ZnO nanowires before (d), and after (e, f) the robustness test are shown, respectively. (b) and (e) show SEM images of the vertical nanowires that were grown at the centre of the seed layer. (c) and (f) show SEM images of the lateral nanowires that were grown at the edges of the seed layer. The robustness test was carried out by 24 h ultrasound sonication of the nanowires in DI water.

Figure 6.16 (d)–(f) show the mechanical stability of the PEI ZnO nanowires that were encapsulated with a 10 nm thin layer of Ti. Interestingly, the encapsulated nanowires are shown to be quite robust, with no damage observed for any of the encapsulated nanowires after 24 h of the sonication. Although the mechanical stability of only Ti encapsulated ZnO nanowires were tested here, the Pt and Cr/Au encapsulations are expected to similarly improve the robustness of the nanowires. The good mechanical stability, as well as the reduced electrochemical impedance, make Ti and Pt encapsulated ZnO-NW MEAs suitable for neuronal applications. Although no study has yet demonstrated biocompatibility of Ti and Pt encapsulated ZnO nanowires, both Ti and Pt are commonly used microelectrode materials in neuronal applications, so no cytotoxicity is expected [33,65,71,72].

6.5 Conclusion

ZnO nanowires were demonstrated to improve the electrochemical impedance of microelectrode arrays (MEAs) by increasing the 3D surface area of the microelectrodes. The morphology of the ZnO nanowires on MEAs was determined to influence the impedance of the MEAs. The ZnO nanowires that were grown with 50 mM of precursor concentration for 4 h achieved to improve the electrical characteristics of MEAs the most by reducing the electrochemical impedance from 835 ± 40 kΩ of planar MEAs to 540 ± 20 kΩ at the frequency of 1 kHz. The resulting nanowires with diameters of 105 ± 40 nm, lengths of 1.56 ± 0.18 µm, aspect ratios of 15 ± 6 and densities of 54 ± 5 NWs/µm^2 were determined as the ideal nanowire morphology for recording neuronal signals.

A modified Randles equivalent circuit was used to examine the electrochemical impedance spectroscopy of the MEAs. While applying ZnO seed layers on MEAs increased the impedance due to the semiconductive characteristics of ZnO, growing ZnO nanowires from the seed layers enhanced the capacitive coupling (reduced the non-faradaic impedance) due to the increased surface area. The overall surface area of the microelectrodes was increased by a factor of 28×, to 55,320 ± 29,750 µm^2 when 50 mM ZnO nanowires were applied, compared to the average surface area of 1,960 µm^2 for the planar MEAs.

The ZnO nanowires that were grown on MEAs with 25 mM of precursor concentration and 6 mM of PEI for 4 h had a morphology comparable to the ZnO nanowires in Chapter 5 that were shown to be biocompatible with human hNT neurons. The addition of PEI is commonly used to mediate and extend the hydrothermal growth time that can result in the nanowires with larger surface areas. The PEI molecules increase the aspect ratio of the ZnO nanowires by sitting on the lateral faces of the nanowires; however, the adsorbed PEI is hypothesised to behave as a passivation layer that can limit the electrochemical conduction paths at the surface of the ZnO nanowires. The EIS measurements showed that the 4 h PEI ZnO nanowires did not improve the electrochemical impedance of the MEAs, 870 ± 35 kΩ compared to 835 ± 40 kΩ of planar Cr/Au MEAs. The MEAs with PEI ZnO nanowires can still be applicable for recording action potential (AP) signals with high signal-to-noise ratios (SNR) from neuronal cells since they have shown to be biocompatible with the human hNT neurons and their impedance is within the range of < 2MΩ as desired for neuronal recording.

Pristine ZnO nanowires were also encapsulated with different metallic layers of (Cr/Au, Ti and Pt) to further reduce the impedance of MEAs. Encapsulating the ZnO nanowires with a 10 nm thin layer of Ti and Pt resulted in the lowest electrochemical impedance of 400 ± 25 kΩ at 1 kHz in this work. The texturised surface of the ZnO nanowires, particularly at the top regions, through the metal encapsulation process, is thought to increase the total surface area of the nanowires that reduced the electrochemical impedance of the MEAs. The Ti and Pt encapsulated ZnO nanowires on the MEAs can, therefore, increase the SNR of the recording AP signals from the neuronal cells.

The ZnO nanowires that were grown with additive PEI were shown in Chapter 5 to be biocompatible for human hNT neurons, but no studies have yet been conducted to show the biocompatibility of pristine ZnO nanowires with the hNT neurons. The dissolution of the ZnO nanowires to ZnO ions in the culture media was hypothesised to cause the variation in the hNT neuron growth by the nanowire morphology. The adsorption of PEI to the lateral faces of the ZnO nanowires could have limited the dissolution rate of the ZnO nanowires that improved their biocompatibility. A mechanical robustness test was carried out by 24 h ultrasound sonication to qualify the robustness of the PEI ZnO nanowires with and without metal encapsulation for long term measurements in the neuronal applications. While PEI ZnO nanowires were damaged by the sonication test, the Ti encapsulated PEI ZnO nanowires as an example of the metal encapsulated ZnO nanowires were found to be robust. The Ti and Pt encapsulated ZnO nanowires can, therefore, improve the mechanical durability as well as the electrochemical characteristics of the MEAs. The ZnO nanowires with morphology of 105 nm ± 40 nm in diameter, 1.56 μm ± 0.18 μm in length, 15 ± 6 in aspect ratio and 54 ± 4 NWs/μm^2 in density that were encapsulated with 10 nm thin layer of Ti or Pt were determined as the ideal nanomaterial on microelectrodes for recording AP signals with high SNR for long term measurements from human hNT neurons.

Chapter 7

Conclusion and Future Work

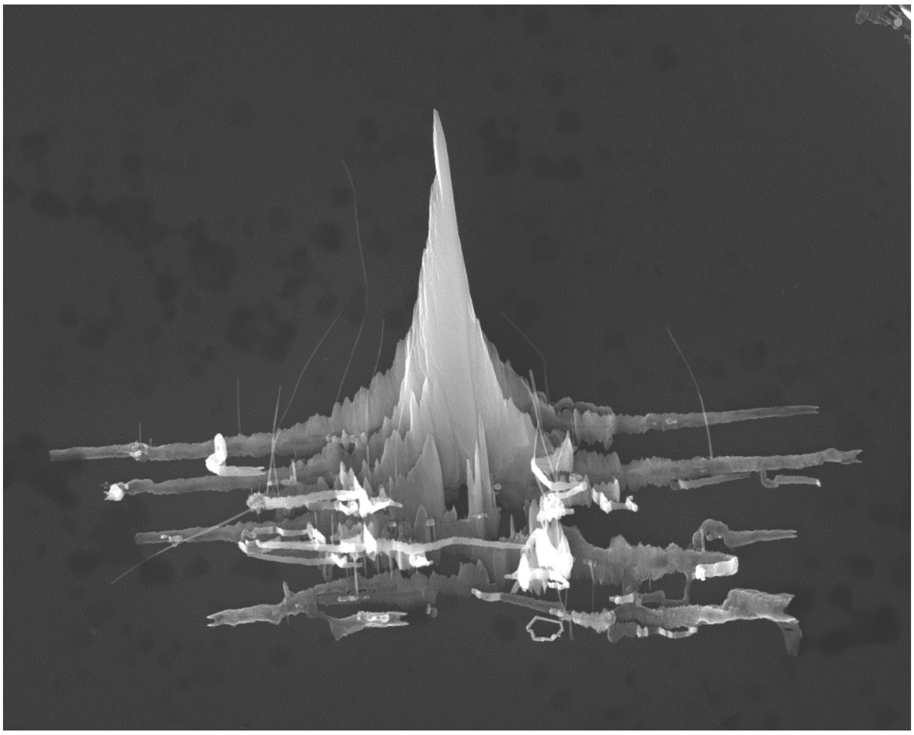

Mt. ZnO, Mt. Taranaki's baby brother with a height of 5.9 µm (1.94×10^{-5} ft) at silicon valley. The smallest mountain that Sir Edmund Hillary regretted for not having a chance to climb.

7.1 Conclusion

This thesis has explored the integration of microelectrode arrays (MEAs) with ZnO nanowires with an end goal of recording action potential (AP) signals from neuronal networks that can improve their signal-to-noise ratio (SNR) and single-cell resolution. ZnO nanowires have successfully been grown via a low temperature hydrothermal synthesis in this work. The morphology of the ZnO nanowires can be controlled by the critical growth parameters such as the precursor concentration, growth time and additive polyethylenimine (PEI). The ZnO seed layer can also be controlled using standard photolithography techniques to grow ZnO nanowires at exact locations across the substrate, which influences the nanowire morphology. The adhesion and growth of human NTera2.D1 (hNT) neurons were investigated on ZnO nanowires for the first time in this work that showed biocompatibility of the ZnO nanowires with the human neurons. The electrical properties of the MEAs, as determined by electrochemical impedance measurement, have also been improved by integration with pristine ZnO nanowires and different metal encapsulated ZnO nanowires (Cr/Au, Ti and Pt). Using both pristine and metal encapsulated ZnO-NW MEAs can pave the way for recording AP signals from neuronal networks with high SNR at single-cell resolution.

7.1.1 Selective growth of ZnO nanowires

ZnO nanowires were grown via the hydrothermal synthesis method at a low temperature (95°C), allowing a low cost and a highly scalable synthesis that can be applied on flexible substrates including the plastics. The morphology of the ZnO nanowires was varied (diameters of 20–300 nm, lengths of 0.15–6.2 μm, aspect ratios of 6–95 and densities of 10–285 NWs/μm^2) by controlling the precursor concentration, growth time and additive PEI.

Increasing the concentration of zinc nitrate hexahydrate and hexamethylenetetramine (HMT) precursors from 2.5 mM to 150 mM resulted in thicker and longer nanowires to be grown. The density of the nanowires was also reduced, and the vertical alignment of the nanowires relative to the substrate was improved as a higher precursor concentration was used. A concentration of 25 mM was chosen as a standard precursor concentration since it has commonly been used in the literature and has shown to result in consistent nanowires with relatively high aspect ratios.

The hydrothermal growth time of 1–4 h was found to be effective when a standard precursor concentration of 25 mM was used. The diameter and length of the nanowires increased as the growth time was increased from 1 h to 4 h. As the growth time was increased beyond 4 h, the concentration of the precursor ions in the solution was reduced due to the consumption of the ions by the ZnO nanowire growth and precipitation of ZnO in the growth bottle. The addition of 6 mM PEI to the growth solution was demonstrated as a technique to mediate the growth and extend the growth time to 20 h or longer, without any need for refreshing the growth solution. Moreover, The PEI molecules were adsorbed on the lateral surfaces of the nanowires that hindered the radial growth and promoted the axial growth of the nanowires. Subsequently, ZnO nanowires with high aspect ratios of 67 ± 21 were achieved compared to 12 ± 3 when no PEI was used.

Standard photolithography techniques were utilised for patterning the ZnO seed layer on the substrate and patterning the areas of the seed layer that were exposed to the growth solution, allowing ZnO nanowires to grow at exact locations across the substrates. The role of the ZnO seed layer geometry was also investigated on the growth of the ZnO nanowires when a constant growth condition (standard precursor concentration of 25 mM and growth time of 4 h) was carried out. The seed layer area ratio, which was determined as a proportion of the seed line width to the sum of the width and the adjacent gap, showed that reducing the area ratio below 50% resulted in the growth rate of the nanowires to be increased. Changing both the seed line width (4 µm–1 mm) and the gap (2 µm–800 µm) resulted in nanowires with a broad range of morphologies to grow across the same substrate (diameters of 50–240 nm, lengths of 1.2–4.6 µm, aspect ratios of 9–34 and densities of 28–120 NWs/µm^2).

7.1.2 Biocompatibility of ZnO nanowires

The biocompatibility of ZnO nanowires was examined by culturing human hNT neurons and analysing the growth of the neurons on the arrays of ZnO nanowire florets. The adhesion and growth of the neurons were found to be both promoted and inhibited depending on the morphology of the nanowires when at least 4% of the substrate area was covered by the nanowires. The growth of the neurons on the nanowire arrays was increased by up to 30% when nanowires with lengths shorter than 500 nm and densities higher than 350 NWs/µm^2 were grown. In contrast, the long nanowires with low densities inhibited the growth of the neurons by 55%, since sparse sharp nanowires less supported the neuronal cells to reside.

The possible dissolution of the ZnO nanowires into Zn^{2+} ions in the culture media could have also caused cell death when large ZnO nanowires were provided. Although Zn^{2+} ions are determined as essential ions for many biological processes, the excessive concentration of Zn^{2+} that could have been released from the large ZnO nanowires could reduce the cell viability. Furthermore, the neurites were demonstrated to grow less on the samples with large ZnO nanowires, which support the hypothesis of excessive Zn^{2+} ions released from the ZnO nanowires. In contrast, the adsorption of the PEI molecules on the lateral surfaces of the nanowires could have limited the dissolution of the ZnO nanowires to the Zn^{2+} ions. The viability of the hNT neurons was also investigated by tracing their cytoplasmic Ca^{2+} concentration as a response to the glutamate stimulation. The hNT neurons on all ZnO nanowires were subsequently determined to be alive and functionally viable.

7.1.3 ZnO-NW MEAs

ZnO nanowires were demonstrated to improve the electrical characteristics of the MEAs by reducing the electrochemical impedance. Growing ZnO nanowires with 50 mM of precursor concentration for 4 h of growth time increased the 3D surface area of the microelectrodes by a factor of 28× that resulted in the reduced impedance from 835 ± 40 kΩ of planar Cr/Au MEAs to 540 ± 20 kΩ at a frequency of 1 kHz. Using a modified Randles equivalent circuit showed that the improved impedance was attributed to the increased capacitive coupling of the ZnO-NW MEAs. The ZnO-NW MEAs can, therefore, be used for improving the SNR of the recording AP signals from neuronal networks.

Using PEI to grow ZnO nanowires with higher surface area (i.e. increasing the aspect ratio by extending the active growth time) has surprisingly resulted in the electrochemical impedance of the MEAs to increase. The adsorption of PEI molecules to the lateral surfaces of the nanowires was hypothesised to form as a passivation layer that could have restricted the electrochemical charge transfer characteristics of the nanowires. Subsequently, the top surface area of the nanowires could be the only surface area that was responsible for the passage of the current at the microelectrode-electrolyte interface, which was reduced from 1,960 μm^2 of planar MEAs to 445 μm^2. The resulting electrochemical impedance was increased from 835 ± 40 kΩ of planar Cr/Au MEAs to 2.25 ± 0.2 MΩ at 1 kHz of frequency. Although the PEI ZnO nanowires have shown a higher impedance compared to the planar MEAs, their impedance is within the range desired for neuronal signal recording. Further optimisation of the PEI ZnO nanowires can improve their electrical characteristics for the neuronal applications alongside their capability for promotion of the human neuronal growth.

The pristine ZnO nanowires that were grown by using standard precursor concentration of 25 mM with 4 h of growth time have also been encapsulated by different metallic layers of Cr/Au, Ti and Pt, using thermal or e-beam evaporation techniques. The metallic encapsulation was demonstrated to further improve the electrochemical impedance of the ZnO-NW MEAs, where the lowest impedance of 400 ± 25 kΩ was achieved for Ti and Pt encapsulated ZnO-NW MEAs. The mechanical stability of the Ti encapsulated ZnO nanowires (as an example of metal encapsulated nanowires) has also been shown to be improved, compared to the PEI ZnO nanowires. While PEI ZnO nanowires with the length longer than 700 nm and densities lower than 220 NWs/μm^2 were demonstrated to be damaged by 24 h sonication in DI water, all Ti encapsulated ZnO nanowires with different morphologies were maintained to be mechanically robust as required for reusability and for the long-term use in neural applications.

In conclusion, this research determines ZnO nanowires as a suitable nanomaterial on microelectrode arrays for integration with neuronal networks. ZnO nanowires are shown to be grown hydrothermally at low temperature (below 100ºC) that can allow fabrication of MEAs on flexible substrates as desired for biological applications. The morphology of the ZnO nanowires can easily be varied within a wide range by controlling the growth parameters suited to the desired applications. The topography of the ZnO nanowires can also be defined through a standard photolithography process that is desirable for the microelectronic fabrication of neural devices. The control of ZnO nanowire morphology and topography can further be adjusted to promote and pattern neuron growth.

Applying Ti and Pt encapsulated ZnO nanowires on Cr/Au microelectrodes is shown to offer a viable microelectrode modality for use in long-term neural applications that require single-cell resolution and high SNR. Figure 7.1 illustrates the ideal microelectrode having ZnO nanowires with 10 nm encapsulation layer of Ti or Pt at the top regions. The ZnO nanowires have the ideal morphology of 105 ± 40 nm in diameter, 1.56 ± 0.18 µm in length, 15 ± 6 in aspect ratio, and 54 ± 4 NWs/µm^2 in density as were hydrothermally grown with 50 mM precursor concentration for 4 h of growth time without using PEI. The specified microelectrode configuration resulted in improved electrical characteristics (reducing the electrical impedance from 835 ± 40 kΩ of planar Cr/Au microelectrodes to 400 ± 25 kΩ at 1 kHz of frequency) and improved mechanical robustness as required for neural applications.

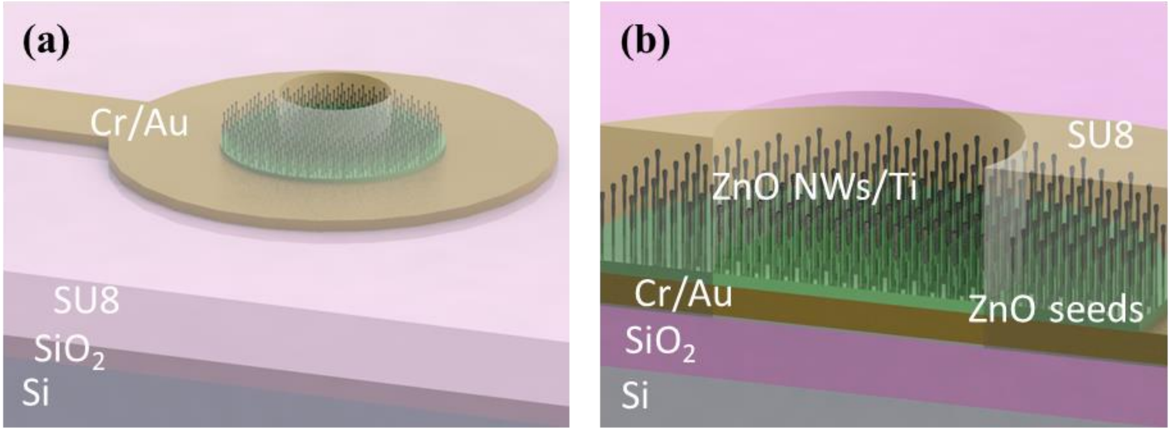

Figure 7.1. Illustration of the ideal microelectrode for neural application. (a) Overview and (b) cross-sectional magnified view of the Ti encapsulated ZnO-NW microelectrodes.

7.2 Future work

This research could have been extended in multiple ways if more time was devoted to it. The role of the additive PEI in the growth of the ZnO nanowires has been demonstrated in this thesis; however, the influence of the PEI on the characteristics of the resulting nanowires is unclear and has not been defined in the literature. The encapsulation of ZnO nanowires with a metallic layer as carried out in this work is a novel technique that requires further optimisation and investigation. In this work, the ZnO nanowires and metal encapsulated ZnO nanowires have shown to improve the electrical characteristics and biocompatibility of MEAs for neuronal applications However the suitability of these novel techniques need to be confirmed by recording AP signals from neuronal cells.

7.2.1 Influence of the PEI on the characteristics of ZnO nanowires

The influence of the PEI is very well known in the literature to control the morphology of the ZnO nanowires through the hydrothermal synthesis. However, no study has been taken on the influence of the PEI on the characteristics of the ZnO nanowires after the growth. In this work, the difference in the electrochemical characteristics of the pristine ZnO nanowires and PEI ZnO nanowires was observed, that could be attributed to the passivation behaviour of the PEI molecules on the lateral surfaces of the ZnO nanowires. Further investigation is therefore required to confirm this, as it can have a significant impact on optimisation of the electronic and sensing applications that utilise ZnO nanowires.

The PEI ZnO nanowires have also been shown to be biocompatible with the human hNT neurons and even to promote the growth of the neurons if nanowires with desired morphology and geometry were provided. The appearance of the PEI on the lateral faces of the nanowires was thought to behave as a factor that limited the dissolution of the ZnO nanowires into the Zn^{2+} ions in the culture media that could have improved their biocompatibility. This hypothesis needs to be further investigated and compared with the biocompatibility of the pristine ZnO nanowires.

7.2.2 Metal encapsulation of ZnO nanowires

Metal encapsulation of ZnO nanowires was demonstrated to improve the electrochemical impedance of the MEAs and the mechanical stability of the nanowires as desired for long term measurement. While Ryu *et al.* [49] reported that the sputtered Cr/Au encapsulation layer on the ZnO nanowires was fused to the underlying microelectrodes, the metal encapsulation that was carried out in this work by thermal and e-beam evaporation demonstrated no connection between the encapsulation layer and the underlying microelectrodes. Further investigation is required on the encapsulation techniques to optimise the electrical characteristics of the ZnO-NW MEAs. The deposition mechanism of the metallic layer/nanoparticles on the ZnO nanowires is also required to be investigated and optimised for the neuronal applications. Studies also need to be conducted on the interaction of the metal encapsulated ZnO nanowires with human neuronal cells to confirm their biocompatibility.

7.2.3 Recording signals form neuronal networks

The integration of ZnO nanowires and metal encapsulated ZnO nanowires with MEAs demonstrated their compatibility for recording signals from human neuronal networks, due to the reduced electrochemical impedance and biocompatibility with human hNT neurons. However, this needs to be confirmed by recording AP signals from human neuronal cells and comparing the recording signal resolution with the industrial planar MEAs. The MEAs should also be examined for electrical stimulation of the neuronal cells that allows neuroscientists to both control and monitor the electrical signal communication with the neuronal networks.

Studying the neuronal networks can be simplified by patterning the networks into dedicated positions and configurations. The MEAs can be integrated with some topological structures (e.g. cages to trap neurons and trenches to guide neurite growth between the neurons) [58,69] and chemical patterning techniques (e.g. Parylene-C strips to guide the growth of neurons and neurites) [140,173,203]. Using the MEAs that comprise of both recording and stimulation sites would allow neuroscientists to study the neuronal networks precisely in a controllable manner that can advance their understanding of the neuronal signal communication and processing.

Appendix A: hNT Neuron Growth and Analysis

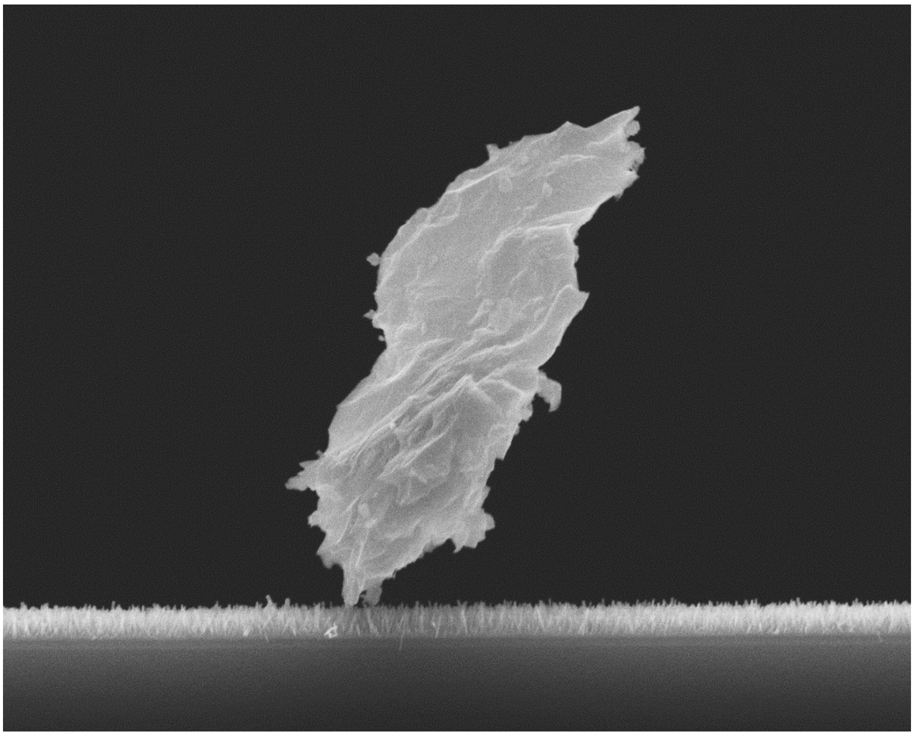

A superbly balanced object on ZnO nanowires in a vacuum down here on earth.

As discussed in Section 3.3.2 of Chapter 4 and Chapter 5, the biological experiments for the growth of hNT neurons have all be done by Brad J. Raos at the University of Auckland. Here, the detailed processes of hNT neuron differentiation and plating, fluorescence labelling and imaging and image processing are described.

A.1 neuron differentiation and plating

hNT neurons were differentiated from the NTera2.D1 (hNT/NT2) cell line (ATCC© CRL-1973™). NT2 cells were differentiated into neurons using a protocol that was first described by Andrews *et al.* [134] with subsequent modifications by Pleasure *et al.* [135], Paquet-Durand *et al.* [204], Jain *et al.* [137], and MacDonald *et al.* [138]. Briefly, NT2 cells were grown in T75 flasks in DMEM:F12 (ThermoFisher Scientific, Cat#12634010) that was supplemented with 10% foetal bovine serum (FBS, Moregate) and 1% Penicillin-Streptomycin-Glutamine (PSG, ThermoFisher Scientific, Cat#10378016) and were cultured at 37°C/5% CO_2. Cells were passaged 1:4 at 80% confluence. NT2 cells were plated in four Petri dishes at 6×10^6 cells per dish in DMEM:F12/10% FBS/1% PSG. On the day following plating, retinoic acid (RA) was added to the media to a final concentration of 10 µM. Cells were replated in fresh Petri dishes and media (DMEM:F12/10% FBS/1% PSG/10 µm RA) every 2–3 days for 2 weeks. Cells were then replated in two T75 flasks in DMEM:F12/10% FBS/1% PSG/10 µm RA and cultured for a further 7–10 days. Cells were replated in T75 flasks and cultured for a further 7 days in DMEM:F12/5% FBS/1% PSG that was supplemented with uridine (10 µM), 5-fluoro-2'-deoxyuridine (10 µM) and β-D-arabinofuranoside (1 µM) for 7 days. Neurons were harvested by selective trypsinization (1 mL 0.25% trypsin-EDTA) and mechanical detachment at room temperature and plated in a T75 flask that had been coated with poly-D-lysine (PDL) and Matrigel (Falcon, Cat#354234). Neurons were cultured for 1 further day, harvested using the selective trypsinization procedure and plated on the ZnO nanowire substrates at approximately 1000 cells per mm^2.

A.2 Fluorescence labelling and imaging

Images were captured on an Olympus BX53 with an Olympus XC50 camera using a 20× magnification water immersion objective (UMPLFLNW 20×, NA 0.50). The microscope stage was contained within an environmental chamber that maintained an atmosphere of 5% CO_2 and 37°C. Fluorescence images were captured using standard GFP and DAPI (470–495/550 nm and 360–370/410 nm, Em/Ex) fluorescence filters. Illumination was provided by a 12 W halogen lamp.

The Ca^{2+} functionality of neurons on ZnO nanowires was measured after 2 DIV (days *in vitro*) by using Fluo-4 (ThermoFisher Scientific, Cat#F14201) to visualise free Ca^{2+} in the cytoplasm. Neurons were labelled with Fluo-4 (2 µM in 1% FBS/Fluorobrite) for 30 minutes, transferred to fresh 1% FBS/Fluorobrite and placed in the microscope incubation chamber for 15 minutes prior to imaging. Images were captured with 500 ms exposures at an inter-frame interval of 1.2 s.

Immediately following Ca^{2+} imaging, the cytoplasm and nuclei of neurons were labelled with the fluorescent stains CellTracker Green CMFDA (2 µM, ThermoFisher Scientific Cat#C2925) and Hoechst 33343 (1 drop per 500 µL media, ThermoFisher Scientific, Cat#R37605). Neurons were labelled in Fluorobrite DMEM (ThermoFisher Scientific, Cat#A1896701) that was supplemented with 1% FBS for 30 minutes. The neurons were then gently washed with 1 mL of Fluorobrite DMEM/1% FBS for 5 minutes and transferred to fresh Fluorobrite DMEM/1% FBS for imaging. Fluorescence images of each entire ZnO sample surface were captured over the entire substrate and stitched into a single image using CellSens Dimension (Olympus).

A.3 Image processing

Image processing was performed using custom software written in MATLAB© (2018b, The MathWorks Inc., Natick, MA). Fluorescence images were converted to binary masks that represented the neuron nuclei. A 5 × 5 Weiner filter was applied to the Hoechst and CMFDA fluorescence images, and a threshold value was manually selected for each sample. The nuclei density was calculated as the proportion of any given area that was covered by nuclei in the binary mask.

The Ca^{2+} imaging experiments were processed by using the nuclei mask to define regions of interest for the measurement of changes in fluorescence. Fluorescence was averaged over each region of interest for every time-point that was recorded. The resulting fluorescence traces were then processed to represent the change in fluorescence over the baseline ($\Delta F/F_0$) according to the method described in detail by Jia *et al.* [205].

Neuron adhesion and patterning was quantified within multiple areas. Binary masks were generated for areas representing: the area within the nanowire array (Figure 3.13 (a)), the area outside of the nanowire array (Figure 3.13 (b)), the area directly on the nanowire florets and the areas within 10 µm concentric bands at increasing distances from the nanowire florets (Figure 3.13 (c)). The influence of various experimental parameters on neuron growth was encapsulated by nuclei and cytoplasm density ratios. The nuclei and cytoplasm density ratios were calculated as the density within a given area, relative to the density outside the nanowire. The area outside the nanowire array was a plain SiO_2 surface that did not contain any nanowires and was, therefore, used as the baseline to measure relative changes in neuron growth. A density ratio of greater than 1 represents increased neuron growth or adhesion compared to bare SiO_2, whereas a nuclei density ratio of less than 1 represents reduced neuron growth or adhesion compared to bare SiO_2.

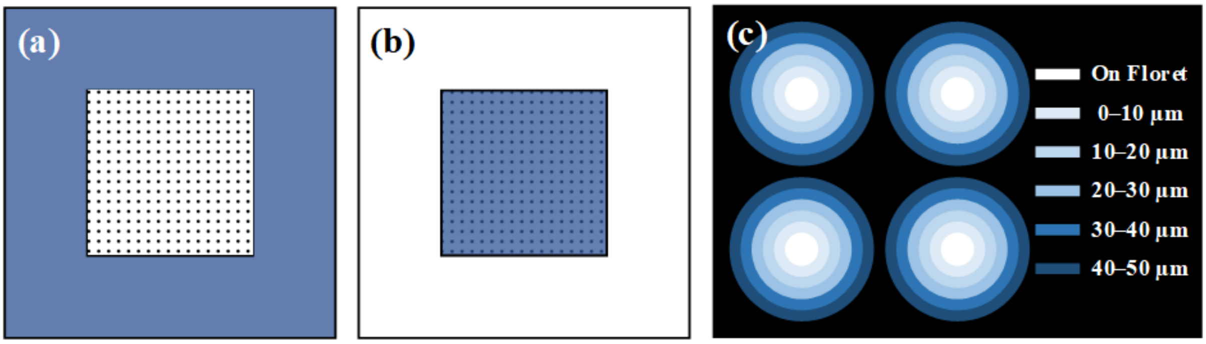

Figure A.1. Schematics showing the areas of the ZnO nanowire samples used for quantification of neuronal adhesion and localisation. (a) The plain substrate area outside of the nanowire array region for controls. (b) The area on the entire nanowire array for defining the neuronal adhesion and growth. (c) The area on the individual floret sites and 10 µm wide concentric band at increasing distances from the florets.

Bibliography

[1] Bertolote J M 2007 Neurological disorders affect millions globally: WHO report *World Heal. Organ.*

[2] World Health Organization 2006 *Neurological Disorders: Public Health Challenges* (World Health Organization)

[3] Pérez-Martínez F C, Carrión B and Ceña V 2012 The Use of Nanoparticles for Gene Therapy in the Nervous System *J. Alzheimer's Dis.* **31** 697–710

[4] Kringelbach M L, Jenkinson N, Owen S L F and Aziz T Z 2007 Translational principles of deep brain stimulation. *Nat. Rev. Neurosci.* **8** 623–35

[5] Dossi E, Blauwblomme T, Nabbout R, Huberfeld G and Rouach N 2014 Multi-electrode array recordings of human epileptic postoperative cortical tissue *J. Vis. Exp. JoVE* 51870

[6] Bossenmeyer-Pourié C, Koziel V and Daval J-L 2000 Effects of hypothermia on hypoxia-induced apoptosis in cultured neurons from developing rat forebrain: comparison with preconditioning *Pediatr. Res.* **47** 385–91

[7] Ginsberg M D and Busto R 1989 Rodent models of cerebral ischemia *Stroke* **20** 1627–42

[8] Wheeler B C and Brewer G J 2010 Designing neural networks in culture *Proc. IEEE* **98** 398–406

[9] Chiappalone M, Pasquale V and Frega M 2019 In Vitro Neuronal Networks *In Vitro Neuronal Networks* Advances in Neurobiology vol 22, ed M Chiappalone, V Pasquale and M Frega (Cham: Springer International Publishing) pp 31–41

[10] Nam Y and Wheeler B C 2011 In vitro microelectrode array technology and neural recordings *Crit. Rev. Biomed. Eng.* **39** 45–62

[11] Fu T-M, Duan X, Jiang Z, Dai X, Xie P, Cheng Z and Lieber C M 2014 Sub-10-nm intracellular bioelectronic probes from nanowire-nanotube heterostructures. *Proc. Natl. Acad. Sci. U. S. A.* **111** 1259–64

[12] Robinson J T, Jorgolli M, Shalek A K, Yoon M-H, Gertner R S and Park H 2012

Vertical nanowire electrode arrays as a scalable platform for intracellular interfacing to neuronal circuits *Nat. Nanotechnol.* **7** 180–4

[13] Duan X, Gao R, Xie P, Cohen-Karni T, Qing Q, Choe H S, Tian B, Jiang X and Lieber C M 2012 Intracellular recordings of action potentials by an extracellular nanoscale field-effect transistor. *Nat. Nanotechnol.* **7** 174–9

[14] Ferguson J E, Boldt C, Puhl J G, Stigen T W, Jackson J C, Crisp K M, Mesce K A, Netoff T I and Redish A D 2012 Nanowires precisely grown on the ends of microwire electrodes permit the recording of intracellular action potentials within deeper neural structures *Nanomedicine* **7** 847–53

[15] Xie C, Lin Z, Hanson L, Cui Y and Cui B 2012 Intracellular recording of action potentials by nanopillar electroporation *Nat. Nanotechnol.* **7** 185–90

[16] Gao R, Strehle S, Tian B, Cohen-Karni T, Xie P, Duan X, Qing Q and Lieber C M 2012 Outside looking in: Nanotube transistor intracellular sensors *Nano Lett.* **12** 3329–33

[17] Brüggemann D, Wolfrum B, Maybeck V, Mourzina Y, Jansen M and Offenhäusser A 2011 Nanostructured gold microelectrodes for extracellular recording from electrogenic cells *Nanotechnology* **22** 265104

[18] Eversmann B, Jenkner M, Hofmann F, Paulus C, Brederlow R, Holzapfl B, Fromherz P, Merz M, Brenner M and Schreiter M 2003 A 128× 128 CMOS biosensor array for extracellular recording of neural activity *Solid-State Circuits, IEEE J.* **38** 2306–17

[19] Hämmerle H, Egert U, Mohr A and Nisch W 1994 Extracellular recording in neuronal networks with substrate integrated microelectrode arrays *Biosens. Bioelectron.* **9** 691–6

[20] Bucher V, Graf M, Stelzle M and Nisch W 1999 Low-impedance thin-film polycrystalline silicon microelectrodes for extracellular stimulation and recording *Biosens. Bioelectron.* **14** 639–49

[21] Nisch W, Böck J, Egert U, Hämmerle H and Mohr A 1994 A thin film microelectrode array for monitoring extracellular neuronal activity in vitro *Biosens. Bioelectron.* **9** 737–41

[22] Connolly P, Clark P, Curtis A S G, Dow J A T and Wilkinson C D W 1990 An

extracellular microelectrode array for monitoring electrogenic cells in culture *Biosens. Bioelectron.* **5** 223–34

[23] Fromherz P 1999 Extracellular recording with transistors and the distribution of ionic conductances in a cell membrane *Eur. Biophys. J.* **28** 254–8

[24] James C D, Spence A J H, Dowell-Mesfin N M, Hussain R J, Smith K L, Craighead H G, Isaacson M S, Shain W and Turner J N 2004 Extracellular recordings from patterned neuronal networks using planar microelectrode arrays *IEEE Trans. Biomed. Eng.* **51** 1640–8

[25] Spira M E and Hai A 2013 Multi-electrode array technologies for neuroscience and cardiology *Nat. Nanotechnol.* **8** 83–94

[26] Anon Multichannel Systems *http://www.multichannelsystems.com/*

[27] Anon 3Brain *http://www.3brain.com/*

[28] Anon MED64 *http://www.med64.com/*

[29] Nick C, Quednau S, Sarwar R, Schlaak H F and Thielemann C 2014 High aspect ratio gold nanopillars on microelectrodes for neural interfaces *Microsyst. Technol.* **20** 1849–57

[30] Hai A, Shappir J and Spira M E 2010 Long-term, multisite, parallel, in-cell recording and stimulation by an array of extracellular microelectrodes *J. Neurophysiol.* **104** 559–68

[31] Yoon H, Deshpande D C, Ramachandran V and Varadan V K 2007 Aligned nanowire growth using lithography-assisted bonding of a polycarbonate template for neural probe electrodes *Nanotechnology* **19** 25304

[32] Kim J-H, Kang G, Nam Y and Choi Y-K 2010 Surface-modified microelectrode array with flake nanostructure for neural recording and stimulation *Nanotechnology* **21** 85303

[33] Gabay T, Ben-David M, Kalifa I, Sorkin R, Ze'ev R A, Ben-Jacob E and Hanein Y 2007 Electro-chemical and biological properties of carbon nanotube based multi-electrode arrays *Nanotechnology* **18** 35201

[34] Wang K, Fishman H A, Dai H and Harris J S 2006 Neural stimulation with a carbon

nanotube microelectrode array *Nano Lett.* **6** 2043–8

[35] Nick C and Thielemann C 2014 Are carbon nanotube microelectrodes manufactured from dispersion stable enough for neural interfaces? *Bionanoscience* **4** 216–25

[36] Namdari P, Daraee H and Eatemadi A 2016 Recent Advances in Silicon Nanowire Biosensors: Synthesis Methods, Properties, and Applications *Nanoscale Res. Lett.* **11** 406

[37] Kawano T, Takao H, Sawada K and Ishida M 2004 Neural recording chip with penetrating Si microprobe electrode array by selective vapor-liquid-solid growth method *Engineering in Medicine and Biology Society, 2004. IEMBS'04. 26th Annual International Conference of the IEEE* vol 1 (IEEE) pp 2066–9

[38] Jin Y-H, Daubinger P, Fiebich B L and Stieglitz T 2011 A novel platinum nanowire-coated neural electrode and its electrochemical and biological characterization *Micro Electro Mechanical Systems (MEMS), 2011 IEEE 24th International Conference on* (IEEE) pp 1003–6

[39] Zhang X M, Lu M Y, Zhang Y, Chen L J and Wang Z L 2009 Fabrication of a high-brightness blue-light-emitting diode using a ZnO-Nanowire array grown on p-GaN thin film *Adv. Mater.* **21** 2767–70

[40] Lupan O, Guérin V M, Tiginyanu I M, Ursaki V V, Chow L, Heinrich H and Pauporté T 2010 Well-aligned arrays of vertically oriented ZnO nanowires electrodeposited on ITO-coated glass and their integration in dye sensitized solar cells *J. Photochem. Photobiol. A Chem.* **211** 65–73

[41] Qin Z, Huang Y, Liao Q, Zhang Z, Zhang X and Zhang Y 2012 Stability improvement of the ZnO nanowire array electrode modified with Al2O3and SiO2for dye-sensitized solar cells *Mater. Lett.* **70** 177–80

[42] Qiu J, Li X, Zhuge F, Gan X, Gao X, He W, Park S-J, Kim H-K and Hwang Y-H 2010 Solution-derived 40 µm vertically aligned ZnO nanowire arrays as photoelectrodes in dye-sensitized solar cells *Nanotechnology* **21** 195602

[43] Zhang Y, Ram M K, Stefanakos E K and Goswami D Y 2012 Synthesis, characterization, and applications of ZnO nanowires *J. Nanomater.* **2012** 20

[44] Liu T-Y, Liao H-C, Lin C-C, Hu S-H and Chen S-Y 2006 Biofunctional ZnO

Nanorod Arrays Grown on Flexible Substrates *Langmuir* **22** 5804–9

[45] Wei A, Sun X W, Wang J X, Lei Y, Cai X P, Li C M, Dong Z L and Huang W 2006 Enzymatic glucose biosensor based on ZnO nanorod array grown by hydrothermal decomposition *Appl. Phys. Lett.* **89** 123902

[46] Jeong Y, Sim M, Shin J H, Choi J-W, Sohn J I, Cha S N, Choi H, Moon C and Jang J E 2015 Psychological tactile sensor structure based on piezoelectric nanowire cell arrays *RSC Adv.* **5** 40363–8

[47] Wang Z L and Song J 2006 Piezoelectric nanogenerators based on zinc oxide nanowire arrays *Science (80-.).* **312** 242–6

[48] Xu S, Qin Y, Xu C, Wei Y, Yang R and Wang Z L 2010 Self-powered nanowire devices *Nat. Nanotechnol.* **5** 366–73

[49] Ryu M, Yang J H, Ahn Y, Sim M, Lee K H, Kim K, Lee T, Yoo S-J, Kim S Y, Moon C, Je M, Choi J-W, Lee Y and Jang J E 2017 Enhancement of interface characteristics of neural probe based on graphene, ZnO nanowires, and conducting polymer PEDOT *ACS Appl. Mater. Interfaces* **9** 10577–86

[50] Hierlemann A, Frey U, Hafizovic S and Heer F 2011 Growing cells atop microelectronic chips: interfacing electrogenic cells in vitro with CMOS-based microelectrode arrays *Proc. IEEE* **99** 252–84

[51] Bean B P 2007 The action potential in mammalian central neurons *Nat. Rev. Neurosci.* **8** 451–465

[52] White J A 2002 Action Potential *Encyclopedia of the Human Brain* (Elsevier) pp 1–12

[53] Potter S M, El Hady A and Fetz E E 2014 Closed-loop neuroscience and neuroengineering. *Front. Neural Circuits* **8** 115

[54] Thomas C A, Springer P A, Loeb G E, Berwald-Netter Y and Okun L M 1972 A miniature microelectrode array to monitor the bioelectric activity of cultured cells *Exp. Cell Res.* **74** 61–6

[55] Pine J 1980 Recording action potentials from cultured neurons with extracellular microcircuit electrodes *J. Neurosci. Methods* **2** 19–31

[56] Pine J 2006 A history of MEA development *Advances in network electrophysiology*

(Springer) pp 3–23

[57] Jang J E, Cha S N, Butler T P, Sohn J I, Kim J W, Jin Y W, Amaratunga G A J, Jung J E and Kim J M 2009 A Characterization Study of a Nanowire-Network Transistor with Various Channel Layers *Adv. Mater.* **21** 4139–42

[58] Maher M P, Pine J, Wright J and Tai Y C 1999 The neurochip: a new multielectrode device for stimulating and recording from cultured neurons *J Neurosci Methods* **87** 45–56

[59] Zeck G and Fromherz P 2001 Noninvasive neuroelectronic interfacing with synaptically connected snail neurons immobilized on a semiconductor chip *Proc. Natl. Acad. Sci.* **98** 10457–62

[60] Tooker A C 2007 *Development of biocompatible Parylene neurocages for action potential stimulation and recording* (California Institute of Technology)

[61] Ghane Motlagh B, Choueib M, Hajhosseini Mesgar A, Hasanuzzaman M and Sawan M 2016 Direct Growth of Carbon Nanotubes on New High-Density 3D Pyramid-Shaped Microelectrode Arrays for Brain-Machine Interfaces *Micromachines* **7** 163

[62] Hai A, Shappir J and Spira M E 2010 In-cell recordings by extracellular microelectrodes *Nat. Methods* **7** 200–2

[63] Hibst N and Strehle S 2016 Direct synthesis of electrically integrated silicon nanowires forming 3D electrodes *Phys. status solidi* **213** 2901–5

[64] Regehr W G, Pine J, Cohan C S, Mischke M D and Tank D W 1989 Sealing cultured invertebrate neurons to embedded dish electrodes facilitates long-term stimulation and recording *J. Neurosci. Methods* **30** 91–106

[65] Gabriel G, Gómez R, Bongard M, Benito N, Fernández E and Villa R 2009 Easily made single-walled carbon nanotube surface microelectrodes for neuronal applications *Biosens. Bioelectron.* **24** 1942–8

[66] Fang S-P, Jao P F, Franca E, DeMarse T B, Wheeler B C and Yoon Y-K 2016 A carbon nanofiber (CNF) based 3-D microelectrode array for in-vitro neural proliferation and signal recording *2016 IEEE 29th International Conference on Micro Electro Mechanical Systems (MEMS)* (IEEE) pp 423–6

[67] Pine J 1980 Recording action potentials from cultured neurons with extracellular microcircuit electrodes *J. Neurosci. Methods* **2** 19–31

[68] Ryu M, Lee K H, Sim M, Kim S, Jun B-O, Jang J E, Ahn Y and Lee Y 2015 Nanowire based flexible electrode array with pedot film for neural recordings *2015 IEEE 15th International Conference on Nanotechnology (IEEE-NANO)* (IEEE) pp 868–71

[69] Erickson J, Tooker A, Tai Y-C and Pine J 2008 Caged neuron MEA: A system for long-term investigation of cultured neural network connectivity *J. Neurosci. Methods* **175** 1–16

[70] Gross G W, Rieske E, Kreutzberg G W and Meyer A 1977 A new fixed-array multi-microelectrode system designed for long-term monitoring of extracellular single unit neuronal activity in vitro *Neurosci. Lett.* **6** 101–5

[71] Hafizovic S, Heer F, Ugniwenko T, Frey U, Blau A, Ziegler C and Hierlemann A 2007 A CMOS-based microelectrode array for interaction with neuronal cultures *J. Neurosci. Methods* **164** 93–106

[72] Frey U, Egert U, Heer F, Hafizovic S and Hierlemann A 2009 Microelectronic system for high-resolution mapping of extracellular electric fields applied to brain slices *Biosens. Bioelectron.* **24** 2191–8

[73] Huys R, Braeken D, Jans D, Stassen A, Collaert N, Wouters J, Loo J, Severi S, Vleugels F and Callewaert G 2012 Single-cell recording and stimulation with a 16k micro-nail electrode array integrated on a 0.18 μm CMOS chip *Lab Chip* **12** 1274–80

[74] Qing Q, Pal S K, Tian B, Duan X, Timko B P, Cohen-Karni T, Murthy V N and Lieber C M 2010 Nanowire transistor arrays for mapping neural circuits in acute brain slices *Proc. Natl. Acad. Sci.* **107** 1882–7

[75] Lacour S P, Benmerah S, Tarte E, Fitzgerald J, Serra J, McMahon S, Fawcett J, Graudejus O, Yu Z and Morrison B 2010 Flexible and stretchable micro-electrodes for in vitro and in vivo neural interfaces *Med. Biol. Eng. Comput.* **48** 945–54

[76] Czeschik A, Offenhäusser A and Wolfrum B 2014 Fabrication of MEA-based nanocavity sensor arrays for extracellular recording of action potentials *Phys. status solidi* **211** 1462–6

[77] Jun S B, Hynd M R, Dowell-Mesfin N, Smith K L, Turner J N, Shain W and Kim S J 2007 Low-density neuronal networks cultured using patterned poly-l-lysine on microelectrode arrays *J. Neurosci. Methods* **160** 317–26

[78] Takayama Y, Moriguchi H, Kotani K, Suzuki T, Mabuchi K and Jimbo Y 2012 Network-wide integration of stem cell-derived neurons and mouse cortical neurons using microfabricated co-culture devices *BioSystems*

[79] Fromherz P 2003 Semiconductor chips with ion channels, nerve cells and brain *Physica E: Low-Dimensional Systems and Nanostructures* vol 16 pp 24–34

[80] Buitenweg J R, Rutten W L C, Willems W P A and Van Nieuwkasteele J W 1998 Measurement of sealing resistance of cell-electrode interfaces in neuronal cultures using impedance spectroscopy *Med. Biol. Eng. Comput.* **36** 630–7

[81] Martinoia S, Bove M and Massobrio G 2004 Cultured neurons coupled to microelectrode arrays: circuit models, simulations and experimental data *IEEE Trans. Biomed. Eng.* **51** 859–64

[82] Hai A, Dormann A, Shappir J, Yitzchaik S, Bartic C, Borghs G, Langedijk J P M and Spira M E 2009 Spine-shaped gold protrusions improve the adherence and electrical coupling of neurons with the surface of micro-electronic devices *J. R. Soc. Interface* **6** 1153–65

[83] Hai A and Spira M E 2012 On-chip electroporation, membrane repair dynamics and transient in-cell recordings by arrays of gold mushroom-shaped microelectrodes *Lab Chip* **12** 2865

[84] Mattson M P, Haddon R C and Rao A M 2000 Molecular functionalization of carbon nanotubes and use as substrates for neuronal growth *J. Mol. Neurosci.* **14** 175–82

[85] Gabriel G, Gómez-Martínez R and Villa R 2008 Single-walled carbon nanotubes deposited on surface electrodes to improve interface impedance *Physiol. Meas.* **29** S203

[86] Hibst N, Knittel P, Biskupek J, Kranz C, Mizaikoff B and Strehle S 2015 The mechanisms of platinum-catalyzed silicon nanowire growth *Semicond. Sci. Technol.* **31** 25005

[87] Yogeswaran U and Chen S-M 2008 A review on the electrochemical sensors and

biosensors composed of nanowires as sensing material *Sensors* **8** 290–313

[88] Nam Y, Chang J C, Wheeler B C and Brewer G J 2004 Gold-coated microelectrode array with thiol linked self-assembled monolayers for engineering neuronal cultures *IEEE Trans. Biomed. Eng.* **51** 158–65

[89] Lu Y, Yang M, Qu F, Shen G and Yu R 2007 Enzyme-functionalized gold nanowires for the fabrication of biosensors *Bioelectrochemistry* **71** 211–6

[90] Ganji M, Elthakeb A T, Tanaka A, Gilja V, Halgren E and Dayeh S A 2017 Scaling Effects on the Electrochemical Performance of poly(3,4-ethylenedioxythiophene (PEDOT), Au, and Pt for Electrocorticography Recording *Adv. Funct. Mater.* **27** 1703018

[91] Mikolajick T and Weber W M 2015 Silicon nanowires: Fabrication and applications *Nanosci. Technol.* **100** 1–25

[92] Bayliss S C, Heald R, Fletcher D I and Buckberry L D 1999 The Culture of Mammalian Cells on Nanostructured Silicon *Adv. Mater.* **11** 318–21

[93] Hochbaum A I, Gargas D, Hwang Y J and Yang P 2009 Single Crystalline Mesoporous Silicon Nanowires *Nano Lett.* **9** 3550–4

[94] Smalley R E, Dresselhaus M S, Dresselhaus G and Avouris P 2003 *Carbon nanotubes: synthesis, structure, properties, and applications* vol 80 (Springer Science & Business Media)

[95] Chen X, Tam U C, Czlapinski J L, Lee G S, Rabuka D, Zettl A and Bertozzi C R 2006 Interfacing carbon nanotubes with living cells *J. Am. Chem. Soc.* **128** 6292–3

[96] Look D C 2001 Recent advances in ZnO materials and devices *Mater. Sci. Eng. B* **80** 383–7

[97] Janotti A and Van De Walle C G 2009 Fundamentals of zinc oxide as a semiconductor *Reports Prog. Phys.* **72** 126501

[98] Morkoc H and Ozgur U 2009 General Properties of ZnO *Zinc Oxide: Fundamentals, Materials and Device Technology* pp 1–76

[99] Özgür Ü, Alivov Y I, Liu C, Teke A, Reshchikov M A, Doğan S, Avrutin V, Cho S J and Morkǫ H 2005 A comprehensive review of ZnO materials and devices *J. Appl.*

Phys. **98** 1–103

[100] Fu Y Q, Luo J K, Du X Y, Flewitt A J, Li Y, Markx G H, Walton A J and Milne W I 2010 Recent developments on ZnO films for acoustic wave based bio-sensing and microfluidic applications: a review *Sensors Actuators, B Chem.* **143** 606–19

[101] Law M, Greene L E, Johnson J C, Saykally R and Yang P 2005 Nanowire dye-sensitized solar cells *Nat. Mater.* **4** 455–9

[102] Baxter J B, Walker A M, Van Ommering K and Aydil E S 2006 Synthesis and characterization of ZnO nanowires and their integration into dye-sensitized solar cells *Nanotechnology* **17** S304–12

[103] Li Z, Yang R, Yu M, Bai F, Li C and Wang Z L 2008 Cellular level biocompatibility and biosafety of ZnO nanowires *J. Phys. Chem. C* **112** 20114–7

[104] Zhou J, Xu N S and Wang Z L 2006 Dissolving behavior and stability of ZnO wires in biofluids: a study on biodegradability and biocompatibility of ZnO nanostructures *Adv. Mater.* **18** 2432–5

[105] Ciofani G, Genchi G G and Mattoli V 2012 ZnO nanowire arrays as substrates for cell proliferation and differentiation *Mater. Sci. Eng. C* **32** 341–7

[106] Burke-Govey C P and Plank N O V. 2013 Review of hydrothermal ZnO nanowires: Toward FET applications *J. Vac. Sci. Technol. B, Nanotechnol. Microelectron. Mater. Process. Meas. Phenom.* **31** 06F101

[107] Xu S and Wang Z L 2011 One-dimensional ZnO nanostructures: solution growth and functional properties *Nano Res.* **4** 1013–98

[108] Vayssieres L 2003 Growth of arrayed nanorods and nanowires of ZnO from aqueous solutions *Adv. Mater.* **15** 464–6

[109] Liu J, She J, Deng S, Chen J and Xu N 2008 Ultrathin seed-layer for tuning density of ZnO nanowire arrays and their field emission characteristics *J. Phys. Chem. C* **112** 11685–90

[110] Ghayour H, Rezaie H R, Mirdamadi S and Nourbakhsh A A 2011 The effect of seed layer thickness on alignment and morphology of ZnO nanorods *Vacuum* **86** 101–5

[111] Ji L-W, Peng S-M, Wu J-S, Shih W-S, Wu C-Z and Tang I-T 2009 Effect of seed

layer on the growth of well-aligned ZnO nanowires *J. Phys. Chem. Solids* **70** 1359–62

[112] Hsiao C-S, Peng C-H, Chen S-Y and Liou S-C 2006 Tunable growth of ZnO nanorods synthesized in aqueous solutions at low temperatures *J. Vac. Sci. Technol. B Microelectron. Nanom. Struct.* **24** 288

[113] Wu W Y, Yeh C C and Ting J M 2009 Effects of seed layer characteristics on the synthesis of ZnO nanowires *J. Am. Ceram. Soc.* **92** 2718–23

[114] Kenanakis G, Vernardou D, Koudoumas E and Katsarakis N 2009 Growth of c-axis oriented ZnO nanowires from aqueous solution: The decisive role of a seed layer for controlling the wires' diameter *J. Cryst. Growth* **311** 4799–804

[115] Xu S, Lao C, Weintraub B and Wang Z L 2008 Density-controlled growth of aligned ZnO nanowire arrays by seedless chemical approach on smooth surfaces *Mater. Res. Express* **23** 2072–7

[116] Lopez O E, Tucker A L, Singh K R, Mamer S B, Sadoqi M and Xu H 2014 Synthesis of zinc oxide nanowires on seeded and unseeded gold substrates: Role of seed nucleation and precursor concentration *Superlattices Microstruct.* **75** 358–70

[117] Wang S-F, Tseng T-Y, Wang Y-R, Wang C-Y, Lu H-C and Shih W-L 2008 Effects of Preparation Conditions on the Growth of ZnO Nanorod Arrays Using Aqueous Solution Method *Int. J. Appl. Ceram. Technol.* **5** 419–29

[118] Chevalier-César C, Capochichi-Gnambodoe M and Leprince-Wang Y 2014 Growth mechanism studies of ZnO nanowire arrays via hydrothermal method *Appl. Phys. A* **115** 953–60

[119] Demes T, Ternon C, Riassetto D, Stambouli V and Langlet M 2016 Comprehensive study of hydrothermally grown ZnO nanowires *J. Mater. Sci.* **51** 10652–61

[120] Guo M, Diao P and Cai S 2005 Hydrothermal growth of well-aligned ZnO nanorod arrays: Dependence of morphology and alignment ordering upon preparing conditions *J. Solid State Chem.* **178** 1864–73

[121] Vernardou D, Kenanakis G, Couris S, Koudoumas E, Kymakis E and Katsarakis N 2007 pH effect on the morphology of ZnO nanostructures grown with aqueous chemical growth *Thin Solid Films* **515** 8764–7

[122] Joo J, Chow B Y, Prakash M, Boyden E S and Jacobson J M 2011 Face-selective electrostatic control of hydrothermal zinc oxide nanowire synthesis. *Nat. Mater.* **10** 596–601

[123] Burke-Govey C P and Plank N O V. 2017 The influence of polyethylenimine molecular weight on hydrothermally-synthesized ZnO nanowire morphology *Int. J. Nanotechnol.* **14** 47–55

[124] Plank N O V, Snaith H J, Ducati C, Bendall J S, Schmidt-Mende L and Welland M E 2008 A simple low temperature synthesis route for ZnO–MgO core–shell nanowires *Nanotechnology* **19** 465603

[125] Kurudirek S V., Pradel K C and Summers C J 2017 Low-temperature hydrothermally grown 100 μm vertically well-aligned ultralong and ultradense ZnO nanorod arrays with improved PL property *J. Alloys Compd.* **702** 700–9

[126] Baruah S and Dutta J 2009 Effect of seeded substrates on hydrothermally grown ZnO nanorods *J. Sol-Gel Sci. Technol.* **50** 456–64

[127] Cui J B, Daghlian C P, Gibson U J, Püsche R, Geithner P and Ley L 2005 Low-temperature growth and field emission of ZnO nanowire arrays *J. Appl. Phys.* **97** 044315

[128] Sohn J I, Jung Y-I, Baek S-H, Cha S, Jang J E, Cho C-H, Kim J H, Kim J M and Park I-K 2014 A low temperature process for phosphorous doped ZnO nanorods via a combination of hydrothermal and spin-on dopant methods *Nanoscale* **6** 2046–51

[129] Xu S, Adiga N, Ba S, Dasgupta T, Wu C F J and Wang Z L 2009 Optimizing and improving the growth quality of ZnO nanowire arrays guided by statistical design of experiments *ACS Nano* **3** 1803–12

[130] Zhang X, Liu Y and Kang Z 2014 3D branched ZnO nanowire arrays decorated with plasmonic Au nanoparticles for high-performance photoelectrochemical water splitting *ACS Appl. Mater. Interfaces* **6** 4480–9

[131] Liu K, Wu W, Chen B, Chen X and Zhang N 2013 Continuous growth and improved PL property of ZnO nanoarrays with assistance of polyethylenimine *Nanoscale* **5** 5986–93

[132] Gao H, Fang G, Wang M, Liu N, Yuan L, Li C, Ai L, Zhang J, Zhou C, Wu S and

Zhao X 2008 The effect of growth conditions on the properties of ZnO nanorod dye-sensitized solar cells *Mater. Res. Bull.* **43** 3345–51

[133] Nayeri F D, Soleimani E A and Salehi F 2013 Synthesis and characterization of ZnO nanowires grown on different seed layers: The application for dye-sensitized solar cells *Renew. Energy* **60** 246–55

[134] Andrews P W 1984 Retinoic acid induces neuronal differentiation of a cloned human embryonal carcinoma cell line in vitro *Dev. Biol.* **103** 285–93

[135] Pleasure S J, Page C and Lee V M 1992 Pure, postmitotic, polarized human neurons derived from NTera 2 cells provide a system for expressing exogenous proteins in terminally differentiated neurons. *J. Neurosci.* **12** 1802–15

[136] Paquet-Durand F, Tan S and Bicker G 2003 Turning teratocarcinoma cells into neurons: Rapid differentiation of NT-2 cells in floating spheres *Dev. Brain Res.* **142** 161–7

[137] Jain P, Cerone M A, LeBlanc A C and Autexier C 2007 Telomerase and neuronal marker status of differentiated NT2 and SK-N-SH human neuronal cells and primary human neurons *J. Neurosci. Res.* **85** 83–9

[138] MacDonald C, Unsworth C P and Graham E S 2014 Enrichment of differentiated hNT neurons and subsequent analysis using flow-cytometry and xCELLigence sensing *J. Neurosci. Methods* **227** 47–56

[139] “Anatomy and Physiology” by the US National Cancer Institute’s Surveillance E and E R (SEER) P 2006 Neuron Structure *https://en.wikipedia.org/wiki/File:Neuron.svg*

[140] Unsworth C P, Holloway H, Delivopoulos E, Murray A F, Simpson M C, Dickinson M E and Graham E S 2011 Patterning and detailed study of human hNT astrocytes on parylene-C/silicon dioxide substrates to the single cell level *Biomaterials* **32** 6541–50

[141] Yang P, Yan H, Mao S, Russo R, Johnson J, Saykally R, Morris N, Pham J, He R and Choi H J 2002 Controlled growth of ZnO nanowires and their optical properties *Adv. Funct. Mater.* **12** 323–31

[142] Cheng B, Shi W, Russell-Tanner J M, Zhang L and Samulski E T 2006 Synthesis of variable-aspect-ratio, single-crystalline ZnO nanostructures *Inorg. Chem.* **45** 1208–14

[143] Hsueh T J, Chen Y W, Chang S J, Wang S F, Hsu C L, Lin Y R, Lin T S and Chen I C 2007 ZnO nanowire-based CO sensors prepared on patterned ZnO:Ga/SiO2/Si templates *Sensors Actuators, B Chem.* **125** 498–503

[144] Song J and Lim S 2007 Effect of seed layer on the growth of ZnO nanorods *J. Phys. Chem. C* **111** 596–600

[145] Maddah M, Unsworth C P and Plank N O V 2018 Selective growth of ZnO nanowires with varied aspect ratios on an individual substrate *Mater. Res. Express* **6** 015905

[146] Boercker J E, Schmidt J B and Aydil E S 2009 Transport limited growth of zinc oxide nanowires *Cryst. Growth Des.* **9** 2783–9

[147] Tian Z R, Voigt J A, Liu J, Mckenzie B, Mcdermott M J, Rodriguez M A, Konishi H and Xu H 2003 Complex and oriented ZnO nanostructures *Nat. Mater.* **2** 821–6

[148] McPeak K M and Baxter J B 2009 ZnO Nanowires Grown by Chemical Bath Deposition in a Continuous Flow Microreactor *Cryst. Growth Des.* **9** 4538–45

[149] Yamabi S and Imai H 2002 Growth conditions for wurtzite zinc oxide films in aqueous solutions *J. Mater. Chem.* **12** 3773–8

[150] Gibbs J W 1878 *Transactions of the Connecticut Academy of Arts and Sciences* vol 3

[151] Yan D, Cen J, Zhang W, Orlov A and Liu M 2017 Hydrothermal growth of ZnO nanowire arrays: fine tuning by precursor supersaturation *CrystEngComm* **19** 584–91

[152] Coltrin M E, Hsu J W P, Scrymgeour D A, Creighton J R, Simmons N C and Matzke C M 2008 Chemical kinetics and mass transport effects in solution-based selective-area growth of ZnO nanorods *J. Cryst. Growth* **310** 584–93

[153] Guillemin S, Rapenne L, Roussel H, Sarigiannidou E, Brémond G and Consonni V 2013 Formation mechanisms of ZnO nanowires: The crucial role of crystal orientation and polarity *J. Phys. Chem. C* **117** 20738–45

[154] Cheng J J, Nicaise S M, Berggren K K and Gradečak S 2016 Dimensional Tailoring of Hydrothermally Grown Zinc Oxide Nanowire Arrays *Nano Lett.* **16** 753–9

[155] Lee J M, No Y S, Kim S, Park H G and Park W Il 2015 Strong interactive growth behaviours in solution-phase synthesis of three-dimensional metal oxide nanostructures *Nat. Commun.* **6** 6325

[156] Bucaro M A, Vasquez Y, Hatton B D and Aizenberg J 2012 Fine-tuning the degree of stem cell polarization and alignment on ordered arrays of high-aspect-ratio nanopillars *ACS Nano* **6** 6222–30

[157] Hällström W, Prinz C N, Suyatin D, Samuelson L, Montelius L and Kanje M 2009 Rectifying and sorting of regenerating axons by free-standing nanowire patterns: A highway for nerve fibers *Langmuir* **25** 4343–6

[158] Duan X, Fu T-M, Liu J and Lieber C M 2013 Nanoelectronics-biology frontier: From nanoscopic probes for action potential recording in live cells to three-dimensional cyborg tissues *Nano Today* **8** 351–73

[159] Suyatin D B, Wallman L, Thelin J, Prinz C N, Jörntell H, Samuelson L, Montelius L and Schouenborg J 2013 Nanowire-based electrode for acute in vivo neural recordings in the brain *PLoS One* **8** e56673

[160] Li Z, Song J, Mantini G, Lu M Y, Fang H, Falconi C, Chen L J and Wang Z L 2009 Quantifying the traction force of a single cell by aligned silicon nanowire array *Nano Lett.* **9** 3575–80

[161] Shalek A K, Robinson J T, Karp E S, Lee J S, Ahn D-R, Yoon M-H, Sutton A, Jorgolli M, Gertner R S and Gujral T S 2010 Vertical silicon nanowires as a universal platform for delivering biomolecules into living cells *Proc. Natl. Acad. Sci.* **107** 1870–5

[162] Lard M, Ten Siethoff L, Generosi J, Månsson A and Linke H 2014 Molecular motor transport through hollow nanowires *Nano Lett.* **14** 3041–6

[163] Prinz C N 2015 Interactions between semiconductor nanowires and living cells *J. Phys. Condens. Matter* **27** 233103

[164] Bonde S, Buch-Månson N, Rostgaard K R, Andersen T K, Berthing T and Martinez K L 2014 Exploring arrays of vertical one-dimensional nanostructures for cellular investigations *Nanotechnology* **25** 362001

[165] Kwak M, Han L, Chen J J and Fan R 2015 Interfacing Inorganic Nanowire Arrays and Living Cells for Cellular Function Analysis *Small* **11** 5600–10

[166] Buch-Månson N, Bonde S, Bolinsson J, Berthing T and Martinez K L 2015 Towards a better prediction of cell settling on nanostructure arrays - Simple means to complicated

ends *Adv. Funct. Mater.* **25** 3246–55

[167] Patolsky F, Timko B P, Zheng G and Lieber C M 2007 Nanowire-Based Nanoelectronic Devices in the Life Sciences *MRS Bull.* **32** 142–9

[168] Persson H, Li Z, Tegenfeldt J O, Oredsson S and Prinz C N 2015 From immobilized cells to motile cells on a bed-of-nails: Effects of vertical nanowire array density on cell behaviour *Sci. Rep.* **5**

[169] Noy A, Artyukhin A B and Misra N 2009 Bionanoelectronics with 1D materials *Mater. Today* **12** 22–31

[170] Lee J, Kang B S, Hicks B, Chancellor T F, Chu B H, Wang H-T, Keselowsky B G, Ren F and Lele T P 2008 The control of cell adhesion and viability by zinc oxide nanorods *Biomaterials* **29** 3743–9

[171] Lee K Y, Shim S, Kim I S, Oh H, Kim S, Ahn J P, Park S H, Rhim H and Choi H J 2010 Coupling of semiconductor nanowires with neurons and their interfacial structure *Nanoscale Res. Lett.* **5** 410–5

[172] MacDonald C, Unsworth C P and Graham E S 2014 Enrichment of differentiated hNT neurons and subsequent analysis using flow-cytometry and xCELLigence sensing *J. Neurosci. Methods* **227** 47–56

[173] Unsworth C P, Graham E S, Delivopoulos E, Dragunow M and Murray A F 2010 First human hNT neurons patterned on parylene-C/silicon dioxide substrates: Combining an accessible cell line and robust patterning technology for the study of the pathological adult human brain *J. Neurosci. Methods* **194** 154–7

[174] Zaveri T D, Dolgova N V., Chu B H, Lee J, Wong J, Lele T P, Ren F and Keselowsky B G 2010 Contributions of surface topography and cytotoxicity to the macrophage response to zinc oxide nanorods *Biomaterials* **31** 2999–3007

[175] H. Müller K, Kulkarni J, Motskin M, Goode A, Winship P, Skepper J N, Ryan M P and Porter A E 2010 pH-Dependent Toxicity of High Aspect Ratio ZnO Nanowires in Macrophages Due to Intracellular Dissolution *ACS Nano* **4** 6767–79

[176] Park J K, Kim Y-J, Yeom J, Jeon J H, Yi G-C, Je J H and Hahn S K 2010 The Topographic Effect of Zinc Oxide Nanoflowers on Osteoblast Growth and Osseointegration *Adv. Mater.* **22** 4857–61

[177] Onesto V, Villani M, Narducci R, Malara N, Imbrogno A, Allione M, Costa N, Coppedè N, Zappettini A, Cannistraci C V., Cancedda L, Amato F, DI Fabrizio E and Gentile F 2019 Cortical-like mini-columns of neuronal cells on zinc oxide nanowire surfaces *Sci. Rep.* **9** 1–17

[178] Raos B J, Maddah M, Graham E S, Plank N O V and Unsworth C P 2020 ZnO nanowire florets promote the growth of human neurons *Materialia* **9** 100577

[179] Du K and Gan Z 2012 Cellular interactions on hierarchical poly(ε-caprolactone) nanowire micropatterns *ACS Appl. Mater. Interfaces* **4** 4643–50

[180] Alexander D. Bershadsky, Nathalie Q. Balaban and Geiger B 2003 Adhesion-Dependent Cell Mechanosensitivity *Annu. Rev. Cell Dev. Biol.* **19** 677–95

[181] Hanson L, Lin Z C, Xie C, Cui Y and Cui B 2012 Characterization of the cell-nanopillar interface by transmission electron microscopy *Nano Lett.* **12** 5815–20

[182] Racca L, Canta M, Dumontel B, Ancona A, Limongi T, Garino N, Laurenti M, Canavese G and Cauda V 2018 Zinc Oxide Nanostructures in Biomedicine *Smart Nanoparticles for Biomedicine* (Elsevier) pp 171–87

[183] Bozym R A, Chimienti F, Giblin L J, Gross G W, Korichneva I, Li Y, Libert S, Maret W, Parviz M, Frederickson C J and Thompson R B 2010 Free zinc ions outside a narrow concentration range are toxic to a variety of cells in vitro *Exp. Biol. Med.* **235** 741–50

[184] Larry R. Squire 2008 *Fundamental Neuroscience* (Elsevier/Academic Press)

[185] Goodfellow C E, Graham S E, Dragunow M and Glass M 2011 Characterization of NTera2/D1 cells as a model system for the investigation of cannabinoid function in human neurons and astrocytes *J. Neurosci. Res.* **89** 1685–97

[186] Podrygajlo G, Tegenge M A, Gierse A, Paquet-Durand F, Tan S, Bicker G and Stern M 2009 Cellular phenotypes of human model neurons (NT2) after differentiation in aggregate culture *Cell Tissue Res.* **336** 439–52

[187] Chen R, Canales A and Anikeeva P 2017 Neural recording and modulation technologies *Nat. Rev. Mater.* **2** 16093

[188] Neto J P, Baião P, Lopes G, Frazão J, Nogueira J, Fortunato E, Barquinha P and

Kampff A R 2018 Does impedance matter when recording spikes with polytrodes? *Front. Neurosci.* **12** 715

[189] Cui X, Hetke J F, Wiler J A, Anderson D J and Martin D C 2001 Electrochemical deposition and characterization of conducting polymer polypyrrole / PSS on multichannel neural probes *Sensors and actuators* **93** 8–18

[190] George P M, Lyckman A W, Lavan D A, Hegde A, Leung Y, Avasare R, Testa C, Alexander P M, Langer R and Sur M 2005 Fabrication and biocompatibility of polypyrrole implants suitable for neural prosthetics *Biomaterials* **26** 3511–9

[191] Stauffer W R and Cui X T 2006 Polypyrrole doped with 2 peptide sequences from laminin *Biomaterials* **27** 2405–13

[192] Cui X and Martin D C 2003 Electrochemical deposition and characterization of poly (3, 4-ethylenedioxythiophene) on neural microelectrode arrays *Sensors Actuators B Chem.* **89** 92–102

[193] Ludwig K A, Langhals N B, Joseph M D, Richardson-Burns S M, Hendricks J L and Kipke D R 2011 Poly(3,4-ethylenedioxythiophene) (PEDOT) polymer coatings facilitate smaller neural recording electrodes. *J. Neural Eng.* **8** 014001

[194] Green R and Abidian M R 2015 Conducting Polymers for Neural Prosthetic and Neural Interface Applications *Adv. Mater.* **27** 7620–37

[195] Green R A, Lovell N H, Wallace G G and Poole-Warren L A 2008 Conducting polymers for neural interfaces: Challenges in developing an effective long-term implant *Biomaterials* **29** 3393–9

[196] Chen L Y, Yin Y T, Chen C H and Chiou J W 2011 Influence of polyethyleneimine and ammonium on the growth of ZnO nanowires by hydrothermal method *J. Phys. Chem. C* **115** 20913–9

[197] Song S, Hong W-K, Kwon S-S and Lee T 2008 Passivation effects on ZnO nanowire field effect transistors under oxygen, ambient, and vacuum environments *Appl. Phys. Lett.* **92** 263109

[198] Shi L, Xu Y, Hark S, Liu Y, Wang S, Peng L M, Wong K and Li Q 2007 Optical and electrical performance of SnO2 capped ZnO nanowire arrays *Nano Lett.* **7** 3559–63

[199] Chen C, He H, Lu Y, Wu K and Ye Z 2013 Surface passivation effect on the photoluminescence of ZnO nanorods *ACS Appl. Mater. Interfaces* **5** 6354–9

[200] Randles J E B 1947 Kinetics of rapid electrode reactions *Discuss. Faraday Soc.* **1** 11–9

[201] Rahman A R A, Lo C-M and Bhansali S 2006 A micro-electrode array biosensor for impedance spectroscopy of human umbilical vein endothelial cells *Sensors Actuators B Chem.* **118** 115–20

[202] Wu J, Sun M, Jia W, Xu C and Gao D 2017 Impedance analysis of ZnO nanowire coated dry EEG electrodes *J. Biomed. Eng. Informatics* **3** 44

[203] Unsworth C P, Delivopoulos E, Gillespie T and Murray A F 2011 Isolating single primary rat hippocampal neurons & astrocytes on ultra-thin patterned parylene-C/silicon dioxide substrates *Biomaterials* **32** 2566–74

[204] Paquet-Durand F, Tan S and Bicker G 2003 Turning teratocarcinoma cells into neurons: rapid differentiation of NT-2 cells in floating spheres *Dev. Brain Res.* **142** 161–7

[205] Jia H, Rochefort N L, Chen X and Konnerth A 2011 In vivo two-photon imaging of sensory-evoked dendritic calcium signals in cortical neurons. *Nat. Protoc.* **6** 28–35